LOW-TEMPERATURE GEOTHERMAL ENERGY: SYSTEMS MODELING, RESERVOIR SIMULATION, AND ECONOMIC ANALYSIS

A Dissertation

Presented to the Faculty of the Graduate School

of Cornell University

in Partial Fulfillment of the Requirements for the Degree of

Doctor of Philosophy

by

Koenraad Johan Hilde Ferdinand Beckers

May 2016

LOW-TEMPERATURE GEOTHERMAL ENERGY:
SYSTEMS MODELING, RESERVOIR SIMULATION,
AND ECONOMIC ANALYSIS

Koenraad Johan Hilde Ferdinand Beckers, Ph.D.
Cornell University 2016

Performance of low-temperature geothermal energy systems has been investigated though systems modeling, reservoir simulation, and economic analysis. Both utilization of deep geothermal energy with focus on direct-use heat though Enhanced Geothermal Systems (EGS) and shallow geothermal energy exploited with hybrid heat pump systems have been studied.

To assess power output and economic competitiveness of deep geothermal energy for production of heat and/or electricity, a computer tool GEOPHIRES has been developed which combines cost correlations and economic models with reservoir, wellbore, and surface plant models. Simulations show that low-grade EGS resources (with geothermal gradients of ~30°C/km) are unattractive for solely electricity production with estimated levelized costs of electricity between 20 and 60 ¢/kWh$_e$. Utilizing low-grade resources instead for low-temperature (<120°C) direct-use heat applications, results in competitive levelized costs of heat (LCOH) between 6 and 14 $/MMBTU (2.0 and 4.8 ¢/kWh$_{th}$). Given that low-grade resources are widely available and the market for low-temperature heat is significant, geothermal energy becoming a major low-temperature heat supplier should be considered.

To evaluate the energetic and economic performance of hybrid geothermal heat pump (GSHP) systems for cooling-dominated applications, a TRNSYS systems model has been developed and validated with data collected at a full-size experimental hybrid GSHP system providing cooling for a Verizon Wireless cellular tower shelter in Varna, NY with

average continuous cooling load of 11 kW_{th}. Simulations indicate that for the Varna Site weather and operational conditions in the base case scenario, GSHP-based systems allow the owner to save up to 30% of lifetime electricity consumption in comparison with air-source heat pump (ASHP)-based systems. However, mainly because of lower upfront capital costs, ASHP-based systems can have up to 10% lower total cost of ownership.

A novel approach for simulating transient heat transfer with slender bodies in a conductive medium, e.g. geothermal wells and slinky-coil heat exchangers, using the slender-body theory (SBT) has been developed. An efficient numerical implementation is obtained based on a judicious choice of the discrete elements used to represent the body and implementation of the Fast Multipole Method (FMM). The SBT requires a one-dimensional spatial discretization only along the axis of the body in contrast to the three-dimensional discretization for finite element models. Two case studies, heat transfer from two parallel cylinders and heat transfer from a slinky-coil heat exchanger, are used to show the speed and accuracy of the SBT model and its ability to model interacting slender bodies of finite length and bodies with centerline curvature and internal advective heat flow.

BIOGRAPHICAL SKETCH

The author is born and raised in Belgium where he graduated magna cum laude with a B.S. (2007) and M.S. (2009) in Mechanical Engineering at KU Leuven (University of Leuven). He developed an interest in transport phenomena, systems modeling and simulating, and energy science and engineering. He conducted his M.S. Thesis on the design and construction of a lab-scale gasification reactor at TU Munich (Technical University of Munich) in Germany, and gained valuable work experience during a 3-month engineering internship with EGAT (Electricity Generating Authority of Thailand) at the Rajjaprabha Hydro Power Plant near Surat Thani, Thailand.

In 2010, Koenraad moved to the U.S. and enrolled in the Chemical Engineering M.Eng. program in Energy Economics and Engineering at Cornell University on a Fulbright Scholarship and continued his education with doctoral research on geothermal energy under the supervision of Prof. Jeff Tester. Throughout his graduate program, he has been grateful for several extracurricular opportunities, including being teaching assistant at the National Geothermal Academy and President at Von Cramm Cooperative Hall, working as a research engineer at ExxonMobil Upstream Research Company, and visiting 35 U.S. states.

“We are not facing a shortage of resources, but a longage of expectations”

(adapted from Nate Hagens)

ACKNOWLEDGEMENTS

My 5 and half years at Cornell would not have been as wonderful and rewarding without the support, guidance, friendship and love from my colleagues, friends and family. Following is a humble attempt to express my gratitude to several individuals and organizations:

First and foremost, thank you to my advisor Prof. Jeff Tester, not only for teaching me the depths of geothermal and the principles of sound research, but more importantly, for being a friend, for encouraging me to follow my own ideas, and for inspiring me with relentless energy and dedication.

Thank you to my other committee members, Prof. Teresa Jordan and Prof. Donald Koch, for providing valuable research ideas and constructive feedback. My sincere thanks to Polly Marion, Tara Walworth, Hilary Cullen, and Teri Carey for in essence keeping the Energy Institute and IGERT Program running.

I am grateful for the help and advice from Prof. Brian Anderson from West Virginia University on EGS economic modeling, Prof. Cy Yavuzturk from University of Hartford on underground heat transfer modeling, Maria Richards and Casey Brokaw with measuring the thermal conductivity of the shale samples, and Jim Feeney and colleagues from Verizon on the cell tower shelter modeling and data logging.

Partial financial support was provided by the U.S. Department of Energy, the Cornell Energy Institute, the Atkinson Center for a Sustainable Future, the Cornell University Robert Frederick Smith School of Chemical and Biomolecular Engineering, Verizon and Verizon Wireless, the Geothermal Resources Council, the Fulbright Program, the King Baudouin Foundation, and Vesuvius plc, and is greatly appreciated.

Work wouldn't have been as fun if it weren't for my friends in the Tester Group, who brought creative ideas to the thermo classes and gossip to the roof-top lunches. In particular, I would like to thank Sean Hillson for never taking my beliefs for granted, Mitchell Ismael for the many bike rides, and Maciej Lukawski, for being my wingman.

Thank you also to the Crammies, including Alex Garcia, Steph Ellman, Hannah Holmes, Brenton White, Rennie Xie, and many others, for providing me a welcoming home for several years on West Campus and introducing me to the "real American experience". And thank you to my other friends from Cornell and beyond, including Veronica Prush, for the many joyful moments we have experienced together.

Finally and most importantly, thank you to my parents and family for their endless love and support.

Koenraad F. Beckers

Ithaca, NY, USA

March 2016

TABLE OF CONTENTS

NOMENCLATURE

List of Abbreviations

1-U	Single-U
2-U	Double-U
AC	Alternating Current
ACAP	Accelerated Climate Action Plan
ACDC	Alternating Current to Direct Current
AE	Air-Economizer
ASHP	Air-Source Heat Pump
BHE	Borehole Heat Exchanger
CAP	Climate Action Plan
CF	Capacity Factor
CFM	Cubic Feet per Meter
CHP	Combined Heat and Power
COP	Coefficient of Performance
CP	Circulation Pump; Current Pulse
CRF	Capital Recovery Factor
CT	Cooling Tower
CURBI	Cornell University Renewable Bioenergy Initiative
DB	Dry-Bulb
DC	Dry-Cooler or Dry-Fluid Cooler
DLL	Dynamic-Link Library
DOE	Department of Energy
DST	Duct Storage Model
E	End of Heat Pulse
EAT	Entering Air Temperature
EER	Energy Efficiency Ratio

EGS	Enhanced or Engineered Geothermal System
EIA	Energy Information Administration
EPA	Environmental Protection Agency
EWT	Entering Water Temperature
ExWT	Exiting Water Temperature
FCR	Fixed Charge Rate
FCS	Finite Cylindrical Source
FEM	Finite Element Modeling or Methods
FL	Full Load
FLS	Finite Line Source
FMM	Fast Multipole Method
GEOPHIRES	Geothermal Energy for Production of Heat and electricity ("IR") Economically Simulated
GETEM	Geothermal Energy Technology Evaluation Model
GPM	Gallon Per Minute
GPRS	General Purpose Research Simulator
GSHP	Ground-Source or Geothermal Heat Pump
GUI	Graphical User Interface
HDPE	High-Density Polyethylene
HDR	Hot Dry Rock
HHV	Higher Heating Value
HP	Heat Pump
HR	Total Heat Rejection
HVAC	Heating, Ventilating, and Air Conditioning
ICS	Infinite Cylindrical Source
IEA	International Energy Agency
IGSHPA	International Ground-Source Heat Pump Association

ILS	Infinite Line Source
INDC	Intended Nationally Determined Contributions
JEDI	Job and Economic Development Impact
LCA	Life Cycle Assessment
LCOE	Levelized Cost of Electricity
LCOH	Levelized Cost of Heat
LHV	Lower Heating Value
MD	Measured Depth
NPV	Net Present Value
NREL	National Renewable Energy Laboratory
NTU	Number of Transfer Units
O&M	Operation & Maintenance
ORC	Organic Rankine cycle
PCCI	Power Capital Costs Index
PL	Part Load
PN	Point Neglected
PP	Previous Pulse
PS	Point Source
PV	Photovoltaic
RD&D	Research, Development & Demonstration
RHS	Right-Hand Side
S	Start of Heat Pulse
SA	Supply Air
SBT	Slender-Body Theory
SC	Sensible Cooling
SLR	Spacing to Length Ratio
SMU	Southern Methodist University

SPF	Seasonal Performance Factor
TC	Total Cooling
TCO	Total Cost of Ownership
TDR	Time Durations Ratio
TESS	Thermal Energy System Specialists
TMY3	Typical Meteorological Year 3
TRNSYS	Transient System Simulation Program
TRT	Thermal Response Test
TT	Two-Stage
VFD	Variable Frequency Drive
WB	Wet-Bulb

List of Symbols

A	Single Side Area of Fracture in GEOPHIRES	[m^2]
b	Half-Width Aperture of Fracture in GEOPHIRES	[m]
$\boldsymbol{b}$	Coordinates of Point B in SBT Model	[{m, m, m}]
B	Exergy or Availability in GEOPHIRES	[W]
Bi	Biot Number	[-]
c	Specific Heat Capacity for Incompressible Solids	[J/(kg·K)]
C	Heat Capacity	[J/K]
	Cost	[U.S. $]
CAP	Capital Cost	[U.S. $]
cf	Correction Factor	[-]
CF	Cash Flow	[U.S. $/year]
COP	Coefficient of Performance	[-]
c_p	Specific Heat Capacity at Constant Pressure	[J/(kg·K)]
CRF	Capital Recovery Factor	[-]

d	Wellbore Inner Diameter	[m]
$\boldsymbol{d}$	Distance Vector in SBT Model	[{m, m, m}]
D	Sample Diameter in Thermal Conductivity Test	[m]
db	Debt Fraction	[-]
e	Pipe Roughness	[m]
E	Electricity or Heat Produced	[kWh; MMBTU]
el	Electricity Rate	[¢/kWh$_e$]
eq	Equity Fraction	[-]
f	Function; Time Function	[various units]
	Darcy Friction Factor in GEOPHIRES	[-]
	Unit Heat Response Function in SBT Model	[K·m/W]
$\boldsymbol{F}(s)$	Location in Coordinate System	[{m, m, m}]
FCR	Fixed Charge Rate	[-]
Fo	Fourier Number	[-]
g	g-function in BHE Model	[-]
	Gravitational Acceleration in GEOPHIRES	[9.81 m/s^2]
G	Green's Function	[various units]
h	Heat Transfer Coefficient	[W/(m^2·K)]
	Specific Enthalpy in GEOPHIRES	[J/kg]
H	Heaviside Function in SBT model	[-]
	Height (of Fractures) in GEOPHIRES	[m]
i	Interest Rate; Discount Rate; Inflation Rate	[-]
I	Income or Revenue in GEOPHIRES	[U.S. $]
k	Thermal Conductivity	[W/(m·K)]
K	Assigned Term in SBT Derivation	[°C·m/W]
	Curve fit Parameter in GEOPHIRES	[various units]
l	Length of Straight Line Element in SBT Model	[m]

L	Borehole Length	[m]
L_t	Total Slender Body Length Along Center-Line	[m]
$LCOE$	Levelized Cost of Electricity	[¢/kWh$_e$]
$LCOH$	Levelized Cost of Heat	[U.S. $/MMBTU]
lt	Lifetime	[year]
m	Mass Flow Rate	[kg/s]
M	Assigned Term in SBT Derivation	[°C]
	Molecular Mass in GEOPHIRES	[g/mol]
MD	Measured Depth	[m]
n	Arbitrary Number	[-]
N	Number of Wells in GEOPHIRES	[-]
	Number of Layers in BHE Model	[-]
MTN	Maintenance Cost	[U.S. $/year]
N_E	Number of Elements	[-]
N_L	Spatial Discretization of Slender Body	[-]
NPV	Net Present Value	[U.S. $]
N_t	Number of Time Steps	[-]
Nu	Nusselt Number	[-]
p	Percentage Temperature Decrease per Year	[-]
P	Pressure	[Pa]
q	Heat Exchange	[W; BTU/h]
Q	Heat Exchange per BHE or Slender Body Length	[W/m]
r	Radius	[m]
r'	Radial Coordinate in Local SBT Coordinate System	[m]
R	Slender Body Radius	[m]
	Thermal Resistance in BHE Model	[K·m/W]
R_b	Borehole Thermal Resistance	[K·m/W]

R_C	Slender Body Radius of Curvature	[m]
Re	Reynolds Number	[-]
R_t	Effective Pipe Thermal Resistance	[K·m/W]
s	Arc-Length Along Slender Body Center-Line	[m]
	Laplace Variable in GEOPHIRES Reservoir Models	[-]
	Specific Entropy in GEOPHIRES	[J/(kg·K)]
S	Spacing	[m]
SLR	Spacing to Length Ratio	[-]
t	Time	(s; year)
T	Temperature	[°C; °F; K]
TCO	Total Cost of Ownership	[U.S. $]
TDR	Time Durations Ratio	[-]
Th	Thickness	[m]
T_i	Imposed Temperature Field	[°C; °F; K]
t_s	Time-Scale in BHE Model	[s]
U	Velocity	[m/s]
v	Volume Flow Rate per Fracture and Unit Depth of Fracture	[m^2/s]
V	Volume of Rock Blocks	[m^3]
w	Spacing Between Center of Pipes in BHE	[m]
W	Electricity or Heat Production; Power Output	[W; kW; MW]
x	1st Coordinate in Cartesian Coordinate System	[m]
y	2nd Coordinate in Cartesian Coordinate System	[m]
z	3rd Coordinate in Cartesian Coordinate System	[m]
	Depth in GEOPHIRES	[m]
z'	Vertical Coordinate in Local SBT Coordinate System	[m]

List of Greek Symbols

α	Thermal Diffusivity	[m^2/s]
β	Parameter in Multiple Parallel Fractures Model	[-]
γ	Euler's Constant	[0.5772...]
Γ	Parameter in Ramey's Model	[m]
δ	Spatial Length	[m]
ΔP	Pressure Drop	[Pa]
ΔT	Temperature Drop	[°C]
Δz	Layer Thickness in BHE Model	[m]
ϵ	Parameter in 1-D linear Heat Sweep Model	[-]
η	Efficiency	[-]
κ	Linear Fit Slope in TRT Analysis	[°C]
λ	Linear Fit Intercept in TRT analysis	[°C]
Λ	Heat Storage Ratio in 1-D Linear Heat Sweep Model	[-]
μ	Dynamic Viscosity	[kg/(m·s)]
ρ	Density	[kg/m^3]
τ	Time-Scale	[s]
ϕ	Parameter in Multiple Parallel Fractures Model	[-]
Φ	Rock Porosity	[-]
χ	Parameter in Multiple Parallel Fractures Model	[-]
ϕ	Parameter in SBT Model	[-]
ω	Geothermal Gradient	[°C/m]

List of Subscripts

0	Initial; Far-Field; Dead-State
A	Point A in SBT Derivation
AE	Air-Economizer

$ASHP$	Air-Source Heat Pump
amb	Ambient
ave	Average
b	Borehole
c	Cooling; Cold Reservoir
cap	Capital
cas	Casing
CP	Current Pulse in SBT Model
cr	Critical
d	Downwards
db	Debt
DC	Dry-Cooler
$distr$	Distribution
e	End-Point
ef	Effective
E	End of Pulse in SBT Model
eq	Equity
$expl$	Exploration
f	Fluid
fc	Fixed Costs
fr	Fracture
g	Grout
grt	Gross Revenue Taxes
$GSHP$	Ground-Source or Geothermal Heat Pump
h	Hating; Hot Reservoir
i	Year; Pipe Element Index in SBT Model; Inner in BHE model
inf	Inflation

inj	Injection Well
it	Income Taxes
itc	Income Tax Credits
in	Inner Solution in SBT Model
$inner$	Inner Radius
j	Pipe Element Index in SBT Model
lt	Lifetime
m	Medium; Mid-Point;Time Step Index in SBT Model
n	Time Step Index; Grout Layer Index in BHE Model
nd	Non-Dimensional
p	Pipe
pt	Property Tax
pp	Power Plant
PP	Previous Pulse in SBT Model
$prod$	Production Well
r	Rock
ref	Reference
res	Residence
rsv	Reservoir
R	Pipe Element Radius in SBT Model
s	Ground (Soil)
S	Start of Pulse in SBT Model
out	Outlet; Outer Solution in SBT Model
o	Outer in BHE Model
$O\&M$	Operation & Maintenance
$stim$	Stimulation
t	Year

u	Upwards in BHE Model
	Utilization in GEOPHIRES
w	Water
well	Wellfield

LIST OF TABLES

LIST OF FIGURES

CHAPTER 1

INTRODUCTION AND MOTIVATION

The world faces a daunting challenge over the next several decades in providing affordable, environmentally-friendly, and reliable energy and other natural resources to feed a growing population, fuel a growing economy, and supply increasing consumption, while dealing with climate change, geopolitical tensions, and soaring national debts. The challenge might look even more profound when acknowledging that the average consumer has little interest in global affairs and elected political officials tend to follow short-term agendas.

Several agencies and energy companies are projecting a steady increase in global energy demand in the next few decades with fossil fuels remaining as the dominant energy source (EIA, 2015; OECD/IEA, 2015; BP, 2015; ExxonMobil, 2015). The International Energy Agency, for example, predicts a 20% increase in global primary energy demand between 2013 and 2030, illustrated in Figure 1.1, for the Intended Nationally Determined Contributions (INDC) scenario which accounts for the measures put forward by several countries for reducing greenhouse gas emissions. Even with these reduction goals, however, the remaining carbon budget to limit the average global temperature rise to 2°C by 2100, would already shrink to zero by 2040, as shown in Figure 1.2. A 2°C temperature rise is the threshold put forward by the Intergovernmental Panel on Climate Change (IPCC, 2014) to limit the impact of climate change on weather, oceans, ecosystems, agriculture, etc., with examples such as rising sea levels, regionally diminishing crop yields, and increased frequency and intensity of severe weather events including droughts and heatwaves. It is evident that bold leadership, massive investments, and unprecedented international cooperation are required to transform to a sustainable, low-carbon global society where clean energy sources such as solar, wind, biomass, geothermal, and potentially nuclear play a prominent role.

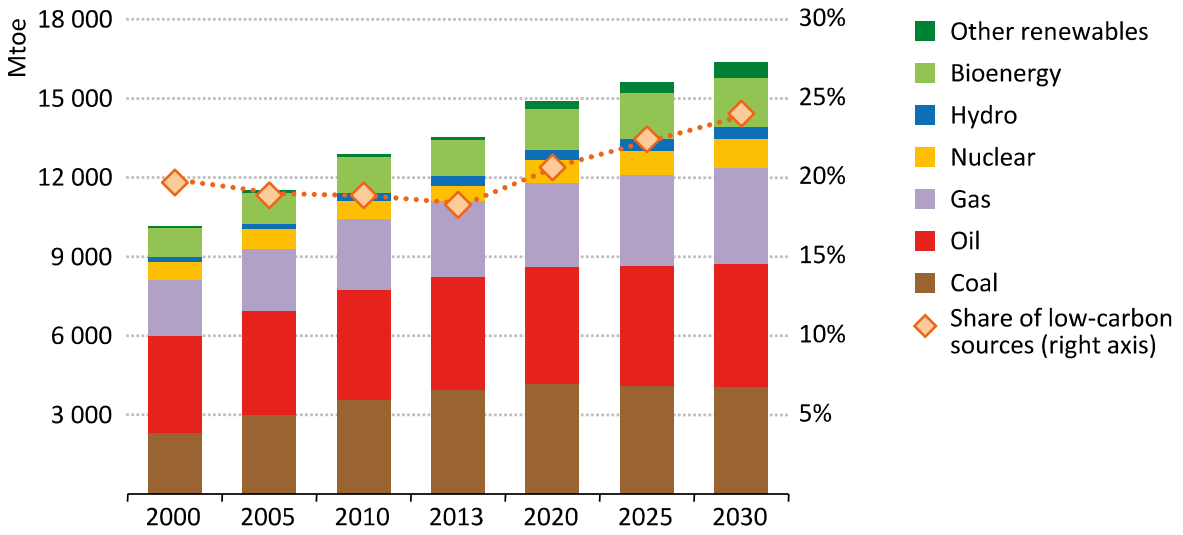

Figure 1.1 – Historic and projected worldwide primary energy consumption by fuel type in Million ton of oil equivalent (Mtoe) for the Intended Nationally Determined Contributions (INDC) scenario by the International Energy Agency (OECD/IEA, 2015). 15,000 Mtoe corresponds to about 630 EJ. "Other renewables" includes geothermal, solar, wind and marine.

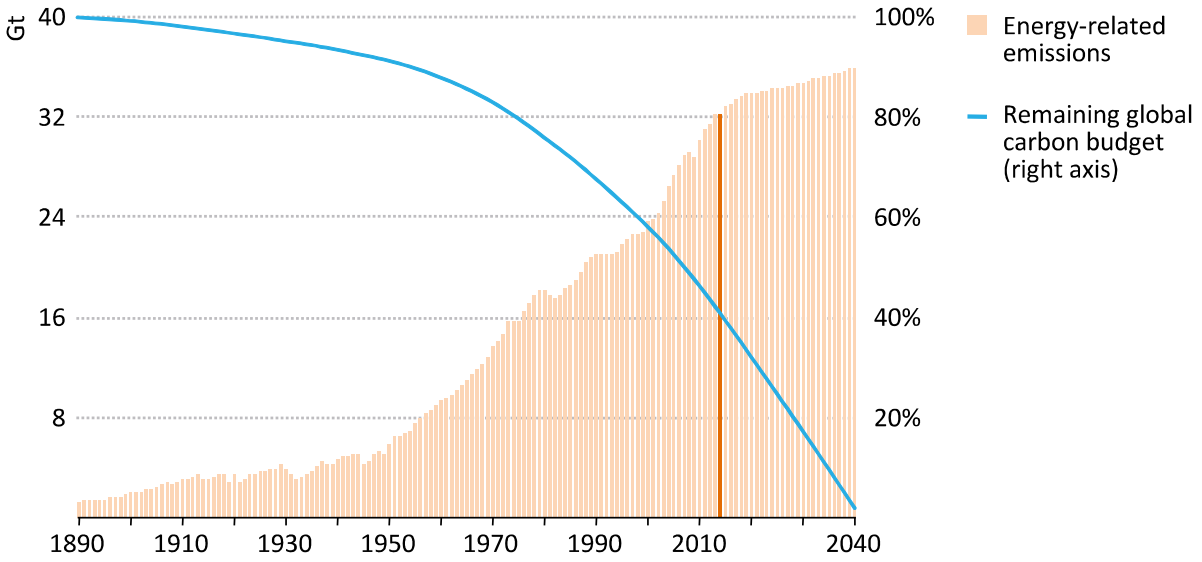

Figure 1.2 – Global energy-related CO_2 emissions in Gt for INDC scenario (red bars; left axis) and remaining carbon budget to limit global temperature rise to 2°C with >50% probability (blue curve; right axis) (OECD/IEA, 2015).

1.1 Geothermal Energy: a Versatile and Reliable Clean Energy Source

Geothermal energy has inherent advantages as a versatile and reliable clean energy source and should therefore be given serious thought as a key player in the future energy system (Tester et al., 2006, 2012; Glassley, 2015). The resource is versatile since it occurs in many forms, qualities, and quantities, and can be utilized for various end-uses including electricity production, direct-use heat and cogeneration of electricity and heat. Deep geothermal energy is defined as resources located at depths from several 100 m to several km and are categorized in this work into (1) hydrothermal resources, (2) hot sedimentary aquifers, and (3) Enhanced or Engineered Geothermal Systems (EGS), also called hot dry rock (HDR). Other deep geothermal resource types and classifications do exist such as magma energy and geopressured systems, but are not further discussed. Hydrothermal resources are the most well-known, with examples as Lardarello in Italy, Hellisheidarvirkjun in Iceland, and the Geysers in California, the latter being the largest geothermal field in the world (DiPippo, 2012). These resources are characterized as having in-situ hot water, and high reservoir permeability and connectivity (see Figure 1.3). They are widely developed globally with a total installed electricity generating capacity of over 12 GW_e (Bertani, 2015), but typically only occur in tectonically or volcanically active regions. The second group, hot sedimentary aquifers, are more geographically distributed with good permeability and connectivity that require moderate drilling depths but typically have lower temperatures and are not as extensively developed. The last category, EGS, typically refers to the thermal energy stored in hot crystalline basement rocks, present anywhere in the world (see Figure 1.4). These reservoirs usually require stimulation to enhance the permeability and connectivity, and moderate to deep drilling depths to reach sufficiently high temperatures. EGS is still in its research phase with few successful pilot field projects that have demonstrated its feasibility at a limited scale (Tester et al., 2006) such as the Fenton Hill project in New Mexico and the Soultz-sous-Forêts project in

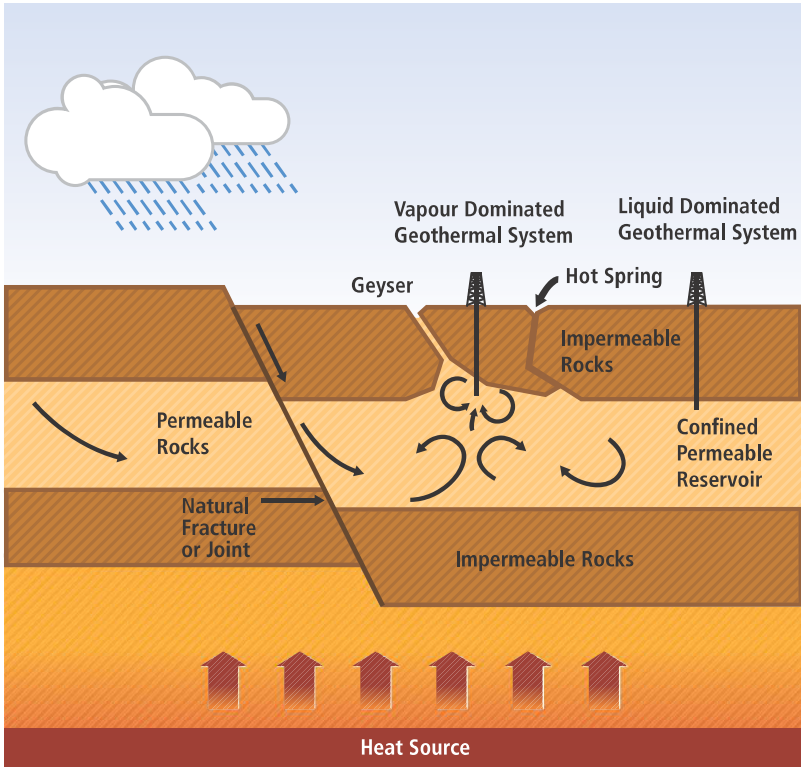

Figure 1.3 – Schematic diagram of hydrothermal geothermal resource, which are characterized as having high reservoir permeability and in-situ hot water (Goldstein et al., 2011).

France. However, due to its massive resource base, developing EGS technology at a commercial scale would be a key factor for geothermal to become a dominant energy player in the 21st century.

Throughout this work, high-, medium-, and low-grade deep geothermal energy resources are interpreted as having high (~70°C/km), medium (~50°C/km) and low (~30°C/km) average geothermal gradients, respectively. Further, high-, medium-, and low-temperature deep geothermal energy resources are considered >200°C, in the range 120-200°C, and <120°C, respectively. In terms of terminology, they are used interchangeably with high, medium, and low geothermal energy supply temperatures. In theory, for a given resource grade, any supply temperature could be achieved depending on the drilling depth. However, from an economic point of view, to obtain high supply tem-

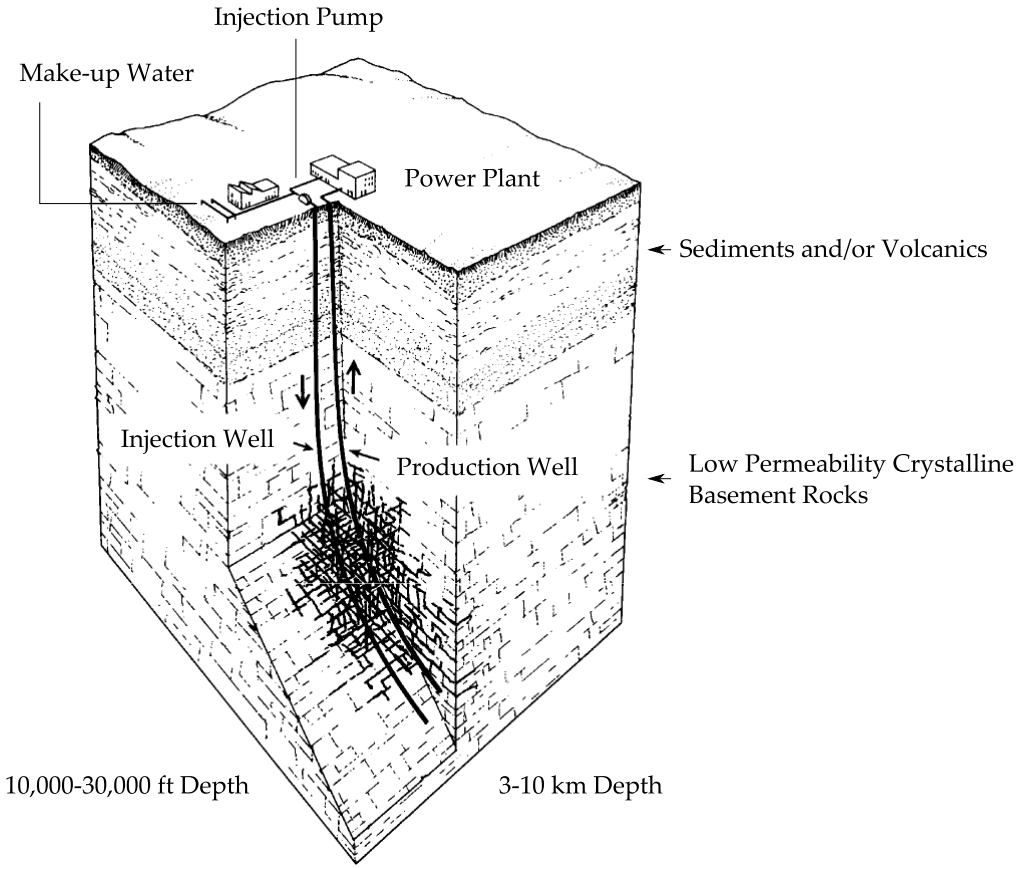

Figure 1.4 – Schematic diagram of Enhanced or Engineered Geothermal System. Heat is extracted from hot crystalline rocks by circulating a heat exchange fluid in a closed-loop through a man-made reservoir (Tester et al., 2006).

peratures, typically high-grade resources are required whereas low supply temperatures could be obtained from any resource grade.

In contrast to deep geothermal energy, shallow geothermal energy is defined as the large thermal source or sink at constant, low temperatures (10-20°C) in the upper 100 to 200 m of the crust. Although not always considered a true geothermal resource, we will refer to it in this work as low-temperature geothermal energy as well, while recognizing that the temperatures are usually too low for direct-use heat. Nevertheless, a shallow geothermal reservoir in combination with a heat pump can efficiently provide space and water heating and cooling. In fact, millions of geothermal heat pump (GSHP) systems have been installed throughout the world.

Geothermal reservoirs have an embedded thermal storage system which allows for reliable baseload, load-following, peak, or dispatchable power production without the need for backup capacity that is typically required for intermittent energy sources such as solar and wind. Further, the amount of thermal energy stored in the Earth, which is a result of the formation of the Earth's core and the decay of radioactive isotopes (Glassley, 2015), is on the order of 10^{13} EJ (Rybach et al., 2000), several orders of magnitude larger than the current worldwide primary energy consumption of about 570 EJ per year (OECD/IEA, 2015). Even when only considering a 1°C drawdown of the upper 10 km of the accessible continental crust, the resource base is still massive, about $2 \cdot 10^6$ EJ (Armstead and Tester, 1987). These huge amounts for stored thermal energy in accessible rocks in the subsurface make up the geothermal resource potential. Unfortunately, some have mistakenly based the geothermal potential on the average steady-state continental heat flux (87 mW/m^2 (Glassley, 2015)), a value much smaller than the solar constant (1,354 W/m^2 (Tester et al., 2012)). In practice, the rate of heat extraction from geothermal systems in commercial use greatly exceeds the steady-state conduction rate, as a result of both convective and conductive heat transfer from the rock mass surrounding the center reservoir. Moreover, research by Fox et al. (2013) has shown that even EGS reservoirs that are governed by heat conduction only can sufficiently recover when deactivated for a period of 2-4 times their initial thermal extraction period. Hence, when applying heat farming strategies by rotating between different reservoirs, EGS methods can be utilized to tap sustainably into the vast geothermal resource base.

Other advantages are that deep geothermal energy systems require no fuel and therefore their operation and economics are not susceptible to volatile fuel prices. Further, they have a relatively low land area footprint and emit few to none greenhouse gas emissions during operation (Tester et al., 2006, 2012; Glassley, 2015). However, greenhouse gases are emitted during construction (e.g. for drilling) and a proper Life Cycle Assessment (LCA) is required to assess the overall environmental impact during the lifetime of the

plant (Frick et al., 2010; Lacirignola and Blanc, 2013; Bayer et al., 2013; Gerber, 2015).

On the other hand, shallow GSHP systems do require electricity (or a heat source with absorption heat pumps) and therefore greenhouse gases are emitted during operation when electricity is derived from fossil fuels. However, when neglecting the electrical grid transmission losses, and assuming an average power plant conversion efficiency of 50%, and a heat pump coefficient of performance (COP) of 4, meaning one unit of electricity is required to supply four units of heat, 50% less energy is consumed in comparison with on-site heating oil or natural gas heating systems.

1.2 Geothermal Energy: an Underused Heat Supplier

Geothermal energy can be utilized for production of electricity, direct-use heat, or for co-generation of electricity and heat, also called combined heat and power (CHP). Medium- and high-grade geothermal resources with supply temperatures of 150°C or higher are required to produce electricity using binary cycle or flash power plants with sufficiently high conversion efficiencies. Resources with lower supply temperatures are ideal to produce direct-use heat for district heating systems, fish farming, greenhouses, and industrial processes such as pasteurization and pulp drying. Other uses for the geothermal brine, not further discussed here, are mineral extraction, and for recreational and medical purposes. Unfortunately, government agencies, utilities, and energy companies often consider geothermal energy solely for electricity production, despite the fact that the majority of the resources are of lower-temperature, with great potential for supplying direct-use heat.

A key improvement in the current energy system would result by properly integrating low-temperature geothermal energy utilization. This would enable achieving a better

match between different energy sources and energy end-uses. Natural gas for example is a high-grade fuel with correspondingly high availability or exergy meaning great potential to do work (Tester et al., 2012). With combustion, temperatures up to 2,000°C are obtained which are ideal for electricity generation in a combined cycle power plant with utilizing some remaining heat for direct-use in a district heating system or industrial process. In contrast, burning natural gas to supply residential heat directly at temperatures around 50°C is from a thermodynamic point of view rather wasteful and results in large amounts of exergy destruction. On the other hand, lower-grade geothermal energy with supply temperatures in the range 50-100°C is a perfect match for supplying residential heat, but is unfortunately often overlooked. In many places around the world, low-temperature heat is predominantly supplied by high-grade fuels such as natural gas and heating oil instead of more appropriate energy sources such as direct-use geothermal, GSHPs, solar thermal and waste heat.

The market for low-temperature heat sources, often forgotten about in national energy debates, is significant. For the U.S., Fox et al. (2011) developed a distribution spectrum of the thermal energy demand in the residential, commercial and industrial sector as a function of its end-use temperature, shown in Figure 1.5. They estimated that a whopping 25 EJ or about 25% of the total U.S. primary energy supply is consumed as low-temperature heat below 120°C, with space and water heating around 50°C accounting for more than half. This compares to about 40% of the primary energy used in the U.S. to generate electricity (EIA, 2011). In the European Union in 2009 (27 member states), the total demand for low-temperature heat in the industrial sector (under 100°C), and for water heating, and space heating and cooling in the residential and commercial sector is estimated at 15 EJ (Pardo et al., 2012), about 20% of the total primary energy demand (EC, 2014). Without a doubt, similar low-temperature heat opportunities are present in other regions around the world.

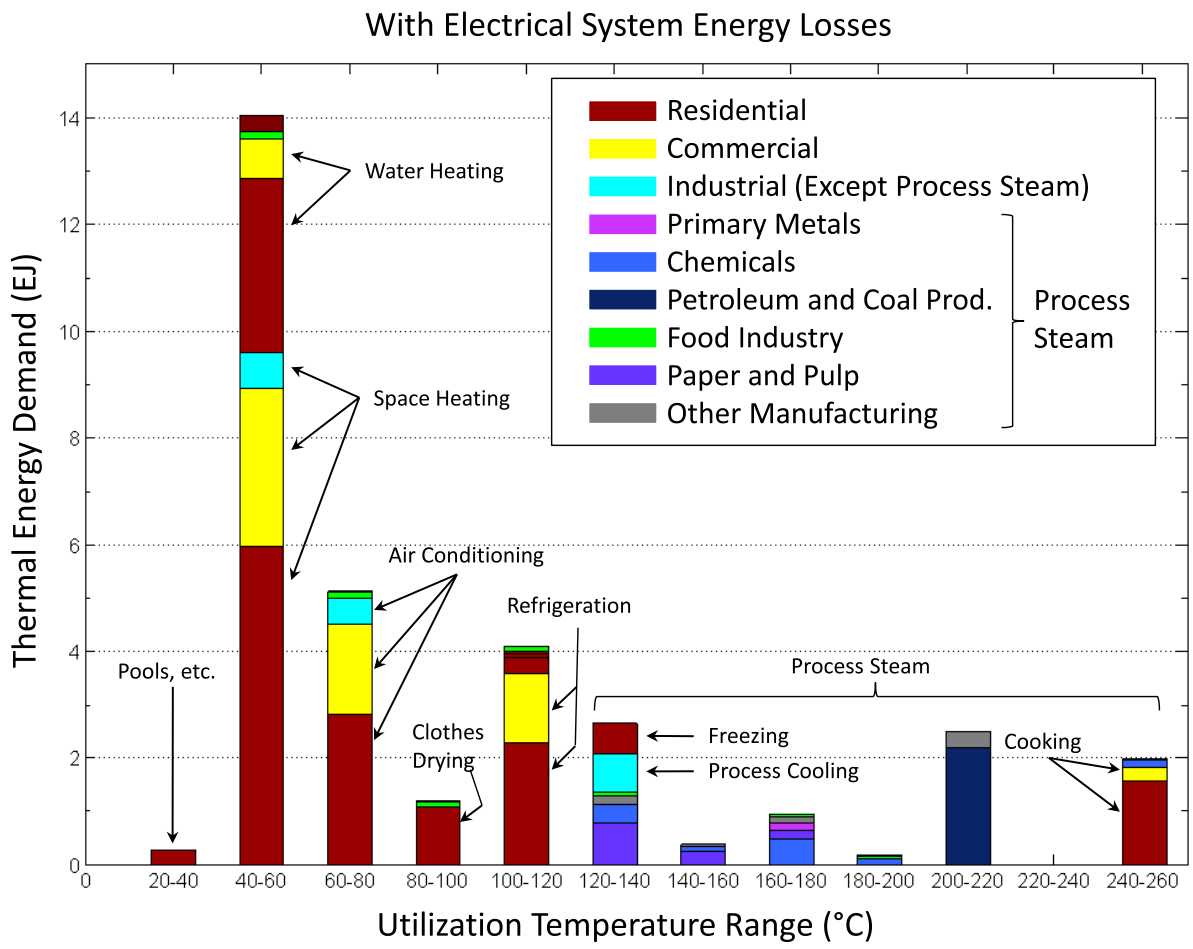

Figure 1.5 – 2008 U.S. thermal energy spectrum. Distribution of thermal energy demand as a function of end-use temperature (Fox et al., 2011).

1.3 Geothermal Energy: Challenges and Solutions

Despite having favorable properties including reliability, sustainability, and versatility, the pace of development of geothermal systems, especially deep geothermal, in many countries including the U.S. is rather low. The compound annual growth rate between 2010 and 2014 for worldwide installed capacity of deep geothermal for electricity production is only 3% (10.9 to 12.6 GW_e) (Bertani, 2015), while for GSHPs around 8.5% (33.1 to 49.9 GW_{th}) (Lund and Boyd, 2015). This is in contrast to an annual growth rate of 13% (198 to 370 GW_e) for wind and 34% (40 to 177 GW_e) for solar photovoltaic (PV)

(REN21, 2015). Key barriers for widespread deployment of both deep and to a certain extent shallow geothermal systems are high investment costs in comparison with alternatives, currently low prices of oil and natural gas (at least in the U.S.), and lack of public understanding coupled with an inherent resistance to change. Other challenges specifically for deep geothermal systems are risks and uncertainty with respect to the resource quality and reservoir productivity.

For developing deep geothermal systems, drilling is required to depths of typically several km which is a capital-intensive operation and can constitute over 50% of the total investment cost of the project. Lukawski et al. (2014) assembled a database of about 150 geothermal wells drilled between 1972 and 2013, and developed an average well drilling and completion cost curve, shown in Figure 1.6. For example, assuming an average geothermal gradient of 30°C/km, a surface temperature of 20°C, and a wellbore temperature drop of 10°C, a doublet system consisting of two wells of 4 km depth would result in an moderate initial production temperature of about 130°C and require a drilling and completion cost of about $11M per well. This illustrates the high upfront capital costs, without even considering that exploration, reservoir stimulation and surface plant costs are incurred before any kWh of heat or electricity are produced. Research is ongoing to develop new and potentially more affordable deep drilling techniques such as jet-assisted, thermal spallation and laser drilling (Maurer, 1980; Pierce et al., 1996; Hillson and Tester, 2015).

Another challenge for exploiting deep geothermal energy is identifying and characterizing the local resource. Unlike wind and solar energy which can be easily measured and quantified, the local geothermal potential can usually not be assessed accurately directly until one or several costly exploration wells have been drilled, since it depends on factors such as the geothermal gradient, the rock permeability and connectivity, and the presence of in-situ hot water. Instead, one utilizes first indirect geological, geochemical

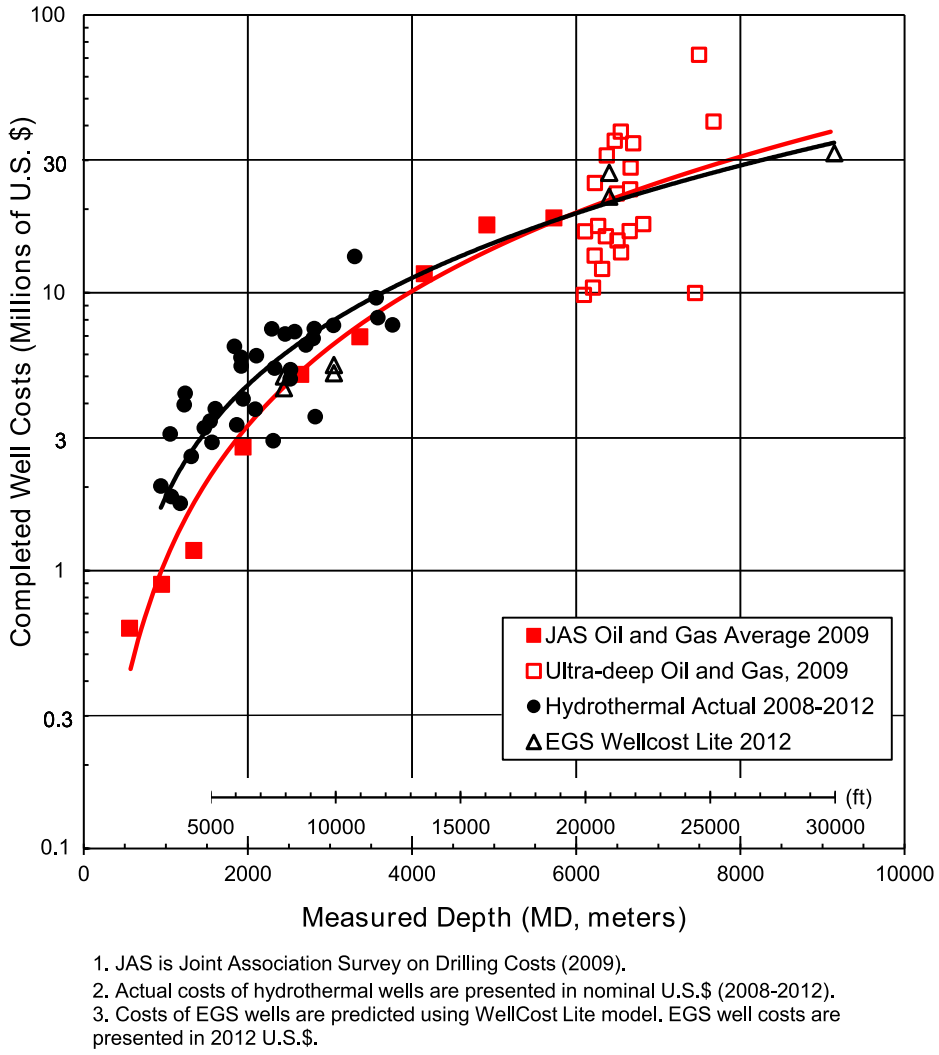

Figure 1.6 – Geothermal Well Drilling and Completion Costs in U.S. M$ as a function of measured depth (Lukawski et al., 2014).

and geophysical methods to collect information on the subsurface (Glassley, 2015), a similar approach as applied in the oil and gas sector. High-grade resources are often found close to active or recently-active volcanoes (e.g. Geysers Field in California), calderas (e.g. Los Humeros Caldera in Mexico), and fault-bounded sedimentary basins (e.g. Imperial Valley in California) or extensional complexes (e.g. Great Basin in Western U.S.). Further, surface manifestations such as geysers, hot springs, and silica sinter and travertine deposits can be an indication of the presence of underground hydrothermal resources. Also, the local fluid composition can reveal the temperature of a potential geothermal

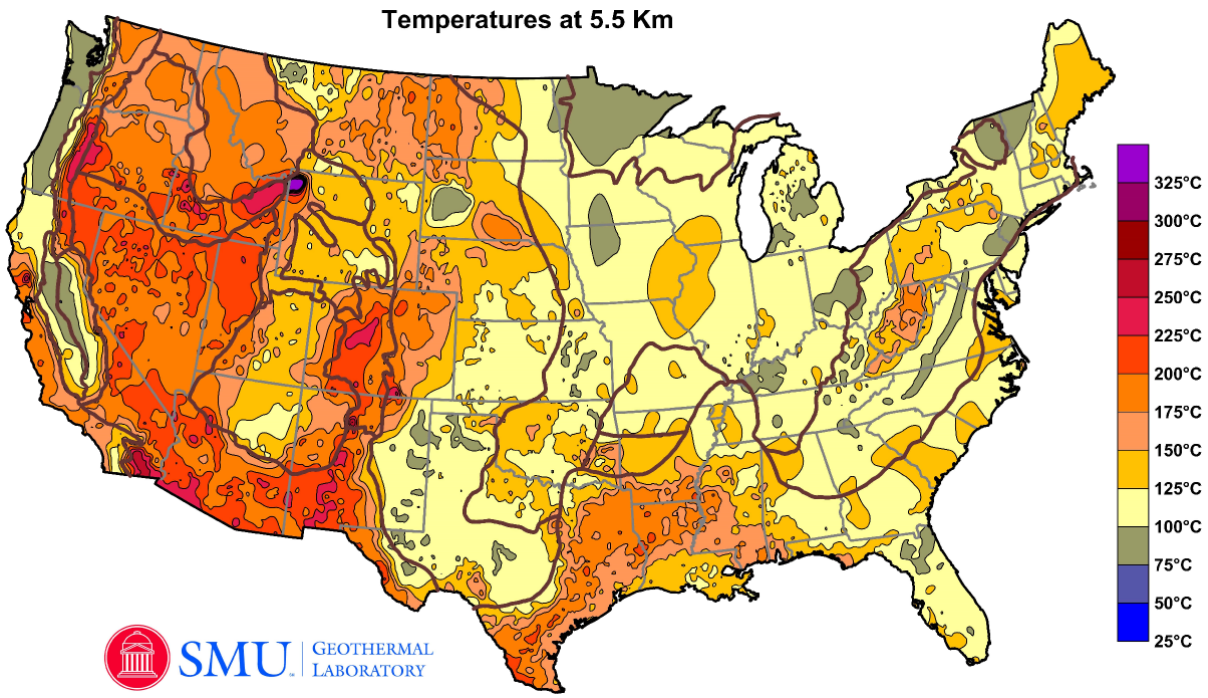

Figure 1.7 – Southern Methodist University (SMU) geothermal resource map for continental U.S.: Temperatures at 5.5 km depth (Blackwell et al., 2013).

reservoir by using Geothermometers (e.g. based on SiO_2) and isotope analysis. More data can be collected through geophysical methods including aeromagnetic, resistivity, magnetotelluric, gravity, and seismic surveys which can reveal subsurface anomalies such as hydrothermally-altered rocks, high fracture density zones, and the presence of in-situ water. Various datasets can be combined to develop favorability maps (e.g. the geothermal potential map for the Great Basin by Coolbaugh et al. (2005)), which can help target promising areas for drilling of exploratory wells. For EGS, one typically creates surface heat flux and temperature-by-depth maps based on well logs from oil, gas, and geothermal exploration and development wells. Examples are the geothermal resource maps for the continental U.S. by researchers from Southern Methodist University (Blackwell et al., 2013) (see Figure 1.7) or the regional maps for the states of New York and Pennsylvania (Stutz et al., 2015).

In order to predict the thermal and hydraulic performance of a potential geothermal

site, or for field management throughout the lifetime of an existing geothermal system, proper reservoir modeling and simulation is required (Grant and Bixley, 2013). Various models can be utilized, from simple analytical to spatially three-dimensional numerical simulators, with or without incorporating data from well logs or productivity tests. O'Sullivan et al. (2001) have provided an excellent overview of geothermal simulators, with TOUGH2 (Pruess, 1991), developed at Lawrence Berkeley Laboratory, probably the most common one. Other examples are the General Purpose Research Simulator (GPRS) from Stanford University (Wong et al., 2015) or the thermo-hydraulic reservoir simulator for fracture-based systems developed by Fox et al. (2014) at Cornell University .

Acid, thermal, or hydraulic stimulation might be necessary to increase the permeability, connectivity and hence productivity of a geothermal reservoir (Tester et al., 2006; Glassley, 2015; Grant and Bixley, 2013). Acid stimulation can be used to remove an obstruction near the wellbore and hereby lower the overall reservoir impedance. Thermal stimulation is achieved by injecting cold water in a hot reservoir, which causes rocks to contract and open up existing fractures. Hydraulic stimulation, the main method applied for creating an EGS reservoir, is based on injecting high-pressure fluids to hydro-shear or hydro-fracture the rocks. Reservoir stimulation can cause induced seismicity (Majer et al., 2007), potentially to unacceptable levels. The Basel 1 EGS site is an example where the occurrence of several microseismic events led to the suspension and later abandonment of the project (Häring et al., 2008). However, with proper operation and management, induced seismicity is expected to be manageable and kept within safe limits (Tester et al., 2006). Research activities (e.g. by McClure (2012)) and field experiments (e.g. the Newberry Volcano EGS Demonstration Project in Oregon (Cladouhos et al., 2015)) are ongoing which provide a better understanding on the link between reservoir stimulation and induced seismic events.

Development of shallow geothermal energy systems is less capital-intensive, less

technically-complex, and typically at a smaller scale (i.e. at the level of an individual home or business owner). However, they are still the subject of extensive research worldwide (Yang et al., 2010; Spitler, 2005; Chua et al., 2010), particularly in the fields of reservoir simulation (e.g. estimating the long-term thermal performance with influence of groundwater flow), and overall system design and hybridization (e.g. integration and optimization of seasonal thermal storage with a hybrid solar-geothermal system). Another specific challenge for GSHPs is raising public awareness of the existence and benefits of this underused technology, e.g. through publicity campaigns (Chua et al., 2010).

1.4 Dissertation Topics and Structure

The dissertation is divided into three parts: Part I: Techno-Economic Analysis of Deep Geothermal Energy for Direct-Use Heat, Electricity and Cogeneration (Chapters 3 to 6); Part II: Techno-Economic Analysis of Hybrid Geothermal Heat Pump Systems for Cooling-Dominated Applications (Chapters 7 to 10); and Part III: Slender-Body Theory for Transient Heat Conduction (Chapters 11 to 15). **Chapter 2** provides the specific dissertation objectives and approach. The key dissertation conclusions and a list of recommendations for future work are given in **Chapter 16**, the final chapter.

Part I of the dissertation provides a techno-economic analysis of deep geothermal energy systems, with focus on EGS for either electricity generation, direct-use heat production, or cogeneration. Given the high investment costs, and resource and reservoir risks and uncertainties of deep geothermal energy, it is crucial to properly evaluate the technical and economic performance of any proposed system. Part I has four chapters: **Chapter 3** sets the tone for Part I with reemphasizing the potential of deep geothermal, specifically EGS, beyond electricity. **Chapter 4** presents a computer program to simulate the heat and/or electricity production of a deep geothermal system, and, combined with capital

and operation and maintenance (O&M) cost models, to evaluate the performance over the lifetime of the system. This program is applied in **Chapter 5** to different case-studies including deep geothermal for solely electricity or direct-use heat production, as well as for cogeneration in a hybrid setting with biomass for the Cornell University campus. The take-away messages are listed in **Chapter 6**.

Part II of the dissertation provides a techno-economic analysis of shallow geothermal energy exploited with hybrid heat pump systems for cooling-dominated, non-residential applications. While GSHPs for residential heating and cooling purposes is nowadays a standard, well-understood HVAC (Heating, Ventilating, and Air Conditioning) option, a better understanding of hybrid systems, as well as of applications beyond the residential sector, is desired. **Chapter 7** provides an introduction to heat pumps, hybridization options and modeling tools. An experimental full-scale hybrid GSHP set-up providing the climate control of a cellular tower shelter on the Cornell University campus is introduced in **Chapter 8**. Numerical simulations and results of various system configurations are presented in **Chapter 9**. The main conclusions are listed in **Chapter 10**.

Part III of the dissertation presents a novel approach using slender-body theory to simulate accurately and computationally-fast the transient heat conduction with slender bodies, e.g. geothermal boreholes and slinky-coil heat exchangers. **Chapter 11** in Part III introduces the slender-body theory and discusses its advantages but also constraints for modeling transient heat conduction. In **Chapter 12**, the theoretical framework is developed and **Chapter 13** presents a possible numerical implementation of the model. Two case-studies to illustrate the applicability and high computational speed of the model are discussed in **Chapter 14**. Finally, a summary and conclusions are given in **Chapter 15**.

References

Armstead, H. C. H. and Tester, J. W. (1987). *Heat Mining*. E. & F.N. Spon Ltd., London and New York.

Bayer, P., Rybach, L., Blum, P., and Brauchler, R. (2013). Review on life cycle environmental effects of geothermal power generation. *Renewable and Sustainable Energy Reviews*, 26: 446–463.

Bertani, R. (2015). Geothermal Power Generation in the World 2010-2014 Update Report. In *Proceedings World Geothermal Congress 2015,* Melbourne, Australia, 19-25 April 2015.

Blackwell, D. D., Richards, M. C., and Frone, Z. S. (2013). *SMU Geothermal Resource Map*. Southern Methodist University (SMU), Dallas, Texas, United States.

BP (2015). *BP Energy Outlook 2035*.

Chua, K., Chou, S., and Yang, W. (2010). Advances in heat pump systems: A review. *Applied Energy*, 87 (12): 3611–3624.

Cladouhos, T. T., Petty, S., Swyer, M. W., Uddenberg, M. E., and Nordin, Y. (2015). Results from Newberry Volcano EGS Demonstration. In *Proceedings World Geothermal Congress 2015,* Melbourne, Australia, 19-25 April 2015.

Coolbaugh, M., Zehner, R., Kreemer, C., Blackwell, D., Oppliger, G., Sawatzky, D., Blewitt, G., Pancha, A., Richards, M., Helm-Clark, C., Shevenell, L., Raines, G., Johnson, G., Minor, T., and Boyd, T. (2005). *Geothermal potential map of the Great Basin, western United States*.

DiPippo, R. (2012). *Geothermal power plants: principles, applications, case studies and environmental impact*. Butterworth-Heinemann, 3rd edition.

EC (2014). *EU energy in figures, Statistical Pocketbook 2014*. European Commission. Available at http://ec.europa.eu/energy/sites/ener/files/documents/2014_pocketbook.pdf.

EIA (2011). *Annual Energy Review 2011*, U.S. Energy Information Administration. DOE/EIA-0384.

EIA (2015). *International Energy Outlook 2015*, U.S. Energy Information Administration.

ExxonMobil (2015). *The Outlook for Energy: A View to 2040*.

Fox, D. B., Sutter, D., and Tester, J. W. (2011). The thermal spectrum of low-temperature energy use in the United States. *Energy & Environmental Science*, 4 (10): 3731–3740.

Fox, D. B., Sutter, D., Beckers, K. F., Lukawski, M. Z., Koch, D. L., Anderson, B. J., and Tester, J. W. (2013). Sustainable heat farming: Modeling extraction and recovery in discretely fractured geothermal reservoirs. *Geothermics*, 46: 42–54.

Fox, D. B., Koch, D. L., and Tester, J. W. (2014). Modeling Discretely Fractured Geothermal Reservoirs: A Focus on Thermal Recovery, Fracture Intersections, and Fracture Roughness. In *GRC Transactions,* 38: 271–280.

Frick, S., Kaltschmitt, M., and Schröder, G. (2010). Life cycle assessment of geothermal binary power plants using enhanced low-temperature reservoirs. *Energy*, 35 (5): 2281–2294.

Gerber, L. (2015). *Designing Renewable Energy Systems: A Life Cycle Assessment Approach.* EPFL Press.

Glassley, W. E. (2015). *Geothermal energy: renewable energy and the environment*. CRC Press, 2nd edition.

Goldstein, B., Hiriart, G., Bertani, R., Bromley, C., Gutiérrez-Negrín, L., Huenges, E., Muraoka, H., Ragnarsson, A., Tester, J., and Zui, V. (2011). Geothermal Energy. In

Edenhofer, O., Pichs-Madruga, R., Sokona, Y., Seyboth, K., Matschoss, P., Kadner, S., Zwickel, T., Eickemeier, P., Hansen, G., Schlömer, S., and von Stechow, C., editors, *IPCC Special Report on Renewable Energy Sources and Climate Change Mitigation*. Cambridge University Press, Cambridge, United Kingdom and New York, NY, USA.

Grant, M. and Bixley, P. F. (2013). *Geothermal Reservoir Engineering*. Elsevier, 2nd edition.

Häring, M. O., Schanz, U., Ladner, F., and Dyer, B. C. (2008). Characterisation of the Basel 1 enhanced geothermal system. *Geothermics*, 37 (5): 469–495.

Hillson, S. D. and Tester, J. W. (2015). Heat Transfer Properties and Dissolution Behavior of Barre Granite as Applied to Hydrothermal Jet Drilling with Chemical Enhancement. In *Proceedings Fortieth Workshop on Geothermal Reservoir Engineering*, Stanford University, Stanford, California, January 26 - January 28, 2015, SGP-TR-204.

IPCC (2014). *Climate Change 2014: Synthesis Report*. Contribution of Working Groups I, II and III to the Fifth Assessment Report of the Intergovernmental Panel on Climate Change [Core Writing Team, R.K. Pachauri and L.A. Meyer (eds.)]. IPCC, Geneva, Switzerland.

Lacirignola, M. and Blanc, I. (2013). Environmental analysis of practical design options for enhanced geothermal systems (EGS) through life-cycle assessment. *Renewable Energy*, 50: 901–914.

Lukawski, M. Z., Anderson, B. J., Augustine, C., Capuano, L. E., Beckers, K. F., Livesay, B., and Tester, J. W. (2014). Cost analysis of oil, gas, and geothermal well drilling. *Journal of Petroleum Science and Engineering*, 118: 1–14.

Lund, J. W. and Boyd, T. L. (2015). Direct Utilization of Geothermal Energy 2015 Worldwide Review. In *Proceedings World Geothermal Congress 2015*, Melbourne, Australia, 19-25 April 2015.

Majer, E. L., Baria, R., Stark, M., Oates, S., Bommer, J., Smith, B., and Asanuma, H. (2007). Induced seismicity associated with enhanced geothermal systems. *Geothermics*, 36 (3): 185–222.

Maurer, W. C. (1980). *Advanced drilling techniques*. Penn Well Books, Tulsa, Oklahoma, United States.

McClure, M. W. (2012). *Modeling and characterization of hydraulic stimulation and induced seismicity in geothermal and shale gas reservoirs*. PhD Dissertation, Stanford University, Stanford, California, United States.

OECD/IEA (2015). *World Energy Outlook Special Report. Energy and Climate Change*, Organisation for Economic Co-operation and Development / International Energy Agency.

O'Sullivan, M. J., Pruess, K., and Lippmann, M. J. (2001). State of the art of geothermal reservoir simulation. *Geothermics*, 30 (4): 395–429.

Pardo, N., Vatopoulos, K., Krook-Riekkola, A., Moya, J. A., and Perez, A. (2012). *Heat and cooling demand and market perspective*. European Commission, JRC Scientific and Policy Reports.

Pierce, K. G., Livesay, B. J., and Finger, J. T. (1996). *Advanced drilling systems study* (No. SAND95-0331). Sandia National Laboratories, Albuquerque, New Mexico, United States.

Pruess, K. (1991). *TOUGH2: A general-purpose numerical simulator for multiphase fluid and heat flow*. Lawrence Berkeley Laboratory, Berkeley, California, United States.

REN21 (2015). *Renewables 2015, Global Status Report, Key Findings*. Renewable Energy Policy Network for the 21st Century. Available at http://www.ren21.net.

Rybach, L., Mégel, T., and Eugster, W. (2000). At what time scale are geothermal resources

renewable? In *Proceedings World Geothermal Congress 2000,* Kyushu - Tohoku, Japan, May 28 - June 10, 2000, volume 2, pages 867–873.

Spitler, J. (2005). Editorial: Ground-source heat pump system researchpast, present, and future. *HVAC&R Research*, 11 (2): 165–167.

Stutz, G. R., Shope, E., Aguirre, G. A., Batir, J., Frone, Z., Williams, M., Reber, T. J., Whealton, C. A., Smith, J. D., Richards, M. C., Blackwell, D. D., Tester, J. W., Stedinger, J. R., and Jordan, T. E. (2015). Geothermal energy characterization in the Appalachian Basin of New York and Pennsylvania. *Geosphere*, 11 (5): 1291–1304.

Tester, J. W., Anderson, B., Batchelor, A., Blackwell, D., DiPippo, R., Drake, E., Garnish, J., Livesay, B., Moore, M. C., Nichols, K., Petty, S., Toksz, M. N., and Veatch Jr., R. W. (2006). *The future of geothermal energy: Impact of enhanced geothermal systems (EGS) on the United States in the 21st century*. MIT.

Tester, J., Drake, E., Driscoll, M., Golay, M., and Peters, W. (2012). *Sustainable Energy: Choosing Among Options*. MIT Press, 2nd edition.

Wong, Z. Y., Horne, R., and Voskov, D. (2015). A Geothermal Reservoir Simulator with AD-GPRS. In *Proceedings World Geothermal Congress 2015,* Melbourne, Australia, 19-25 April 2015.

Yang, H., Cui, P., and Fang, Z. (2010). Vertical-borehole ground-coupled heat pumps: a review of models and systems. *Applied Energy*, 87 (1): 16–27.

CHAPTER 2

OBJECTIVES AND APPROACH

2.1 Dissertation Objectives

The objectives of this dissertation are twofold:

1. Assess the technical and economic performance of deep geothermal energy systems, with a focus on low-temperature Enhanced Geothermal Systems (EGS) for electricity, direct-use heat and cogeneration.
2. Assess the technical and economic performance of shallow geothermal energy systems, with a focus on hybrid geothermal heat pumps for cooling-dominated, non-residential applications.

2.2 Dissertation Approach

The first objective, the topic of Part I of the dissertation, is addressed by developing a simulation tool, called GEOPHIRES (Geothermal Energy for Production of Heat and electricity ("IR") Economically Simulated). This tool incorporates reservoir, wellbore, and power plant models, as well as economic models and capital and operation & maintenance (O&M) cost correlations, in order to calculate the heat and/or electricity output over the lifetime of the plant, and estimate the overall required investment and levelized cost of electricity and/or heat. Different end-uses, i.e. direct-use heat, electricity, and cogeneration, are evaluated for different resources grades and different technology assumptions. Further, a comparison is made with other energy technologies to identify challenges and opportunities for developing deep geothermal energy systems.

The second objective is the subject of Part II of the dissertation. It is approached by developing validated system models using the software packages TRNSYS and MATLAB, in order to conduct transient simulations of hybrid geothermal heat pump systems and assess their energetic performance and costs over the lifetime of the system. The models are validated with data from a full-scale experimental set-up of a hybrid shallow geothermal system providing the climate control of a Verizon cellular tower shelter on the Cornell University campus, as well as with data from literature and data collected at a residential heat pump system in Lansing, NY. The Cornell-Verizon hybrid heat pump system consists of six shallow geothermal boreholes, three heat pump units, a dry-cooler, and air-economizer. Further, the computer models are used to assess the total cost of ownership, and lifetime electricity consumption and CO_2 emissions of various system configurations.

For modeling both deep and shallow geothermal systems, accurate and efficient thermal simulation of the subsurface reservoir is required. A novel approach for simulating transient heat transfer with slender bodies in a conductive medium, using the slender-body theory, is derived in Part III of the dissertation. Based on the theoretical framework, a computationally-fast calculation tool is developed, which is validated with two case-studies. The slender-body theory model allows for simulating complex slender geometries, encountered in many geothermal applications (e.g. deviated geothermal wells and slinky-coil heat exchangers), for which currently no standard heat transfer model exists beyond finite element models, which are typically cumbersome and computationally-intense. Part III contributes both to the first objective of the dissertation, e.g. for estimating wellbore heat transmission with deep deviated geothermal wells which causes a decrease in fluid production temperature and corresponding decrease in heat and electricity output, as well as to the second objective, e.g. for efficiently calculating g-functions utilized in the TRNSYS borehole heat exchanger model.

Part I

Techno-Economic Analysis of Deep Geothermal Energy for Direct-Use Heat, Electricity and Cogeneration

CHAPTER 3

RETHINKING DEEP GEOTHERMAL ENERGY BEYOND ELECTRICITY

Given the benefits and challenges of deep geothermal, a call was made in the introduction (Chapter 2), to consider this energy source not only for electricity production, but also for direct-use heat and cogeneration. Iceland provides a successful example of an integrated geothermal energy infrastructure, where deep geothermal supplies 62% of the country's primary energy demand including about 90% of its space heating demand (Tester et al., 2015b). Nevertheless, only few countries are blessed with high-grade hydrothermal resources like Iceland, and therefore the focus in Part I of the dissertation will be on extracting deep geothermal through Enhanced Geothermal Systems (EGS) for various end-uses, applicable nearly anywhere in the world.

When utilizing thermal energy of the geothermal fluid for supplying low-temperature heat for e.g. district heating instead of electricity generation, one avoids low conversion efficiencies and correspondingly large amounts of waste heat and poor system energetic performance. In addition, lower geothermal fluid temperatures might be acceptable for the direct-use application, which results in lower drilling depths, lower drilling costs, and a decrease in risk and uncertainty. Figure 3.1 shows schematically an EGS scheme producing both electricity in an Organic Rankine Cycle (ORC) or Kalina cycle (DiPippo, 2012), and direct-use heat for a district heating system.

Direct-use and cogeneration typically increase the techno-economic performance of a deep geothermal energy system with respect to pure electricity generation. However, to quantify by how much, careful modeling of the entire system including reservoir, wellbore and surface plant, along with capital and O&M cost predictions for each system component are required. Therefore, a software tool fulfilling this function is developed in Chapter 4 and applied to various case-studies in Chapter 5 to estimate typical power

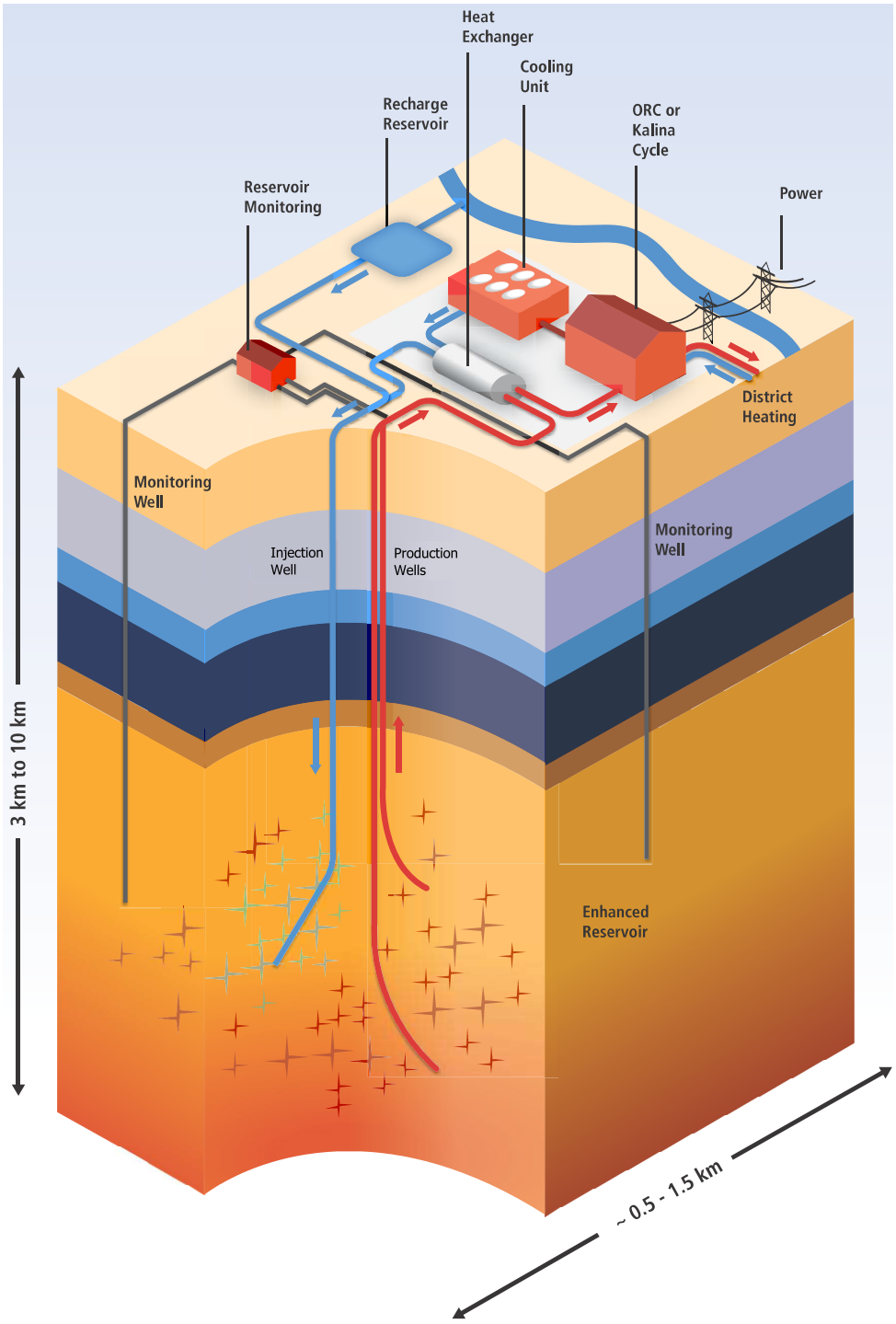

Figure 3.1 – Schematic diagram of deep geothermal energy extraction through EGS for cogeneration (Goldstein et al., 2011).

outputs, required capital investment and cost-competitiveness of deep geothermal not only for electricity, by also for direct-use heat and cogeneration. Also, a comparison with alternatives, and take-away messages are provided.

References

DiPippo, R. (2012). *Geothermal power plants: principles, applications, case studies and environmental impact*. Butterworth-Heinemann, 3rd edition.

Goldstein, B., Hiriart, G., Bertani, R., Bromley, C., Gutiérrez-Negrín, L., Huenges, E., Muraoka, H., Ragnarsson, A., Tester, J., and Zui, V. (2011). Geothermal Energy. In Edenhofer, O., Pichs-Madruga, R., Sokona, Y., Seyboth, K., Matschoss, P., Kadner, S., Zwickel, T., Eickemeier, P., Hansen, G., Schlömer, S., and von Stechow, C., editors, *IPCC Special Report on Renewable Energy Sources and Climate Change Mitigation*. Cambridge University Press, Cambridge, United Kingdom and New York, NY, USA.

Tester, J. W., Reber, T. J., Beckers, K. F., and Lukawski, M. Z. (2015). Deep geothermal energy for district heating: Lessons learned from the U.S. and beyond. In *Advanced District Heating and Cooling (DHC) Systems*. Woodhead Publishing.

CHAPTER 4

GEOPHIRES SIMULATION TOOL

4.1 Motivation and History

Given the risks, uncertainties and upfront costs associated with deep geothermal projects, it is necessary to model and simulate the reservoir, wellbores, and surface plant prior to any site development. Predictions of both technical and economic performance are necessary for comparing with other energy sources, selecting the best location for a new plant, optimizing a system at a given location, developing an optimal reservoir management strategy, or for estimating future behavior using historical operating data.

The Geothermal Energy Technology Evaluation Model (GETEM) (DOE, 2012) and Hot Dry Rock economic (HDRec) (Heidinger et al., 2006) are two examples of techno-economic models used to simulate deep geothermal systems. However, the focus of these and other prior models is solely on generation of electricity, which may not be the most appropriate end-use, at least not for low-grade geothermal. Therefore, a new software tool is developed, called GEOPHIRES, that not only allows simulating production of electricity but also production of direct-use heat and combined heat and power (CHP) or cogeneration. GEOPHIRES is an acronym that stands for **GEO**thermal energy for the **P**roduction of **H**eat and electricity ("**IR**") **E**conomically **S**imulated with "IR" representing electric current and resistance and referring to the electricity mode.

The GEOPHIRES program is built upon previous research and models that date back to the 1970's Fenton Hill HDR (Hot Dry Rock) project at Los Alamos National Laboratory. The work in the Los Alamos project resulted in the thermo-economic HDR model which was used in the "Heat Mining" book by Armstead and Tester (1987). The HDR model was upgraded in the late 1980's culminating in the release of the MIT-HDR model (Tester

and Herzog, 1990). Further upgrades were implemented to produce a Windows version of the MIT-HDR model (Kitsou et al., 2000). In the 2000's, the Windows version became formally known as the "MIT-EGS" model, and was used in the "Future of Geothermal Energy" study (Tester et al., 2006).

In 2012-2014, the "MIT-EGS" model was modified extensively to develop GEOPHIRES. In addition to incorporating different end-uses beyond only electricity production, GEOPHIRES includes new capital and operation&maintenance (O&M) cost models such as the latest geothermal well drilling and completion cost correlations (Lukawski et al., 2014), updated power plant models developed in AspenPlus and MATLAB, and a new economic, reservoir, and wellbore model.

GEOPHIRES was first introduced at the Stanford Geothermal Workshop (Beckers et al., 2013) and later described in detail in an article published in the Journal of Renewable and Sustainable Energy (Beckers et al., 2014a,b). This latter publication forms the basis for most of the material presented in this chapter and the first case-study, utilizing GEOPHIRES, in Chapter 5 (Section 5.1). The other two case-studies in Chapter 5 (Sections 5.2 and 5.3) are based on the journal paper by Reber et al. (2014) on the potential for deep geothermal district heating systems in NY and PA, and the Stanford Geothermal Workshop paper by Beckers et al. (2015) on a hybrid geothermal-biomass cogeneration system for Cornell University, respectively.

4.2 GEOPHIRES Model Structure

GEOPHIRES combines reservoir, wellbore, power plant, and economic models to simulate the electricity and/or direct-use heat production and predict the capital investment, O&M costs, and Levelized Cost of Electricity (LCOE) and/or Levelized Cost of

Heat (LCOH). The LCOE and LCOH are expressed in 2012 U.S. ¢/kWh$_e$ and 2012 U.S. ¢/MMBTU (1 ¢/ kWh$_{th}$= 2.931 $/MMBTU), respectively.

GEOPHIRES has 96 input parameters grouped into 7 categories: resource parameters, engineering parameters, reservoir parameters, financial and operating parameters, capital cost parameters, O&M cost parameters and optimization parameters. The user can choose to either perform a simulation of the geothermal system for a fully determined set of parameters or optimize the system for a minimum LCOE or LCOH with respect to a subset of parameters. GEOPHIRES can either be used as a stand-alone program through a Graphical User Interface (GUI) or as a subroutine to be called from a user-developed master program. The GUI is written in VB.net 9.0 and the underlying calculations are implemented in FORTRAN 77 and 90. Figure 4.1 shows the GEOPHIRES operating scheme. The GUI components are shown in orange ellipses and the FORTRAN components in green rectangles. "Input.txt" and "Output.txt" are text files with respectively the input parameters and output results.

4.3 Correlations and Component Models in GEOPHIRES

The next section provides a detailed description of the GEOPHIRES correlations and component models. Section 4.3.1 explains in detail the 4 different available models implemented in GEOPHIRES to simulate the thermal output of a geothermal reservoir. Consecutively, the production wellbore heat and pressure losses are calculated using a wellbore model, outlined in Section 4.3.2. Next, the surface plant is modeled using correlations provided in Section 4.3.3. The available end-use options are electricity, direct-use heat or combined heat and power (cogeneration). The electricity and/or direct-use heat production over the lifetime of the plant are used in conjunction with capital and O&M cost predictions (Section 4.3.4) to calculate the levelized cost of energy. Three levelized cost

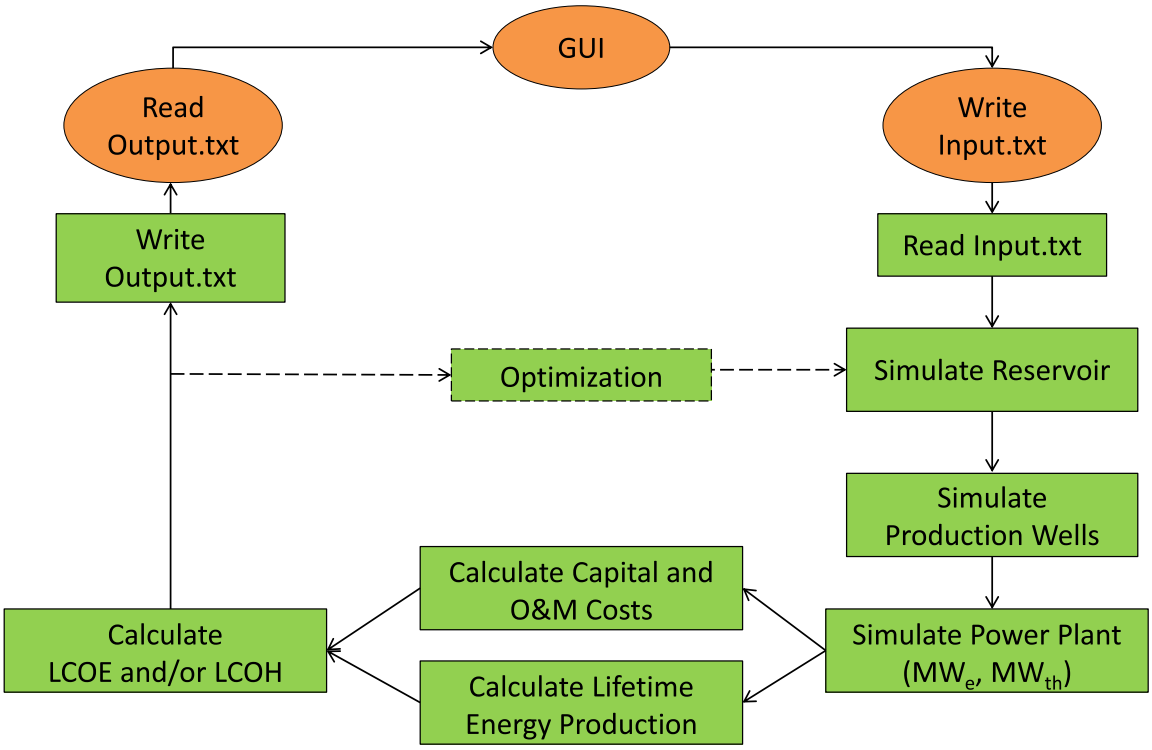

Figure 4.1 – GEOPHIRES operating scheme. GUI components are shown with orange ellipses; the FORTRAN model components are represented by green rectangles.

models, presented in Section 4.3.5, are available to estimate the LCOE and/or LCOH of the system. In simulation mode, GEOPHIRES calculates the LCOE and/or LCOH in a single run with a set of specified input parameters; in optimization mode, the calculations are iterated with updated parameter values using the NAG E04 Numerical Library (NAG, 2011) until a minimum LCOE or LCOH is obtained.

For some components in GEOPHIRES, various models are available with varying levels of detail and complexity. This allows the user to perform simulations of a deep geothermal system with different levels of accuracy ranging from a rough estimate to an in-depth technical and economic feasibility study of a specific project.

4.3.1 Reservoir Models

GEOPHIRES has four built-in models to simulate the reservoir thermal drawdown: (1) the Multiple Parallel Fractures Model, (2) the 1-D Linear Heat Sweep Model, (3) the m/A Thermal Drawdown Parameter Model, and (4) the Percentage Temperature Drawdown Model.

Multiple Parallel Fractures Model

The first model is the Multiple Parallel Fractures Model developed by Gringarten et al. (1975) in which the reservoir is represented by an infinite series of parallel, equidistant and vertical fractures with uniform aperture. The heat extraction occurs through thermal convection with 1-D water flow in the fractures and thermal conduction within the homogeneous, isotropic, and impermeable rock. The reservoir outlet temperature is calculated in the Laplace domain and numerically converted back into the time domain. The water temperature T_w and the fracture spacing S_{fr} are non-dimensionalized as follows:

$$T_{w,nd} = \frac{T_{r,0} - T_w}{T_{r,0} - T_{w,inlet}} \tag{4.1}$$

and

$$S_{fr,nd} = \frac{S_{fr}}{2b} \tag{4.2}$$

with $T_{r,0}$ the initial rock temperature at the point of injection (which is equal to the far-field rock temperature at the same depth), $T_{w,inlet}$ the water inlet temperature, and b the half-width aperture of the fracture. The solution for the dimensionless water outlet temperature $T_{w,outlet,nd}$ in the Laplace domain is given by:

$$\bar{T}_{w,outlet,nd} = \frac{1}{s}\left(1 + \frac{\phi}{\beta}\right)\exp(-\beta) + \frac{\phi}{s} - \frac{\phi}{s\beta} \tag{4.3}$$

with

$$\beta = \tanh\left(\frac{S_{fr,nd} - 1}{\chi}\sqrt{s}\right)\sqrt{s}\,, \tag{4.4}$$

$$\phi = \frac{\omega H_{fr}}{T_r - T_{w,inlet}}, \tag{4.5}$$

$$\chi = \frac{2k_r H_{fr}}{\rho_w c_w v b}. \tag{4.6}$$

In these equations, s is the Laplace variable, k_r is the thermal conductivity of the rock, ρ_w is the density of the water, c_w is the specific heat capacity of the water, ω is the geothermal gradient, H_{fr} is the height (distance along the flow path) of the fractures, and v is the volume flow rate per fracture and per unit depth of the fracture. In order to use this model, the user has to provide a full geometric description of the reservoir in terms of number, spacing and one-side surface area of fractures.

1-D Linear Heat Sweep Model

The second model is the 1-D Linear Heat Sweep Model (Hunsbedt et al., 1984). It assumes that the fractured Enhanced Geothermal System (EGS) reservoir can be modeled as a porous medium with fluid surrounding blocks of rock characterized by a lumped effective rock radius. The heat transfer occurs through 1-D linear heat sweep of water. When non-dimensionalizing the water temperature using:

$$T_{w,nd} = \frac{T_w - T_{w,inlet}}{T_{r,0} - T_{w,inlet}}, \tag{4.7}$$

the solution for the water outlet temperature in the Laplace domain becomes:

$$\bar{T}_{w,outlet,nd} = \frac{1}{s}(1 - \exp(-\epsilon s)) \tag{4.8}$$

with

$$\epsilon = 1 + \frac{NTU}{\Lambda(s + NTU)}. \tag{4.9}$$

The outlet temperature is numerically converted back into the time domain using the Stehfest algorithm (Hunsbedt et al., 1984). NTU and Λ are the number of heat transfer units and the heat storage ratio, respectively. They are calculated as:

$$NTU = \frac{t_{res}}{\tau_{ef,r}} \tag{4.10}$$

and

$$\Lambda = \frac{\rho_w c_w}{\rho_r c_r} \frac{\Phi}{1-\Phi} \,. \tag{4.11}$$

In these equations, Φ is the rock porosity, t_{res} is the residence time of water in the reservoir which can be calculated from the reservoir dimensions and fluid flow rate, and $\tau_{ef,r}$ is the effective rock time constant. Typical porosities for fractured hard rocks in EGS reservoirs are 1 to 7% (Tester et al., 2006); in GEOPHIRES the porosity for this equation is set at 4%. Further, c_r and ρ_r are the specific heat capacity and density of the rock, respectively. The effective rock time constant is given by:

$$\tau_{ef,r} = \frac{r_{ef,r}^2}{3\alpha} \left(0.2 + \frac{1}{Bi} \right) . \tag{4.12}$$

In this equation, $r_{ef,r}$ is the effective rock radius representing the entire collection of rock blocks, α the thermal diffusivity and Bi the Biot number. The value 0.2 represents the typical ratio of conduction path length to $r_{ef,r}$ for spherical shapes (Hunsbedt et al., 1984). $r_{ef,r}$ and Bi are calculated as:

$$r_{ef,r} = 0.83 \left(\frac{3V}{4\pi} \right)^{1/3} \tag{4.13}$$

and

$$Bi = \frac{h r_{ef,r}}{k_r} \tag{4.14}$$

with V the mean volume of the rock blocks, and h the rock surface heat transfer coefficient. This heat transfer coefficient will be relatively large but its exact value is unimportant, assuming that the heat transfer in the reservoir is dominated by the thermal conduction in the rock. Therefore in GEOPHIRES, a value of 500 W/(m^2·K) is heuristically taken for h. The value 0.83 in Equation (4.13) is the Kuo sphericity and represents the typical mean sphericity of a distribution of irregularly shaped rock blocks found in geothermal reservoirs (Hunsbedt et al., 1984).

In order to use the 1-D linear heat sweep model, the user has to provide reservoir dimensions and properties, similar to the first model.

m/A Thermal Drawdown Parameter Model

The third model is the m/A Thermal Drawdown Parameter Model discussed by Armstead and Tester (1987), which treats the reservoir as a single rectangular fracture of specified area with a uniform flow of fluid passing over the fracture surface. The user has to provide the value for the mass loading parameter m/A along with the rock properties k_r, ρ_r, and c_r. The term m/A is defined as the mass flow rate per unit area A of a single side of the fracture. The solution for the dimensionless water outlet temperature $T_{w,outlet,nd}$ is given by:

$$T_{w,outlet,nd} = \frac{T_{w,outlet} - T_{w,inlet}}{T_{r,0} - T_{w,inlet}} = \text{erf}\left(\frac{1}{m/A}\frac{1}{c_w}\sqrt{\frac{k_r \rho_r c_r}{t}}\right) \tag{4.15}$$

with erf the error function and t representing the time in seconds.

Percentage Temperature Drawdown Model

The fourth model is the Percentage Temperature Drawdown Model which expresses the reservoir thermal drawdown in percentage temperature decrease per year. This model is similar to the GETEM thermal drawdown model (DOE, 2012). With p being the percentage temperature decrease per year, the dimensionless water outlet temperature $T_{w,outlet,nd}$ after t years is calculated as:

$$T_{w,outlet,nd} = \frac{T_{w,outlet} - T_{w,inlet}}{T_{r,0} - T_{w,inlet}} = \left(1 - \frac{p}{100}\right)^t . \tag{4.16}$$

Since the Percentage Temperature Drawdown Model is non-dimensionalized in GEOPHIRES, the percentage temperature decrease per year p is independent of the units of the outlet temperature (°C or K).

Which reservoir thermal model to select depends on how much information is available about the subsurface. The Multiple Parallel Fractures Model and the 1-D Linear Heat Sweep Model are the most advanced models, but they also require detailed knowledge

of the fracture and reservoir dimensions which is not always available. Also, a geometry of parallel and equidistant fractures could be too idealistic for a real EGS reservoir, while modeling the heat extraction through heat sweep around spheres might be a better fit for highly permeable and porous hydrothermal systems. If the user wants to implement a known temperature drawdown profile obtained e.g. through measurements of an existing EGS or from a detailed subsurface reservoir model, the Percentage Temperature Drawdown Model may be the best suited. In cases with no prior knowledge of EGS reservoir characteristics or only limited experimental data available, analyzing the expected drawdown for a range of m/A values with the m/A Thermal Drawdown Parameter Model might be the best strategy.

Reservoir Pressure Drop Model

The user inputs in GEOPHIRES the reservoir impedance per well-pair in units of GPa/(m^3/s) in order to calculate the reservoir pressure drop. A typical value would be 0.15 GPa/(m^3/s) (Tester et al., 2006). To calculate the pumping power, this pressure drop is added to the wellbore pressure losses and buoyancy effect (Section 4.3.2). No hydraulic drawdown is considered in GEOPHIRES, only thermal drawdown. This means the mass flow rate per production well remains constant over the lifetime of the plant. However, the circulation pump power will increase with thermal drawdown to offset the decreasing buoyancy effect and maintain a constant mass flow rate.

4.3.2 Wellbore Models

There are two approaches available in GEOPHIRES to calculate the temperature drop from bottom to top in the production wells. Either the user provides a constant tem-

perature drop, or the temperature drop over time is predicted with Ramey's wellbore transient heat transmission model (1962). In Ramey's model, the water temperature drop ΔT_w is given by:

$$\Delta T_w = (T_{r,0} - T_w) - \omega\,(z_{rsv} - \Gamma) + (T_w - \omega\Gamma - T_{r,0}) \exp\left(\frac{-z_{rsv}}{\Gamma}\right) \tag{4.17}$$

with $T_{r,0}$ being the initial average rock temperature in the reservoir, z_{rsv} the average depth of the reservoir, and Γ a parameter defined as (assuming that the thermal resistances of the well casing and cement are negligible):

$$\Gamma = \frac{mc_w f(t)}{2\pi k_r}\,. \tag{4.18}$$

In Equation (4.18), $f(t)$ is the time function which for a line heat source is given by:

$$f(t) = -\ln\left(\frac{r_{cas}}{2\sqrt{\alpha t}}\right) - 0.29 \tag{4.19}$$

with r_{cas} being the outside radius of the casing. For an outside casing diameter of 0.2 m or less, the line source time function is expected to give accurate results after approximately 1 week of operation.

For geologic formations with multiple geothermal gradients, Equation (4.18) has to be applied for each gradient. In such case, z_{rsv} becomes the thickness of each gradient segment, T_w stands for the water outlet temperature from the previous segment and $T_{r,0}$ is the initial or far-field rock temperature at the bottom of the considered segment.

The temperature increase in the injection well is neglected because the reservoir models in Section 4.3.1 assume a constant reservoir inlet temperature over time. Nevertheless, a small change in reservoir inlet temperature causes only a negligible change in reservoir outlet temperature. Therefore, this simplification has no impact on the final result.

The frictional pressure drop in the injection and production wells is calculated using the Darcy-Weisbach equation (Fox et al., 2004):

$$\Delta p = f\frac{L}{d}\frac{\rho_w U^2}{2} \tag{4.20}$$

with f being the Darcy friction factor, L the borehole length, d the borehole inner diameter and U the average water velocity in the borehole. The Darcy friction factor is estimated iteratively with the Colebrook-White equation for turbulent flow in pipes (Fox et al., 2004):

$$\frac{1}{\sqrt{f}} = -2\log_{10}\left(\frac{e/d}{3.7} + \frac{2.51}{Re\sqrt{f}}\right) \tag{4.21}$$

with e being the borehole pipe surface roughness and Re representing the Reynolds number. In GEOPHIRES, a surface roughness of well casing is set at 0.0001 m.

The buoyancy effect on the pressure drop is calculated as:

$$\Delta P = gL\left(\rho_{w,prod} - \rho_{w,inj}\right) \tag{4.22}$$

with g being the gravitational acceleration, L the wellbore length, and $\rho_{w,prod}$ and $\rho_{w,inj}$ the average fluid density in the production and injection wellbores, respectively. The total pressure drop the pump has to overcome is calculated by adding the reservoir pressure drop to the injection wellbore, production wellbores and buoyancy correction pressure drops.

4.3.3 Power Plant Models

The user can choose from three different end-use options: electricity, direct-use heat, and combined heat and power (CHP).

Electricity Generation Model

In electricity mode, all the heat extracted from the geothermal fluid is utilized in a power plant to generate electricity. This power plant can be either an Organic Rankine Cycle (ORC) unit or a flash power plant (DiPippo, 2012). The electricity output W is calculated

as:

$$W = \eta_u B \tag{4.23}$$

where η_u is the utilization efficiency and B the exergy or availability of the geothermal fluid. The exergy of geothermal fluid is calculated as:

$$B = m\left(h_{prod} - h_0 - T_0(s_{prod} - s_0)\right) \tag{4.24}$$

with m, h, s and T_0 the geothermal fluid mass flow rate, its specific enthalpy, specific entropy, and dead state (ambient) temperature, respectively.

The net electricity production is calculated by subtracting the geothermal fluid pumping power from the electricity production calculated using Equation (4.23). The pumping power is calculated as:

$$W_{pump} = \frac{m\Delta P}{\rho_w \eta_{pump}} \tag{4.25}$$

where ΔP is the total pressure drop as discussed in Section 4.3.2 and η_{pump} is the efficiency of the pump.

The utilization efficiency of binary cycle power plants is evaluated using models of a conventional subcritical as well as a supercritical ORC created in Aspen Plus V7.0 software. These models were modified from work done by Randall Field and Chad Augustine (Augustine, 2009) and are continually being updated in our group (Lukawski, 2016). Thermodynamic properties of working fluids are calculated based on the Benedict-Webb-Rubin-Starling (BWRS) equation of state. The design specifications related to the heat exchangers, turbines, and pumps are adopted from Augustine (2009). The model optimization procedure maximized the cycle utilization efficiency and converged to a unique solution by varying the turbine inlet and outlet pressures. In the supercritical cycle, which has an additional degree of freedom, the working fluid mass flow rate is adjusted indirectly by varying the temperature difference at the hot end of the primary heat exchanger. In both ORC models, a heat recuperator is used, if necessary, to recover the heat from tur-

bine exhaust fluid before it is passed to air-cooled condensers. In addition, the turbine exhaust steam quality is limited to ≥0.9 to avoid erosion of the turbine blades. The drop in efficiency due to wet expansion is calculated using the Baumann rule (DiPippo, 2012). Additionally, the condensing pressure in the air cooled condensers is maintained above 1 bar to avoid contamination of the working fluid and its deterioration.

Both the power plant's utilization efficiency η_u and the temperature of reinjected geothermal fluid $T_{w,inj}$ are dependent on the temperatures of heat source T_{prod} and heat sink T_0. Using the Aspen Plus models, η_u and $T_{w,inj}$ are evaluated for geothermal fluid wellhead temperatures of 100-200°C and dry-bulb ambient temperatures of 0-30°C. For each resource temperature, a working fluid maximizing the utilization efficiency is chosen from 25 fluids listed in Table 4.1. Figure 4.2 shows the utilization efficiency of optimal configurations of sub- and supercritical ORC as a function of geothermal fluid wellhead temperature. They are implemented in GEOPHIRES using the following correlation:

$$\eta_u = K_2 \cdot T_{prod}^2 + K_1 \cdot T_{prod} + K_0 \tag{4.26}$$

with the coefficients K provided in Table 4.2.

Single- and double-flash power plants are simulated in MATLAB using the methodology described by DiPippo (2012). A dry-turbine isentropic efficiency of 85% is assumed. The efficiency is corrected using the Baumann Rule if wet expansion occurred. The flash pressures are chosen using the "equal-split temperature rule". The condenser temperature is heuristically set at 25°C above the ambient dry-bulb temperature. The models assume all the geothermal fluid, including the condensed fluid after the turbine, is reinjected to obtain a closed system as desired for EGS. This explains why reinjection temperatures below 100°C can be obtained for flash power plants. The results for the utilization efficiency (η_u) for a single- or double-flash power plant as a function of the geothermal production temperature (T_{prod}) and ambient temperature (T_0) are shown in Figure 4.2. The correlation is given by Equation (4.26) with the coefficients K provided in Table 4.3.

Table 4.1 – Working fluids considered in sub- and supercritical ORC power plant models. Molecular masses (M) of these fluids are listed together with their critical temperatures (T_{cr}) and pressures (P_{cr}).

Fluid	Subcritical	Supercritical	M	T_{cr} (K)	P_{cr} (MPa)
Propane	No	Yes	44.1	369.9	4.25
Isobutene	Yes	Yes	56.2	418.1	4.01
Isobutane	Yes	Yes	58.1	407.8	3.63
Butene	Yes	Yes	56.1	419.3	4.01
Butane	Yes	Yes	58.1	425.1	3.80
Isopentane	Yes	Yes	72.2	460.4	3.38
Pentane	Yes	Yes	72.2	469.7	3.37
Isohexane	Yes	Yes	86.2	497.7	3.04
Hexane	Yes	Yes	86.2	507.8	3.03
Cyclopropane	Yes	Yes	42.1	398.3	5.58
Cyclopentane	Yes	No	70.1	511.8	4.50
Cyclohexane	Yes	No	84.2	553.6	4.08
R32	No	Yes	52.0	351.3	5.78
R152a	Yes	Yes	66.1	386.4	4.52
R134a	Yes	Yes	102.0	374.2	4.06
R245ca	Yes	Yes	134.1	447.6	3.93
R236ea	Yes	Yes	152.0	412.4	3.50
R227ea	Yes	Yes	170.0	376.0	2.93
R218	No	Yes	188.0	345.0	2.64
R142b	Yes	Yes	100.5	410.3	4.06
R141b	Yes	No	117.0	477.5	4.21
Ammonia	Yes	No	17.0	405.4	11.33
Benzene	Yes	No	78.1	562.1	4.89
Toluene	Yes	No	92.1	591.8	4.13

Table 4.2 – Parameter values for ORC utilization efficiency correlation.

	Subcritical Power Plants			Supercritical Power Plants		
T_0	K_2	K_1	K_0	K_2	K_1	K_0
5 °C	0	2.746 e-3	-8.38 e-2	-1.550 e-5	7.604 e-3	-3.78 e-1
15 °C	0	2.713 e-3	-9.18 e-2	-1.499 e-5	7.427 e-3	-3.79 e-1
25 °C	0	2.676 e-3	-1.01 e-1	-1.550 e-5	7.550 e-3	-4.04 e-1

Table 4.3 – Parameter values for flash power plant utilization efficiency correlation.

	Single-Flash Power Plants			Double-Flash Power Plants		
T_0	K_2	K_1	K_0	K_2	K_1	K_0
5 °C	-0.650e-6	0.969e-3	1.673e-1	-1.431e-6	1.334e-3	2.149e-1
15 °C	-0.837e-6	1.085e-3	1.449e-1	-1.680e-6	1.490e-3	1.883e-1
25 °C	-1.057e-6	1.221e-3	1.192e-1	-1.975e-6	1.673e-3	1.533e-1

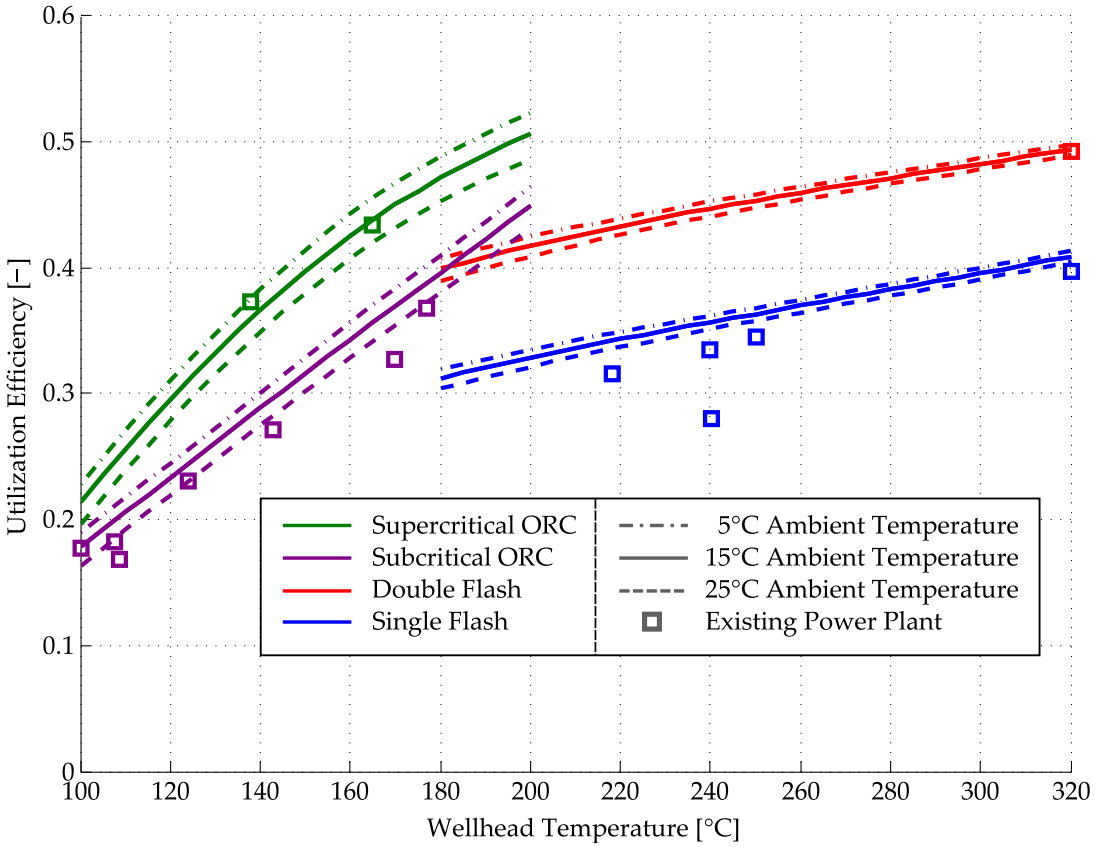

Figure 4.2 – Utilization efficiency η_u for different power plant types as a function of wellhead temperature and dry-bulb ambient temperature.

These utilization efficiency correlations presented are implemented in GEOPHIRES. Linear interpolation and extrapolation is used for different dry-bulb ambient temperatures (T_0).

The utilization efficiency of ORC and flash power plants has been validated using η_u of existing geothermal power plants (DiPippo, 2012, 2004), shown in Figure 4.2 with square markers. Due to lack of data for supercritical ORC, the performance of the supercritical ORC model was compared with advanced subcritical ORC plants (dual-level and double pressure U.S. Geothermal Raft River plant and original dual-fluid Magmamax plants (DiPippo, 2012)). The utilization efficiency of power plants in GEOPHIRES correlates well with performance of existing plants. The slightly higher η_u in GEOPHIRES can be

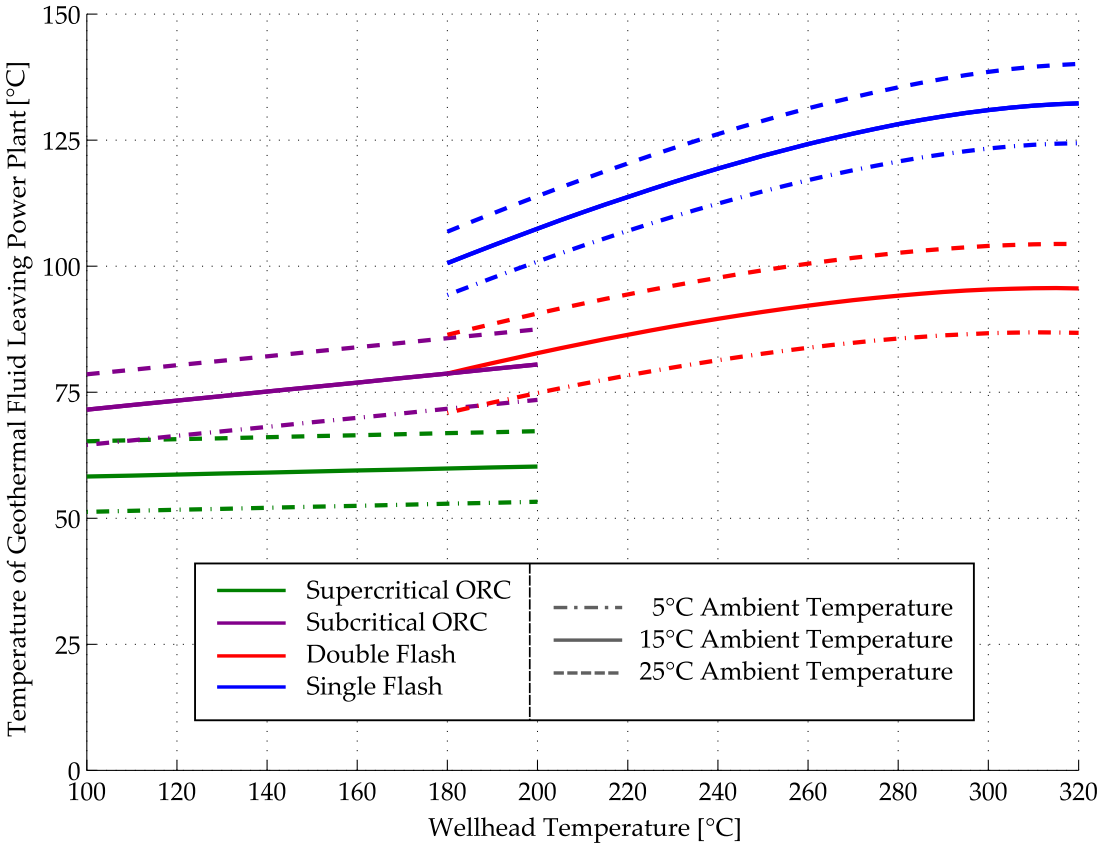

Figure 4.3 – Geothermal fluid exit temperature for different power plant types as a function of wellhead temperature and dry-bulb ambient temperature.

explained by: (1) not including parasitic power losses for downhole pumps in η_u of our models as it is subtracted later by the program, (2) incorporating heat recuperators in all Aspen Plus ORC models, (3) no non-condensable gases present in geothermal fluid in GEOPHIRES, (4) many existing power plants have been designed decades ago, and (5) no constraint on the minimum temperature of geothermal fluid leaving the power plant was assumed in GEOPHIRES.

The temperature of the geothermal fluid leaving the power plant as a function of the ambient and production temperature is shown in Figure 4.3. As mentioned in Section 4.3.2, a constant reinjection temperature is required for the reservoir models. The user provides this temperature but GEOPHIRES verifies it is lower than the geothermal fluid temperature leaving the power plant. In the case-studies conducted in the next

chapter, only subcritical ORC and double-flash power plants are considered because the capital cost correlations are developed for these types of power plants only. The levelized cost is calculated as levelized cost of electricity (LCOE) in 2012 U.S. ¢/kWh$_e$.

Direct-Use Heat Generation Model

In direct-use heat mode, all the heat extracted from the geothermal fluid is used in a direct-use heat application such as an industrial process or a district heating system. No specific process models are built-in into GEOPHIRES but the user can develop its own heat exchanger models, coupled to GEOPHIRES. An example of using GEOPHIRES in a geothermal district heating study is done in the work by Reber (2013), further discussed in Chapter 5.

The pumping power electricity consumption is modeled as an operating expense with user-defined electricity cost. The economic feasibility of direct-use geothermal projects is evaluated in terms of levelized cost of heat (LCOH) and expressed in 2012 $/MMBTU.

Cogeneration or Combined Heat and Power (CHP) Models

In CHP mode, three different configurations are available: a topping cycle, a bottoming cycle and a parallel cycle. In a topping cycle, a high temperature heat-to-power conversion cycle is in series with a low-temperature direct-use heat process. In less common bottoming cycles the geothermal fluid first goes through a high temperature direct-use heat process and consecutively a low-temperature heat-to-power conversion process. In a parallel cycle, the geothermal fluid splits into two streams serving a heat-to-power and direct-use heat process at the same temperature.

In a topping cycle, the temperature of the geothermal fluid leaving the power plant

is assumed to be the input temperature for the direct-use heat process. In a bottoming cycle, the user provides the temperature of the geothermal fluid leaving the direct-use heat process, which is assumed to be the fluid temperature entering the power plant. In a parallel cycle, the user provides the mass fraction of geothermal fluid used for electricity production. In each configuration, the geothermal fluid pump power is subtracted from the gross electricity production to calculate the net electricity production.

The levelized cost in CHP mode can be calculated in GEOPHIRES either as LCOE using the heat sales as operating income with a user-defined heat price ($/MMBTU), or as LCOH using the electricity sales as operating income with a user-defined electricity price (¢/kWh$_e$). The program can also evaluate both the LCOE and LCOH with the fraction of the shared costs attributed to the electricity and direct-use heat production based on their respective use of thermal energy contained in the geothermal fluid.

4.3.4 Cost Correlations

GEOPHIRES has built-in correlations to estimate the capital costs and operation & maintenance (O&M) costs of EGS projects. The user can use these cost correlations directly, multiply them by a certain factor or provide their own costs.

Capital Cost Correlations

The capital costs (C_{cap}) are calculated as the sum of the geothermal well drilling and completion costs ($C_{cap,well}$), the surface plant costs ($C_{cap,pp}$), the reservoir stimulation costs ($C_{cap,stim}$), the fluid distribution costs ($C_{cap,distr}$) and the resource exploration costs ($C_{cap,expl}$):

$$C_{cap} = C_{cap,well} + C_{cap,pp} + C_{cap,stim} + C_{cap,distr} + C_{cap,expl}\,. \tag{4.27}$$

The geothermal well drilling and completion costs are calculated as (in 2012 U.S. M$) (Lukawski et al., 2014):

$$C_{cap,well} = N \cdot C_{cap,1well} = N \cdot \left(1.72 \cdot 10^{-7} \cdot MD^2 + 2.3 \cdot 10^{-3} \cdot MD - 0.62\right) \tag{4.28}$$

with N the number of wells drilled (assuming all identical), and MD the measured depth of one well (i.e. length of the wellbore along path) in meters. In comparison with the 2004 drilling cost correlation in the Future of Geothermal Energy report (Tester et al., 2006), the drilling costs have been increased 30 to 80% as a function of depth with an average of about 50%.

The power plant capital cost correlations are presented in Figure 4.4. The correlations for Organic Rankine Cycle (ORC) power plants are based on the revised cost correlation by Mines (2008), the correlations used in the Job and Economic Development Impact (JEDI) Model (Johnson et al., 2012) and the correlations used in the Future of Geothermal Energy report (Tester et al., 2006). The cost data is brought to 2012 U.S. $ using the IHS CERA Power Capital Costs Index (PCCI) (IHS, 2013). The correlation for a 15 MW_e ORC is given by (in $):

$$C_{cap,pp} = \begin{cases} W \cdot \left(K_3 \cdot T_{prod}^3 + K_2 \cdot T_{prod}^2 + K_1 \cdot T_{prod} + K_0\right) & \text{if } T_{prod} < 170°\text{C} \\ W \cdot \left(2{,}212.5 - 0.514 \cdot \left(T_{prod} - 170°\text{C}\right)\right) & \text{if } T_{prod} \geq 170°\text{C} \end{cases} \tag{4.29}$$

with

$$\begin{cases} K_3 = 1.45833 \text{ e-3} \\ K_2 = 7.6875 \text{ e-1} \\ K_1 = -1.34792 \text{ e2} \\ K_0 = 1.0075 \text{ e4} \end{cases} \tag{4.30}$$

and W the nominal power output (installed capacity) expressed in kW_e. For a power plant with output different than 15 MW_e, the capital cost is calculated as the cost for a 15 MW_e ORC multiplied with a correction factor:

$$C_{cap,pp} = \left(C_{cap,pp} \text{ for } 15{,}000 \text{ kW}_\text{e}\right)\left(\frac{W}{15{,}000 \text{ kW}_\text{e}}\right)^{-0.06} \tag{4.31}$$

with W expressed in kW_e. For a double-flash power plant, the capital costs correlations are derived from 2012 GETEM capital cost data (DOE, 2012). GEOPHIRES calculates the costs as:

$$K_2 \cdot T_{prod}^2 + K_1 \cdot T_{prod} + K_0 \tag{4.32}$$

with parameters K specified in Table 4.4.

Table 4.4 – Parameter values for double-flash power plant capital cost correlation.

W_{ref}	K_2	K_1	K_0
5 MW_e	4.847 e-2	-35.219	8.447 e3
10 MW_e	4.060 e-2	-29.382	6.991 e3
25 MW_e	3.277 e-2	-23.552	5.526 e3
50 MW_e	3.472 e-2	-23.814	5.179 e3
75 MW_e	3.527 e-2	-24.396	5.197 e3
100 MW_e	3.391 e-2	-23.489	5.024 e3

For installed capacities different than those given above, the capital costs are estimated using interpolation/extrapolation with a power law curve. The power law curve is fitted to the lower and upper bound of the bin containing the actual power output W for interpolation or to the two closest values (5 and 10 MW_e or 75 and 100 MW_e) for extrapolation.

In direct-use heat mode, the surface plant equipment cost strongly depends on the application. The built-in correlation in GEOPHIRES is (in $):

$$C_{cap,pp} = 150 \cdot W \tag{4.33}$$

with W the nominal thermal output (installed capacity) in kW_{th}. In CHP mode, the power plant capital investment is the sum of the electric power plant and direct-use heat plant costs, which are calculated using the equations above.

For the reservoir stimulation costs, it is assumed that only the injection well is stimulated with a flat rate of $2.5M per injection well (Mines and Nathwani, 2013). The maximum number of production wells per injection well is set at four.

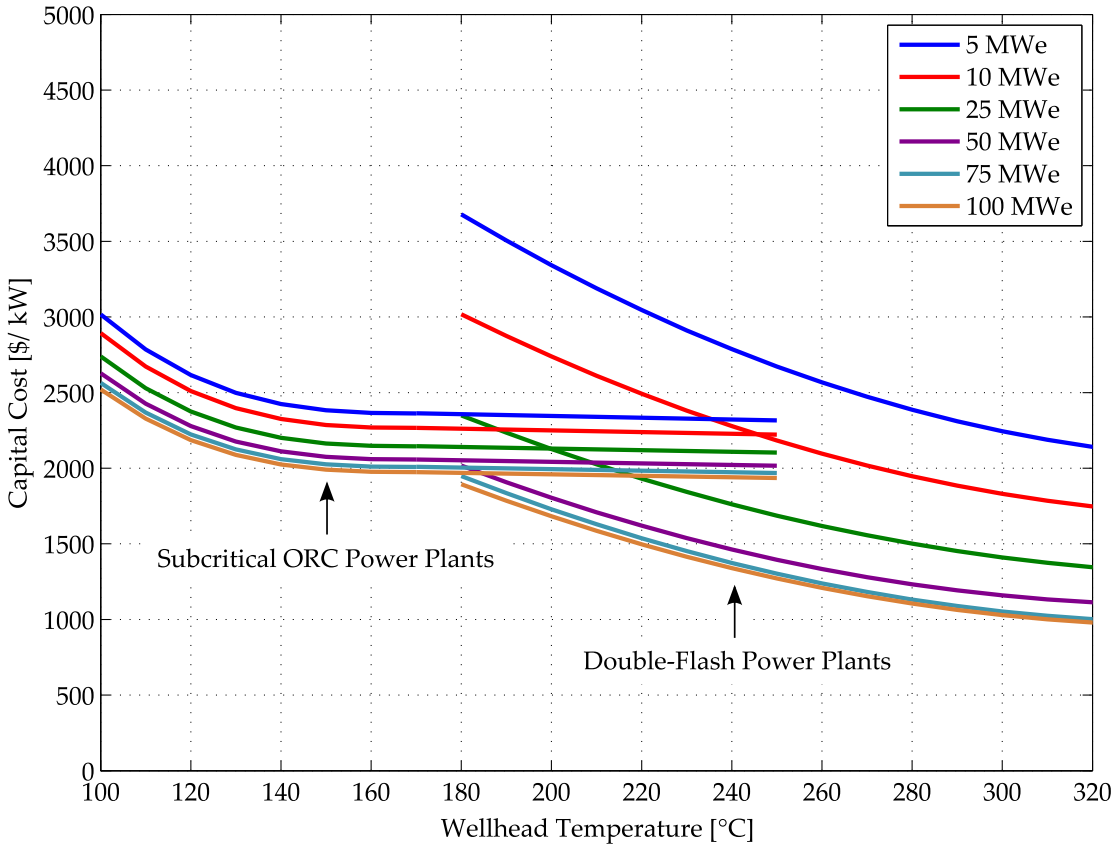

Figure 4.4 – Capital cost correlations for subcritical ORC and double-flash power plants as a function of initial wellhead temperature (production temperature) and installed generating capacity.

The fluid distribution costs are the capital costs related to the surface brine gathering system and are estimated as (in $):

$$C_{cap,distr} = 50 \cdot W \tag{4.34}$$

where W is the thermal energy extracted from geothermal fluid in kW_{th}. These expenditures cover only the piping between production and injection wells and the plant. In the case of a geothermal district heating system, the user has to provide additional cost figures to account for these expenses.

The resource exploration cost correlation in GEOPHIRES is loosely based on the correlation used in GETEM (DOE, 2012) and is given by:

$$C_{cap,expl} = 1.12 \cdot (\$1\text{M} + 0.6 \cdot C_{1\,well}) \tag{4.35}$$

which assumes one slim-hole well is drilled at 60% of the cost of a regular well (production or injection well), \$1M are the expenses to cover non-drilling activities such as geophysical surveys and field work, and the factor 1.12 accounts for the technical and office support expenses. This correlation is arbitrary and will not represent the exploration cost of every EGS project. Depending on the success rate of the exploration wells and whether the site is in a "green field" or "brown field", different projects require different non-drilling related work and a different number of exploration wells. Further, the cost of each exploration well depends on whether it is a core-hole, slim-hole or production-size well. Finally, some projects require drilling of confirmation wells.

O&M Cost Correlations

The annual operation and maintenance (O&M) costs are calculated as the sum of the power plant O&M costs ($C_{O\&M,pp}$), wellfield O&M costs ($C_{O\&M,wf}$) and make-up water costs ($C_{O\&M,w}$):

$$C_{O\&M} = C_{O\&M,pp} + C_{O\&M,wf} + C_{O\&M,w}\,. \tag{4.36}$$

To estimate the power plant O&M costs, it is assumed they consist of 75% of the total labor costs and 1.5% of the upfront power plant capital costs, a similar approach as used in the GETEM program (DOE, 2012) (in \$/year):

$$C_{O\&M,pp} = 0.75 \cdot C_{labor} + 1.5\% \cdot C_{cap,pp} \tag{4.37}$$

where C_{labor} is the annual labor cost, calculated in electricity mode using the following correlation based on the GETEM correlation(DOE, 2012) (in k\$):

$$C_{labor} = \begin{cases} 236 & \text{if } W < 2.5 \text{ MW}_\text{e} \\ 589 \cdot \ln(W) - 304 & \text{if } W \geq 2.5 \text{ MW}_\text{e} \end{cases} \tag{4.38}$$

where W is the nominal output of the plant in MW_e and ln the natural logarithm. In direct-use heat and CHP mode, the correlation for the labor cost is (in k$):

$$C_{labor} = \begin{cases} 236 & \text{if } W < 12.5 \text{ MW}_{\text{th}} \\ 589 \cdot \ln(W/5) - 304 & \text{if } W \geq 12.5 \text{ MW}_{\text{th}} \end{cases} \tag{4.39}$$

where W is the amount of heat withdrawn from the geothermal fluid in MW_{th}.

The wellfield O&M costs consist of the remaining 25% of the labor costs and 1% of the total well capital costs, again similar to the correlation in GETEM (DOE, 2012) (in $/year):

$$C_{O\&M,wf} = 0.25 \cdot C_{labor} + 1\% \cdot C_{cap,well} \,. \tag{4.40}$$

In the case of reservoir temperature drawdown beyond a user-defined threshold, redrilling is required. The capital cost for these wells are modeled as O&M costs by dividing their cost by the lifetime of the plant and adding them to the wellfield O&M costs.

The user has to input the water loss rate occurring in the EGS reservoir. The annual expenses to pay for the make-up water are calculated using a water rate of $660/Ml ($2.5 per 1000 gallons).

All the capital and O&M cost correlations provided in this section come with inherent uncertainties. To address these uncertainties, a sensitivity analysis is performed when evaluating the levelized costs for various EGS scenarios in Section 5.1.

4.3.5 Levelized Cost Models

Three models are available in GEOPHIRES to calculate the levelized cost of electricity (LCOE) or heat (LCOH): (1) the Fixed Charge Rate Model, (2) the Standard Levelized Cost Model, and (3) the BICYCLE Levelized Life Cycle Cost Model.

Fixed Charge Rate (FCR) Model

The first model is the Fixed Charge Rate (FCR) Model in which the LCOE/LCOH is calculated as (Armstead and Tester, 1987):

$$LCOE \text{ or } LCOH = \frac{FCR \cdot C_{cap} + C_{O\&M}}{E} \tag{4.41}$$

with C_{cap} the total capital investment, $C_{O\&M}$ the yearly operation and maintenance (O&M) cost and E the average annual electricity output in kWh_e or direct-use heat generation in MMBTU. The FCR is a single number, e.g. 12.8% in the National Energy Modeling System (Tester et al., 2006), which is multiplied by the total capital cost to obtain the annual cost of invested capital. The FCR is estimated based on several financial parameters, e.g. debt interest rate, rates of return on equity capital, and tax rates (Armstead and Tester, 1987):

$$FCR = CRF + f(CRF(i, n), \text{tax credits}) \tag{4.42}$$

with CRF the capital recovery factor. The CRF is the fraction of capital investment that must be paid back every year to fully repay a loan within n years at an interest rate i. It is calculated as (Armstead and Tester, 1987):

$$CRF(i, n) = \frac{i}{1 - (1 + i)^{-n}} \,. \tag{4.43}$$

Standard Levelized Cost Model

The second model is the Standard Levelized Cost Model which discounts both expenditures and revenues to current day dollars (OECD/IEA, 2010):

$$LCOE \text{ or } LCOH = \frac{C_{cap} + \sum_{t=1}^{lt} \frac{C_{O\&M,t} - I_t}{(1+i)^t}}{\sum_{t=1}^{n} \frac{E_t}{(1+i)^t}} \tag{4.44}$$

with lt being the lifetime of the plant, C_{cap} the capital investment, and $C_{O\&M,t}$, I_t and W_t representing the O&M cost, revenue from heat or electricity sales in CHP mode, and electricity or direct-use heat generation in year t, respectively.

BICYCLE Levelized Cost Model

The third and most advanced economic model is the BICYCLE Levelized Life Cycle Cost Model developed at Los Alamos National Laboratory (Hardie, 1981). This model assumes that the financing of the EGS project occurs through debt (bonds) and equity and allows for variable debt/equity return rates. The ratio of outstanding debt to outstanding equity remains constant while paying off over the lifetime of the plant. Furthermore, the model takes into account inflation, tax rates and tax credits. The levelized cost is calculated as:

$$LCOE \text{ or } LCOH = \frac{NPV}{\sum_{t=1}^{lt} \frac{W_t \cdot (1+i_{inf})^t}{(1+i_{ave})^t}} \tag{4.45}$$

where NPV is the net present value, i_{inf} the inflation rate and i_{ave} the average return on investment (tax and inflation adjusted), calculated as:

$$i_{ave} = db \cdot i_{db} \cdot (1 - i_{it}) + eq \cdot i_{eq} \tag{4.46}$$

with db, eq, i_{db}, i_{it} and i_{eq} the fraction of investment through debt, the fraction of investment through equity ($eq = 1 - db$), the inflated debt interest rate, income tax rate, and the inflated equity return rate, respectively.

The NPV in Equation (4.45) is calculated as:

$$NPV = NPV_{cap} + NPV_{O\&M} + NPV_{fc} + NPV_{it} + NPV_{grt} - NPV_{itc} \tag{4.47}$$

with NPV_{cap}, $NPV_{O\&M}$, NPV_{fc}, NPV_{it}, NPV_{grt} and NPV_{itc} representing the net present value contribution due to the capital costs, O&M costs, fixed charges, income taxes, gross revenue taxes, and investment tax credits. They are calculated as follows:

$$NPV_{cap} = \sum_{t=1}^{lt} \left(\frac{C_{cap} \cdot CRF(i_{ave}, n)}{(1 + i_{ave})^t} \right), \tag{4.48}$$

$$NPV_{O\&M} = \sum_{t=1}^{lt} \left(\frac{C_{O\&M,t} \cdot (1 + i_{inf})^t}{(1 + i_{ave})^t} \right), \tag{4.49}$$

$$NPV_{fc} = \sum_{t=1}^{lt} \left(\frac{C_{cap} \cdot i_{pt} \cdot (1 + i_{inf})^t}{(1 + i_{ave})^t} \right), \tag{4.50}$$

$$NPV_{it} = \sum_{t=1}^{lt} \left(\frac{\left(\frac{i_{it}}{1-i_{it}}\right)\left(C_{cap} \cdot CRF(i_{ave}, lt) - C_{cap}\frac{1}{lt}\right)}{(1 + i_{ave})^t} \right), \tag{4.51}$$

$$NPV_{grt} = \left(\frac{i_{grt}}{1 - i_{grt}} \right) (NPV_{cap} + NPV_{O\&M} + NPV_{fc} + NPV_{it} - NPV_{itc}), \tag{4.52}$$

$$NPV_{itc} = \frac{C_{cap} \cdot i_{itc}}{1 - i_{it}} \tag{4.53}$$

with i_{it}, i_{grt}, i_{pt}, i_{inf} and i_{itc} representing the income tax rate, gross revenue tax rate, property tax rate, inflation rate and investment tax credit rate, respectively. In Equation (4.51), the term (C_{cap}/lt) represents linear depreciation. Further, the term C_{cap} represents the overnight capital cost which can be adjusted for inflation during construction.

Which economic model to use depends on how rigorous the economic analysis should be. The BICYCLE model is believed to more closely represent market conditions, but requires a good understanding and knowledge of the different economic parameters. The FCR and Standard Levelized Cost Model on the other hand are easier to understand and to apply but may be less realistic.

References

Armstead, H. C. H. and Tester, J. W. (1987). *Heat Mining*. E. & F.N. Spon Ltd., London and New York.

Augustine, C. R. (2009). *Hydrothermal spallation drilling and advanced energy conversion technologies for Engineered Geothermal Systems*. PhD Dissertation, Massachusetts Institute of Technology, Cambridge, Massachusetts, United States.

Beckers, K. F., Lukawski, M. Z., Reber, T. J., Anderson, B. J., Moore, M. C., and Tester, J. W. (2013). Introducing GEOPHIRES v1.0: Software Package for Estimating Levelized

Cost of Electricity and/or Heat from Enhanced Geothermal Systems. In *Proceedings Thirty-Eighth Workshop on Geothermal Reservoir Engineering*, Stanford University, Stanford, California, February 11 - February 13, 2013, SGP-TR-198.

Beckers, K. F., Lukawski, M. Z., Anderson, B. J., Moore, M. C., and Tester, J. W. (2014a). Levelized costs of electricity and direct-use heat from Enhanced Geothermal Systems. *Journal of Renewable and Sustainable Energy*, 6, 013141.

Beckers, K. F., Lukawski, M. Z., Anderson, B. J., Moore, M. C., and Tester, J. W. (2014b). Erratum: "Levelized costs of electricity and direct-use heat from Enhanced Geothermal Systems" [J. Renewable Sustainable Energy 6, 013141 (2014)]. *Journal of Renewable and Sustainable Energy*, 6, 059902.

Beckers, K. F., Lukawski, M. Z., Aguirre, G. A., Hillson, S. D., and Tester, J. W. (2015). Hybrid Low-Grade Geothermal-Biomass Systems for Direct-Use and Co-Generation: from Campus Demonstration to Nationwide Energy Player. In *Proceedings Fortieth Workshop on Geothermal Reservoir Engineering*, Stanford University, Stanford, California, January 26 - January 28, 2015, SGP-TR-204.

DiPippo, R. (2004). Second law assessment of binary plants generating power from low-temperature geothermal fluids. *Geothermics*, 33 (5): 565–586.

DiPippo, R. (2012). *Geothermal power plants: principles, applications, case studies and environmental impact*. Butterworth-Heinemann, 3rd edition.

DOE (2012). *Geothermal Electricity Technology Evaluation Model (GETEM), Version August 2012.* U.S. Department of Energy Geothermal Technologies Program. Available at http://www1.eere.energy.gov/geothermal/getem.html.

Fox, R. W., Pritchard, P. J., and McDonald, A. T. (2004). *Introduction to Fluid Mechanics*. John Wiley & Sons, 6th edition.

Gringarten, A. C., Witherspoon, P. A., and Ohnishi, Y. (1975). Theory of heat extraction from fractured hot dry rock. *Journal of Geophysical Research*, 80 (8): 1120–1124.

Hardie, R. W. (1981). *BICYCLE II: A Computer Code for Calculating Levelized Life-Cycle Costs*, LA-89089. Los Alamos National Laboratory, Los Alamos, New Mexico, United States.

Heidinger, P., Dornstädter, J., and Fabritius, A. (2006). HDR economic modelling: HDRec software. *Geothermics*, 35 (5): 683–710.

Hunsbedt, A., Lam, S. T.-F., and Kruger, P. (1984). *User's manual for the one-dimensional linear heat sweep model*. Stanford Geothermal Program, Interdisciplinary Research in Engineering and Earth Sciences, Stanford University, Stanford, California, United States.

IHS (2013). IHS CERA Power Capital cost Index (PCCI). Available at http://www.ihs.com/info/cera/ihsindexes/index.aspx.

Johnson, C., Augustine, C., and Goldberg, M. (2012). *Jobs and Economic Development Impact (JEDI) Model Geothermal User Reference Guide*, Technical Report NREL/TP-6A20-55781. National Renewable Energy Laboratory (NREL), Golden, Colorado, United States.

Kitsou, O. I., Herzog, H. J., and Tester, J. W. (2000). Economic modeling of HDR enhanced geothermal systems. In *Proceedings World Geothermal Congress 2000,* Kyushu - Tohoku, Japan, May 28 - June 10, 2000, pages 3779–3784.

Lukawski, M. Z., Anderson, B. J., Augustine, C., Capuano, L. E., Beckers, K. F., Livesay, B., and Tester, J. W. (2014). Cost analysis of oil, gas, and geothermal well drilling. *Journal of Petroleum Science and Engineering*, 118: 1–14.

Lukawski, M. Z. (2016). *Comparison of Subcritical and Supercritical Organic Rankine Cycles (ORC) for Efficient Conversion of Low- and Medium-Temperature Heat to Electricity*. Internal Report, Cornell Energy Institute, Cornell University, Ithaca, New York, United States.

Mines, G. (2008). Geothermal Electricity Technologies Evaluation Model DOE tool for Assessing Impact of Research on Cost of Power. In *Thirty-Third Workshop on Geothermal Reservoir Engineering*, Stanford University, Stanford, California, January 28 - January 30, 2008.

Mines, G. and Nathwani, J. (2013). Estimated power generation costs for EGS. In *Proceedings Thirty-Eighth Workshop on Geothermal Reservoir Engineering*, Stanford University, Stanford, California, February 11 - February 13, 2013, SGP-TR-198.

NAG (2011). *NAG Fortran Library Manual - Mark 23*. The Numerical Algorithms Group Limited.

OECD/IEA (2010). *Projected Costs of Generating Electricity: 2010 Edition*. OECD NEA/IEA, Organisation for Economic Co-operation and Development Nuclear Energy Agency / International Energy Agency.

Ramey Jr, H. J. (1962). Wellbore heat transmission. *Journal of Petroleum Technology*, 14 (04): 427–435.

Reber, T. J. (2013). *Evaluating Opportunities for Enhanced Geothermal System-Based District Heating in New York and Pennsylvania*. Master Thesis, Cornell University, Ithaca, New York, United States.

Reber, T. J., Beckers, K. F., and Tester, J. W. (2014). The transformative potential of geothermal heating in the US energy market: A regional study of New York and Pennsylvania. *Energy Policy*, 70: 30–44.

Tester, J. W. and Herzog, H. J. (1990). *Economic Predictions for Heat Mining: A Review and Analysis of Hot Dry Rock (HDR) Geothermal Energy Technology*, Massachusetts Institute of Technology Energy Laboratory Report MIT-EL 90-001. U.S. Department of Energy, Geothermal Technology Division.

Tester, J. W., Anderson, B., Batchelor, A., Blackwell, D., DiPippo, R., Drake, E., Garnish, J., Livesay, B., Moore, M. C., Nichols, K., Petty, S., Toksz, M. N., and Veatch Jr., R. W. (2006). *The future of geothermal energy: Impact of enhanced geothermal systems (EGS) on the United States in the 21st century*. MIT.

CHAPTER 5

GEOPHIRES CASE-STUDIES

This chapter presents three case-studies utilizing GEOPHIRES to investigate the technical and economic performance of deep geothermal energy using Enhanced Geothermal Systems (EGS) for electricity and direct-use heat (Section 5.1), district heating systems (Section 5.2), and cogeneration (Section 5.3). The sections are based on material published in (Beckers et al., 2014a,b), (Reber et al., 2014), and (Beckers et al., 2015), respectively. Other published works utilizing GEOPHIRES, not further discussed here, are (Tester et al., 2015a) and (Tester et al., 2015b).

5.1 Case-Study 1: Deep Geothermal for Electricity and Direct-Use Heat

5.1.1 Parameter Values for EGS Scenarios

Three different technology maturity levels (today's, mid-term, and commercially mature technology), are combined with three different resource quality levels (low-grade, medium-grade and high-grade) to estimate ranges of levelized costs, capital investment and operation & maintenance (O&M) costs of EGS plants. All 9 proposed cases are evaluated for both electricity and direct-use heat resulting in 18 EGS scenarios in total. Tables 5.1 and 5.2 contain the values of technology, economic, and resource parameters used in this study.

The main differences between the three considered technology maturity levels are reservoir productivity rates scaled by the geothermal water mass flow rate per production well and the reservoir temperature decline or drawdown rate. The today's technology case assumes a well productivity of 30 kg/s and a 2% temperature drop per year (see

Table 5.1 – Technical and economic parameter values for EGS Scenarios.

Parameter	Today's Technology	Mid-Term Technology	Commercially Mature Technology
Reservoir Thermal Model	Percentage Temperature Drawdown		
Reservoir Temp. Drawdown	2%/year	1.5%/year	1%/year
Fluid Temp. Drawdown Threshold	19%	21%	14%
Geofluid Flow Rate per producer	30 kg/s	50 kg/s	70 kg/s
Pump Electr. Rate in Direct-Use	7 ¢/kWh$_e$	7 ¢/kWh$_e$	7 ¢/kWh$_e$
Drilling Costs Multiplier (Eq. (4.28))	100%	90%	80%
Hydraulic Impedance per Well-Pair	0.15 MPa·s/L	0.15 MPa·s/L	0.15 MPa·s/L
Wellbore Thermal Model	Ramey	Ramey	Ramey
Maximum Borehole Temp.	350°C	375°C	400°C
Water Loss Rate	2%	2%	2%
Geofluid Pump Efficiency	80%	80%	85%
Well Casing Inner Diameter	0.2 m	0.2 m	0.22 m
Levelized Cost Model	BICYCLE	BICYCLE	BICYCLE
Discount Rate	7%	7%	7%
Inflation Rate	2%	2%	2%
Income Tax Rate	39.2%	39.2%	39.2%
Plant Lifetime	30 years	30 years	30 years
Capacity Factor	90%	90%	95%

Table 5.2 – Resource parameter values for EGS scenarios with E and D-U referring to electricity and direct-use, respectively.

Parameter	Low-Grade		Medium-Grade		High-Grade	
Ambient Temp.	15°C		15°C		15°C	
Geothermal Grad.	30°C /km		50°C /km		70°C /km	
	E	D-U	E	D-U	E	D-U
Well Depth	6 km	4 km	5 km	2.5 km	4 km	1.8 km
Bottom Hole Temp.	195°C	135°C	265°C	140°C	295°C	141°C
Power Plant Type	ORC	N/A	Flash	N/A	Flash	N/A
Injection Temp.	70°C	50°C	75°C	50°C	80°C	50°C
No. of Inj. Wells	1	1	1	1	1	1
No. of Prod. Wells	2	2	4	2	4	2

Section 4.3.1 for more information on the Percentage Temperature Drawdown Model). The mid-term technology and commercially mature technology cases assume a production well flow rate of 50 and 70 kg/s and a percentage temperature drop per year of 1.5% and 1%, respectively. To obtain both a lower annual temperature drop and an increase in well flow rate with improving technology requires that also the surface area of the fractures increases (larger reservoir). Other differences between the three technology cases include well drilling and completion costs, circulation pump efficiency, and maximum allowable bottom hole temperature. The latter is determined by the maximum allowable operating conditions for downhole tools and completion equipment and is assumed to improve from 350°C for today's technology to 400°C for commercially mature technology (Tester et al., 2006). Further, in contrast to the production temperature decline, no decline in production well flow rate (hydraulic drawdown) is assumed for EGS in GEOPHIRES. However, pump power requirements do change over time due to changes in buoyancy effects (see Section 4.3.1). Ramey's model is used to estimate the temperature drop due to heat losses in the production wells (Section 4.3.2). The "Fluid Temperature Drawdown Threshold" refers to the thermal drawdown rate that triggers redrilling of all the wells. In every scenario, both for electricity and direct-use heat, this parameter is chosen so that redrilling is performed once at the mid-life point of the plant, which would make most economic sense. It is expected that the required improvements between today's and mid-term technology and between mid-term and commercially mature technology are evolutionary and do not rely on any fundamental technological breakthroughs.

The low-grade, medium-grade and high-grade resource cases have average geothermal gradients of 30°C/km, 50°C/km and 70°C/km, respectively. While temperature gradients of up to 30°C/km are typical for the Eastern U.S., 50°C/km is commonly available in the Western U.S. (Tester et al., 2006). Gradients of 70°C/km or more can be found in some of the "hot spots", for example at existing hydrothermal sites in the Western U.S. (e.g. the Geysers Field in California) or areas of relatively recent volcanism (e.g. the New-

berry Caldera in Oregon). For the electricity scenarios, an Organic Rankine Cycle (ORC) power plant with one injection and two production wells and a well depth of 6 km (195°C) is chosen for the low-grade resource. For the medium- and high-grade resources, double-flash power plants with one injection and four production wells are used and the drilling depths are respectively 5 km (265°C) and 4 km (295°C). For the direct-use heat scenarios, the bottom hole temperature is set at approximately 140°C in each case which translates into drilling depths of 4, 2.5 and 1.8 km for the low-, medium- and high-grade resources, respectively.

The BICYCLE levelized cost model is used for the calculation of the levelized cost of electricity (LCOE) or levelized cost of heat (LCOH) in each scenario. A discount rate of 7%, lifetime of 30 years and income tax rate of 39.2% is assumed for each case in order to allow comparison with reported values for other energy technologies from the OpenEI Transparent Cost Database (U.S. DOE, 2013). In addition, capacity factors of 90 to 95% are assumed depending on the technology case, for both the electricity and direct-use heat scenarios. The capacity factor is defined as the percentage of time the plant runs in baseload operation which is very similar to the percentage of the actual net electricity generation to the maximum possible net electricity generation within e.g. one year. With this definition, the capacity factor is equivalent to the availability of the plant. In GEOPHIRES, the EGS plant is either on in baseload or off for maintenance; variable geothermal fluid flow rates for load-following operation are not considered. Other definitions of capacity factor are found in the literature; applying those to these cases would not necessarily lead to the same values for capacity factor as those in Table 5.1. The relatively high capacity factors for direct-use heat applications would apply only for industrial or commercial processes that can operate continuously and constantly use the delivered heat. Some examples are paper processing, food pasteurization, and biomass drying; other examples are provided in Section 5.1.3. In contrast, geothermal district heating systems for residential and commercial buildings operate at lower capacity factors because heat is required

only on cold days. Reber (2013) conducted a separate study using GEOPHIRES focusing on these systems using a capacity factor of 50% for heating only, and developed a geothermal district heating supply curve for the states of New York and Pennsylvania. Some of his key findings are included in the discussion of results (Section 5.1.3) and further presented in Section 5.2.

The capital investment and levelized costs calculated in this paper for both the electricity and direct-use heat cases do not include transmission or distribution costs, only energy extraction and conversion costs. In the energy conversion process, it is assumed that all the enthalpy available between the production and injection temperature is utilized either to generate electricity (with a certain utilization efficiency) in the electricity cases or directly as heat delivered to a process or series of processes in the direct-use heat cases. An example of a series of processes is a high-temperature industrial process cascaded with a low-temperature industrial process, water heating or space heating. The reinjection temperature in the direct-use heat cases is set at 50°C. The reinjection temperature in the electricity scenarios is determined by the type of power plant, ambient temperature and production temperature as discussed in Section 4.3.3.

5.1.2 GEOPHIRES Simulation Results

Power Output, and Capital, O&M, and Levelized Costs for EGS Scenarios

The generating capacity (power output), capital costs, O&M cost and levelized costs for the 18 EGS scenarios are presented in Table 5.3. Figure 5.1 shows the levelized cost of electricity and direct-use heat for the 18 EGS scenarios. Further, Figure 5.2 shows the capital cost distribution for the 18 EGS scenarios. The bottom bars represent the geothermal resource exploration costs. The middle bars represent the geothermal well drilling and

reservoir stimulation costs. Finally, the top bars represent the surface equipment costs which consist of the power plant costs and the fluid distribution costs.

Table 5.3 – EGS scenarios GEOPHIRES simulation results with E and D-U referring to electricity and direct-use, respectively.

	Low-Grade		Medium-Grade		High-Grade	
	E	D-U	E	D-U	E	D-U
	Today's Technology					
Power (MW_e or MW_{th})	2.5	16.6	11.4	17.4	15.0	17.0
Drilling Costs (M$/well)	19.5	10.1	14.5	4.8	10.1	2.8
Surface Plant Cost (M$)	8.1	3.5	32.3	3.7	35.3	3.7
Stimulation Cost (M$)	2.5	2.5	2.5	2.5	2.5	2.5
Exploration Cost (M$)	14.2	7.9	10.9	4.3	7.9	3.0
Total Capital Cost (M$)	83.2	44.4	118.2	24.9	96.4	17.6
Capital Cost ($/kW)	27,600	2,200	9,410	1,180	5,900	860
O&M Cost (M$/year)	5.1	3.2	7.4	2.0	5.9	1.5
LCOE (¢/kWh_e) or LCOH ($/MMBTU)	56.9	14.4	17.8	8.1	10.9	6.1
	Mid-Term Technology					
Power (MW_e or MW_{th})	3.7	28.2	16.9	29.2	24.4	28.4
Drilling Costs (M$/well)	17.5	9.1	13.1	4.3	9.1	2.5
Surface Plant Cost (M$)	15.0	6.2	49	6.4	53.2	6.3
Stimulation Cost (M$)	2.5	2.5	2.5	2.5	2.5	2.5
Exploration Cost (M$)	12.9	7.3	9.9	4.0	7.3	2.8
Total Capital Cost (M$)	82.9	43.3	126.7	25.8	108.6	19.2
Capital Cost ($/kW)	18,920	1,280	6,910	750	4,150	580
O&M Cost (M$/year)	3.3	2.8	5.2	2.1	4.5	1.8
LCOE (¢/kWh_e) or LCOH ($/MMBTU)	31.3	7.8	10.6	5.1	6.4	4.2
	Commercially Mature Technology					
Power (MW_e or MW_{th})	5.5	41.4	25.1	42.6	34.5	41.4
Drilling Costs (M$/well)	15.6	8.1	11.6	3.8	8.1	2.2
Surface Plant Cost (M$)	21.7	8.8	64.2	9.1	69.5	8.9
Stimulation Cost (M$)	2.5	2.5	2.5	2.5	2.5	2.5
Exploration Cost (M$)	11.6	6.6	8.9	3.7	6.6	2.6
Total Capital Cost (M$)	82.5	42.2	133.7	26.7	119.1	20.8
Capital Cost ($/kW)	12,890	860	4,970	540	3,260	440
O&M Cost (M$/year)	3.4	3.5	5.3	2.9	4.7	2.6
LCOE (¢/kWh_e) or LCOH ($/MMBTU)	20.1	5.5	7.1	4.0	4.6	3.5

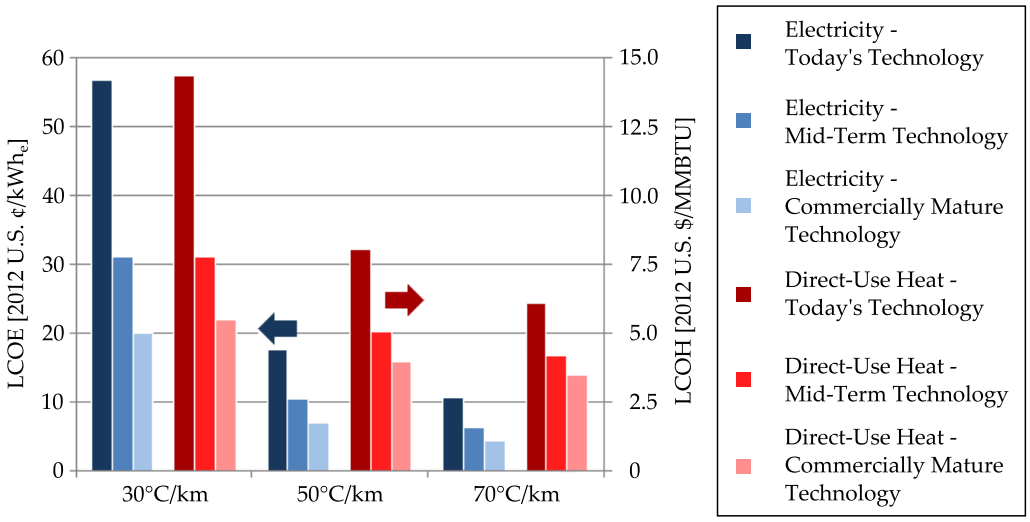

Figure 5.1 – Levelized costs for 18 EGS scenarios. The blue bars represent the levelized cost of electricity (LCOE) in 2012 U.S. ¢/kWh$_e$ for the electricity scenarios (left axis); the red bars represent the levelized cost of heat (LCOH) in 2012 U.S. $/MMBTU for the direct-use heat scenarios (right axis).

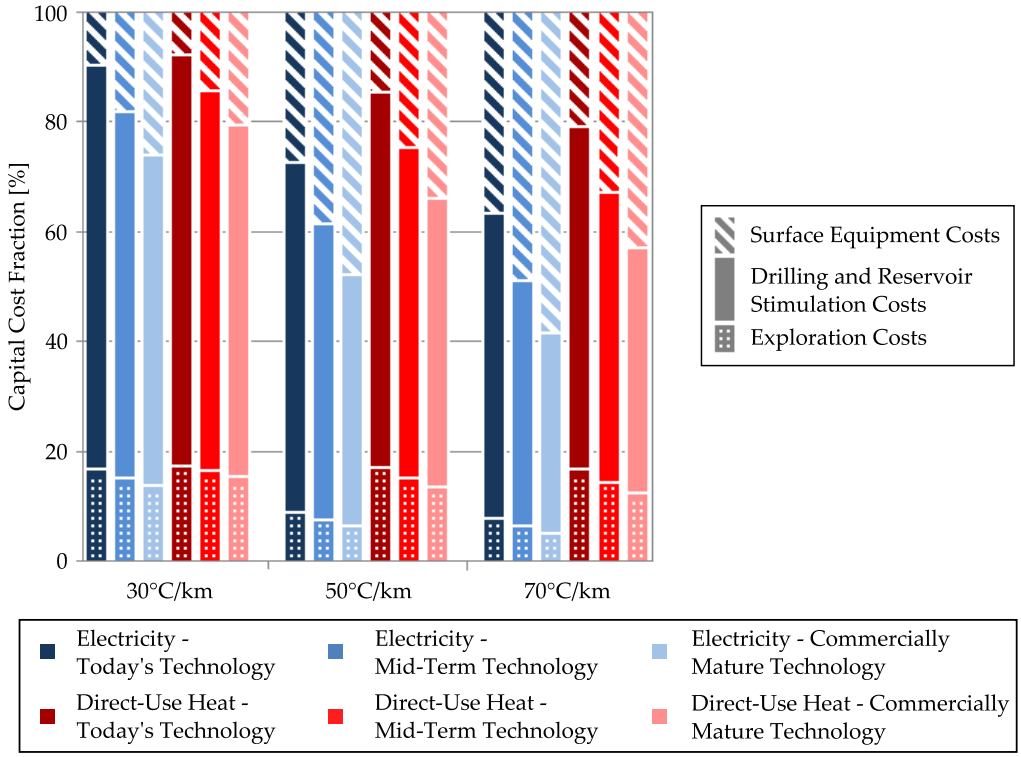

Figure 5.2 – Fraction of capital cost (initial investment) associated with resource exploration (bottom bars), drilling and reservoir stimulation (middle bars), and surface equipment (top bars) for the 18 EGS scenarios.

LCOE and LCOH Sensitivity Analysis for Medium-Grade Resource and Mid-Term Technology Case

A sensitivity analysis is performed on the LCOE and LCOH for the mid-term technology case in combination with the medium-grade geothermal resource. The base case LCOE and LCOH are 10.6 ¢/kWh$_e$ and 5.1 $/MMBTU (1.7 ¢/kWh$_{th}$), respectively (see Table 5.3). The parameters considered in the analysis are the capital cost of drilling, reservoir stimulation, surface plant, fluid distribution system and resource exploration, the O&M costs of surface plant and wellfield, and the thermal drawdown rate, discount rate, reservoir or plant lifetime, and drilling depth. Figure 5.3 shows the effect of all the cost parameters, the drawdown rate, and the reservoir or plant lifetime on the levelized cost of end-product. For each datapoint, one parameter value is decreased or increased by 10, 20 or 30%. When changing the lifetime of the system, the thermal drawdown threshold for drilling new production wells is modified to keep the moment for redrilling at the mid-life point.

Figure 5.4 shows the effect of drilling depth on the LCOE and LCOH for the medium-grade resource and mid-term technology case. The drilling depth in the LCOE and LCOH base case scenario is 5 km and 2.5 km, respectively. When drilling deeper, the increase in production of direct-use heat and especially of electricity still outweigh the increase in drilling and surface plant costs, explaining the decrease in LCOH and LCOE. More discussion on the sensitivity analysis results presented in Figures 5.3 and 5.4 is provided in the next section.

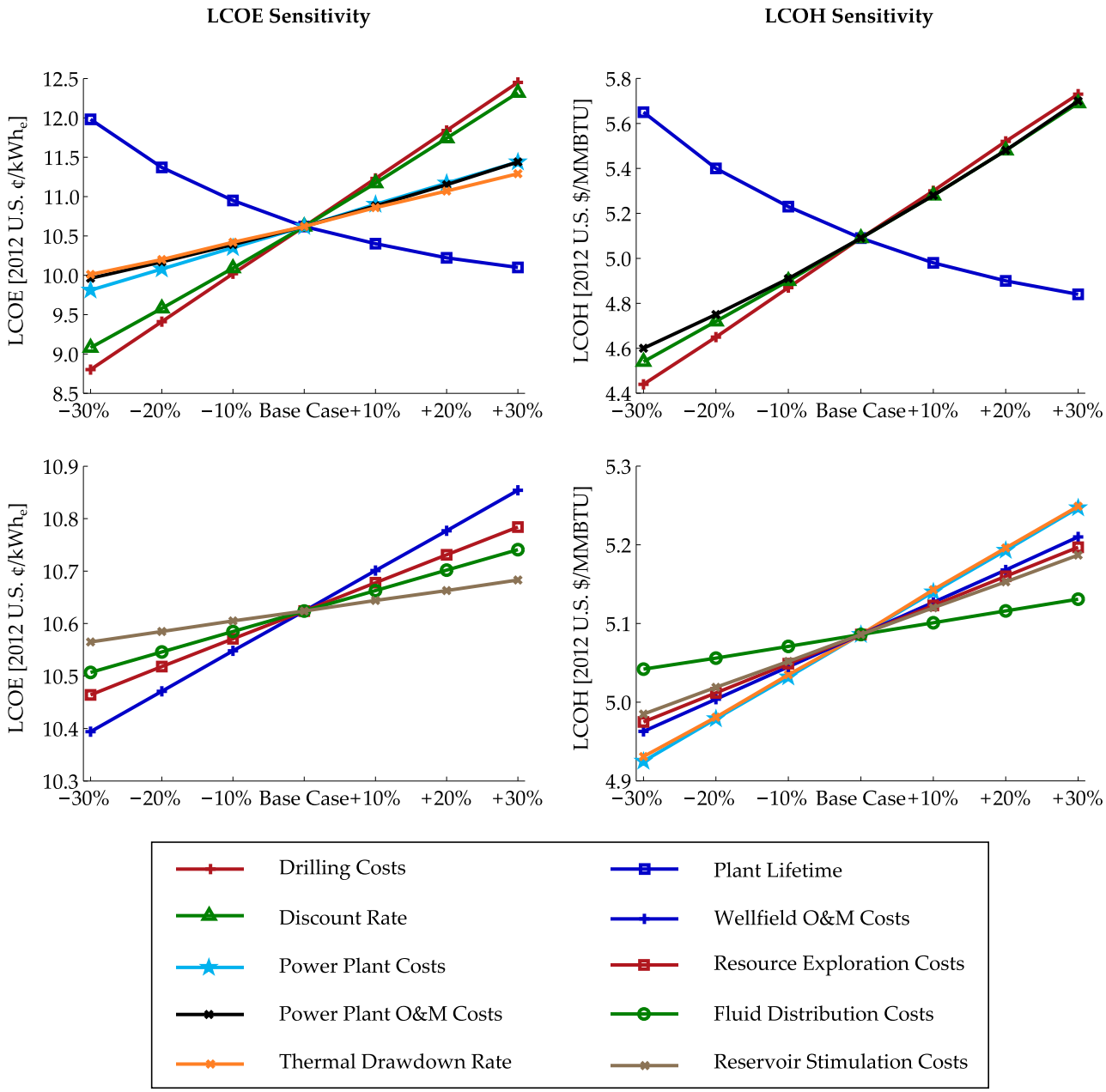

Figure 5.3 – Sensitivity of LCOE (left figures) and LCOH (right figures) to various parameters for medium-grade resource and mid-term technology case. High-sensitive and low-sensitive parameters are shown in top and bottom figures, respectively. The base case LCOE and LCOH are 10.6 ¢/kWh$_e$ and 5.1 $/MMBTU, respectively.

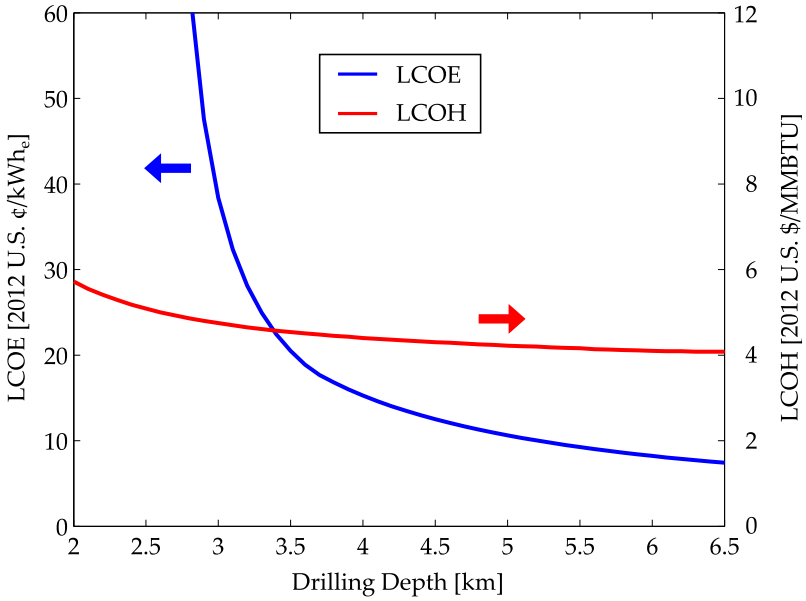

Figure 5.4 – Effect of drilling depth on the LCOE and LCOH for medium-grade resource and mid-term technology case. The geothermal gradient is constant at 50°C/km. For the LCOE, the power plant type is a subcritical Organic Rankine Cycle for wells shallower than 3.7 km, and a double-flash power plant for wells deeper than 3.7 km.

5.1.3 Discussion of Results

Deep Geothermal with EGS for Electricity Generation

As shown in Figure 5.1, the Levelized Cost of Electricity (LCOE) from EGS as estimated with GEOPHIRES varies widely depending on the resource grade and maturity of EGS technology. For geothermal gradients of 30°C/km, which are commonly available in the Eastern United States (Tester et al., 2006), the LCOE is estimated at almost 60 ¢/kWh$_e$ with today's technology and could drop to about 20 ¢/kWh$_e$ in the future with anticipated technology improvements. For a gradient of 50°C/km, which is widespread in the Western United States and can be found in some other regions such as West Virginia and Texas (Tester et al., 2006), the LCOE with today's technology is about 18 ¢/kWh$_e$ and is estimated to drop below 10 ¢/kWh$_e$ in the future. For the geothermal "hot spots" in the U.S. with a geothermal gradient of 70°C/km or more (Tester et al., 2006), the LCOE with

today's technology is on the order of 10 ¢/kWh$_e$ or less and is predicted to fall below 5 ¢/kWh$_e$ in the future.

The sensitivity analysis (Figure 5.3) shows that the drilling costs have the highest impact on the LCOE, followed by the discount rate, plant lifetime, power plant capital costs, power plant O&M costs and the thermal drawdown rate of the reservoir. Breakthroughs in new drilling techniques might therefore have the highest potential to significantly lower the LCOE, especially in the Eastern United States. Lower interest rates are another way to significantly lower the LCOE. They might be obtained by financing the EGS project through state or federal partnerships or by mitigating risks and uncertainties by targeting areas with prior knowledge of the subsurface ("brown fields" rather than "green fields"). The capacity factor is not included in the sensitivity analysis because it does not have the same level as uncertainty as the considered parameters. Nevertheless, when looking at e.g. Equation (4.41), one can find that, to a first approximation, the LCOE is inversely proportional to the capacity factor. This strong dependence highlights the importance of designing an EGS for operation at high capacity factors.

Figure 5.2 shows the capital cost distribution of the EGS scenarios. The large contribution of the drilling costs (about 40% for high-grade resources and up to 60% or above for low-grade resources) in combination with large capital costs in general (3,000 to 6,000 \$/kW$_e$ for high-grade resources and above 10,000 \$/kW$_e$ for low-grade resources (see Table 5.3)) is the main reason for the high sensitivity of LCOE to the drilling costs. Further, large upfront capital costs in combination with a long time period until any revenue is generated and the uncertainty on how big this revenue stream will be, form the main drawbacks for investors.

Figure 5.5 compares the EGS LCOE estimates from GEOPHIRES with the LCOE for other electricity generating technologies, obtained from the OpenEI Transparent Cost Database (U.S. DOE, 2013) developed by the U.S. DOE (Department of Energy) and NREL

(National Renewable Energy Laboratory). The LCOE values taken from this database are the median values from an extensive list of reported or calculated values for each electricity generating technology. All LCOE data in Figure 5.5 are calculated for the same economic parameters (7% discount rate, 30 years lifetime and 39.2% income tax rate). Cost of transmission lines, subsidies and tax incentives are not included. The LCOE from EGS at their early stage of development can only compete with concentrating and photovoltaic solar energy in medium- and high-grade geothermal resources. However, for commercially mature EGS technology, which is expected to be available by 2030 (assuming proper support for field demonstrations in the next several years), systems utilizing medium-grade resources are predicted to become economically competitive with other renewable and non-renewable energy sources including wind, nuclear, hydro, coal IGCC, and natural gas turbines. For high-grade resources, EGS is projected to even compete with combined cycle natural gas and pulverized & scrubbed coal power plants. In comparison with the Energy Information Administration (EIA) 2013 Annual Energy Outlook (EIA, 2013), the prospects for EGS also look favorable. The EIA predicts a generation electricity price by 2030 of 6 ¢/kWh$_e$ in 2011 U.S. $, well within the range of the GEOPHIRES estimates for medium-grade and high-grade resources, 7.1 and 4.6 ¢/kWh$_e$, respectively.

The LCOE numbers for EGS from the OpenEI Transparent Cost Database are based on data from the Market Allocation (MARKAL) model (Fishbone and Abilock, 1981), NREL (Logan et al., 2009), EEE (2010), and Lazard (2013). These studies do not reveal all major assumptions for e.g. geothermal gradient or well productivities, and therefore do not allow for an accurate comparison with the GEOPHIRES results. Nonetheless, other geothermal economic assessment studies are available with full disclosure of the assumptions. For example, Mines and Nathwani (2013) reports LCOE values using GETEM from 76 ¢/kWh$_e$ to 13 ¢/kWh$_e$ for geothermal gradients ranging from 40 to 70°C/km, bottom hole temperatures ranging from 100 to 325°C, and 40 kg/s mass flow rate per production well. Although these EGS scenarios slightly differ from the scenarios in this study, the

values for the LCOE presented by Mines and Nathwani are comparable to the projections with GEOPHIRES. Good agreement also exists with the values reported in the "Future of Geothermal Energy" report (Tester et al., 2006). For a resource with 50°C/km gradient, the "MIT-EGS" model estimates an LCOE of 17.5 ¢/kWh$_e$ in the today's technology case (20 kg/s per production well) and 5.2 ¢/kWh$_e$ in the commercially mature technology case (80 kg/s per production well). The values projected by GEOPHIRES for a 50°C/km gradient are 17.8 ¢/kWh$_e$ in the today's technology case (30 kg/s per production well) and 7.1 ¢/kWh$_e$ in the commercially mature technology case (70 kg/s per production well). The GEOPHIRES estimates are higher but the increase in LCOE can be explained by the higher drilling costs used in comparison with the earlier study which used 2004 drilling costs (Tester et al., 2006; Lukawski et al., 2014).

GEOPHIRES calculations and the comparison with other energy technologies should be interpreted with care. The LCOE for the non-renewable energy sources depends on the consumption of the market commodity fuels natural gas, oil and coal, and therefore they are inherently uncertain with pending fluctuations in prices and availability. The LCOE for EGS projects will look less promising when including the costs of permits, federal land leases and other infrastructure requirements, for example, transmission lines and water supply pipelines. Moreover, in real EGS projects, the exploration costs might be higher than assumed in GEOPHIRES. The reason is that several exploration and confirmation wells might be required instead of only one, especially in areas with no prior knowledge of the subsurface ("green fields"). On the other hand, CO_2 credits, subsidies and tax incentives will have a positive impact on the EGS costs. Also, learning effects, especially related to well drilling and stimulation within a certain field, will have a positive effect on the levelized and capital costs. Furthermore, the reservoir drawdown rate, even for the commercially mature technology case, might be overestimated. Mines and Nathwani (2013) consider a drawdown rate of 0.5%/year and Augustine et al. (2010) a target rate of only 0.3%/year, in comparison with the 1%/year for the commercially mature case in

GEOPHIRES. Finally, the LCOE in the different scenarios has not been optimized with respect to the drilling depth. For example, Figure 5.4 shows that for the medium-grade resource and mid-term technology case, the LCOE is not yet minimized within the considered drilling depth range of 2.5 to 6.5 km. When drilling deeper, the combination of higher geothermal fluid exergy and higher power plant utilization efficiency can still outweigh the increase in drilling costs. Nevertheless, an increased drilling trouble probability and higher uncertainties associated with ultra-deep EGS might increase the LCOE for such projects. Therefore, for this particular EGS scenario, the drilling depth was limited to 5 km.

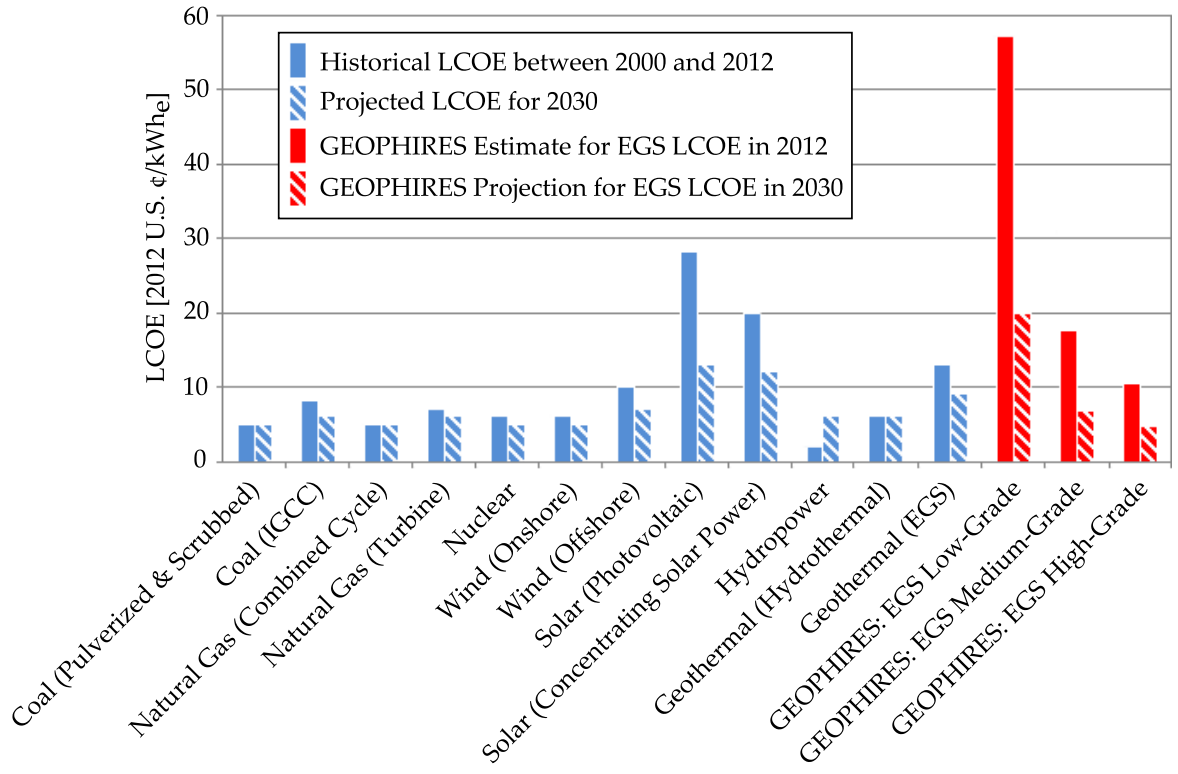

Figure 5.5 – Comparison of LCOE expressed in 2012 U.S. ¢/kWh$_e$ for EGS obtained using GEOPHIRES (red bars) with LCOE for different electricity generating technologies (blue bars). LCOE values for other energy technologies are taken from the OpenEI Transparent Cost Database (U.S. DOE, 2013). The solid bars and striped bars represent the current LCOE and projected LCOE for 2030, respectively. The GEOPHIRES commercially mature technology EGS scenarios are used to model the projected system performance in the year 2030.

Deep Geothermal with EGS for Direct-Use Heat Production

The GEOPHIRES model estimates the LCOH for direct-use applications at 14.4 \$/MMBTU (4.9 ¢/kWh$_{th}$) for today's technology and 5.5 \$/MMBTU (1.9 ¢/kWh$_{th}$) for commercially mature technology (see Figure 5.1) in areas where a geothermal gradient of 30°C/km is available. For a geothermal gradient of 50°C/km, widely found in the Western U.S., these numbers drop to 8.1 \$/MMBTU (2.8 ¢/kWh$_{th}$) and 4.0 \$/MMBTU (1.4 ¢/kWh$_{th}$), respectively. For a high-grade geothermal resource with a gradient of 70°C/km, the LCOH is only 6.1 \$/MMBTU (2.1 ¢/kWh$_{th}$) for today's technology and only 3.5 \$/MMBTU (1.2 ¢/kWh$_{th}$) for future technology.

Figure 5.6 compares these numbers with the LCOH from natural gas boilers. The latter LCOH was calculated using the same discount rate of 7%, a lifetime of 30 years and a capacity factor of 90-95%. The natural gas boiler price was taken at 50 \$/kWth, found to be a good estimate for boilers with thermal output on the order of 100 to 1,000 kW$_{th}$. The delivered natural gas prices for industrial and residential sectors in 2011 (5.0 and 11.0 \$/MMBTU) and projections for 2030 (6.7 and 13.7 \$/MMBTU) were taken from the EIA 2013 Annual Energy Outlook (EIA, 2013) and assuming a Higher Heating Value (HHV) of 1,020 BTU per cubic feet. The HHV efficiency of the natural gas boiler was taken at 90%. Figure 5.6 also includes the LCOH for EGS district heating systems as calculated by Reber (2013) using GEOPHIRES. Reber assumed a discount rate of 4% (instead of 7%), a lifetime of 30 years and a capacity factor of 50% (instead of 90%), and included the capital and O&M costs for the district heating system. The flow rate per producer was 30 kg/s for the today's technology case and 80 kg/s (instead of 70 kg/s) for the commercially mature technology case. The discount rate is lower because it is assumed the EGS project will be executed by a utility or public agency, which can borrow money at lower interest rates. Also, the capacity factor is lower because the EGS district heating system is only used for space and water heating whose demand varies significantly throughout the year.

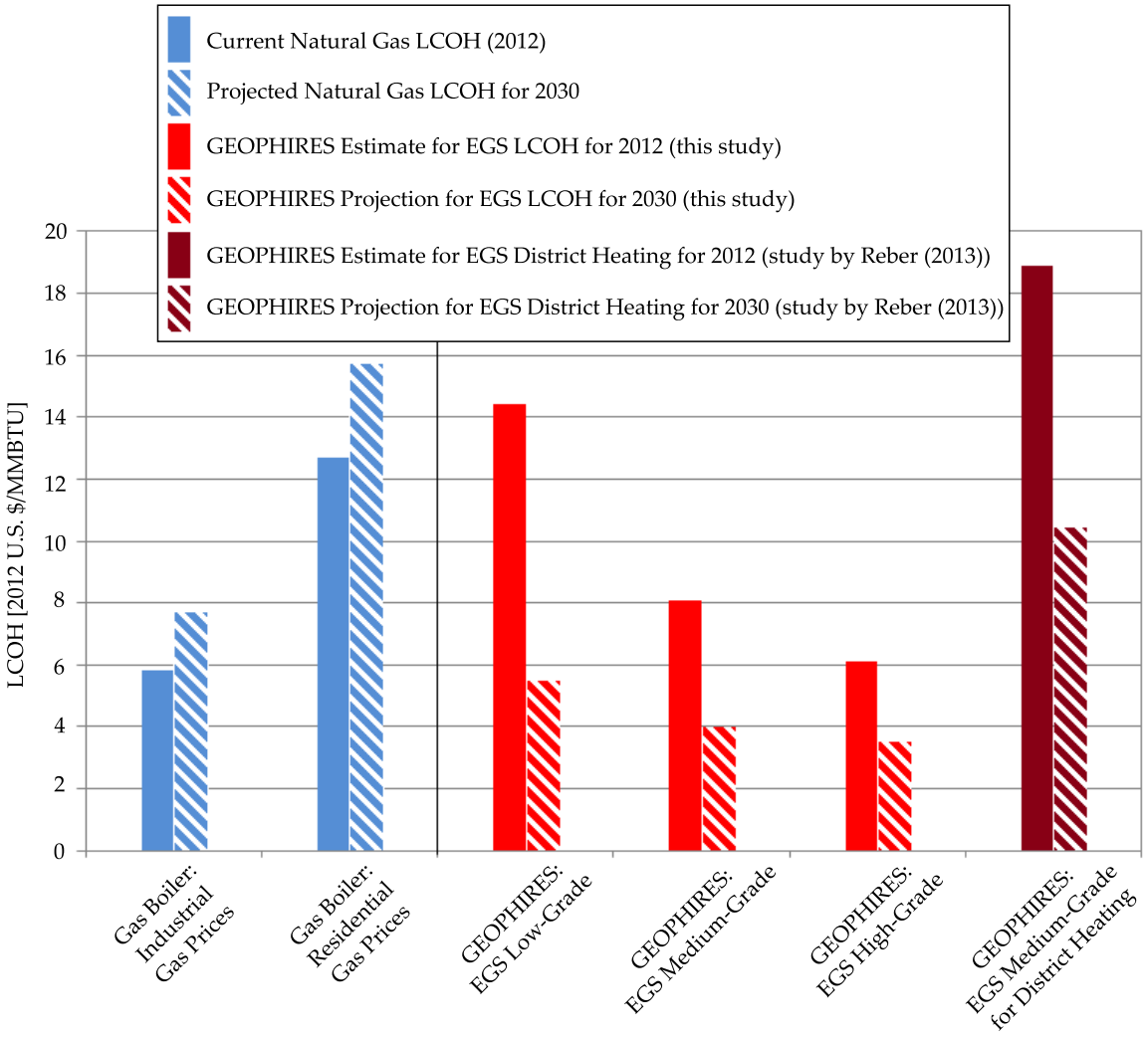

Figure 5.6 – Comparison of LCOH (2012 U.S. $/MMBTU) from EGS estimated with GEOPHIRES for industrial direct-use heat processes (light red bars) and district heating systems (dark red bars) with LCOH from natural gas boilers (blue bars). The current and projected residential and industrial gas prices are taken from the 2013 EIA Annual Energy Outlook (EIA, 2013). It is assumed that the today's technology EGS scenarios in GEOPHIRES represent the 2012 costs. The commercially mature technology EGS scenarios are used to model the projected system performance in the year 2030. Low-, medium-, and high-grade resource refer a geothermal gradient of 30, 50, and 70°C/km, respectively.

The results were presented as a supply curve for New York State and Pennsylvania. The systems with lowest LCOH on this supply curve correspond to geothermal gradients of around 40-50°C/km, which are labeled as "Medium-grade resource" in Figure 5.6. This figure shows that with current low industrial natural gas prices, no EGS scenario from this study (light solid red bars) is cost-competitive. However, by 2030, all considered geothermal scenarios are predicted to be economically viable. Furthermore, in comparison with

residential natural gas prices, EGS district heating systems with medium-grade resource are currently not cost competitive but are predicted to be so by 2030. The LCOH for natural gas boilers are presented in Figure 5.6 for a capacity factor of 90% though, not 50%. Nevertheless, in comparison with the annual fuel costs, the capital costs of a boiler are so insignificant over the lifetime of the system that the capacity factor has barely any impact on the LCOH. Therefore, for a capacity factor of 50%, the LCOH would only increase by about 1% in these cases. The LCOH for natural gas boilers to a first approximation is only governed by the natural gas price. This means the large difference in natural gas LCOH between the residential and industrial case as shown in Figure 5.6 is caused by the large difference in residential and industrial natural gas price. The higher LCOH for EGS district heating systems in comparison with the LCOH for EGS direct-use heat cases is caused mainly by the lower capacity factor and higher capital and O&M costs for EGS district heating systems.

Both the projections for the natural gas price and the GEOPHIRES estimates for the LCOH in 2030 should be interpreted with care. No model can accurately predict future natural gas prices. Over the last 10 years for example, the annual average Henry Hub spot price for natural gas rose from around 4 \$/MMBTU (1.4 ¢/kW_{th}) in 2002 to peak around 10 \$/MMBTU (3.4 ¢/kW_{th}) in 2005 and drop below 3 \$/MMBTU (1.0 ¢/kW_{th}) in 2012 as a result of the unconventional gas boom (EIA, 2013).

Similar to the LCOE in the previous section, several factors which could affect the LCOH are not taken into account in the GEOPHIRES model. These include, among others, permits and federal leases, subsidies and tax incentives, learning effects in drilling, and the cost of transmission pipelines to the end-consumer.

The assumed parameter values for the different technology cases presented in Table 5.1 also have their inherent uncertainties. Figure 5.3 shows the LCOH sensitivity to several of these parameters. The LCOH is again most sensitive to the drilling costs but

the effect is not as strong as with the LCOE. The reason is that the drilling costs are again the major cost for a direct-use heat system; however, its dominance is not as high as in the case of electricity production (see Table 5.3 for exact cost numbers). Moreover, a better learning curve and an overall average drilling cost decline on a system-wide basis can be expected for direct-use heat systems in comparison with electricity systems, since more wells at a lower completion cost can be drilled for e.g. a large industrial process or large district heating system. Other high impact parameters include discount rate, followed by power plant O&M costs and plant lifetime.

Similar to the electricity case, the capacity factor is not included in the sensitivity analysis because it is not an uncertain parameter; a high capacity factor can be designed for in an industrial process. Nevertheless, the capacity factor has a large impact on the LCOH as can been seen from the inversely proportional relationship between the two (Equation (4.41)). This explains directly why EGS district heating systems suffer from lower capacity factors.

Finally, Figure 5.4 shows that the LCOH is much less dependent on the drilling depth that the LCOE. The reason is that the LCOE, unlike the LCOH, is highly sensitive to the geofluid temperature because a change in temperature affects the heat-to-power conversion twice. Both the geofluid exergy and the utilization efficiency increase with increasing geofluid temperature resulting in a stronger than linear dependence of the electricity production on the drilling depth. The direct-use heat production for the LCOH changes only linearly with depth. Also, for a direct-use heat application, one might not be interested to drill as deep as possible because the production temperature might eventually no longer suit the intended application.

Even though EGS, and in general geothermal energy, is usually associated with electricity production, its potential for direct-use heat should be considered given their potential for having projected costs that would compete favorably with natural gas. Even

for low-grade geothermal resources, direct-use heat, unlike electricity, is expected to become cost-competitive with natural gas by 2030, with only a minor increase in natural gas prices assumed (from 5.0 to 6.7 $/MMBTU in industrial sector and 11.0 to 13.7 $/MMBTU in residential sector). Furthermore, the required well depths are shallower and the capital costs are lower, which means lower risk and probably lower discount rates. Also, the potential is large in the U.S. Recently, Fox et al. (2011) calculated that about 25% of the total U.S. primary energy demand (25 EJ out of 100 EJ per year) is consumed as heat below 120°C, in comparison to 40% of total U.S. primary energy being converted to electricity (EIA, 2011). Unfortunately, most U.S. homes, businesses and companies meet their heating demand for space and water heating and low-temperature industrial processes by using a combustion furnace fueled by natural gas or oil. To change the current energy supply system for heat would require significant new infrastructure to deliver thermal energy from where it is produced in a geothermal field to where it is consumed. Given that the U.S. has to deal with its aging infrastructure problems in the next few decades, a real opportunity of such transformational change exists.

Geothermal energy in many cases is ideal to provide heat or both heat and electricity in cascaded, integrated systems. Examples of low-temperature heat processes with geothermal potential (Lund, 2010; Gudmundsson et al., 1985) are space and water heating, space and water cooling (through absorption chillers), heating greenhouses, fish farming, food processes such as pasteurization, lumber drying, paper processing including pulping and drying, biofuels production, and snow melting. The Lindal diagram (Gudmundsson et al., 1985) ranks several of these applications according to their process temperature. Iceland's utilization of its geothermal resources in a fully integrated fashion for electricity and direct-use heat provides a poignant example of what can be done to utilize the potential value of geothermal resources (Ragnarsson, 2000, 2005, 2010).

5.1.4 Conclusions

In the first case-study, GEOPHIRES was used to simulate 18 EGS scenarios using parameter values and assumptions described in Tables 5.1 and 5.2. Both electricity and direct-use heat were considered as end-products for 3 different resource grades (low-, medium-, and high-grade resource, represented by average geothermal gradients of 30, 50, and 70°C/km, respectively) and 3 different levels of technological maturity (today's, mid-term, and commercially mature technology represented by production rate improvements from 30 to 70 kg/s per well). Over the entire range of scenarios studied, the levelized cost of electricity ranged from 4.6 to 57 ¢/kWh$_e$ and was 11 ¢/kWh$_e$ for the base case scenario (medium-grade resource and mid-term technology). The levelized cost of heat for the direct-use heat scenarios ranged from 3.5 to 14 $/MMBTU (1.2 to 4.8 ¢/kWh$_{th}$) and was 5.1 $/MMBTU (1.7 ¢/kWh$_{th}$) for the base case scenario. A sensitivity analysis on uncertain parameter values in the base case scenarios showed that the drilling costs have the biggest impact on the LCOE and LCOH. The importance of designing the system for high capacity factors was also emphasized in the discussion.

GEOPHIRES LCOE estimates are comparable with values found in literature for similar EGS conditions, as for example in some of the cases studied by Mines and colleagues using GETEM. When comparing EGS with other renewable (including hydrothermal) and non-renewable energy technologies for electricity generation, EGS is not expected to be cost-competitive currently except with photovoltaic and concentrated solar energy. However, with moderate technological improvements that would emulate the production characteristics of commercial hydrothermal systems in operation today, EGS utilizing medium- and high-grade geothermal resources is predicted to become cost-competitive with all renewables, including hydrothermal, and most non-renewable energy technologies. Because of the low natural gas prices that exist in the U.S. today (around 5 $/MMBTU (1.7 ¢/kW$_{th}$) in 2011 as delivered to industrial consumers), no technology

can compete with high efficiency natural gas fired combined cycles for electricity generation. In addition, even for industrial direct-use heat, EGS using today's technology is not economically competitive with natural gas boilers with today's wholesale industrial gas prices. Also in comparison with natural gas boilers for space and water heating using residential gas prices (11 $/MMBTU (3.8 ¢/$kW_{th}$)), EGS district heating systems are currently not cost-competitive. For commercially mature technology though, it is predicted that even for low-grade geothermal resources, EGS for industrial direct-use heat would be cost-competitive with projected 2030 industrial natural gas prices (7 $/MMBTU (2.4 ¢/$kW_{th}$)). Further, EGS district heating systems for medium-grade resources are expected to become cost-competitive with natural gas boilers at projected 2030 residential natural gas prices (14 $/MMBTU (4.8 ¢/$kW_{th}$)).

The results of the GEOPHIRES simulations reported in this case-study should be interpreted with care. Several factors that have not been taken into account may affect the LCOE or LCOH. Examples of factors that may increase the levelized cost are the cost for transmission lines, confirmation wells and royalties, and the potential delays due to unsuccessful wells and permitting issues. On the other hand, subsidies, incentives, and greenhouse gas credits would have a beneficial impact on the levelized cost. The levelized cost is also not the only criterion to evaluate an EGS project. When assessing the feasibility of the project or comparing with other energy technologies, EGS will benefit from its high capacity factors, low environmental impact, and its versatility as energy source. On the contrary, large upfront capital costs for power plant components and well drilling and uncertainties and risks associated with the resource itself and the ability to stimulate reservoir production to commercial levels are currently the main barriers for investors. Taking all into consideration, the prospect for EGS as a major energy source in the 21st century looks promising. In the next 10-20 years, with proper Research, Development & Demonstration (RD&D) support for field demonstrations to lower risks and prove the scalability of the technology, the potential of EGS for electricity generation in

medium- and high-grade regions and for direct-use heat, even in lower-grade regions, is significant.

5.2 Case-Study 2: Deep Geothermal for District Heating in NY and PA

GEOPHIRES has been used by Reber in his graduate work on assessing the potential for deep geothermal district heating systems in the states of New York and Pennsylvania (Reber, 2013). Based on climate data, Residential and Commercial Buildings Energy Survey data from the Energy Information Administration, and building and economic data from the U.S. Census Bureau, Reber estimated first the thermal energy demand for space and water heating for each town in NY and PA (2894 places in total) (Beckers et al., 2013). Combined with an updated geothermal gradient map for the region, and estimates of the local capital and O&M costs for a district heating system based on the total street length, Reber calculated the LCOH for deep geothermal district heating systems at each place, using a MATLAB program incorporating the GEOPHIRES tool. He considered three different cases of technological maturity, a similar approach as in Case-Study 1. A map with the result for the commercially mature case is shown in Figure 5.7. A key take-away message from his work is that for a moderate LCOH of 15 \$/MMBTU (5.1 ¢/kWh$_{th}$), about 20 GW$_{th}$ in development across NY and PA becomes economically attractive in the mid-term. A full description on the methodology, and an in-depth discussion of all results can be found in (Reber, 2013) and (Reber et al., 2014).

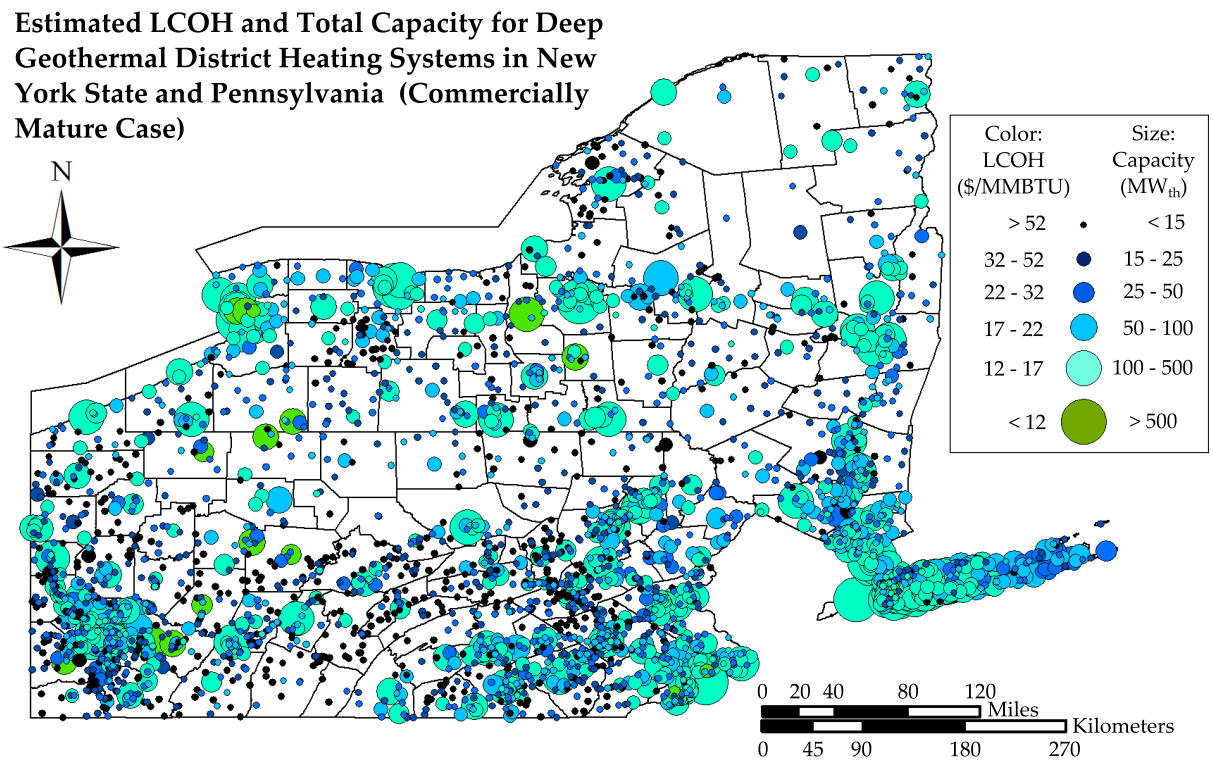

Figure 5.7 – Estimated LCOH ($/MMBTU) and total capacity (MW_{th}) for deep geothermal district heating systems in various places in New York State and Pennsylvania for commercially mature case. Adapted from (Reber, 2013).

5.3 Case-Study 3: Hybrid Low-Grade Geothermal-Biomass Cogeneration System for Cornell University Campus

5.3.1 Introduction and Background Information

In 2009, students, faculty and staff of Cornell University developed the Climate Action Plan (CAP) in response to the university's commitment to become carbon-neutral by 2050 (Cornell University, 2014a). The CAP consists of 62 actions aimed to cut carbon emissions to zero while setting an example for other campuses and creating a living laboratory for education and research on climate, energy and sustainability. Key actions include implementing building standards and energy conservation initiatives, producing heat and elec-

tricity from sustainable energy sources, and offsetting unavoidable CO_2 emissions with forest management and community projects. In 2013, accelerated action was called upon by the Faculty Senate in order to become carbon neutral by 2035. A report on the updated action plan, labeled the Accelerated Climate Action Plan (ACAP), has been released in 2015 (Cornell University, 2015).

The existing energy system on campus already consists of several energy-efficient and low-carbon-intense components such as two 15 MW_e natural gas turbines with heat recovery steam generators co-producing electricity and heat, a campus-wide district heating and cooling network, a lake-source cooling system, a 1.1 MW_e hydroelectric power plant, and a 1.8 MW_e solar photovoltaic (PV) array. Under the CAP, an extension of the solar PV array is suggested to 10 MW_e, as well as electricity generation from the 11.9 MW_e Black Oak Wind Farm, improvements in the district heating network by switching from steam to hot water, and a hybrid geothermal-biomass cogeneration system (Cornell University, 2014a). The envisioned future energy system for the campus is illustrated in Figure 5.8.

Integrating energy sources in a hybrid configuration can allow us to take advantage of synergetic effects by obtaining a higher combined energy output and efficiency or lower overall levelized cost, or by offsetting weaknesses of one energy source with strengths of another. In literature, geothermal energy is most often combined with solar energy when investigating its hybrid potential (Astolfi et al., 2011; Ghasemi et al., 2014). Examples of regional case-studies are a hybrid geothermal-solar system for Mexico (Lentz and Almanza, 2006), Australia (Zhou et al., 2013), and Nevada, USA (Greenhut et al., 2010). In 2012, Enel Green Power developed the first commercial-scale hybrid geothermal-solar PV plant in Nevada and recently expanded it with a concentrated solar thermal system (DiMarzio et al., 2015). Hybrid geothermal-biomass plants have also been investigated. Examples are the case-study for hybridizing an existing geothermal plant in New Zealand

(Thain and DiPippo, 2015), and in Italy (Srinivas et al., 2014). Another case-study of integrating geothermal energy with biomass for generating electricity, liquefying gas (air), and providing drying, heating and cooling was conducted by Malik et al. (2015). Recently, Enel Green Power announced plans to develop the first hybrid geothermal-biomass plant in Tuscany, Italy (Enel Green Power, 2014).

Given Cornell University's location in Upstate New York characterized by cold winters and correspondingly large heating demands, a hybrid geothermal-biomass cogeneration system is recommended by the CAP to cover most of the heating load while cutting CO_2 emissions by up to 40%. With the exception of a few isolated hot springs, no known hydrothermal resources have been identified in Upstate New York. Therefore, the geothermal system envisioned for Cornell in this study is an Enhanced Geothermal System (EGS), although a hot sedimentary aquifer might be possible as well. The overall heat flow and average geothermal temperature gradients, while locally higher than the averages for the Northeast region, are still below the higher-grade systems in the Western U.S. Nevertheless, indigenous geothermal energy and biomass are clear choices because: (1) even a lower-grade geothermal gradient of around 25°C/km is still acceptable when focusing on direct-use heat applications, (2) Cornell's agriculture and forest land holdings are extensive. Cornell University owns 4,000 acres ($1.6 \cdot 10^7$ m^2) of idle pasture or crop land where bio-energy crops could be cultivated, and about 8,000 acres ($3.2 \cdot 10^7$ m^2) of forested land that could be harvested sustainably. Additional biomass resources might include campus food and solid waste, and manure from Cornell's two dairy farms. Further (3), alternative renewable heating sources, such as solar thermal, are lower-grade and intermittent. A small modular nuclear reactor for cogeneration could be another option but permitting and gaining public acceptance in Tompkins County would be extremely difficult and hence is not considered here.

Geothermal energy and biomass can be integrated in several ways, with different con-

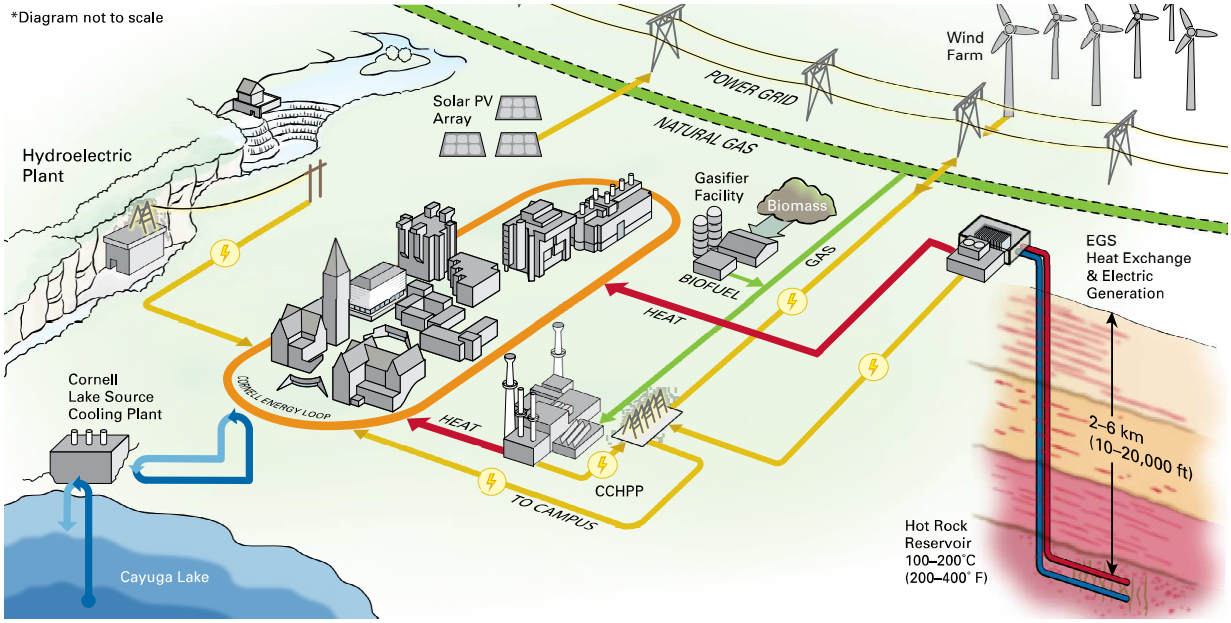

Figure 5.8 – Future energy system on the Cornell University campus as envisioned by the Climate Action Plan (Cornell University, 2014a). When fully converted to a carbon-neutral campus, a large part of the heating and electricity consumption would be supplied by a hybrid geothermal-biomass cogeneration system.

figurations shown in the works by Thain and DiPippo (2015) and Srinivas et al. (2014). In the configuration proposed by the CAP and analyzed in this study, the geothermal system covers the majority of the heating load during the cold months and generates electricity during the summer. During very cold winter days when geothermal energy alone is not sufficient, pretreated biomass is converted in a gasifier to syngas and combusted in the existing natural gas units to produce additional heat with electricity as co-product. The objective of this study was to investigate a base case scenario of the proposed hybrid geothermal-biomass system at Cornell. Using a geothermal simulation tool, cost correlations and resource maps for the area, all recently developed in our research group, new results on the performance of EGS in Ithaca are reported. This study continued the analysis in our team by providing an update and expansion of previous studies by Tester et al. (2010) and Lukawski et al. (2013). The results in this study are for a base case scenario only. Future work will look into variations on this base case to explore the sensitivity of the technical and economic system performance to several parameters including drilling

costs, discount rate, and reservoir performance.

The existing Cornell energy system is described in more detail in Section 5.3.2 where data on current energy production, consumption, efficiency, and CO_2 emissions are provided. The proposed geothermal-biomass cogeneration system for Cornell is presented in Section 5.3.3. Simulation parameters and results are given in Section 5.4.4. The simulation model is based on GEOPHIRES in combination with capital and O&M costs correlations, as well as energy conversion efficiencies for the biomass gasifier from literature. The overall capital and levelized cost, energy output, and avoided CO_2 emissions of the hybrid system are estimated for two cases (small-scale pilot project and large-scale full conversion system). The focus of this study is on the generation of heat and electricity, not its distribution. In Section 5.3.5, the results are put in perspective by comparing them with results from previous studies on utilizing geothermal energy for Cornell (Tester et al., 2010; Lukawski et al., 2013) and with a traditional natural gas boiler system. Finally, conclusions of this case-study are given in Section 5.3.6.

5.3.2 Existing Energy System at Cornell University

Cornell University's main campus in Ithaca, New York represents a mid-size community in the Northeastern United States with around 31,000 students, faculty and staff (Cornell University, 2014a,b). In 2013, the campus gross area was around 14,000,000 ft^2 (1,300,000 m^2), with almost 10,000,000 ft^2 (930,000 m^2) of net building area and 200,000 ft^2 (19,000 m^2) of greenhouse area. The campus energy consumption in 2013 for heating, electricity and cooling was around 1 trillion BTU (290 GWh), 0.75 trillion BTU (220 GWh), and 0.5 trillion BTU (145 GWh), respectively (Cornell University, 2014a). Figure 5.9 shows that, despite a significant growth in campus buildings gross area, campus energy needs have remained steady over the last several years, thanks to the recently implemented energy conserva-

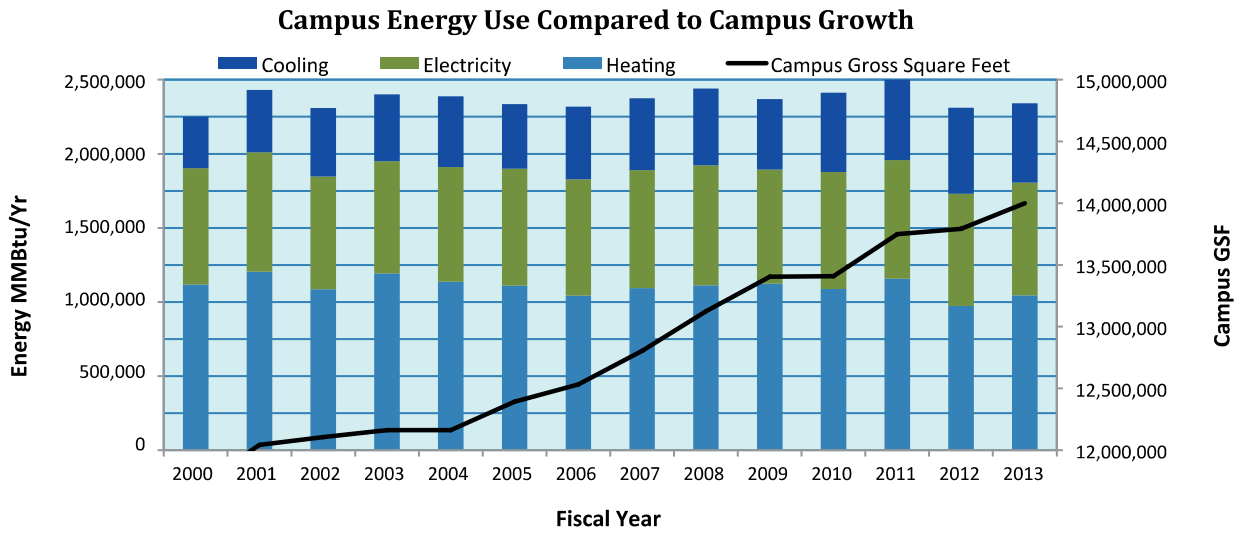

Figure 5.9 – Campus heating, electricity and cooling consumption (in 1,000 BTU/year) and campus gross area (in ft^2) from 2000 to 2013. Despite campus area growth, total energy consumption has remained steady due to energy conservation initiatives (Cornell University, 2014a).

tion initiatives. Cornell's location in Upstate New York characterized by long and cold winters explains the large heating demand with 7,182 annual standard heating degree-days in contrast to only 315 cooling degree-days (Lukawski et al., 2013). The monthly heating demand ranges between 11 and 53 GWh for campus buildings and 0.45 and 2.3 GWh for the greenhouses. This data was utilized as input data for the simulations.

A state-of-the-art natural gas combined heat and power (CHP) system was commissioned at Cornell in 2009 and covers the majority of the campus heating and electricity demand. This system consists of two identical natural gas turbines with generators rated at 15 MW_e each, and a heat recovery steam generator producing up to 22,500 pounds per hour (2.8 kg/s) of low-pressure stream and 136,000 pounds per hour (17.1 kg/s) of high-pressure steam (see Figure 5.10). After combining the steam outputs from both units, the low-pressure steam is directly fed to the campus district heating system, while the high-pressure steam passes first through two back-pressure steam turbines, installed in 1986, with a total nominal output of 7.5 MW_e before eventually feeding into the district heating network as well. The steam supply temperature and pressure to the district heating sys-

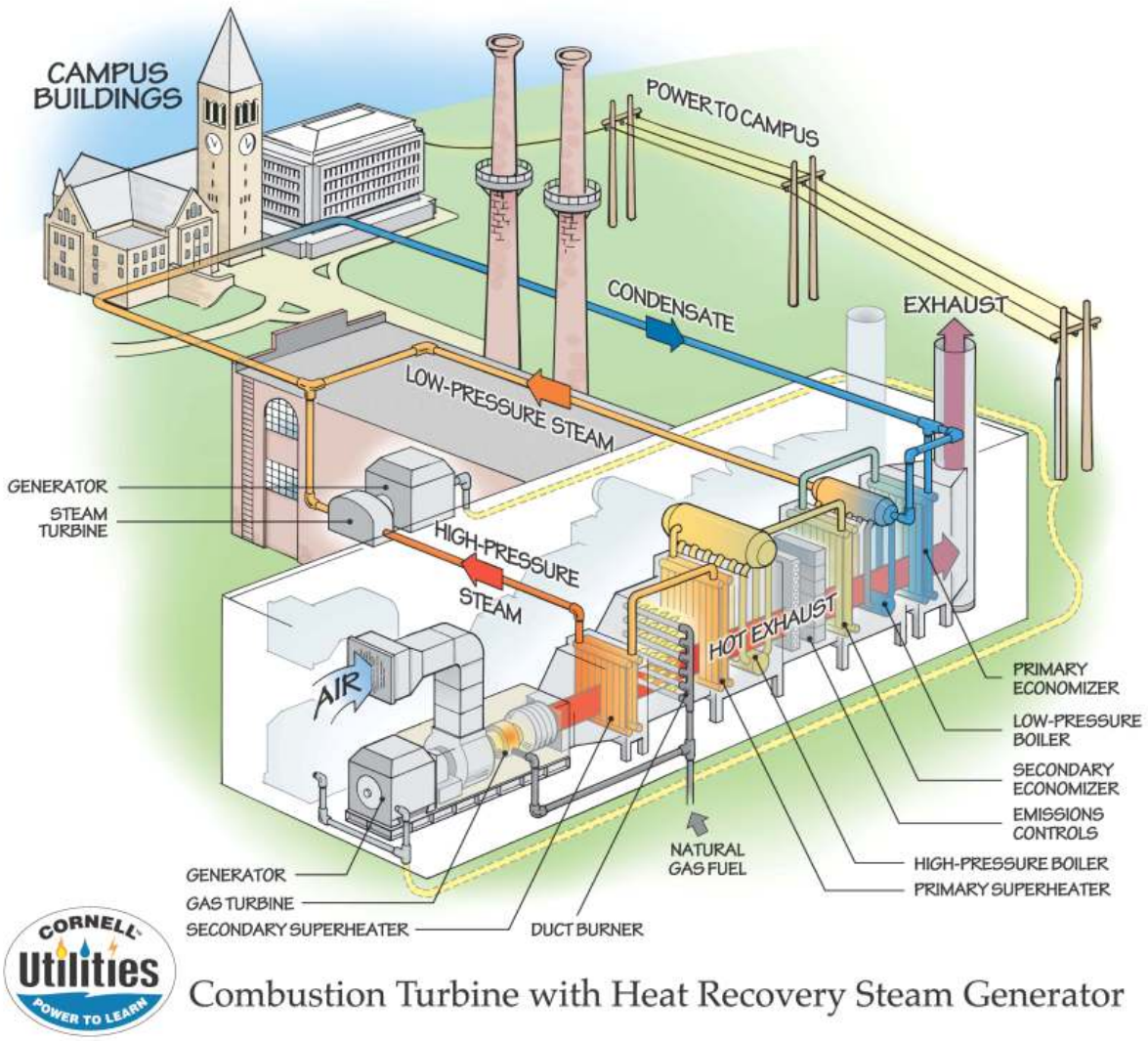

Figure 5.10 – Diagram illustrating one of two identical natural gas combustion turbines with exhaust gas heat recovery system for generation of low- and high-pressure steam (Cornell Utilities, 2009).

tem range between 320 and 475°F (160 and 246°C) and between 75 and 90 psia (5.2 and 6.2 bara), respectively. For cold days, additional steam can be generated using natural gas boilers. The total length of the district heating network is about 28.5 miles (46 km) and approximately 17% of the distributed heat is lost. In 2013, the CHP system generated 215 GWh of electricity and 1.25 trillion BTU (366 GWh) of steam. The total amount of natural gas input was 1.98 trillion BTU (580 GWh) resulting in an overall energetic efficiency of 77%. An additional 4,000 MWh of electricity were generated by a 1.1 MW_e hydroelec-

tric plant, and a net amount of 15,700 MWh of electricity was purchased from the grid. The recent installation of a 1.8 MW_e solar PV array is expected to produce 2,500 MWh of electricity annually. Further, 99% of the cooling demand was covered by the lake source cooling system, commissioned in 2000, and operating with a coefficient of performance (COP) of 23.

In 2012, the total campus carbon footprint was 218,000 metric tons of CO_2-eq with on-site combustion, commuting and air travel, and purchased electricity responsible for 142,000 tons, 59,000 tons, and 17,000 tons, respectively (Cornell University, 2014a). Notably, the 2012 carbon emissions were 32% lower than the 2008 emissions, amounting to a reduction of 101,000 metric tons per year. This decrease was mainly due to switching from coal-fired power to the natural gas-based CHP plant in 2009 and from that point on eliminating all on-site coal combustion.

Seven key actions were identified in the CAP to further cut the CO_2 emissions by 85% with respect to 2012 levels: (1) develop the hybrid geothermal-biomass system (38%), (2) offset emissions by carbon management strategies such as forest management and community projects (27%), (3) purchase around 42 GWh of electricity expected to be produced by the Black Oak Wind Farm (5%), (4) implement all campus conservation initiatives (5%), (5) fully integrate building energy standards on campus (5%), (6) optimize the heat distribution network by switching from steam to hot water (3%), and (7) develop the Cornell University Renewable Bioenergy Initiative (CURBI) to convert campus waste streams to biogas (1%). The remaining 15% of emissions would be eliminated by an additional 18 action steps such as expansion of the solar PV system and efficiency improvements of the hydroelectric power plant. With an anticipated 38% reduction in emissions compared to 2012 levels, corresponding to 82,000 metric tons of CO_2-eq, the hybrid geothermal-biomass system acts as a core player in the CAP. In the following sections, the technical and economic performance and required capital investment of such a system are studied.

5.3.3 Proposed Hybrid Geothermal-Biomass Cogeneration System for Cornell University

Cornell has several options available for sustainable electricity generation, including wind, solar PV and to a small extent hydro energy; however, the options for renewable heat production are limited to geothermal and biomass. As discussed in Section 5.3.5, only a geothermal system can realistically be scaled up on Cornell lands to provide approximately 1 trillion BTU (293 GWh) of heat per year to meet the current annual heating demand. Therefore, the aim of the proposed hybrid geothermal-biomass cogeneration system is to supply the bulk of the campus heating load with EGS as a base-load heat provider, and biomass as an auxiliary heating source for cold winter days. Technically, the geothermal system could be sized to cover all daily heat loads even in winter without the need for a biomass back-up system. However, such design would not be optimal from an economic point of view. An oversized geothermal system would be expensive because it would operate at its maximum thermal output for only a few weeks a year, while the required capital investment scales according to maximum power output. Furthermore, to avoid having the geothermal system stand idle in summer, electricity will be generated using an Organic Rankine Cycle (ORC), hereby increasing the overall capacity factor. The proposed biomass operation consists of sustainable cultivation of bio-crops on Cornell lands, drying them using geothermal heat, converting the wood chips in a gasifier to syngas ($CO + H_2$), and burning this fuel in the existing CHP plant to generate supplemental heat and electricity. The biomass could be utilized in different ways, e.g. in torrefaction and wood powder combustion. However, since the investment in the state-of-the-art CHP plant, described in Section 5.3.2, has been made, gasifying the biomass and burning the syngas in this plant is the more attractive choice even though it would require some derating of the plant's generation capacity. A simplified diagram of the integrated hybrid geothermal-biomass cogeneration system is shown in Figure 5.11.

As stated earlier, the geothermal system envisioned for the Cornell campus is an Enhanced or Engineered Geothermal System (EGS). The anticipated geothermal gradient in the area is approximately 25°C/km (Stutz et al., 2015), typical for an above-average gradient in the Eastern U.S. but much lower than the gradients seen in the Western U.S. We assumed 25°C/km as an average value for our study albeit accepting that there is inherent uncertainty in that value until the gradient is measured in a deep exploration hole at the site. The focus is on direct-use heat and cogeneration rather than just electricity production in order to obtain acceptable levelized costs for these lower-grade resources (see also Case-Study 1 and 2). The EGS would consist of several injection and production wells intersecting a hydraulically stimulated reservoir of "hot dry rocks" used to circulate water in a closed loop. The well depths are expected to be on the order of 5 km (16,400 ft.) to obtain average geofluid production temperatures around 125°C. This temperature would be sufficient for campus district heating assuming that the Cornell heat distribution system is switched from steam to pressurized liquid water. A geofluid temperature of 125°C would also still provide an acceptable utilization efficiency of the ORC power plant. Lower-temperature water from the lake could be used to provide efficient heat rejection from the ORC. After a fraction of heat carried by the geothermal fluid is extracted by the district heating system or ORC plant, the remaining low-temperature heat will be used for drying of the biomass. An alternative to the proposed geothermal option, a campus-scale geothermal heat pump system, is technically possible but would significantly increase the electricity consumption and is not considered here.

As mentioned earlier, several biomass feedstocks are available at Cornell to be converted to bio-gas, including food waste, manure, harvested forest products and bio-energy crops including willow and switchgrass. The performance and potential of many of these feedstocks for Cornell are analyzed in the CURBI project, one of the key actions in the CAP (see Section 5.3.2). To simplify our preliminary feasibility study, willow, sustainably cultivated on Cornell lands, was selected as the biomass source. The U.S. 1-billion-

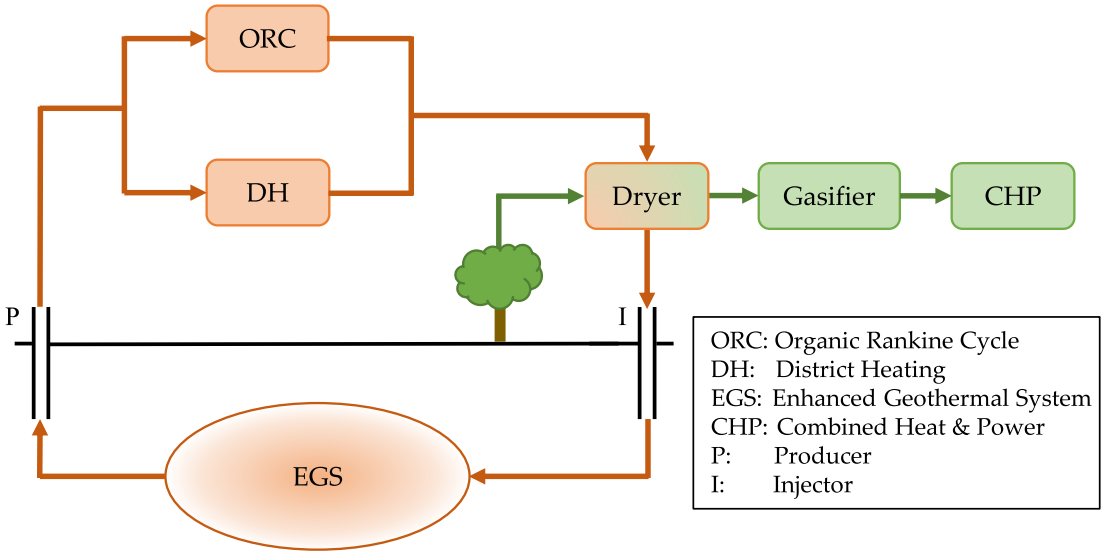

Figure 5.11 – Simplified diagram of the proposed hybrid geothermal-biomass cogeneration system. Red streams refer to geothermal fluid, green streams refer to biomass.

ton study (Perlack and Stokes, 2011) identified willow as an appealing bio-crop for the Northeastern U.S. because of: (1) its high yields, (2) ease of breeding, (3) decades of experimental research being available on willow in Europe and North America, and (4) willow having a high positive net-energy ratio of 1:50, and low carbon intensity when considering the production, harvest, transportation and conversion. Field tests in central New York (CURBI, 2014) produced willow with yields between 3.7 and 5.2 dry tons/acre/year (1 ton equals 907 kg). For this study, an average value of 4.45 dry tons/acre/year was assumed, close to the value reported by the U.S. DOE study (5.1 dry tons/acre/year). The maximum amount of idle pasture and crop land available for willow cultivation at Cornell is about 4,000 acres ($1.6{\cdot}10^7$ m^2) Cornell University (2014a).

5.3.4 Simulation Parameters and Results

Two hybrid geothermal-biomass cases are investigated in this study: Case 1 represents a pilot or demonstration project with only one doublet (one production well and one in-

Table 5.4 – Base case technical and financial parameter values.

Parameter	Case 1 - Pilot Project (20%)	Case 2 - Full Conversion (98%)
EGS Engineering and Financial Parameters		
Geothermal Gradient	25°C/km	
Well Depth	5 km	
Well configuration	Doublet	Triplet
Number of producers	1	6
Number of injectors	1	3
Ambient Temperature	15°C	
Bottom Hole Temperature	140°C	
Producer Flow Rate	50 kg/s per Producer	
Reservoir Thermal Model	Percentage Thermal Drawdown	
Reservoir Temperature Drawdown Rate	1%/year	
Reservoir Impedance per Well-Pair	0.10 MPa·s/L	
Reservoir Water Loss Rate	2%	
Production Wellbore Temperature Drop	Ramey's Model	
Average Well Casing Inner Diameter	0.254 m (10")	
Reservoir Capacity Factor	90%	
Geothermal Fluid Pump Efficiency	85%	
Fluid Temperature Drawdown Threshold	14%	
Geothermal Power Plant Type	Subcritical Organic Rankine Cycle (ORC)	
EGS Capital costs	GEOPHIRES Correlations	
EGS O&M costs	GEOPHIRES Correlations	
Electricity Rate	7 ¢/kWh$_e$	
Reinjection temperature	60°C	
Biomass System Engineering and Financial Parameters		
Biomass Cultivating Acreage	500 acres	2,500 acres
Biomass Crop	Willow	
Annual biomass Yield	4.45 dry tons/acre	
Lower Heating Value (LHV)	17.6 MJ/kg	
Gasifier efficiency (based on LHV)	85%	
Gasifier Capital Cost	3,250 \$/kW$_{th}$	
Gasifier O&M Cost	4.5% of Installed Cost + 0.0037 \$/kWh$_{th}$	
Biomass Establishment Cost	1,120 \$/acre	
Biomass Feedstock Price	50 \$/dry metric ton	
General Financial Parameters		
System Lifetime	30 years	
Construction Time	2 years	
Discount Rate	5%	
Inflation Rate	2%	
Levelized Cost Model	Standard Discounting LCOH model	

Table 5.5 – Base case simulation results.

	Case 1	Case 2
EGS Power Output Results		
EGS Peak Heat Generating Capacity (MW_{th})	14.2	85.4
EGS Peak Net Electricity Generating Capacity (MW_e)	0.7	4.1
EGS Average Annual Heat Production (GWh_{th}/year)	72.9	362.8
EGS Average Annual Net Electricity Prod. (GWh_e/year)	0.5	5.7
Biomass Power Output Results		
Biomass Peak Heat Generating Capacity (MW_{th})	0.8	4.5
Biomass Peak Electricity Generating Capacity (MW_e)	0.5	2.6
Biomass Average Annual Heat Prod. (GWh_{th}/year)	3.3	16.3
Biomass Average Annual Electricity Prod. (GWh_e/year)	1.9	9.5
EGS Financial Results		
EGS Total Capital Investment (M$)	39.5	176.6
of which: Well Drilling and Completion Cost (M$)	30.4	136.6
Piping, Heat Exchangers and ORC Cost (M$)	5.5	31.4
Reservoir Stimulation Cost (M$)	2.5	7.5
Exploration Cost (M$)	1.1	1.1
EGS O&M Costs (M$/year)	0.7	3.3
Biomass Financial Results		
Biomass Total Capital Investment (M$)	7.4	40.2
Biomass O&M Cost (M$/year)	0.4	2.3
Overall Financial and CO_2 Emissions Results		
Total Capital Cost (M$)	46.9	216.8
Total O&M Cost (M$/year)	1.1	5.6
Levelized Cost of Heat (LCOH) ($/MMBTU)	17.3	15.9
Net Avoided CO_2 emissions (metric tons/year)	19,000	94,000

jection well) for the geothermal system and a small-scale biomass operation of 500 acres ($2.0{\cdot}10^6$ m^2), which together supply about 20% of the campus heating load. Case 2 represents a full-scale (98%) conversion project with six production and three injection wells and 2,500 acres ($1.0{\cdot}10^7$ m^2) for willow cultivation. A MATLAB code (MathWorks, 2012) has been developed to simulate the technical and economic performance of the hybrid system. This program incorporates (1) a standard discounted levelized cost model, (2) performance and cost data for biomass cultivation and gasifier conversion as reported in literature, and (3) reservoir, wellbore, and ORC performance and cost data for the geothermal system from GEOPHIRES. The discount rate in the levelized cost model was set at 5%

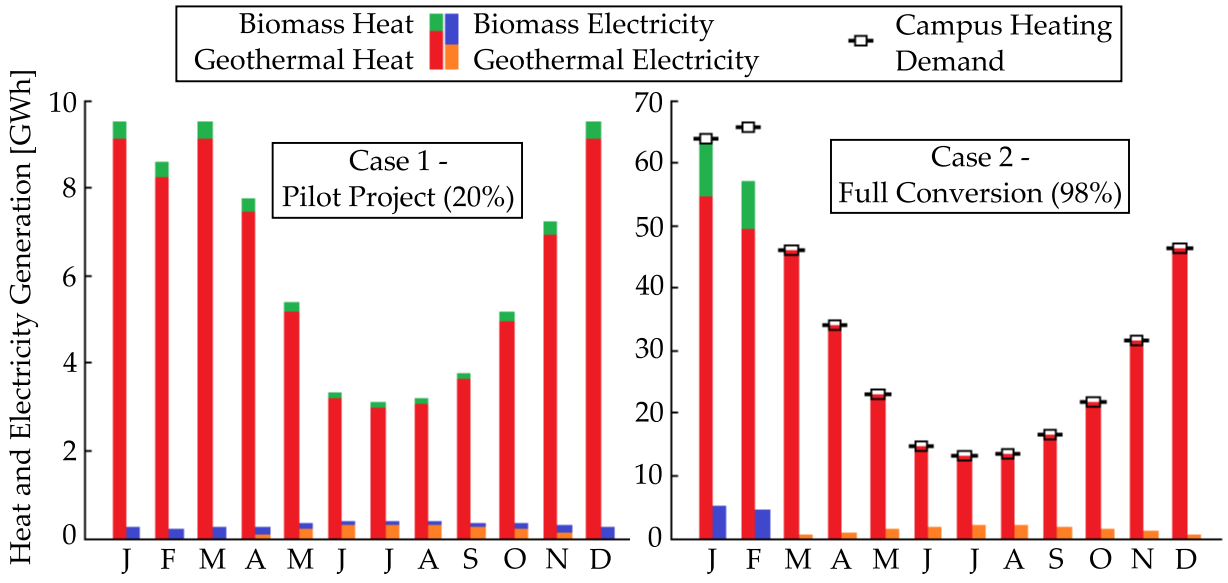

Figure 5.12 – Monthly geothermal and biomass heat and electricity generation for Case 1 (left) and Case 2 (right).

- a low value reflecting Cornell's long-term time horizon of this infrastructure investment. All input parameters for the two cases are listed in Table 5.4.

All geothermal parameters and models related to the design and performance of the EGS reservoir and surface plant are described in detail in Chapter 4 and to a certain extent Section 5.1 (Case-Study 1). Most parameter values such as a 50 kg/s flow rate per producer or 1%/year drawdown rate are taken from the "mid-term technology" and "commercially mature technology" cases (Section 5.1), which we feel is a reasonable assumption given that the time frame for the implementation of Cornell's system is around 2030. At a thermal drawdown of 14%, occurring after 15 years (mid-point lifetime), all wells are replaced with newly drilled wells. A high overall capacity factor of 90% is assumed for the geothermal system because during times of lower heating demand, i.e. summer months, the geothermal system will produce both electricity and hot water for use in Cornell's buildings and laboratories. Further, it is assumed the first well drilled serves both as exploration well and eventual production well. Potentially, more exploration wells are required, which would increase the total investment costs and LCOH.

Performance and cost data on willow cultivating and gasifying are taken from literature. Annual willow biomass yields for central New York have been reported by a CURBI feasibility study at Cornell (CURBI, 2014). A report by the International Renewable Energy Agency (IRENA, 2012) provides lower heating values (LHV) for willow feedstocks, and average gasifier capital and O&M costs. The gasifier type selected for this study is a fixed-bed gasifier. Further, it is assumed that the feedstock cost, which includes cost for harvesting, chipping, transportation, drying, storage, and maintaining the field is 50 $/dry ton, which is in the range of values reported by CURBI (2014) and IRENA (2012). Also, the "1-billion ton study" reports a willow field establishment cost of 1,120 $/acre (Perlack and Stokes, 2011). A gasifier conversion efficiency of 85% has been reported by Ptasinski (2008). Switching from natural gas to syngas poses technical challenges including flame stability issues, component overheating, and increased corrosion potential (Gibbons and Wright, 2009). Various research has been conducted, e.g. by Chacartegui et al. (2012b; 2012a; 2013), on the performance and potential of running natural gas turbines on syngas. This research shows that off-design operation without retrofitting is possible but a higher performance and durability can be obtained by optimizing certain components such as the turbine cooling system and combustor. Identifying the specific retrofitting requirements for the Cornell system is out of the scope of this study. However, a drop of 20% in CHP conversion efficiency to heat and electricity is considered as a penalty for switching from natural gas to syngas. Retrofitting costs are neglected as they are assumed as being part of a regular major overhaul investment.

The results for both cases for the heat and electricity generating capacity and annual production, as well as the capital and O&M costs, LCOH (levelized cost of heat), and avoided CO_2 emissions are listed in Table 5.5. Since the main product of the cogeneration system is heat, it is opted to express the levelized costs as LCOH with electricity sales incorporated into the calculation as positive income cash flow at a rate of 7 ¢/kWh$_e$. Net avoided CO_2 emissions are based on decreased natural gas consumption in the CHP

plant for heat generation with lost electricity purchased from the grid with CO_2 emissions factor of 501 lbs/MWh_e (227 g/kWh_e) (Cornell University, 2014b). No embedded CO_2 emissions in the geothermal plant or biomass operation are included. The average monthly heat and electricity generation by the geothermal and biomass systems for both cases is shown in Figure 5.12. For Case 2, the monthly campus heat demand includes the heat demand for buildings and greenhouses and assumes a 5% thermal energy distribution loss.

5.3.5 Discussion of Results

The results show that an investment of around $47M in a demonstration-scale hybrid geothermal-biomass system can supply around 20% of the campus heating demand and produce an additional 2.4 GWh of electricity per year while saving annually 19,000 metric tons of CO_2 emissions. A full conversion to cover 98% of the heating load requires around $217M of initial investment, and generates annually 15.2 GWh of electricity while saving 94,000 metric tons of CO_2 emissions. The 15.2 GWh of electricity corresponds to about 7% of the current campus electricity demand. The LCOH is slightly lower in Case 2 due to economies of scale for the EGS (three triplets instead of one doublet), as reflected by a lower EGS capital cost per heat generating capacity (2,070 \$/kW_{th} vs. 2,780 \$/kW_{th}). One could have designed a hybrid system to cover 100% of the heating load by increasing either the EGS reservoir capacity (e.g. four instead of three triplets), or the biomass output (more acres and larger gasifier). However, in both cases, the LCOH would be higher because either the geothermal or biomass system would be significantly oversized. The remaining 2% could be covered by geothermal heat pumps or natural gas, whose emissions could then be offset by other means. For the pilot project (Case 1), it would be possible to operate the EGS reservoir at nearly full capacity for 12 months without requiring an ORC. The LCOH would be lower, however, the performance of the cogeneration

aspect in this demonstration project could then not have been assessed.

An LCOH around 16 to 17 $/MMBTU (5.5 to 5.8 ¢/kWh$_{th}$) is of the same order as the LCOH found in Case-Study 1 (Section 5.1) and Case-Study 2 (Section 5.2). In a 2010 study on EGS for Cornell, Tester et al. reported LCOH values that are 2-3 times lower; this can be explained by their assumptions of a higher flow rate per producer, a higher gradient, drilling costs that are not current, a negligible drawdown rate, and no cogeneration. Also in an earlier hybrid EGS-biomass study for Cornell by Lukawski et al. (2013), different parameter values were assumed such as a higher flow rate per producer, higher geothermal gradient, lower drawdown rate and shorter system lifetime. Further, they considered torrefied biomass boilers instead of gasification and expressed the results as levelized cost of electricity (LCOE) instead of heat (LCOH). Nevertheless, they calculated a $34M investment for a hybrid geothermal biomass cogeneration system to supply 25% of the campus heat demand, 4% of the campus electricity demand (9 GWh) and save 25,500 metric tons of CO_2 emissions per year.

Due to low natural gas prices, the geothermal-biomass system is currently not economically-competitive with natural gas boilers. In today's energy markets with record low prices for natural gas, the LCOH for heat generated with natural gas boilers is on the order of 6 to 12 $/MMBTU (2.0 to 4.1 ¢/kWh$_{th}$) for industrial and residential rates, respectively (see Section 5.1), considerably lower than the LCOH of around 16 $/MMBTU (5.5 ¢/kWh$_{th}$) calculated in this case-study. Nevertheless, natural gas heating systems are exposed to price volatility and are subject to CO_2 emissions. Gas price increases and some valuation of "environmental damage"costs for emitted carbon are likely to occur in the coming decades.

The results presented in Figure 5.12 and Table 5.5 should be interpreted with care. The required capital investment and resulting LCOH are highly sensitive to drilling costs, geothermal gradient, capacity factor, flow rate per producer, surface plant O&M costs,

and drawdown rate (Section 5.1). Moreover, the LCOH also depends significantly on plant lifetime and discount rates. Furthermore, no costs for permitting, transmission lines, and water supply pipes are included. On the other hand, no subsidies, tax incentives, CO_2 credits, and learning effects are incorporated, and a drawdown rate of 1% might be too high (see Section 5.1). In addition, a lower LCOH could most likely be obtained by performing a full system optimization and considering other components for biomass utilization such as boilers instead of only the CHP plant. Nevertheless, we believe the base case results cited in this preliminary study provide a measure of the technical and economic feasibility of a hybrid geothermal-biomass plant for Cornell. One could envision starting with a demonstration-scale project employing a small geothermal system using an EGS well doublet and small biomass operation and gradually adding more geothermal wells and biomass cultivation area to scale up to full capacity over a period of 20 years. Eventually saving 94,000 metric tons per year of CO_2 emissions, covering 98% of the campus heating load and supplying an additional 15.2 GWh of electricity, could be a viable key strategy in the CAP.

5.3.6 Conclusions

This case-study analyzed the technical and economic feasibility of a hybrid geothermal-biomass cogeneration system for the Cornell University campus as a key action of the CAP to cut carbon emissions to zero by 2050 or sooner. Cornell University represents an average-sized community, with an existing district heating and cooling system, high heating load, easy access to biomass resources, and still acceptable geothermal gradient within the Northeast, and therefore forms the ideal setting to demonstrate the feasibility of these types of systems before scaling up and replicating at other communities. With about 25% of the U.S. primary energy demand consumed as low-temperature heat, and low to medium-grade EGS and biomass resources widely available throughout the coun-

try, a hybrid geothermal-biomass cogeneration system could become a nationwide energy player. This scenario appears more likely if one also considers the likely future environment of higher fossil fuel prices, the need to replace aging infrastructure and the urgency to cut CO_2 emissions.

The geothermal system at Cornell would use EGS technology for engineering the reservoir. This system would produce heat at times of high heating demand and both heat and electricity at other times. Peak heating demand during winter would be met by gasifying biomass, and combusting the syngas in the existing CHP plant. In this preliminary study willow was used as the biomass resource. As a starting point for this study, we assumed a set of base case conditions to specify required resource, technical performance and economic parameters for both the geothermal and biomass components. A MATLAB computer model was developed to model the system by incorporating output from GEOPHIRES for the specified geothermal system, and relying on cost and performance data published in literature for the biomass system. Two case-studies were investigated for the Cornell campus. Case 1 represents a pilot project with one EGS doublet, and 500 acres ($2.0 \cdot 10^6$ m^2) for cultivated willow, together capable of covering 20% of the heating demand. Case 2 represents a full conversion system, covering about 98% of the campus heating load, supplied by three EGS triplets and 2,500 acres ($1.0 \cdot 10^7$ m^2) of willow cultivation.

Key results from the simulations are that the pilot project (Case 1) requires $47M of capital investment, and produces 76.2 GWh of heat and 2.4 GWh of electricity per year. The CO_2 emissions are cut by 19,000 metric tons per year, and the levelized cost of heat (LCOH) is 17.3 $/MMBTU (5.9 ¢/$kWh_{th}$). The full-conversion project (Case 2) requires $217M, and generates annually 379 GWh of heat (98% of campus supply) and 15.2 GWh of electricity (7% of campus consumption). The net avoided CO_2 emissions are 94,000 metric tons per year (43% of 2012 campus emissions) and the LCOH is 15.9 $/MMBTU

(5.4 ¢/kWh$_{th}$). These results are for a base case scenario; to address the uncertainty in this analysis, future work will look into the sensitivity of the required capital investment, LCOH, and heat and electricity output to many of the financial and technical parameters including drilling costs, discount rate and reservoir performance.

References

Aguirre, G. A. (2014). *Geothermal Resource Assessment: A Case Study of Spatial Variability and Uncertainty Analysis for the State of New York and Pennsylvania*. Master Thesis, Cornell University, Ithaca, New York, United States.

Astolfi, M., Xodo, L., Romano, M. C., and Macchi, E. (2011). Technical and economical analysis of a solar–geothermal hybrid plant based on an Organic Rankine Cycle. *Geothermics*, 40 (1): 58–68.

Augustine, C., Young, K. R., and Anderson, A. (2010). Updated U.S. Geothermal Supply Curve. In *Proceedings Thirty-Fifth Workshop on Geothermal Reservoir Engineering*, Stanford University, Stanford, California, February 1 - February 3, 2010, SGP-TR-191.

Beckers, K. F., Lukawski, M. Z., Reber, T. J., Anderson, B. J., Moore, M. C., and Tester, J. W. (2013). Introducing GEOPHIRES v1.0: Software Package for Estimating Levelized Cost of Electricity and/or Heat from Enhanced Geothermal Systems. In *Proceedings Thirty-Eighth Workshop on Geothermal Reservoir Engineering*, Stanford University, Stanford, California, February 11 - February 13, 2013, SGP-TR-198.

Beckers, K. F., Lukawski, M. Z., Anderson, B. J., Moore, M. C., and Tester, J. W. (2014a). Levelized costs of electricity and direct-use heat from Enhanced Geothermal Systems. *Journal of Renewable and Sustainable Energy*, 6, 013141.

Beckers, K. F., Lukawski, M. Z., Anderson, B. J., Moore, M. C., and Tester, J. W. (2014b).

Erratum: "Levelized costs of electricity and direct-use heat from Enhanced Geothermal Systems" [J. Renewable Sustainable Energy 6, 013141 (2014)]. *Journal of Renewable and Sustainable Energy*, 6, 059902.

Beckers, K. F., Lukawski, M. Z., Aguirre, G. A., Hillson, S. D., and Tester, J. W. (2015). Hybrid Low-Grade Geothermal-Biomass Systems for Direct-Use and Co-Generation: from Campus Demonstration to Nationwide Energy Player. In *Proceedings Fortieth Workshop on Geothermal Reservoir Engineering,* Stanford University, Stanford, California, January 26 - January 28, 2015, SGP-TR-204.

Chacartegui, R., Sánchez, D., de Escalona, J. M., Jimenez-Espadafor, F., Munoz, A., and Sánchez, T. (2012a). SPHERA project: Assessing the use of syngas fuels in gas turbines and combined cycles from a global perspective. *Fuel Processing Technology*, 103: 134–145.

Chacartegui, R., Sánchez, D., de Escalona, J. M., Monje, B., and Sánchez, T. (2012b). On the effects of running existing combined cycle power plants on syngas fuel. *Fuel Processing Technology*, 103: 97–109.

Chacartegui, R., Sánchez, D., de Escalona, J. M., Muñoz, A., and Sánchez, T. (2013). Gas and steam combined cycles for low calorific syngas fuels utilisation. *Applied energy*, 101: 81–92.

Cornell University (2014a). *Climate Action Plan Update 2013 & Roadmap 2014 - 2015*. Available at http://www.sustainablecampus.cornell.edu/initiatives/climate-action-plan.

Cornell University (2014b). *Fiscal Year 2013 Cornell University Central Energy Plant (CEP) Fast Facts*. Available at http://energyandsustainability.fs.cornell.edu/file/FY_2013_DRF_CU_Energy_Fast_Facts_Master.pdf.

Cornell University (2015). *Cornell Leadership for Climate Neutrality - Strategies & 12-Month Milestones to Accelerate the Climate Action Plan*. Climate Action Plan Acceleration Working Group, Cornell University.

Cornell Utilities (2009). *Combined Heat and Power Plant*. Available at http:// energyandsustainability.fs.cornell.edu/util/heating/production/cep.cfm.

CURBI (2014). *CURBI (Cornell University Renewable Bioenergy Initiative) Feasibility Study*. Available at http://cuaes.cals.cornell.edu/sustainability/curbi/.

DiMarzio, G., Angelini, L., Price, W., Chin, C., and Harris, S. (2015). The Stillwater Triple Hybrid Power Plant: Integrating Geothermal, Solar Photovoltaic and Solar Thermal Power Generation. In *Proceedings World Geothermal Congress 2015,* Melbourne, Australia, 19-25 April 2015.

EEE (2010). *Capital Cost Recommendations for 2009 TEPPC Study*, EEE, Energy and Environmental Economics, Inc. Available at http://www.wecc.biz/committees/ BOD/TEPPC/Versions/ 100106_TEPPC_E3_CapitalCosts.ppt_2.0.ppt.

EIA (2011). *Annual Energy Review 2011*, U.S. Energy Information Administration. DOE/EIA-0384.

EIA (2013). *Annual Energy Outlook 2013*, U.S. Energy Information Administration.

EIA (2015). *International Energy Outlook 2015*, U.S. Energy Information Administration.

Enel Green Power (2014). *Press Release: In Tuscany, first plant in the world to integrate geothermal and biomass*. Available at http://www.enelgreenpower.com/eWCM/ salastampa/comunicati_eng/1662787-1_PDF-1.pdf.

Fishbone, L. G. and Abilock, H. (1981). Markal, a linear-programming model for energy systems analysis: Technical description of the bnl version. *International journal of Energy research*, 5 (4): 353–375.

Fox, D. B., Sutter, D., and Tester, J. W. (2011). The thermal spectrum of low-temperature energy use in the United States. *Energy & Environmental Science*, 4 (10): 3731–3740.

Ghasemi, H., Sheu, E., Tizzanini, A., Paci, M., and Mitsos, A. (2014). Hybrid solar–geothermal power generation: Optimal retrofitting. *Applied Energy*, 131: 158–170.

Gibbons, T. B. and Wright, I. G. (2009). *A review of materials for gas turbines firing syngas fuels*, ORNL/TM-2009/137. Oak Ridge National Laboratory, Oak Ridge, Tennessee, United States.

Greenhut, A. D., Tester, J. W., DiPippo, R., Field, R., Love, C., Nichols, K., Augustine, C., Batini, F., Price, B., Gigliucci, G., and Fastelli, I. (2010). Solar-geothermal hybrid cycle analysis for low enthalpy solar and geothermal resources. In *Proceedings World Geothermal Congress 2010,* Bali, Indonesia.

Gudmundsson, J. S., Freeston, D. H., and Lienau, P. J. (1985). The Lindal Diagram. In *GRC Transactions,* 9 (1): 15–19.

IRENA (2012). (International Renewable Energy Agency): Renewable Energy Technologies: Cost Analysis Series: Volume 1: Power Sector, Issue 1/5, Biomass for Power Generation, (2012). Available at http://www.irena.org/DocumentDownloads/Publications/RE_Technologies_Cost_Analysis-BIOMASS.pdf.

Lazard (2013). *Levelized Cost of Energy Analysis - Version 4.0*. Available at http://www.dpuc.state.ct.us/DEEPEnergy.nsf/c6c6d525f7cdd1168525797d0047c5bf/8525797c00471adb852579ea00731d74/$FILE/Ex 13 - Lazard 2010 Levelized Cost of Energy - v 4.0.pdf.

Lentz, Á. and Almanza, R. (2006). Solar–geothermal hybrid system. *Applied Thermal Engineering*, 26 (14): 1537–1544.

Logan, J., Sullivan, P., Short, W., Bird, L., James, T. L., and Shah, M. R. (2009). *Evaluating a Proposed 20% National Renewable Portfolio Standard*, Technical Report, NREL/TP-6A2-45161. National Renewable Energy Laboratory (NREL), Golden, Colorado, United States.

Lukawski, M. Z., Vilaetis, K., Gkogka, L., Beckers, K. F., Anderson, B. J., and Tester, J. W. (2013). A proposed hybrid geothermal-natural gas-biomass energy system for cornell university. technical and economic assessment of retrofitting a low-temperature geothermal district heating system and heat cascading solutions. In *Proceedings Thirty-Eighth Workshop on Geothermal Reservoir Engineering*, Stanford University, Stanford, California, February 11 - February 13, 2013, SGP-TR-198.

Lukawski, M. Z., Anderson, B. J., Augustine, C., Capuano, L. E., Beckers, K. F., Livesay, B., and Tester, J. W. (2014). Cost analysis of oil, gas, and geothermal well drilling. *Journal of Petroleum Science and Engineering*, 118: 1–14.

Lund, J. W. (2010). Direct utilization of geothermal energy. *Energies*, 3 (8): 1443–1471.

Malik, M., Dincer, I., and Rosen, M. A. (2015). Development and analysis of a new renewable energy-based multi-generation system. *Energy*, 79: 90–99.

MathWorks (2012). *MATLAB Release 2012a*, The Mathworks, Inc., Natick, Massachusetts, United States.

Mines, G. and Nathwani, J. (2013). Estimated power generation costs for EGS. In *Proceedings Thirty-Eighth Workshop on Geothermal Reservoir Engineering*, Stanford University, Stanford, California, February 11 - February 13, 2013, SGP-TR-198.

U.S. DOE (2013). *Transparent Cost Database*. National Renewable Energy Laboratory, Golden, Colorado, United States. U.S. Department of Energy. Available at http://en.openei.org/wiki/ Transparent_Cost_Database.

Perlack, R. and Stokes, B. (2011). *U.S. Billion-Ton Update: Biomass Supply for a Bioenergy and Bioproducts Industry*, ORNL/TM-2011/224. Oak Ridge National Laboratory, Oak Ridge, Tennessee, United States.

Ptasinski, K. J. (2008). Thermodynamic efficiency of biomass gasification and biofuels conversion. *Biofuels, Bioproducts and Biorefining*, 2 (3): 239–253.

Ragnarsson, A. (2000). Geothermal development in Iceland 1995-1999. In *Proceedings World Geothermal Congress 2000,* Kyushu - Tohoku, Japan, May 28 - June 10, 2000, volume 1, pages 363–375.

Ragnarsson, A. (2005). Geothermal development in Iceland 2000-2004. In *Proceedings World Geothermal Congress 2005,* Antalya, Turkey.

Ragnarsson, A. (2010). Geothermal development in Iceland 2005-2009. In *Proceedings World Geothermal Congress 2010,* Bali, Indonesia.

Reber, T. J. (2013). *Evaluating Opportunities for Enhanced Geothermal System-Based District Heating in New York and Pennsylvania*. Master Thesis, Cornell University, Ithaca, New York, United States.

Reber, T. J., Beckers, K. F., and Tester, J. W. (2014). The transformative potential of geothermal heating in the US energy market: A regional study of New York and Pennsylvania. *Energy Policy*, 70: 30–44.

Srinivas, S., Eisenberg, D., Seifkar, N., Leoni, P., Paci, M., and Field, R. P. (2014). Simulation-Based Study of a Novel Integration: Geothermal–Biomass Power Plant. *Energy & Fuels*, 28 (12): 7632–7642.

Stutz, G. R., Shope, E., Aguirre, G. A., Batir, J., Frone, Z., Williams, M., Reber, T. J., Whealton, C. A., Smith, J. D., Richards, M. C., Blackwell, D. D., Tester, J. W., Stedinger, J. R., and Jordan, T. E. (2015). Geothermal energy characterization in the Appalachian Basin of New York and Pennsylvania. *Geosphere*, 11 (5): 1291–1304.

Tester, J. W., Anderson, B., Batchelor, A., Blackwell, D., DiPippo, R., Drake, E., Garnish, J., Livesay, B., Moore, M. C., Nichols, K., Petty, S., Toksz, M. N., and Veatch Jr., R. W.

(2006). *The future of geothermal energy: Impact of enhanced geothermal systems (EGS) on the United States in the 21st century*. MIT.

Tester, J. W., Joyce, W. S., Brown, L., Bland, B., Clark, A., Jordan, T., Andronicos, C., Allmedinger, R., Beyers, S., Blackwell, D., Richards, M., Frone, Z., and Anderson, B. (2010). Co-Generation Opportunities for Lower Grade Geothermal Resources in the Northeast - A Case Study of the Cornell Site in Ithaca, NY. In *GRC Transactions,* 34: 440–448.

Tester, J., Reber, T., Beckers, K., Lukawski, M., Camp, E., Aguirre, G. A., Jordan, T., and Horowitz, F. (2015a). Integrating geothermal energy use into re-building american infrastructure. In *Proceedings World Geothermal Congress 2015,* Melbourne, Australia, 19-25 April 2015.

Tester, J. W., Reber, T. J., Beckers, K. F., and Lukawski, M. Z. (2015b). Deep geothermal energy for district heating: Lessons learned from the U.S. and beyond. In *Advanced District Heating and Cooling (DHC) Systems*. Woodhead Publishing.

Thain, I. and DiPippo, R. (2015). Hybrid geothermal-biomass power plants: applications, designs and performance analysis. In *Proceedings World Geothermal Congress 2015,* Melbourne, Australia, 19-25 April 2015.

Zhou, C., Doroodchi, E., and Moghtaderi, B. (2013). An in-depth assessment of hybrid solar–geothermal power generation. *Energy Conversion and Management*, 74: 88–101.

CHAPTER 6

TECHNO-ECONOMIC ANALYSIS OF DEEP GEOTHERMAL ENERGY SYSTEMS: KEY CONCLUSIONS

In order to evaluate the technical and economic performance of deep geothermal energy extraction through Enhanced Geothermal Systems (EGS) for various end-uses, the simulation tool GEOPHIRES has been developed, which was presented in Chapter 4. GEOPHIRES incorporates reservoir, wellbore and surface plant models in combination with capital and operation & maintenance (O&M) cost correlations to estimate the power output, and investment and levelized costs of the geothermal plant. GEOPHIRES has been applied to three case-studies in Chapter 5, from which the following key conclusions can be drawn:

- Deep geothermal with EGS for solely electricity generation is only attractive for medium- and high-grade resources, defined as having geothermal gradients of 50 and 70°C/km, respectively. For these resources, the levelized cost of electricity (LCOE) is in the range 5 to 18 ¢/kWh$_e$ with lower values for higher gradients and more mature technology. In contrast, for low-grade resources (geothermal gradients of 30°C/km), the LCOE varies from 20 to almost 60 ¢/kWh$_e$, depending on the level of technology maturity. These high values indicate that subsidies or financial incentives would be required to make low-grade EGS electricity production cost-competitive with traditional fossil fuel and other renewable energy technologies, which typically have LCOE's between 5 and 10 ¢/kWh$_e$.
- Deep geothermal with EGS for direct-use industrial applications (excluding district heating systems) has values for levelized cost of heat (LCOH) between 6 and 14 $/MMBTU (2.0 and 4.8 ¢/kW$_{th}$) for low-grade resources and 4 and 8 $/MMBTU (1.4 and 2.7 ¢/kW$_{th}$) for medium- and high-grade resources. Even for low-grade

resources, these values compare favorably with the end-use LCOH for natural gas boilers, which ranges between 6 and 16 $/MMBTU (2.0 and 5.5 ¢/$kW_{th}$), depending on industrial or residential and current or projected future natural gas prices.

- Deep geothermal with EGS for district heating typically has a higher LCOH because of the additional capital cost of a district heating system, and a lower capacity factor. Nevertheless, the values for LCOH for medium-grade resources are between 10 to 19 $/MMBTU (3.4 and 6.5 ¢/$kW_{th}$), which are still attractive.
- Hybridization and cogeneration can increase the performance of the plant. In a case-study for the Cornell University campus (which has an existing district heating system), a hybrid geothermal-biomass cogeneration plant is proposed where hybridizing with biomass peak boilers allows for slightly undersizing the geothermal system and hereby increasing its capacity factor. In addition, by cogenerating electricity and heat during summer, the capacity factor of the geothermal system is increased further. Despite the relatively low assumed average geothermal gradient of 25°C/km, the LCOH of the system is only about 16 $/MMBTU (5.5 ¢/$kW_{th}$).
- Given that low-grade geothermal resources are much more common than medium- or high-grade resources, and the market for low-temperature heat is significant, the levelized energy costs provided above convincingly indicate that deep geothermal energy for direct-use and cogeneration could play a major role in the future energy system for the U.S. and many other countries.

Part II

Techno-Economic Analysis of Hybrid Geothermal Heat Pump Systems for Cooling-Dominated Applications

CHAPTER 7

INTRODUCTION TO HYBRID GEOTHERMAL HEAT PUMP SYSTEMS

7.1 Heat Pump Basics

A heat pump is a device that transfers heat from a heat source reservoir to a heat sink reservoir using external power input, as illustrated in the left diagram of Figure 7.1 (Çengel and Boles, 2007; Staffell et al., 2012; Tester et al., 2012). The heat source temperature T_c is typically colder than the heat sink temperature T_h, which means the heat transfer is opposite to the direction of spontaneous heat flow. A heat pump is in essence the reverse of a heat engine which generates work using heat flow from a hot reservoir to a cold reservoir (right diagram in Figure 7.1).

A heat pump can efficiently provide heating, cooling, or both. The efficiency is expressed as a dimensionless coefficient of performance (COP) and is calculated for heating and cooling as:

$$COP_{heating} = \frac{q_h}{W}, \tag{7.1}$$

$$COP_{cooling} = \frac{q_c}{W} \tag{7.2}$$

with W the external power input (in Watt), and q_c and q_h the heat exchange (in Watt) with the heat source (cooling) and heat sink (heating), respectively. The theoretical efficiency (Carnot efficiency), is given by (Tester et al., 2012):

$$COP_{heating,Carnot} = \frac{T_h}{T_h - T_c}, \tag{7.3}$$

$$COP_{cooling,Carnot} = \frac{T_c}{T_h - T_c} \tag{7.4}$$

with T_h and T_c expressed in Kelvin. Theoretical COP's of 10 or higher are not uncommon, meaning 10 units of heating or cooling are supplied for 1 unit of work input. However, actual heat pumps COP's are substantially lower, typically in the range 3-6. In contrast,

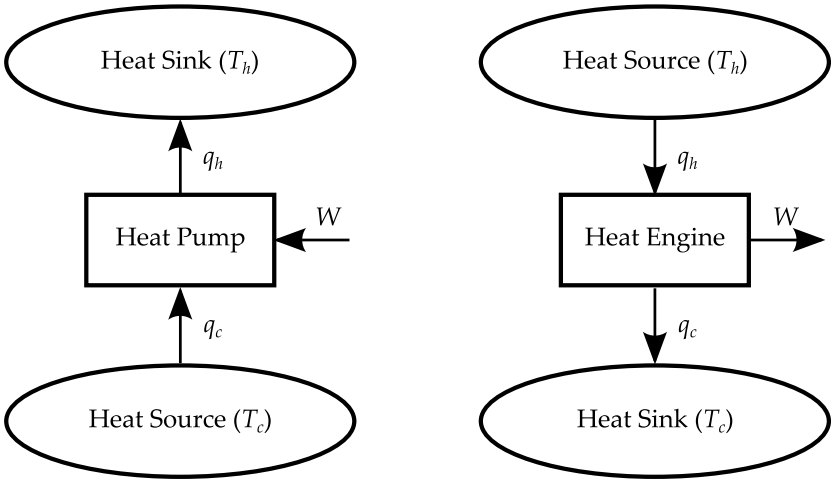

Figure 7.1 – Simplified diagram of heat pump and heat engine.

the COP of electrical resistance heaters is 1. In the U.S., the cooling efficiency is sometimes expressed as the Energy Efficiency Ratio (EER) with q_c in BTU/h instead of Watt, resulting in $EER = 3.41213 \cdot COP$, since 1 W = 3.41213 BTU/h (Staffell et al., 2012). Also, the COP is a steady-state measure which does not capture changes in performance throughout the year. One can use instead the Seasonal Performance Factor (SPF), which represents the average annual performance of the system at a certain location (Staffell et al., 2012), and can account for the energy consumption and production of other components such as auxiliary heaters.

The fluid exchanging heat between the heat pump working fluid and the source or sink is typically air or water (possibly with antifreeze). Depending on the configuration, one uses the terms air-to-air, air-to-water (or water-to-air), or water-to-water heat pump system. Heat pumps exchanging heat with the air environment are also called air-source heat pumps (ASHPs), of which a traditional air-conditioning unit is an example. In the case of a ground-loop system exchanging heat with the underground soil and rock, one speaks of a ground-source or geothermal heat pump system (GSHP).

The most common heat pump operation mechanisms are based on the vapor-

compression and vapor-absorption cycle. In a simple vapor-compression cycle, a refrigerant (e.g. R-410A) undergoes in a closed cycle: (1) compression, (2) condensation, (3) expansion, and (4) evaporation (Çengel and Boles, 2007; Staffell et al., 2012). The work input (W) is the electricity required for the compressor and the circulation pump. Figure 7.2 shows a simplified diagram of the different components in a water-to-air GSHP system in cooling mode based on the vapor-compression cycle. In heating mode, the evaporator is coupled to the ground-loop system and the condenser to the air supply. In a vapor-absorption cycle, an absorber replaces the compressor where the refrigerant is absorbed into an liquid. The liquid solution is pumped to higher pressures and eventually the refrigerant is released again as vapor, typically using an external heat source.

Depending on the heat pump source and sink temperatures, as well as the power plant conversion and electrical grid transmission efficiencies, heat pumps can have excellent energetic performance in comparison with natural gas, heating oil, and electrical resistance heating systems. In addition, there are no on-site emissions and the heating and/or cooling is carbon-free in case the electricity is generated from nuclear or renewable resources. Furthermore, heat pumps are highly reliable devices, partially because of the use of standard, low-tech components, no occurrence of high temperatures due to combustion, and, specifically for ground-source heat pumps, no direct contact with the outside environment. For residential and commercial space heating and cooling, ground-source heat pumps usually perform slightly better (i.e. higher COP) than ASHPs since the ground temperature is typically higher than the outside temperature during heating season (winter), and lower during cooling seasons (summer).

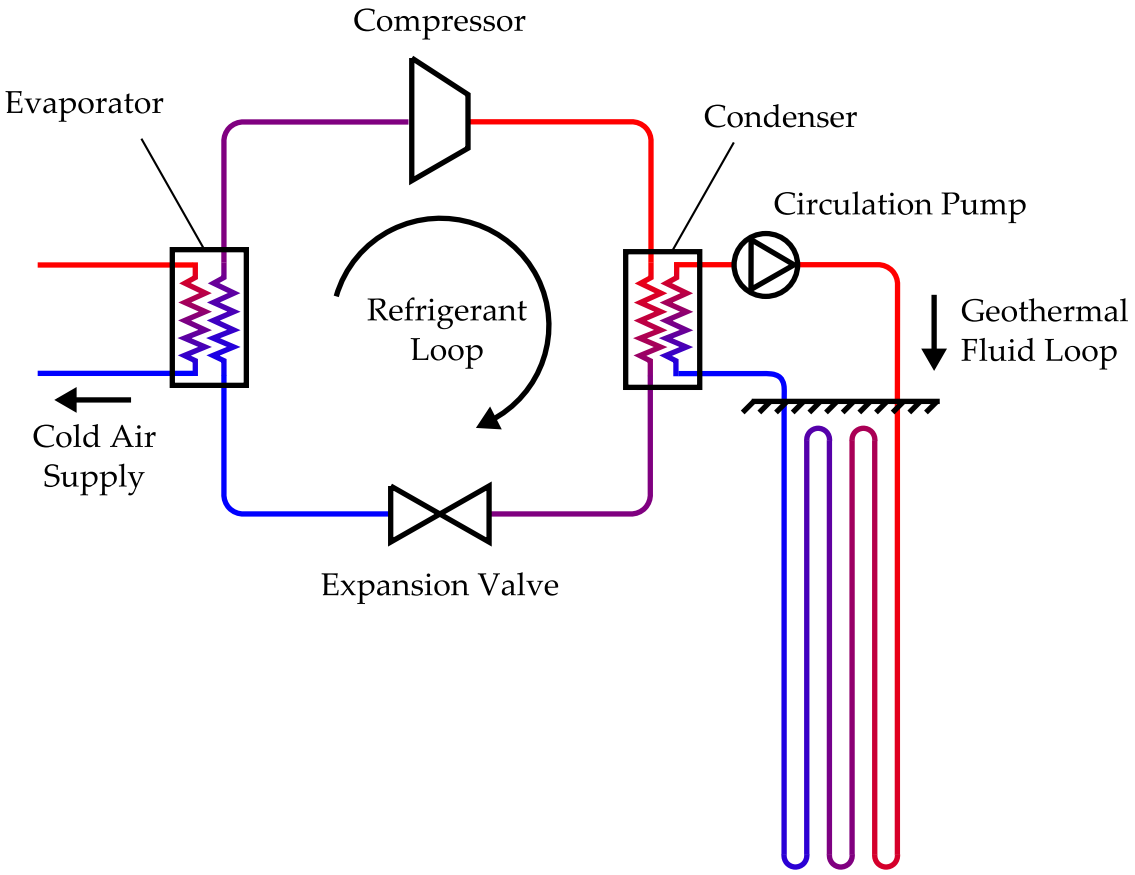

Figure 7.2 – Simplified diagram of water-to-air GSHP system in cooling mode. Red and blue colors represent arbitrarily warm and cold fluid temperatures, respectively. Drawing not too scale.

7.2 Opportunities, Challenges, and Examples of Hybrid Heat Pump Systems

In cooling- (or heating-) dominated applications, utilizing regular heat pump systems will result in thermal imbalance in the ground heat exchange, meaning heat is predominantly injected (or extracted) from the reservoir. This can lead to long-term ground temperature changes and degrading system performance over time. One solution lies in oversizing the geothermal reservoir, which leads to higher capital costs and does not decrease the thermal imbalance, but rather diminishes its negative impact on the system performance. Another solution is hybridizing the system by accompanying the GSHP with

supplemental heat rejection or heat generation systems, in the case of cooling-dominated or heating-dominated applications, respectively. These extra components do require additional investment costs but might lead to a smaller geothermal reservoir and correspondingly lower geothermal borehole heat exchanger (BHE) field costs. Even in some cases without thermal imbalance occurring, hybridizing the system can be beneficial as it can lead to lower overall costs over the lifetime. Challenges with hybrid systems are more complicated designs, more complicated operation control schemes, and potentially higher maintenance costs.

Figure 7.3 provides a few simplified examples of hybrid water-to-air GSHP systems for cooling-dominated applications. Case (a) is the base case non-hybridized water-to-air heat pump system with HP, CP and SA referring to heat pump, circulation pump and supply air, respectively. In case (b), the system is hybridized with an air-economizer (AE) which provides cooling using cold outside air directly and allows the heat pump system to be turned off. In case (c), supplemental heat rejection is obtained using radiative cooling (Man et al., 2011). In case (d), a dry-cooler (DC) (also called dry-fluid cooler) removes heat by forcing ambient air to flow through the DC and cool down the circulating fluid flowing through a tube bank. In case (e), supplemental heat rejection is provided using evaporative water cooling in a cooling tower. Some examples of case-studies and research on GSHPs hybridized with a cooling tower are the works by Xu (2007), Yi et al. (2008), and Hackel and Pertzborn (2011).

In cases (c), (d), and (e), the valve system allows for various operation modes. With the heat pump running, the supplemental heat rejection can be operated as "pre-cooler" in series with the BHE field, or as sole system for heat rejection by bypassing the BHE field. Alternatively, the heat pump can be bypassed and the supplemental heat rejection system can actively cool down or recharge the geothermal field such as for seasonal thermal storage (Lhendup et al., 2014). Other valve systems could allow for other operation

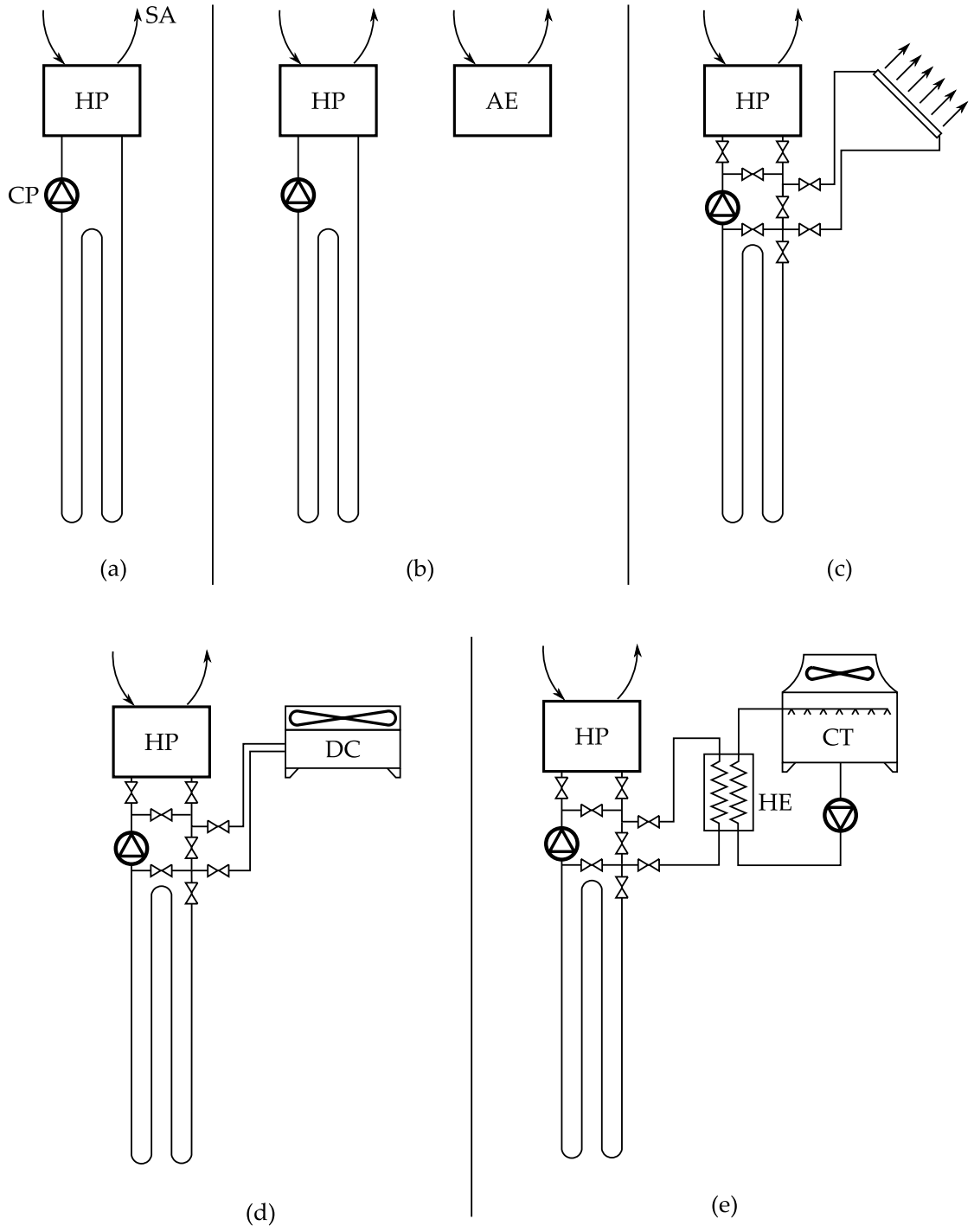

Figure 7.3 – Examples of hybrid water-to-air GSHP systems for cooling-dominated applications. Base case is shown in case (a) with HP, SA, and CP referring to heat pump, supply air, and circulation pump, respectively. In case (b), an air-economizer (AE) supplies cool air in parallel to the GSHP system. Supplemental heat rejection in cases (c), (d), and (e) can be provided in various configurations by radiative cooling, dry-cooler (DC) and cooling tower (CT), respectively. In case (e), HE refers to heat exchanger.

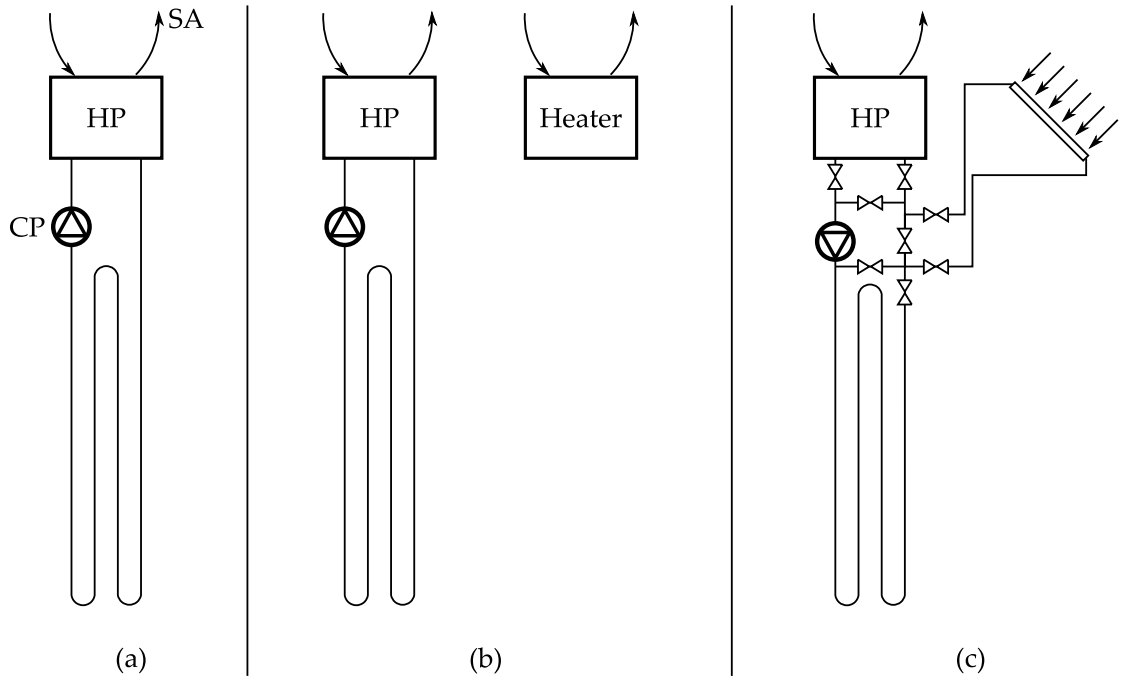

Figure 7.4 – Examples of hybrid water-to-air GSHP systems for heating-dominated applications. Base case is shown in case (a) with HP, SA, and CP referring to heat pump, supply air, and circulation pump, respectively. In case (b), a heater (e.g. natural gas heater) supplies warm air in parallel to the GSHP system. In case (c), a solar thermal heater can provide supplemental heating in various configurations.

modes, e.g. a fraction of the fluid could be cooled by the BHE field and a fraction by the supplemental heat rejection system.

A few simplified examples of hybrid water-to-air GSHP systems for heating-dominated applications are illustrated in Figure 7.4. Again, case (a) is the base case with the same component labeling as in Figure 7.3. In case (b), supplemental heat is provided in parallel to the heat pump by a heater, e.g. a natural gas or heating oil heater (Hackel and Pertzborn, 2011). In case (c), depending on the operation mode, solar thermal energy can be used (1) for thermal recharging of the geothermal field, (2) as sole system for heat supply to the heat pump by bypassing the geothermal field, or (3) as supplemental heating in series with the geothermal field. Several studies have been conducted on GSHPs hybridized with solar thermal energy such as the works by Chua et al. (2010), Wang et al. (2012), Rad et al. (2013), and Chiasson and Yavuzturk (2014). Other components have

been integrated in a hybrid set-up such as solar photovoltaic panels or water thermal energy storage tanks.

Various, sometimes complicated control schemes are available for optimal operation of a hybrid GSHP system. For example, for a water-to-air GSHP hybridized with a cooling tower for a cooling-dominated application, Wang et al. (2015) and Yavuzturk and Spitler (2000) have investigated several control schemes: e.g. activation of the heat pump and/or cooling tower can be dependent on the heat pump entering (EWT) or exiting water temperature (ExWT), the difference between EWT or ExWT and ambient dry-bulb or wet-bulb temperature, or based on a fixed time schedule such as nightly winter operation for ground recharge during the cold season.

7.3 Design and Modeling of Hybrid Geothermal Heat Pump Systems

Optimal design of hybrid GSHP systems is a rather difficult task because of the large number of system parameters, and available configurations and control schemes. A rule of thumb often applied when hybridizing a GSHP is to size the supplemental heat supply or rejection component such that annual balance in ground heat exchange is obtained (Yavuzturk and Spitler, 2000). This approach will prevent any system performance degradation caused by a long-term rise (cooling-dominated applications) or decline (heating-dominated applications) in circulating fluid temperature. However, it might not lead to the optimal configuration in terms of total cost of ownership or net present value over the lifetime of the system (Hackel, 2008). Hackel (2008) and Hackel et al. (2009) developed guidelines for optimizing hybrid systems utilizing TRNSYS (SEL, 2014a), a simulation tool discussed below. For example, they argue that for a cooling-dominated application, the optimal size of the BHE is for it to meet the peak heating demand while the supplemental heat rejection component should be sized so that it meets the peak cooling

demand that is not met by the geothermal system. Other research on optimal design of hybrid systems is the work by Chiasson (2007), Alavy et al. (2013), and the many studies by Kavanaugh, the most recent one being (Kavanaugh and Rafferty, 2014).

For an in-depth analysis of hybrid GSHP systems, computer modeling and simulating are required, for which various software tools are available. One example is utilizing the open-source, equation-based language Modelica (Mattsson et al., 1998), originally developed at Lund University in Sweden, for modeling complex physical systems. Huchtemann and Müller (2009) present a case-study using Modelica libraries for simulating a hybrid GSHP with boiler and water storage tank. Another approach is using Simulink (MathWorks, 2012), e.g. in combination with HAMBASE, a building thermal load model developed at University of Eindhoven in the Netherlands (De Wit, 2006). Gaspredes et al. (2014) followed this method to conduct a short and long time-scale analysis of a GSHP system. Other popular software is EnergyPlus, a whole building simulation tool developed at the U.S. Department of Energy (Crawley et al., 2001). Sankaranarayanan (2005) investigated hybrid GSHP systems in EnergyPlus for his master thesis. Another tool is HVACSIM+, originally developed at the National Bureau of Standards to study HVAC systems for buildings (Park et al., 1985). Cui et al. (2008) have used HVACSIM+ for a hybrid ground-source heat pump case-study with hot water storage tank. Finally, TRNSYS (TRaNsient SYstem Simulation program) has been developed at the Solar Energy Laboratory at the University of Wisconsin - Madison (SEL, 2014a), and is probably the most widely used software program for analyzing hybrid GSHP systems. TRNSYS is introduced in more detail below and is applied in this dissertation for analysis of a hybrid GSHP for a cooling-dominated application (Chapter 9). More background information on some of these software tools including the underground heat transfer model they have incorporated is provided by (Spitler et al., 2009) and (Yang et al., 2010).

TRNSYS is a graphically-based software tool for analysis of transient system behav-

ior, originally developed to study solar hot water systems but now with applications in various fields, mostly related to energy, such as fuel cells, GSHPs, wind turbines, etc. It uses a component-based modeling approach, in a sense similar to the tools HVACSIM+ and Simulink, where the system is represented by an interconnected set of components (called Types in TRNSYS), such as pumps, heat exchangers, controllers, loads, etc. TRNSYS comes delivered with a built-in library of Types, however, also third party Types are available, for example the TESS (Thermal Energy System Specialists) GHP library (TESS, 2014) for modeling BHEs (see Chapter 9).

Dozens if not hundreds of studies on GSHP and hybrid GSHP utilizing TRNSYS have been published in literature. A few examples relevant to this work are the studies by Wang et al. (2012) and Kjellsson et al. (2010) on hybrid geothermal solar thermal systems, the optimization study by (Cui et al., 2015) on a cooling tower either in series or in parallel with a GSHP, the study by Chiasson and Yavuzturk (2009) on the development of a spreadsheet tool for design of hybrid GSHP for cooling-dominated applications, based on 90+ TRNSYS simulations, and the work by Hackel (2008) mentioned earlier, on the design of guidelines for hybrid GSHP for cooling-dominated applications.

References

Alavy, M., Nguyen, H. V., Leong, W. H., and Dworkin, S. B. (2013). A methodology and computerized approach for optimizing hybrid ground source heat pump system design. *Renewable energy*, 57 : 404–412.

Çengel, Y. and Boles, M. (2007). *Thermodynamics: An Engineering Approach*. McGraw Hill, 6th edition.

Chiasson, A. D. (2007). *Simulation and Design of Hybrid Geothermal Heat Pump Systems*. PhD Dissertation, University of Wyoming, Laramie, Wyoming, United States.

Chiasson, A. D. and Yavuzturk, C. (2009). A design tool for hybrid geothermal heat pump systems in cooling-dominated buildings. *ASHRAE Transactions*, 115 (2).

Chiasson, A. and Yavuzturk, C. (2014). Simulation of hybrid solar-geothermal heat pump systems. In *Proceedings Thirty-Ninth Workshop on Geothermal Reservoir Engineering*, Stanford University, Stanford, California, February 24 - February 26, 2014, SGP-TR-201.

Chua, K., Chou, S., and Yang, W. (2010). Advances in heat pump systems: A review. *Applied Energy*, 87 (12): 3611–3624.

Crawley, D. B., Lawrie, L. K., Winkelmann, F. C., Buhl, W. F., Huang, Y. J., Pedersen, C. O., Strand, R. K., Liesen, R. J., Fisher, D. E., Witte, M. J., and Glazer, J. (2001). EnergyPlus: creating a new-generation building energy simulation program. *Energy and buildings*, 33 (4): 319–331.

Cui, P., Yang, H., Spitler, J. D., and Fang, Z. (2008). Simulation of hybrid ground-coupled heat pump with domestic hot water heating systems using HVACSIM+. *Energy and Buildings*, 40 (9): 1731–1736.

Cui, W., Zhou, S., and Liu, X. (2015). Optimization of design and operation parameters for hybrid ground-source heat pump assisted with cooling tower. *Energy and Buildings*, 99: 253–262.

De Wit, M. (2006). *HAMBASE: Heat Air and Moisture model for Building and Systems Evaluation*.

Gaspredes, J. L., Masada, G. Y., and Moon, T. J. (2014). A Simulink®-Based Building Load-Ground Source Heat Pump Model Used to Assess Short-and Long-Term Heat Pump and Ground Loop Performance. *Journal of Thermal Science and Engineering Applications*, 6 (2): 021013.

Hackel, S. P. (2008). *Development of Design Guidelines for Hybrid Ground-Coupled Heat Pump Systems*. Master Thesis, University of Wisconsin - Madison, Madison, Wisconsin, United States.

Hackel, S., Nellis, G., and Klein, S. (2009). Optimization of cooling-dominated hybrid ground-coupled heat pump systems. *ASHRAE Transactions*, 115 (1).

Hackel, S. and Pertzborn, A. (2011). Effective design and operation of hybrid ground-source heat pumps: three case studies. *Energy and Buildings*, 43 (12): 3497–3504.

Huchtemann, K. and Müller, D. (2009). Advanced simulation methods for heat pump systems. In 7th *Modelica Conference,* Como, Italy, September 20 - September 22, 2009.

Kavanaugh, S. and Rafferty, K. (2014). *Geothermal Heating and Cooling: Design of Ground-Source Heat Pump Systems*. ASHRAE.

Kjellsson, E., Hellström, G., and Perers, B. (2010). Optimization of systems with the combination of ground-source heat pump and solar collectors in dwellings. *Energy*, 35 (6): 2667–2673.

Lhendup, T., Aye, L., and Fuller, R. J. (2014). Thermal charging of boreholes. *Renewable Energy*, 67: 165–172.

Man, Y., Yang, H., Spitler, J. D., and Fang, Z. (2011). Feasibility study on novel hybrid ground coupled heat pump system with nocturnal cooling radiator for cooling load dominated buildings. *Applied Energy*, 88 (11): 4160–4171.

MathWorks (2012). *MATLAB Release 2012a*, The Mathworks, Inc., Natick, Massachusetts, United States.

Mattsson, S. E., Elmqvist, H., and Otter, M. (1998). Physical system modeling with modelica. *Control Engineering Practice*, 6 (4): 501–510.

Park, C., Clark, D. R., and Kelly, G. E. (1985). An overview of hvacsim+, a dynamic building/hvac/control systems simulation program. In *1st Building Energy Simulation Conference,* International Building Performance Simulation Association, Seattle, Washington, August 21 - August 22, 1985.

Rad, F. M., Fung, A. S., and Leong, W. H. (2013). Feasibility of combined solar thermal and ground source heat pump systems in cold climate, canada. *Energy and Buildings*, 61: 224–232.

Sankaranarayanan, K. P. (2005). *Modeling, verification and optimization of hybrid ground source heat pump systems in EnergyPlus*. Master Thesis, Oklahoma State University, Stillwater, Oklahoma, United States.

SEL (2014). *TRNSYS 17 (TRaNsient SYstems Simulation program)*. University of Wisconsin - Madison, Solar Energy Laboratory (SEL). Available at http://sel.me.wisc.edu/trnsys/.

Spitler, J., Cullin, J., Bernier, M., Kummert, M., Cui, P., Liu, X., Lee, E., and Fisher, D. (2009). Preliminary intermodel comparison of ground heat exchanger simulation models. In *11th International Conference on Thermal Energy Storage,* Effstock, Sweden, June 14 - June 17, 2009.

Staffell, I., Brett, D., Brandon, N., and Hawkes, A. (2012). A review of domestic heat pumps. *Energy & Environmental Science*, 5 (11): 9291–9306.

TESS (2014). *TESS Component Library Package*. Thermal Energy System Specialists, Inc., Madison, Wisconsin. Available at http://www.trnsys.com/tess-libraries/.

Tester, J., Drake, E., Driscoll, M., Golay, M., and Peters, W. (2012). *Sustainable Energy: Choosing Among Options*. MIT Press, 2nd edition.

Wang, E., Fung, A. S., Qi, C., and Leong, W. H. (2012). Performance prediction of a hybrid solar ground-source heat pump system. *Energy and Buildings*, 47: 600–611.

Wang, S., Liu, X., and Gates, S. (2015). Comparative study of control strategies for hybrid gshp system in the cooling dominated climate. *Energy and Buildings*, 89: 222–230.

Xu, X. (2007). *Simulation and optimal control of hybrid ground source heat pump systems*. PhD Dissertation, Oklahoma State University, Stillwater, Oklahoma, United States.

Yang, H., Cui, P., and Fang, Z. (2010). Vertical-borehole ground-coupled heat pumps: a review of models and systems. *Applied Energy*, 87 (1): 16–27.

Yavuzturk, C. and Spitler, J. D. (2000). Comparative study of operating and control strategies for hybrid ground-source heat pump systems using a short time step simulation model. *ASHRAE Transactions*, 106:192.

Yi, M., Hongxing, Y., and Zhaohong, F. (2008). Study on hybrid ground-coupled heat pump systems. *Energy and Buildings*, 40 (11): 2028–2036.

CHAPTER 8

CORNELL-VERIZON HYBRID GEOTHERMAL HEAT PUMP PROJECT: BACKGROUND INFORMATION AND VARNA SITE

8.1 Background Information

The equipment at a cellular site other than the antennas is typically housed in a shelter for protection against environmental conditions and vandalism. The equipment comprises batteries, cabling, and telecommunication electronics and generates roughly 8 to 11 kW_{th} of internal heat that remains fairly constant year-round. Given the construction specifications and space use characteristics, the thermal load inside the shelter is usually cooling-dominated, even in colder climates, with wall-mounted air-source HVAC units being the standard cooling option. Tens of thousands of these shelters are installed across the U.S.

Geothermal heat pumps are an attractive alternative to provide climate control for cellular tower shelters. On warm days, the ground temperature is typically lower than the ambient temperature which results in a higher coefficient of performance (COP) for ground-source (geothermal) heat pumps (GSHPs) versus air-source heat pumps (ASHPs). The reverse is true on colder days but then an air-economizer (AE) might be sufficient. The higher performance of geothermal heat pumps leads to lower electricity consumption and correspondingly lower CO_2 emissions and lower operational costs. A second advantage of geothermal heat pumps is superior reliability. Due to its isolation from the ambient air, the cooling system is not subject to dust particles or extreme weather conditions. This results in lower maintenance costs and a lower chance of system failure. Failure of the cooling system can lead to down-time of the telecommunications equipment and must unconditionally be avoided. Further, the thermal load is typically known

in advance which allows for efficient design of the cooling system. Nevertheless, because this application is cooling-dominated, one should be aware of potential thermal imbalance of the geothermal reservoir. In such case, oversizing the boreholes or hybridizing the system, e.g. using a dry-cooler (DC), is recommended.

In an earlier "proof-of-concept" study conducted in our group in collaboration with Verizon Wireless, LaBrozzi et al. (2010) argue that GSHPs in combination with AEs are a more energy-efficient and in some cases also a more cost-effective alternative to conventional HVAC units for cooling of cellular tower shelters. Using the commercial software tools GLHEPRO v4.0 by the International Ground Source Heat Pump Association (IGSHPA), and GLD2009 by Gaia Geothermal, LaBrozzi et al. assessed the overall life cycle cost of ground-source heat pumps versus ASHPs, both with or without AEs, for seven different climate zones across the country. They concluded that in warmer climate regions, GSHP are not recommended with today's energy costs, however, in colder regions, hybrid GSHP with AEs are the most energy-efficient option. When utilizing horizontal heat exchangers and assuming discounted prices for bulk purchases of GSHP units, they are also the most cost-effective option.

After the promising study of LaBrozzi et al., a full-scale and fully-equipped demonstration system was designed and built during the period 2011-2013, to continue in more depth the investigation of the performance and potential of (hybrid) geothermal heat pumps for cellular tower shelter cooling. The demonstration site is located near a newly-built cellular tower on the grounds of the Cornell University campus in the Cornell Plantations and started full operation during the first half of 2014. In the remainder of the dissertation, the field site will be referred to as the Varna Site. The set-up consists of six borehole heat exchangers (BHEs), three ground-source heat pump units, an AE, a DC and a data monitoring and logging system to closely observe the behavior and performance of the geothermal reservoir and the hybrid cooling system. Alongside the experimental

analysis, the current more in-depth study includes systems numerical modeling and simulating beyond the capabilities of standard commercial software such as GHELPRO. The specific goals in the current phase of the project are fourfold:

1. Develop a techno-economic model to simulate a hybrid ground-source heat pump system providing climate control for cellular tower shelters.
2. Monitor the system performance at the Varna Site and utilize collected data to validate the techno-economic model.
3. Using a validated techno-economic model, investigate various configurations of the hybrid ground-source heat pump system. System variables are heat pump, AE, and DC size and type, BHE geometry and type, borehole field layout, and management strategy.
4. Assess the potential of energy, CO_2, and cost savings using hybrid ground-source heat pumps for cellular tower shelters nationwide.

In this dissertation, the first, second, and partially the third goal are addressed in Chapters 8 and 9. In a follow-on study in our group (Aguirre, 2016), more of goal 3 and goal 4 is addressed.

In Section 8.2, the hybrid GSHP system at the Varna Site is discussed in more detail, along with diagrams and photographs of the set-up, and a full list of the components and monitoring sensors installed. The geology and thermal properties of the geothermal reservoir are characterized in Section 8.3, based on the results of a thermal response test, and drill cuttings and rock sample analysis. This chapter is in large part based on a conference paper presented at the 11^{th} IEA (International Energy Agency) Heat Pump Conference (Beckers et al., 2014). While the specific application studied in this and the next chapter is cooling of cellular tower shelters, it is believed the results apply (to a first

approximation) to other cooling-dominated applications as well, e.g. cooling of small data centers and cooled industrial storage of food and beverages.

8.2 Varna Site System Set-Up and Logging Data

A full-scale and fully-equipped hybrid ground-source heat pump system was designed and built during the period 2011-2013 to provide the climate control (i.e. cooling) for a newly-built Verizon Wireless cellular tower shelter in the Cornell Plantations. The system start-up phase was completed by the end of 2013 and as of 2014, all telecommunication, HVAC, and data acquisition equipment were in full operation. The site consists of a wide array of sensors to monitor the technical and economic performance of the hybrid GSHP system, and provide data to validate the models for simulating the geothermal reservoir, BHEs, heat pumps, etc. Figure 8.1 shows the drill rig for drilling of the geothermal and monitoring wells in May 2013. Figure 8.2 shows the equipment shelter and monopole cellular tower towards the end of construction, in September 2013.

Due to relatively cold winters in Upstate New York, the hybrid system includes an AE and DC. The AE brings cold outside air into the shelter when the ambient temperature drops below a certain setpoint temperature, which allows the geothermal reservoir to partially thermally recover as no heat rejection from the shelter to the ground is taking place when the AE is on. Nevertheless, the use of an AE requires regularly replacing the air filters which increases shelter maintenance costs. In addition, there is increased risk for dust particles entering the shelter and potentially damaging the electronics. The DC allows for actively cooling down of the reservoir ("recharging") to offset the imbalance in heat exchange and enhance the long-term performance of the GSHP. In addition, the DC could be utilized as pre-cooler in series with the geothermal reservoir. The projected annual cooling demand of the shelter depends on the telecommunication technology in-

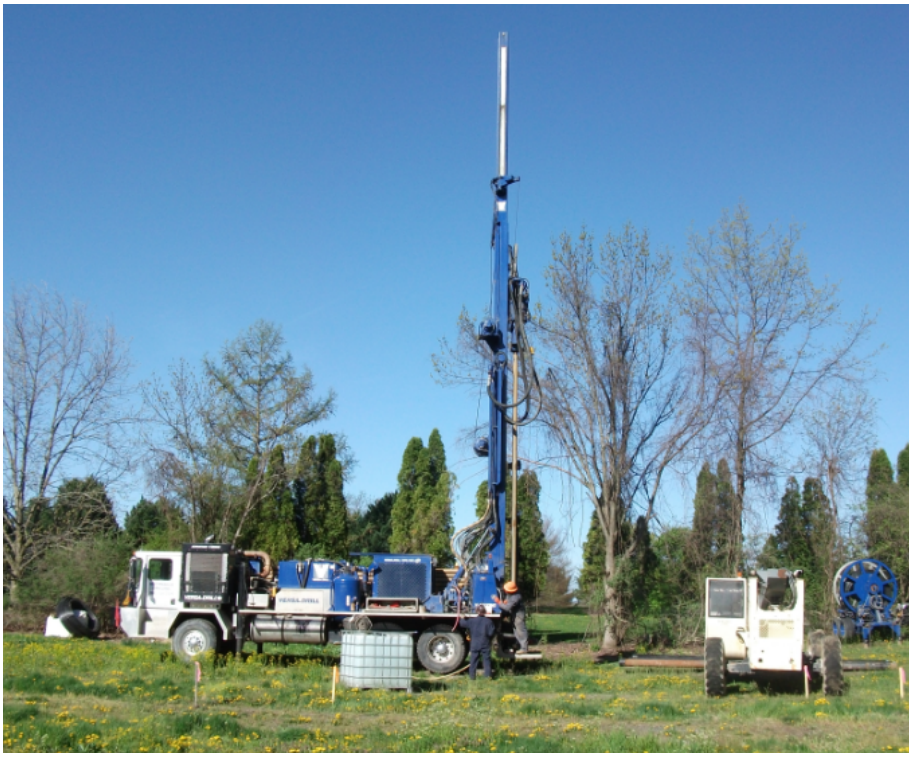

Figure 8.1 – Photograph taken at the beginning of construction of the Varna Site in May 2013, showing the drill rig for drilling the geothermal and monitoring wells.

Figure 8.2 – Photograph of Varna Site taken during construction in September 2013, showing the equipment shelter in the middle and the monopole cellular tower on the right. The geothermal borehole field is behind the shelter on the left.

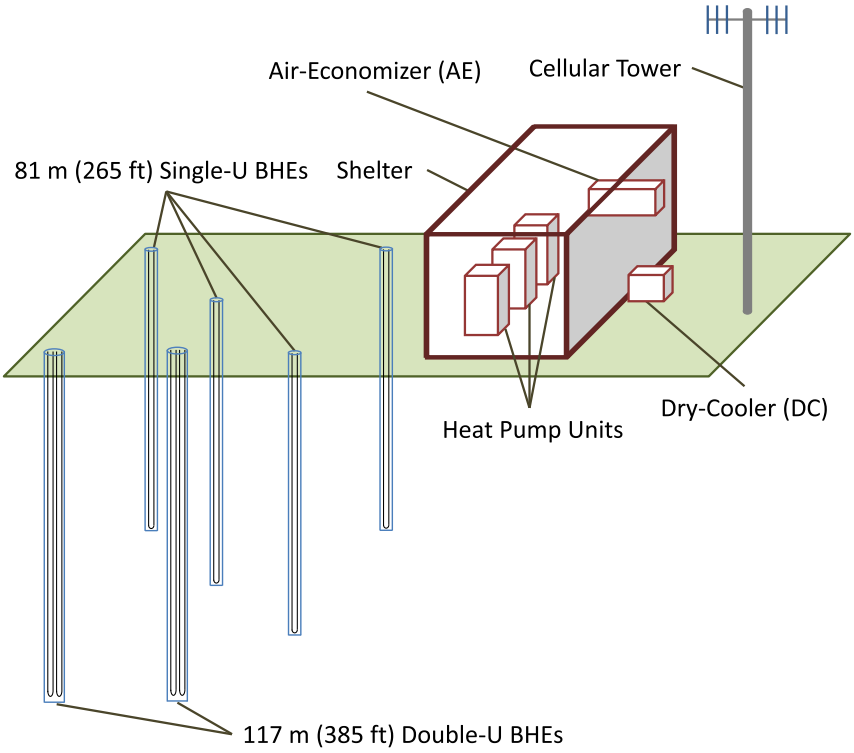

Figure 8.3 – Three-dimensional simplified schematic of the Varna Site.

stalled and is in the range of 80 to 100 MWh_{th} (273 to 341 million BTU). The peak hourly load is estimated at 12 kW_{th} (41,000 BTU/hour).

Figure 8.3 shows the three-dimensional simplified sketch of the cellular site with the location of the BHEs. The BHE field consists of four single-U (1-U) BHEs (81 m (265 ft) depth each) and two double-U (2-U) BHEs (117 m (385 ft) depth each and pipes within BHE are in parallel with each other), with each set of supply and return pipes individually controlled by a valve. The BHEs are located relatively close to one another (5.5 to 7.8 m) so that significant thermal interference is expected. The total BHE length is almost 560 m (1837 ft), about 30% more than the recommended length by the International Ground Source Heat Pump Association (IGSHPA, 2009) for these conditions. The reasons for this surplus of BHE length are (1) a potential future expansion of cellular equipment which will increase the rate of heat generation, (2) to allow collecting experimental data on both single-U and double-U BHEs, and (3) to allow investigating different BHE field

Table 8.1 – Component overview and specifications of shelter and HVAC system at Varna Site.

Shelter	
Volume	65.5 m^3
External wall + roof area	81.52 m^2
Wall thickness	0.112 m
Wall R-value	3.0 $K{\cdot}m^2/W$ (R-17)
Wall R-value	3.0 $K{\cdot}m^2/W$ (R-17)
Thermal capacitance	2400 kJ/K
Heat Pump Units	
Manufacturer	ClimateMaster
Model number	Tranquility 27 Two Stage Series 026
Cooling capacity	6.1 kW_{th} (part load) ; 7.7 kW_{th} (full load)
Number of units installed	3 (lead, lag, standby)
Dry-Cooler (DC)	
Manufacturer	Liebert
Model number	DDNC092YS30938
Type	Variable Frequency Drive (VFD)
Nominal fan power consumption	0.56 kW (0.75 hp)
Number of units installed	1
Air-Economizer (AE)	
Manufacturer	Greenheck
Model number	BSQ-130-7
Type	Variable Frequency Drive (VFD)
Nominal fan power consumption	0.56 kW (0.75 hp)
Number of units installed	1
Circulation Pumps	
Manufacturer	Bell & Gossett
Model number	Series 90 1-/4AA
Type	Variable Frequency Drive (VFD)
Nominal motor power consumption	1.12 kW (1.5 hp)
Number of units installed	2

management options, e.g. rotating between BHEs or making strategic use of the anticipated groundwater flow in the reservoir. The three heat pump units are identical two-stage water-to-air heat pumps which operate rotationally in lead, lag, and standby mode. Table 8.1 provides an overview and model specifications of the shelter and each HVAC component. Two circulation pumps are installed for redundancy, and operate alternately. Table 8.2 provides specifications on the geothermal BHEs and circulating fluid. Data on the underground rock properties are provided in Section 8.3.

Table 8.2 – Geothermal BHE and circulating fluid specifications at Varna Site.

Borehole Heat Exchanger (BHE) Field	
Depth of 1-U BHEs	80.8 m (265 ft)
Number of 1-U BHEs installed	4
Depth of 2-U BHEs	117.3 m (385 ft)
Number of 2-U BHEs installed	2
BHE radius	0.0889 m
Location of and spacing between BHEs	See Figure 8.4
1-U BHE pipe inner radius	0.0134 m
1-U BHE pipe outer radius	0.0167 m
2-U BHE pipe inner radius	0.0170 m
2-U BHE pipe outer radius	0.0211 m
Spacing between center pipes	0.11 m
Pipe material	HDPE PE4710
Pipe thermal conductivity	0.45 W/(m·K)
Pipe density	960 kg/m^3
Pipe specific heat capacity	1930 J/(kg·K)
Grout thermal conductivity	1.73 W/(m·K)
Grout density	1670 kg/m^3
Grout specific heat capacity (est.)	2000 J/(kg·K)
Far-field temperature	9°C
Circulating Fluid	
Mixture (volume-based)	60% water - 40% ethylene glycol
Thermal conductivity	0.41 W/(m·K)
Specific heat capacity	3600 J/(kg·K)
Density	1060 kg/m^3
Dynamic viscosity	0.0022 kg/(m·s)
Freezing point	-25°C

The monitoring system logs a wide array of data in the shelter and BHE field including ambient temperature, shelter temperature, fluid supply and return temperatures of the BHE field, the fluid supply and return temperature of each heat pump, fluid flow rate for each BHE and each heat pump, power consumption of different components, and the reservoir temperature at 30 different locations. A full list of relevant data logged at the Varna Site is provided in Table 8.3. The reservoir temperature sensors are distributed over one single-U BHE, one double-U BHE, and three monitoring wells (see Figure 8.4). In each well, the sensors are equally spaced at five different depths and are installed in duplicate for a total of 60 field temperature sensors. Since groundwater flow was observed during

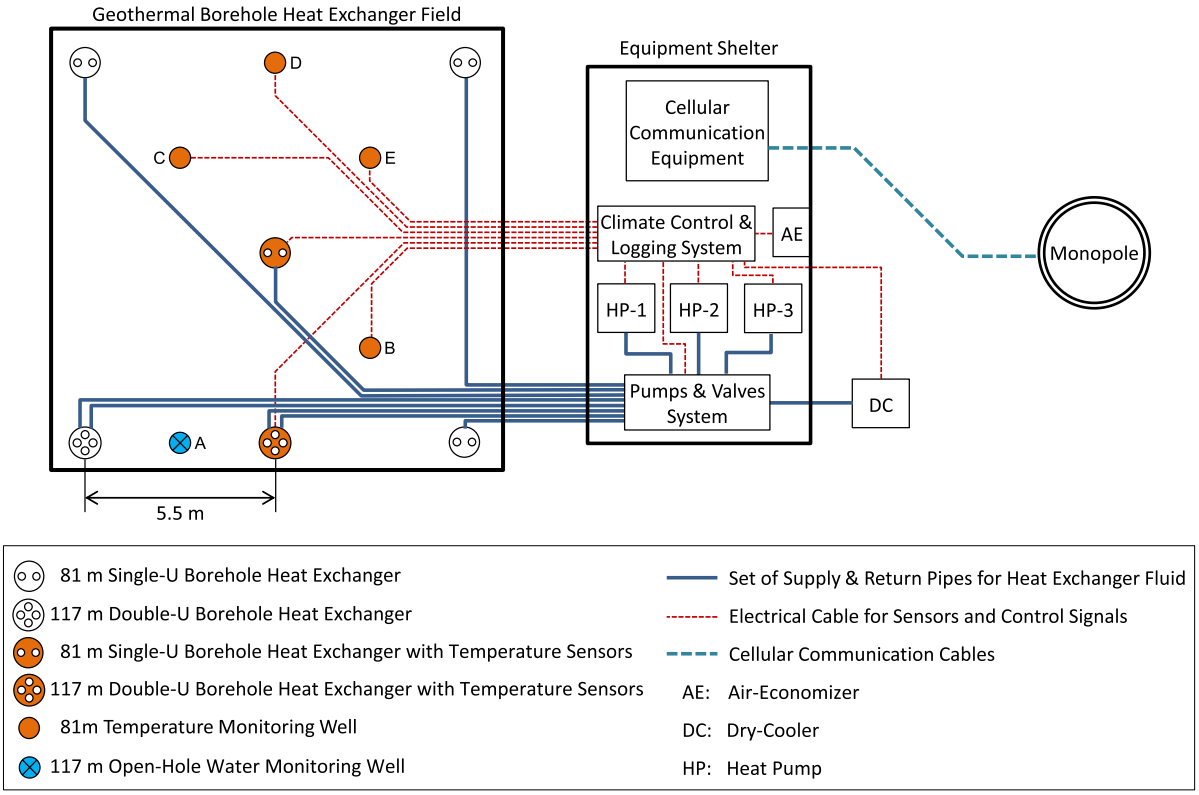

Figure 8.4 – Lay-out of BHE field, equipment shelter and cellular tower of Verizon hybrid geothermal heat pump project at Varna Site.

drilling and the in-situ thermal response test (see Section 8.3.2), an open-hole water monitoring well was also installed. This well is not permanently equipped with sensors but allows lowering a tool at regular times to assess groundwater presence. Moreover, it is anticipated that the large number of reservoir temperature sensors will reveal over time information on groundwater flow as well. The data acquisition frequency is set at once per hour for slow-changing data such as far-field temperature, while it is once per minute or once per five minutes for fast-changing data such as supply and return temperatures. In addition, a fully-equipped and Cornell-operated weather station is located about 300 m away from the cellular site. This weather station collects hourly data on ambient temperature, humidity, solar radiation, rain and snow fall, wind speed, wind direction and soil temperature at 4 and 8 inch (10 and 20 cm) depths.

Table 8.3 – List of relevant data logged at Varna Site. Status refers to on or off.

Shelter
Shelter temperature; Shelter relative humidity; Outside temperature; Outside relative humidity; Alternating Current (AC) supply voltages; AC supply kWh counter; Alternating Current to Direct Current (ACDC) Plant power
Heat Pump Units
Compressor stage 1 status; Compressor stage 2 status; Electric current; Circulating fluid valve status; Circulating fluid supply temperature; Circulating fluid return temperature; Air supply temperature; Fan status
Dry-Cooler (DC)
DC status; DC supply voltage; DC supply current; Circulating fluid valve status; Circulating fluid supply temperature; Circulating fluid return temperature; Fan motor VFD frequency; Fan motor speed
Air-Economizer (AE)
AE status; AE supply voltage; AE supply current; Circulating fluid valve status; Circulating fluid supply temperature; Circulating fluid return temperature; Air supply temperature; Air return temperature; Fan motor VFD frequency; Fan motor speed
Circulation Pumps
Pump 1 status; Pump 1 supply voltage; Pump 1 supply current; Pump 1 power; Pump 1 motor VFD frequency; Pump 1 motor VFD speed; Pump 1 run time; Pump 1 kWh counter; Pump 2 status; Pump 2 supply voltage; Pump 2 supply current; Pump 2 power; Pump 2 motor VFD frequency; Pump 2 motor VFD speed; Pump 2 run time; Pump 2 kWh counter
Borehole Heat Exchanger (BHE) Field
Circulating fluid supply temperature; Circulating fluid return temperature; 265 ft monitoring wells temperature at 15, 75, 135, 195, and 255 ft depth; 265 ft 1-U BHE well temperature at 15, 75, 135, 195, and 255 ft depth; 385 ft 2-U BHE well temperature at 15, 105, 195, 285, and 375 ft depth; BHE geofluid valve status

Figures 8.5 to 8.7 present some temperature data collected at the Varna Site since measurements started during the Summer of 2014. Figure 8.5 shows the shelter and ambient temperature. The shelter setpoint temperature has been modified at several occasions. In general, the controller and cooling system, alternating between one heat pump in part load and two heat pumps in full load, have been able to keep the shelter temperature within the requested hysteresis around the specified setpoint. Some anomalies in shelter

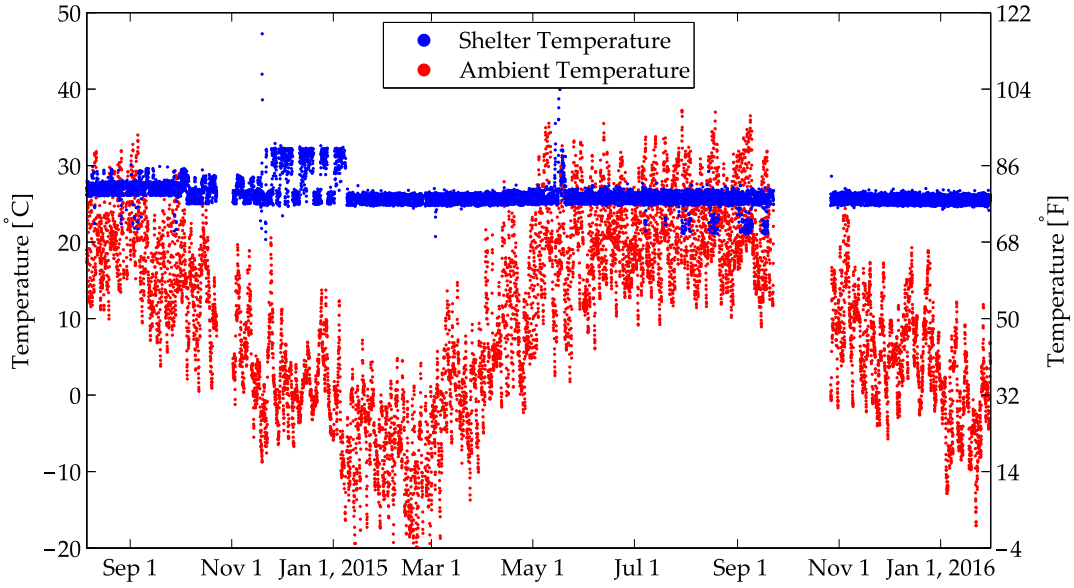

Figure 8.5 – Shelter and ambient temperature at Varna Site from August 5th, 2014 till January 30th, 2016. Due to technical issues, some data is missing around November 1st, 2014 and during the Fall of 2015.

temperature are a result of testing of equipment or maintenance at the site. Due to technical issues, some data had not been logged around November 1st, 2014 and during the Fall of 2015.

Figure 8.6 shows the circulating fluid (geofluid) supply and return temperature. Before March 3rd, 2015, no hybrid component had been activated and all heat had been injected in the geothermal reservoir. After March 3rd, 2015 until the end of the measurements shown, the DC had been running continuously. The DC runs in parallel with the heat pumps meaning that part of the circulating fluid leaving the BHE field enters the heat pump while the other part enters the DC. This operation mode results in supply and return temperatures in some cases overlapping each other, and closely following the ambient temperature. The measured circulating fluid temperatures are only approximate because the temperature sensors are attached to the outside the pipes (of copper material) and will be influenced by the shelter temperature. Again, due to technical issues, some data is missing around November 1st, 2014 and during the Fall of 2015.

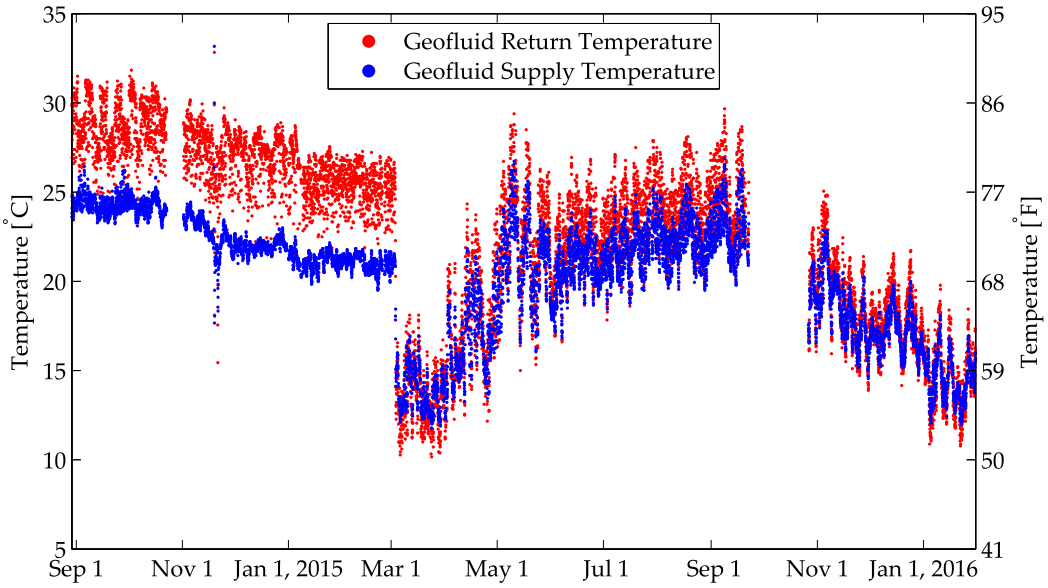

Figure 8.6 – Circulating fluid (geofluid) return (leaving the shelter) and supply (entering the shelter) temperature at Varna Site from August 29th, 2014 till January 30th, 2016. Around March 1st, 2015, the DC was activated. Due to technical issues, some data is missing around November 1st, 2014 and during the Fall of 2015.

The average circulating fluid supply temperature, which is equal to the heat pump entering fluid temperature, is about 20°C. The total heat pump run time in part load and full load so far is about 5,700 and 13,600 hours, respectively. Due to technical issues no flow rate data has been collected with the installed flow meters at the site. Nevertheless, based on the temperature data and flow rate measurements with an acoustic clamp-on flow meter, the flow rates are expected to be in the range 4 to 7 GPM (0.25 to 0.44 l/s) per heat pump running. Assuming an average flow rate of 5.0 GPM (0.32 l/s), and excluding the circulating pump power, the average heat pump COP from end of August 2014 to end of January 2016 is about 6.1. When including the power for the circulating pump, the COP drops to 5.1 If also considering the power for the DC, the COP drops further to 4.8. An ASHP during this time period would have had an average COP of about 3.3.

Figure 8.7 plots the temperature measured at four different depths in wellbore D, whose location in the BHE field is shown in Figure 8.4. So far, only the two 2-U BHEs have been in operation, which are located on the other side in the BHE field. Figure 8.7 shows

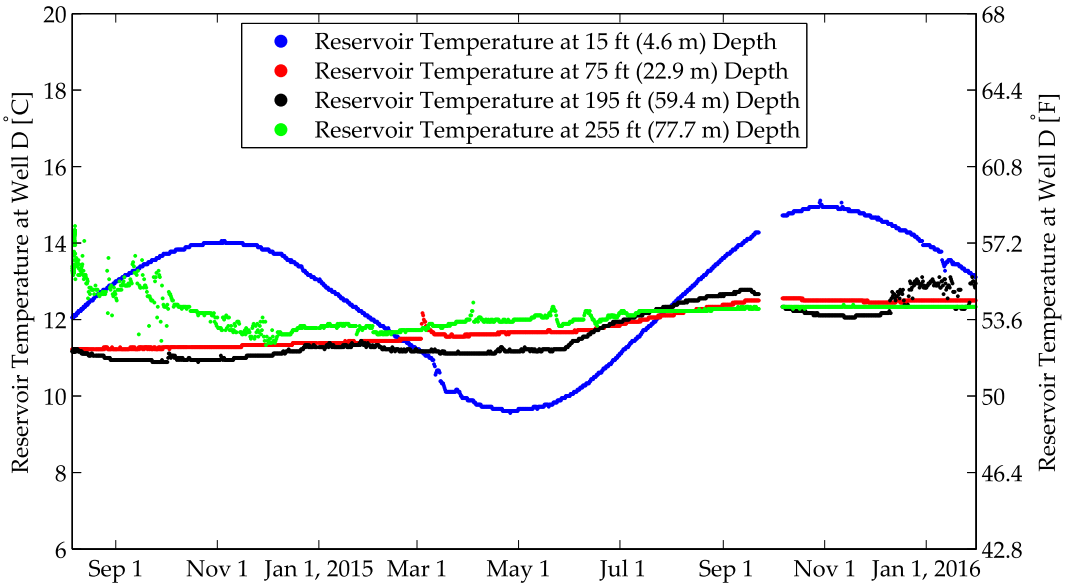

Figure 8.7 – Reservoir temperature at four different depths in borehole D (see Figure 8.4) at Varna Site from August 5th, 2014 till January 30th, 2016. Due to technical issues, some data is missing during the Fall of 2015.

a trend of slowly increasing reservoir temperature for all four depths shown, presumably caused by the continuous injection of heat in the underground. Due to temperature sensor malfunctioning, no data is collected in wellbore D at the depth of 135 ft (41.2 m). The shallow reservoir temperature measured at 15 ft (4.6 m) depth follows a sinusoidal profile caused by the seasonal sinusoidal ambient temperature profile (see Figure 8.5), but shifted in time and decreased in amplitude. This behavior is matched by a simple transient heat conduction model simulating a semi-infinite domain with sinusoidal ambient temperature at the boundary (Bandos et al., 2009). For a constant and uniform thermal diffusivity of $0.62 \cdot 10^{-6}$ m^2/s, the model predicts at 4.6 m depth a sinusoidal profile with a time delay of 3.5 months and amplitude decrease of about 84% (from 14°C to 2.25°C), corresponding well with the observed temperature profile. As discussed in Section 8.3, a value of $0.62 \cdot 10^{-6}$ m^2/s lies in the range of expected values for thermal diffusivity for unconsolidated rocks making up the top soil part.

8.3 Varna Site Geothermal Reservoir Characterization

In order to conduct representative thermal simulations of the geothermal reservoir, as well as to correctly interpret the measured in-situ reservoir and circulating fluid return (i.e. leaving the BHE field) temperatures, proper understanding of the shallow geology and corresponding thermophysical properties is necessary. This section presents the methodology and results of the reservoir characterization at the Varna Site using drill cuttings analysis, a thermal response test, and thermal conductivity measurements of rock samples.

8.3.1 Drill Cuttings Analysis

During drilling of one of the 265 ft (81 m) depth temperature monitoring wells, drill cuttings were collected at 10 ft (3.0 m) intervals from 0 to 60 ft (18.3 m) depth, and 20 ft (6.1 m) intervals from 60 ft (18.3 m) depth to the bottom (see right diagram in Figure 8.8). Based on analysis of these cuttings in combination with general knowledge of the local geology (Tester et al., 2010; USDA, 2015; NYSDEC, 2015), the shallow underground geology at the Varna Site is (to a first approximation) interpreted as Quaternary unconsolidated alluvial and glacial deposits topping Devonian shale (left diagram in Figure 8.8). The drillers reported shale starting at 123 ft (37.5 m) depth.

The dominant rock type in the reservoir is shale. Reported values in literature for shale thermal conductivity (k), specific heat capacity (c_p), density (ρ), and thermal diffusivity $\left(\alpha = \frac{k}{\rho c_p}\right)$ are listed in Table 8.4. Based on this data, expected values for k and α, which are the parameters used in the simulations, are in the range 1-2 W/(m·K), and around 10^{-6} m^2/s, respectively. Expected values for thermophysical properties for the unconsolidated sediments (soil) are in the range 1.2-2.4 W/(m·K) for thermal conductivity and

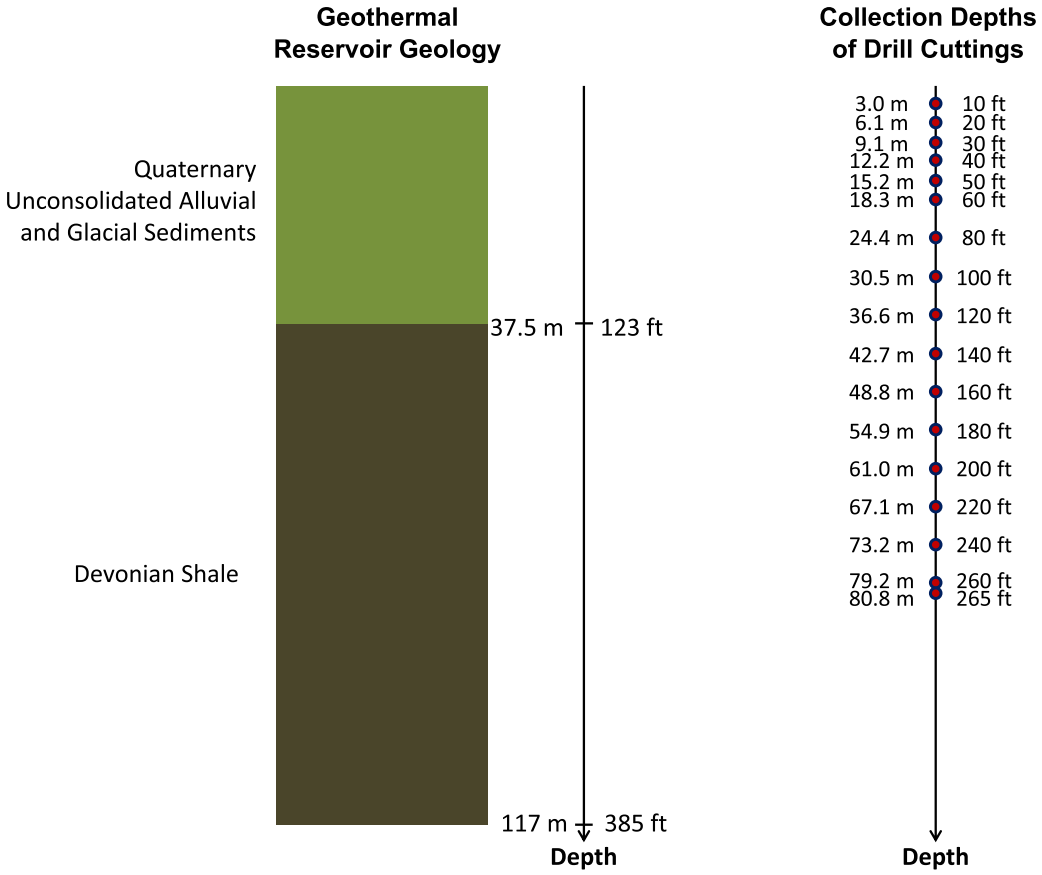

Figure 8.8 – Diagram of geothermal reservoir geology and drill cuttings collection depths at Varna Site.

0.5-1·10^{-6} m^2/s for thermal diffusivity (Hellström, 1991). The value 0.62·10^{-6} m^2/s derived in Section 8.2 using temperature data collected at the Varna Site lies within the expected range for thermal diffusivity. Lumped-parameter thermal properties for the entire reservoir could be obtained by averaging the parameter values for each layer weighted by the layer thickness.

Groundwater was encountered during drilling. Darcy-like flow (matrix flow) is expected in the top part (unconsolidated sediments) while fracture-dominated flow is expected in the bottom part (shale). Groundwater flow enhances the heat dissipation and is therefore advantageous for the system performance. Nevertheless, limited data are available on the quantity, direction and location of the fluid flow and hence, the corresponding advective heat transfer contribution is difficult to model correctly in the simulations. In

Table 8.4 – Published thermophysical properties for shale.

Min	Max	Mean	Reference
Thermal conductivity k (W/(m·K))			
0.8	2.1		(Rybach and Muffler, 1981)
1.63	2.51		(Reiter and Tovar, 1982)
0.55	4.25	2.07	(Čermák and Rybach, 1982)
0.64	1.24	0.92	(Gilliam and Morgan, 1987)
0.96	1.8		(Beach et al., 1987)
1.05	1.45		(Blackwell and Steele, 1989)
0.8	4.0		(EPRI, 1989)
1.5	3.5		(Hellström, 1991)
0.6	4.0		Barker
Specific heat capacity c_p (J/(kg·K))			
880	1,440	1,180	(Čermák and Rybach, 1982)
880	1,090	980	(Gilliam and Morgan, 1987)
950	2,200		(Hellström, 1991)
Density ρ (kg/m^3)			
2,350	2,850		(Čermák and Rybach, 1982)
2,300	2,750		(Schön, 2011)
Thermal diffusivity α (10^{-6} m^2/s)			
0.53	1.6	0.94	(Čermák and Rybach, 1982)

response, an open-hole water monitoring well (currently unequipped) has been installed in the BHE field (see Figure 8.4) which could be used in the future to collect more data on the reservoir.

8.3.2 Thermal Response Test

A thermal response test (TRT), also called thermal conductivity test, is an on-site, multi-day experiment to estimate average effective thermal properties of the geothermal BHE field (Spitler and Gehlin, 2015). For a time period of usually 48 to 96 hours, one circulates a fluid (typically water) with constant flow rate in a closed loop in a completed BHE while continuously supplying constant heat of several kW to the fluid. By measuring the supply (injection) and return (production) temperature, one can derive a lumped-parameter

thermal conductivity of the geothermal reservoir, as well as the thermal resistance of the BHE as installed. Generally, a TRT is conducted after the first BHE is installed to assess whether or not the reservoir thermal conductivity matches the design value. In case of underestimation (overestimation) of the thermal conductivity, one can adjust the design to prevent oversizing (undersizing) of the geothermal BHE field. In May 2013, a TRT was conducted at the Varna Site, shown in Figure 8.9.

Zhang et al. (2014) review different analytical and numerical methods to derive the average thermal properties using TRT. The impact of groundwater flow is studied in depth by Gehlin (2002). An historical review on thermal response testing is provided by Spitler and Gehlin (2015). Other interesting studies that provide an overview of TRT and model equations to estimate the reservoir thermal conductivity and borehole thermal resistance are the works by Yang et al. (2013) and Al-Khoury (2012).

In a simple analytical TRT model (Yang et al., 2013), one assumes the average circulating fluid temperature $T_{f,ave}$ in the BHE as the average of the fluid inlet and outlet temperature:

$$T_{f,ave} = \frac{T_{f,inlet} + T_{f,outlet}}{2} . \tag{8.1}$$

Assuming quasi steady-state heat transfer within the BHE, the heat flux Q (in W/m) from the fluid to the surrounding rocks is calculated as:

$$Q = \frac{(T_{f,ave} - T_b)}{R_b} \tag{8.2}$$

with T_b and R_b the borehole wall temperature and borehole thermal resistance, respectively. T_b as a function of time t can be calculated as the ground temperature evaluated at the borehole radius r_b using a simple infinite line source model (ILS):

$$T_b(t) = T_0 + \frac{Q}{4\pi k} \mathrm{E}_1 \left(\frac{r_b^2}{4\alpha t} \right) \cong T_0 + \frac{Q}{4\pi k} \left[\ln \left(\frac{4\alpha t}{r_b^2} \right) - \gamma \right] \tag{8.3}$$

with T_0, k, α and γ the far-field (or initial) reservoir temperature, reservoir thermal conductivity, reservoir thermal diffusivity, and Euler's constant (0.5772...), respectively. $\mathrm{E}_1(x)$

Figure 8.9 – 96-hour thermal response test (TRT) at Varna Site conducted in May, 2013.

is the exponential integral function $\left(\int_x^\infty \frac{\exp(-u)}{u} \mathrm{d}u\right)$, which simplifies to $\ln\left(\frac{1}{x}\right) - \gamma$ for large x, with ln the natural logarithm (Abramowitz and Stegun, 1964). This model assumes the BHE is infinitely long. This is an acceptable assumption since the thermal diffusion length during a TRT (~0.6 m for a four-day TRT with ground thermal diffusivity of 10^{-6} m^2/s) is much smaller than the actual borehole length (~100 m). Combining Equations (8.2) and (8.3), one can find the following expression for $T_{f,ave}$, valid for $t > \frac{5r_b^2}{\alpha}$:

$$T_{f,ave} = \frac{Q}{4\pi k}\left[\ln\left(\frac{4\alpha t}{r_b^2}\right) - \gamma\right] + T_0 + Q \cdot R_b \tag{8.4}$$

$$= \underbrace{\frac{Q}{4\pi k}}_{\kappa} \ln(t) + \underbrace{\frac{Q}{4\pi k}\left[\ln\left(\frac{4\alpha}{r_b^2}\right) - \gamma\right] + T_0 + Q \cdot R_b}_{\lambda} = \kappa \cdot \ln(t) + \lambda \tag{8.5}$$

which means the average fluid temperature can be approximated as a line in a semi-log plot. The geothermal reservoir thermal conductivity is then estimated using the slope κ

as:

$$k = \frac{Q}{4\pi\kappa} = \frac{q}{4\pi\kappa L} \tag{8.6}$$

with q and L the total heat supplied by the heater to the fluid (in W), and the BHE length, respectively. Using the intercept λ, one can find a value for the borehole resistance, assuming one has an estimate or assumed value for the reservoir thermal diffusivity and far-field reservoir temperature:

$$R_b = \frac{\lambda}{Q} - \frac{1}{4\pi k}\left[\ln\left(\frac{4\alpha}{r_b^2}\right) - \gamma\right] - \frac{T_0}{Q}\,. \tag{8.7}$$

At the Varna Site, the TRT was conducted on one loop of a double-U BHE with 117.3 m (385 ft) depth. About 7.5 kW of heat was supplied to the circulating fluid which was water. The total test duration was 96 hours, however, during the last six hours the heat input slightly changed and hence, only 90 hours of measured test data are considered. The measured average fluid temperature $T_{f,ave}$ from 1 to 90 hours is shown by the blue curve in Figure 8.10 on a semi-log plot. A linear fit was applied to the data after discarding the first 12 hours of measurements (a similar approach as by Spitler and Gehlin (2015)), and is shown in Figure 8.10 as the red dashed line. Based on the slope and intercept of this linear fit, Equations (8.6) and (8.7) result in a reservoir thermal conductivity and borehole thermal resistance of 4.0 W/(m·K) and 0.16 m·K/W, respectively. All TRT model input parameters and results are listed in Table 8.5.

An effective thermal conductivity of 4.0 W/(m·K) is rather high in comparison with reported values for shale, which are in the range 0.6 to 4.25 W/(m·K) (see Section 8.3.1). The reason for a high value at the Varna Site is the likely presence of groundwater flow, as reported by the drillers. When replacing the ILS with a moving infinite line source (MILS) model (Diao et al., 2004), one can, to a first approximation, account for uniform horizontal Darcy-like groundwater flow. With this model, assuming a ground thermal diffusivity of 10^{-6} m^2/s, a preliminary analysis shows that the measured average fluid

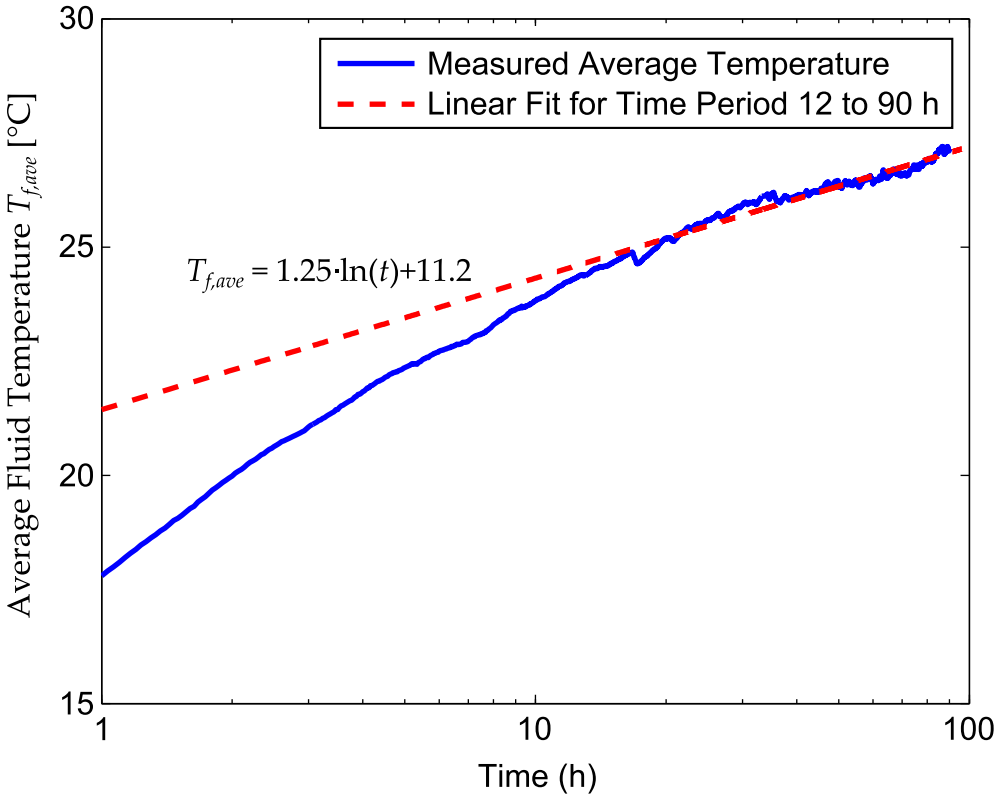

Figure 8.10 – Measured average fluid temperature and linear fit for thermal response test at Varna Site.

Table 8.5 – Model input parameter values and results for Varna Site thermal response test.

TRT Model Input Parameters		
Thermal diffusivity (est.)	α	10^{-6} m^2/s
Borehole radius	r_b	0.073 m
Borehole depth	L	117.3 m
Heat input	q	7,416 W
Far-field ground temperature	T_0	10.6°C
Test total time duration		96 h
Linear fit time period		12-90 h
TRT Model Results		
Linear fit slope	κ	1.25
Linear fit intercept	λ	11.2
Effective thermal conductivity	k	4 W/(m·K)
Borehole thermal resistance	R_b	0.163 m·K/W

temperature data of the TRT is best matched with a ground thermal conductivity of 2.0 W/(m·K), a uniform average groundwater velocity of 10^{-6} m/s, and a borehole thermal resistance of 0.10 m·K/W.

8.3.3 Shale Sample Thermal Conductivity Measurement

The thermal conductivity is the most important rock property in conduction-dominated reservoirs. It determines how effectively heat dissipates and what the required BHE length is. Although groundwater flow and correspondingly advective heat transfer is known to be present at the Varna Site, it is still desirable to accurately know the rock thermal conductivity in order to simulate the worst-case scenario (conductive heat transfer only) and assess the impact of the groundwater flow on the system performance.

A rock sample was taken from a mudstone outcrop in a gorge near the Varna Site. The thermal conductivity of the rock sample was measured at the Southern Methodist University (SMU) Geothermal Lab, using the apparatus shown in Figure 8.11. This apparatus is based on the divided bar technique (Goss and Combs, 1976; Blackwell and Spafford, 1982), illustrated schematically for this set-up in Figure 8.12. This method is a steady-state test to estimate the thermal conductivity of a specimen (here shale sample) by forcing a heat flux through the specimen and through a material of known thermal conductivity, and measuring the temperature drops. Specifically for this apparatus, the temperature drops are measured over an upper heat flux meter, over the specimen, and over a lower heat flux meter, and compared with the temperature drops when running the experiment for a specimen with known thermal conductivity (here silica glass or quartz material). The heat flux meters consist of a layer of material with certain conductivity in between two copper discs. The specimen is loaded under axial pressure to represent in-situ conditions and limit the contact thermal resistances. The heat source and sink are

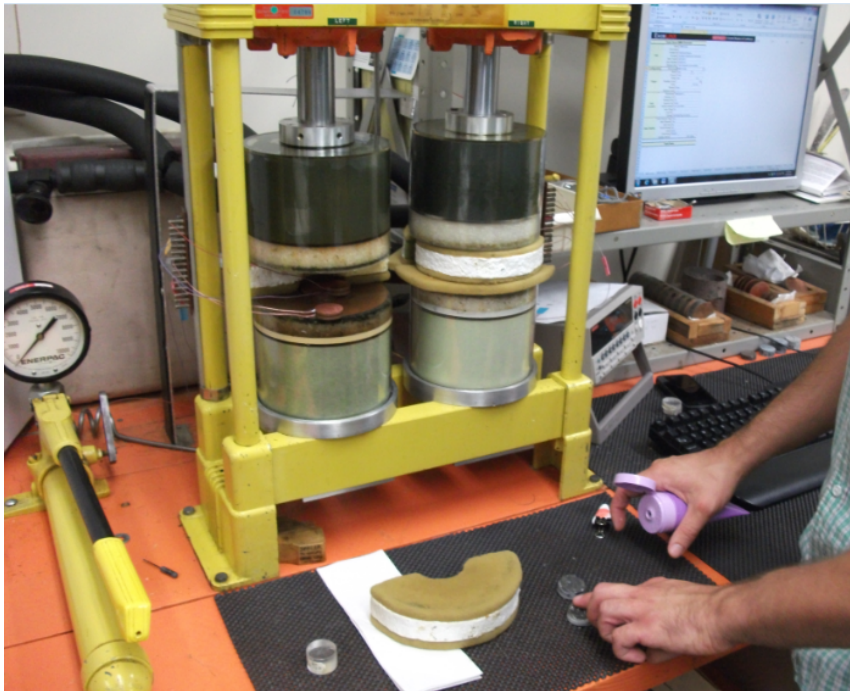

Figure 8.11 – Apparatus at Southern Methodist University (SMU) Geothermal Lab used for measuring thermal conductivity of shale sample from outcrop near Varna Site.

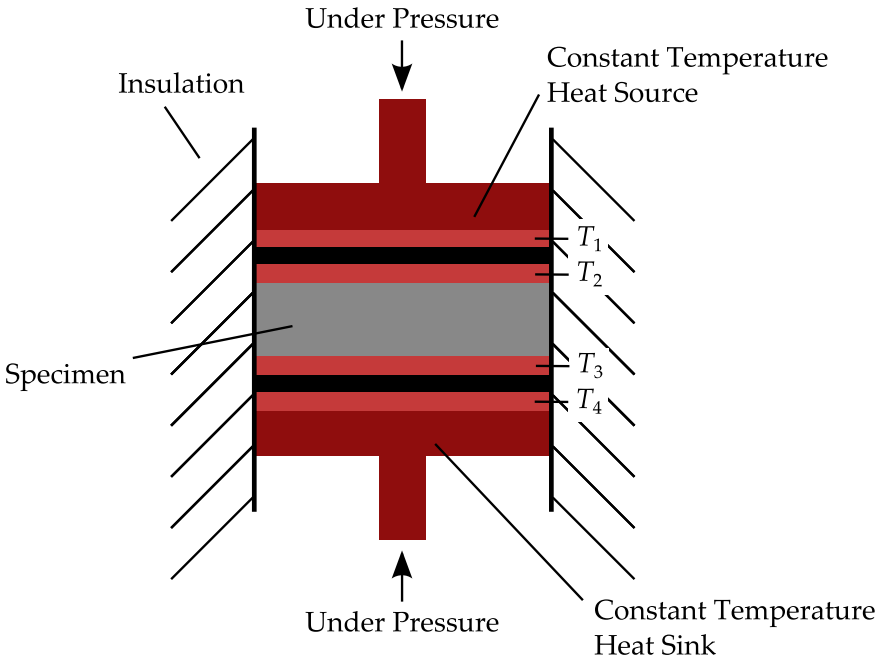

Figure 8.12 – Schematic diagram of apparatus to measure thermal conductivity of specimen, based on the divided bar technique. The temperatures T_1 to T_4 are measured inside the red copper discs of the heat flux meters.

supplied by constant temperature circulating baths. The thermal conductivity of the shale sample k_{shale} is then calculated as (Blackwell and Spafford, 1982):

$$k_{shale} = \left(\frac{\Delta T_{1,shale} + \Delta T_{3,shale}}{2\Delta T_{2,shale}}\right)\left(\frac{\Delta T_{1,ref} + \Delta T_{3,ref}}{2\Delta T_{2,ref}}\right)\frac{Th_{shale}}{Th_{ref}}\frac{D_{ref}^2}{D_{shale}^2} \tag{8.8}$$

with ΔT_1, ΔT_2, and ΔT_3 calculated as T_1-T_2, T_2-T_3, and T_3-T_4, respectively, with T_1 to T_4 the temperatures measured inside the copper discs of the heat flux meters (red discs in Figure 8.12). The subscripts shale and ref refer to the shale sample and to the reference material. Further, Th_{shale}, Th_{ref}, D_{ref}, and D_{shale} are the thickness and diameter of the shale and reference specimen, respectively.

The thermal conductivity measured for the shale sample is about 1.0 W/(m·K), which falls in the range of reported values in literature (see Table 8.4), and could be interpreted as an approximate value for a lower bound for the effective thermal conductivity for a reservoir that is subject only to heat conduction. At the Varna Site, we postulated that advection by groundwater flow is an added factor. As discussed earlier, the effective thermal conductivity measured with the TRT is about four times higher, which substantiates the significant impact of groundwater flow on reservoir heat dissipation.

References

Abramowitz, M. and Stegun, I. A. (1964). *Handbook of mathematical functions: with formulas, graphs, and mathematical tables*. Number 55. Courier Corporation, Mineola, New York.

Aguirre, G. A. (2016). *Nationwide Potential of Hybrid Ground-Source Heat Pump Systems for Climate Control of Cellular Tower Shelters*. Internal Report, Cornell Energy Institute, Cornell University, Ithaca, New York, United States.

Al-Khoury, R. (2012). *Computational Modeling of Shallow Geothermal Systems*. CRC Press.

Bandos, T. V., Montero, Á., Fernández, E., Santander, J. L. G., Isidro, J. M., Pérez, J., de Córdoba, P. J. F., and Urchueguía, J. F. (2009). Finite line-source model for borehole heat exchangers: effect of vertical temperature variations. *Geothermics*, 38 (2): 263–270.

Beach, R. D. W., Jones, F. W., and Majorowicz, J. A. (1987). Heat flow and heat generation estimates for the Churchill basement of the Western Canadian Basin in Alberta, Canada. *Geothermics*, 16 (1): 1–16.

Beckers, K. F., Yavuzturk, C. C., and Tester, J. W. (2014). *Techno-Economic Modeling and Monitoring of Hybrid Ground-Source Heat Pump System with Borehole Heat Exchangers for Cooling-Dominated Cellular Tower Application*. 11th IEA Heat Pump Conference, Montreal, Canada.

Blackwell, D. and Spafford, R. (1982). *Standard Method of Test for Thermal Conductivity of Rock Using Divided Bar.* Submitted to AMTS 1982. SMU Geothermal Laboratory, Dallas, Texas, United States.

Blackwell, D. D. and Steele, J. L. (1989). Thermal conductivity of sedimentary rocks: measurement and significance. In *Naeser, N. D., McCulloh, T. H. (Eds.), Thermal History of Sedimentary Basins.* Springer-Verlag.

Čermák, V. and Rybach, L. (1982). Thermal conductivity and specific heat of minerals and rocks. In *Beblo, M. et al. (Eds.), Geophysics - Physical Properties of Rocks, Chapter: Landolt-Börnstein Numerical Data and Functional Relationships in Science and Technology, New Series, Group V, Geophysics and Space Research, Vol. 1*, pages 305–343. Springer.

Diao, N., Li, Q. and Fang, Z. (2004). Heat transfer in ground heat exchangers with groundwater advection. *International Journal of Thermal Sciences*, 43 (12): 1203–1211.

EPRI (1989). *Soil and Rock Classification for the Design of Ground-Coupled Heat Pump Systems*. Electric Power Research Institute, EPRI CU-6600, Research Projects 2892-3 and 2892-5.

Gehlin, S. (2002). *Thermal Response Test. Model Development and Evaluation*. PhD Dissertation, Luleå University of Technology, Luleå, Sweden.

Gilliam, T. M. and Morgan, I. L. (1987). *Shale: Measurement of thermal properties*. ORNL/TM-10499, Oak Ridge National Laboratory, Oak Ridge, Tennessee, United States.

Goss, R. and Combs, J. (1976). *Thermal conductivity measurement and prediction from geophysical well log parameters with borehole application*. Institute for Geosciences, The University of Texas at Dallas, Richardson, Texas, United States.

Hellström, G. (1991). *Ground Heat Storage: Thermal Analyses of Duct Storage Systems*. PhD Dissertation, Lund University, Lund, Sweden.

IGSHPA (2009). *Ground Source Heat Pump Residential and Light Commercial Design and Installation Guide*. International Ground Source Heat Pump Association, Oklahoma State University, Stillwater, Oklahoma, United States.

LaBrozzi, B., Dodge, E., and Tester, J. (2010). *Utilization of Closed Loop Geothermal Heat Pumps at Verizon Wireless Cellular Towers*. Cornell Energy Institute, Cornell University, Ithaca, New York, United States.

NYSDEC (2015). *Final Supplemental Generic Environmental Impact Statement on the Oil, Gas and Solution Mining Regulatory Program*. New York State, Department of Environmental Conservation.

Reiter, M. and Tovar, J. C. (1982). Estimates of terrestrial heat flow in northern Chihuahua, Mexico, based upon petroleum bottom-hole temperatures. *Geological Society of America Bulletin*, 93 (7): 613–624.

Rybach, L. and Muffler, L. J. P. (1981). *Geothermal systems: principles and case histories*. John Wiley & Sons.

Schön, J. (2011). *Physical properties of rocks: A workbook*, volume 8. Elsevier.

Spitler, J. D. and Gehlin, S. E. (2015). Thermal response testing for ground source heat pump systemsan historical review. *Renewable and Sustainable Energy Reviews*, 50: 1125–1137.

Tester, J. W., Joyce, W. S., Brown, L., Bland, B., Clark, A., Jordan, T., Andronicos, C., Allmedinger, R., Beyers, S., Blackwell, D., Richards, M., Frone, Z., and Anderson, B. (2010). Co-Generation Opportunities for Lower Grade Geothermal Resources in the Northeast - A Case Study of the Cornell Site in Ithaca, NY. In *GRC Transactions*, 34: 440–448.

USDA (2015). *Web Soil Survey*. Soil Survey Staff, Natural Resources Conservation Service, United States Department of Agriculture. Available at http://websoilsurvey.nrcs.usda.gov/.

Yang, W., Chen, Z., Shi, M., and Zhang, C. (2013). An in situ thermal response test for borehole heat exchangers of the ground-coupled heat pump system. *International Journal of Sustainable Energy*, 32 (5): 489–503.

Zhang, C., Guo, Z., Liu, Y., Cong, X., and Peng, D. (2014). A review on thermal response test of ground-coupled heat pump systems. *Renewable and Sustainable Energy Reviews*, 40: 851–867.

CHAPTER 9

CORNELL-VERIZON HYBRID GEOTHERMAL HEAT PUMP PROJECT: TRNSYS SYSTEM ANALYSIS

9.1 TRNSYS Systems Model

An in-depth analysis of the performance of hybrid geothermal heat pump systems for cooling of cellular tower shelters requires the development of a versatile and rigorous computer simulation model. A preliminary model was developed in MATLAB and presented at the 11th IEA Heat Pump Conference in Montreal (Beckers et al., 2014). Building upon this model, a more detailed and elaborate simulation tool was developed using the software platform TRNSYS (SEL, 2014a), which is presented in this section. TRNSYS was chosen for its proven success with simulating geothermal heat pump systems (see Section 7.3).

An example of the TRNSYS model developed for this study is shown in Figure 9.1. This model consists of various blocks representing the different system components, e.g. shelter, heat pumps, air-economizer (AE), dry-cooler (DC), etc., all discussed in the following sections. Simulation results utilizing this model are presented in Section 9.3. Most components selected for use in the TRNSYS model are similar to those at the Varna site. There were a few exceptions because of economic or technical reasons. For example, a smaller DC is selected to better match the circulation flow rates and shelter heat requirements. Further, not six but about three to four borehole heat exchangers (BHEs) will minimize the total cost of ownership (TCO). Also, the reservoir heat transfer model assumes conduction-only heat transfer, even though groundwater flow is present at the Varna Site. Nevertheless, an "effective" reservoir thermal conductivity can, to a first approximation, capture the effects of both conduction and advection.

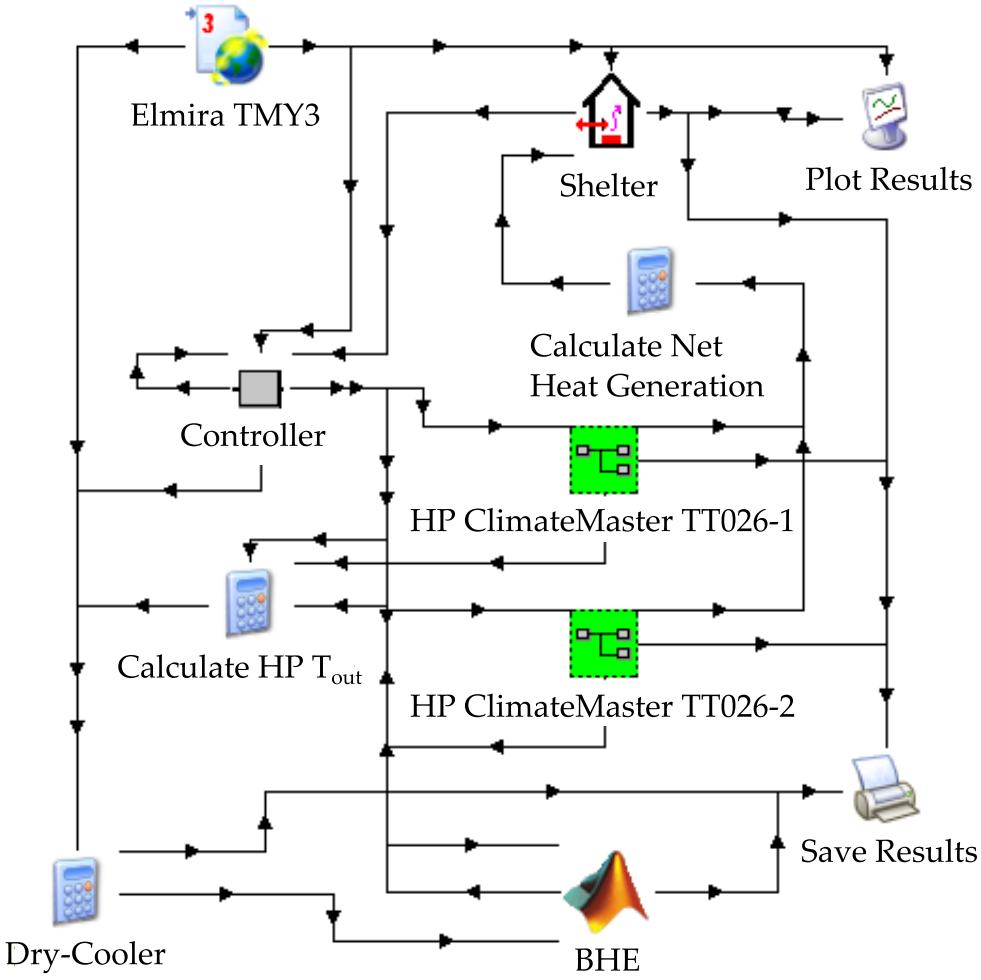

Figure 9.1 – Example of TRNSYS model of hybrid geothermal heat pump system. This model corresponds to Case 3 (GSHP + DC) studied in Section 9.3.

9.1.1 Shelter Component

The shelter which houses the telecommunication equipment and requires climate control is modeled using the lumped capacitance building component (Type 88) (SEL, 2014b) and labeled as "Shelter" in Figure 9.1. Type 88 is a simplified single-zone building simulation component which assumes the internal thermal mass can be represented by a single building thermal capacitance parameter, and the heat exchange through the walls by the overall external wall area and wall R-value. The Varna Site shelter parameter values have been provided in Table 8.1. The shelter thermal capacitance has been experimentally de-

termined by measuring the shelter temperature drop over a 30 minute period when all three heat pumps are in first stage cooling mode. Further, in the TNRYS model, as well as with the actual system at the Varna Site, only the shelter dry-bulb temperature is controlled, not the humidity. Based on logging data at the Varna Site, the relative humidity inside the shelter fluctuates between 10 and 50%.

In calculating the heat exchange with the environment, only heat transfer through the external walls and roof are considered; heat losses through the ground are neglected. Also, the emergency diesel generator room, which is directly attached to one of the small walls of the shelter, is not climate-controlled and has been neglected in the TRNSYS model.

9.1.2 Alternating Current to Direct Current Plant Heat Generation Component

The Alternating Current to Direct Current (ACDC) Plant converts alternating current to direct current to provide power for the telecommunication equipment in the shelter. This power is dissipated as heat inside the shelter, requiring the shelter to be constantly cooled. Figure 9.2 shows the ACDC Plant heat generation during the first 30 days of December 2014. The heat generation stays fairly constant with an average value of 11.5 kW_{th}. Since the daily fluctuations are small, a constant value was assumed in the TRNSYS model using the equation calculator. Because of heat exchange between the shelter and the environment, the instantaneous cooling load fluctuates between about 10 and 12 kW_{th}. In the analysis in Section 9.3, different values for heat generation are considered because different shelters across the country can house different telecommunication equipment. Also, even for one shelter, the telecommunication equipment can be replaced over time, with the adoption of new technology.

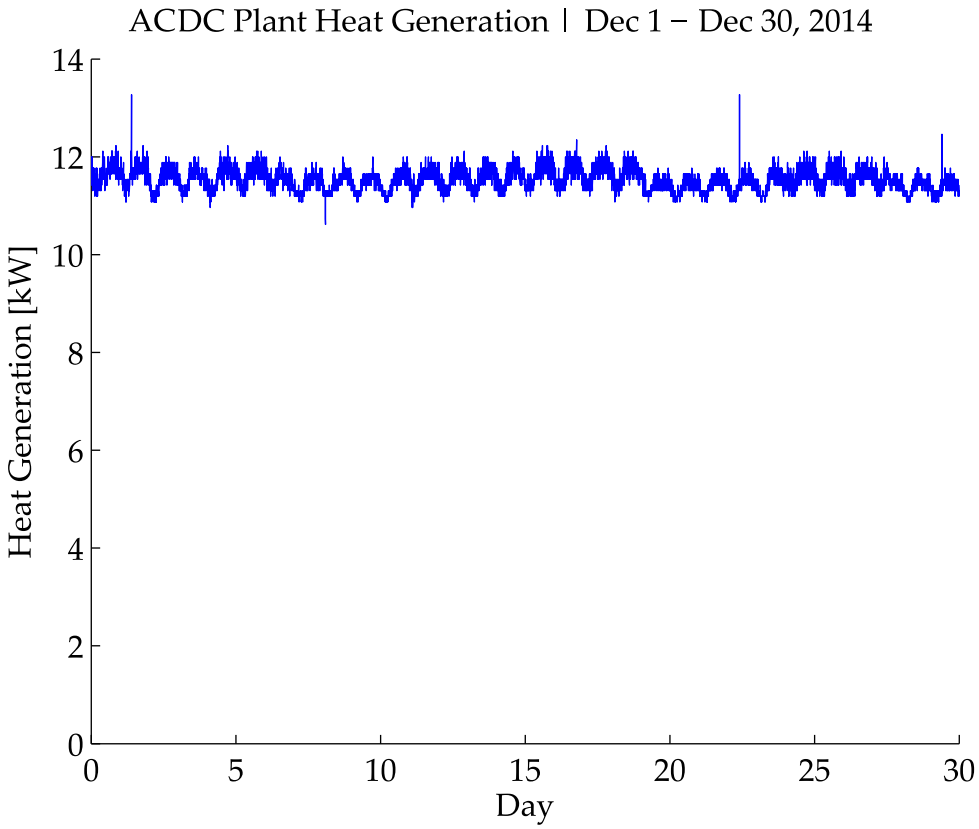

Figure 9.2 – ACDC Plant heat generation in kW at Varna Site during first 30 days of December 2014.

9.1.3 Weather Component

The ambient (dry-bulb) temperature has an impact on the operation and performance of the system at several levels. It determines whether or not the AE and DC can be utilized at a given moment and directly affects their performance. It determines the heat losses or gains through the shelter walls and the annual average ambient temperature is a proxy for the local initial ground temperature. In the TRNSYS model, the ambient temperature is incorporated with a TMY3 (Typical Meteorological Year 3) weather file (Wilcox and Marion, 2008), using Type 15, as shown in Figure 9.1. Locally measured temperature data at the Varna site can easily be converted into the TMY3 data format using Excel. For the nationwide analysis, existing TMY3 weather files for hundreds of U.S. cities based on historical climatic data are publicly available. For long-term simulations at the Varna Site,

the TMY3 weather file for the weather station at the Elmira Corning Regional Airport is utilized.

Other weather aspects that have a minor influence on the system performance, but that are not considered in this study, are: solar irradiance which impacts the shelter heat exchange with the environment, ambient relative humidity which affects the AE and air-source heat pump (ASHP) performance, and rain fall which can influence the rate of underground heat dissipation.

9.1.4 Heat Pump Component

A TRNSYS macro component has been developed to represent a ClimateMaster Tranquility Two-Stage (TT) 026 water-to-air heat pump. This component is labeled HP ClimateMaster TT 026 in Figure 9.1, and simulates the cooling performance of the heat pump based on the manufacturer's datasheet, which are included in Appendix A. The macro-subcomponents are the TRNSYS equation calculator and Type 42 to read external data files (see Figure 9.3). Calculated are the total and sensible cooling, power consumption, heat rejection, and coefficient of performance (COP), based on the entering water temperature, water flow rate, entering dry- and wet-bulb air temperature, air flow rate, and whether the heat pump is operating in part load or full load.

Due to technical issues with the flow rate measurement system, accurate validation of the TRNSYS heat pump component could not be performed with the data obtained at the Varna Site. Nevertheless, calibrated data has been collected at a residential heat pump system in Lansing, NY. This heat pump is the ClimateMaster Tranquility Two-Stage (TT) 049 water-to-air heat pump, which is the same model and from the same manufacturer but of larger size than the Varna Site heat pumps. Figure 9.4 shows excellent agreement between the measured fluid outlet temperature and simulated fluid outlet temperature

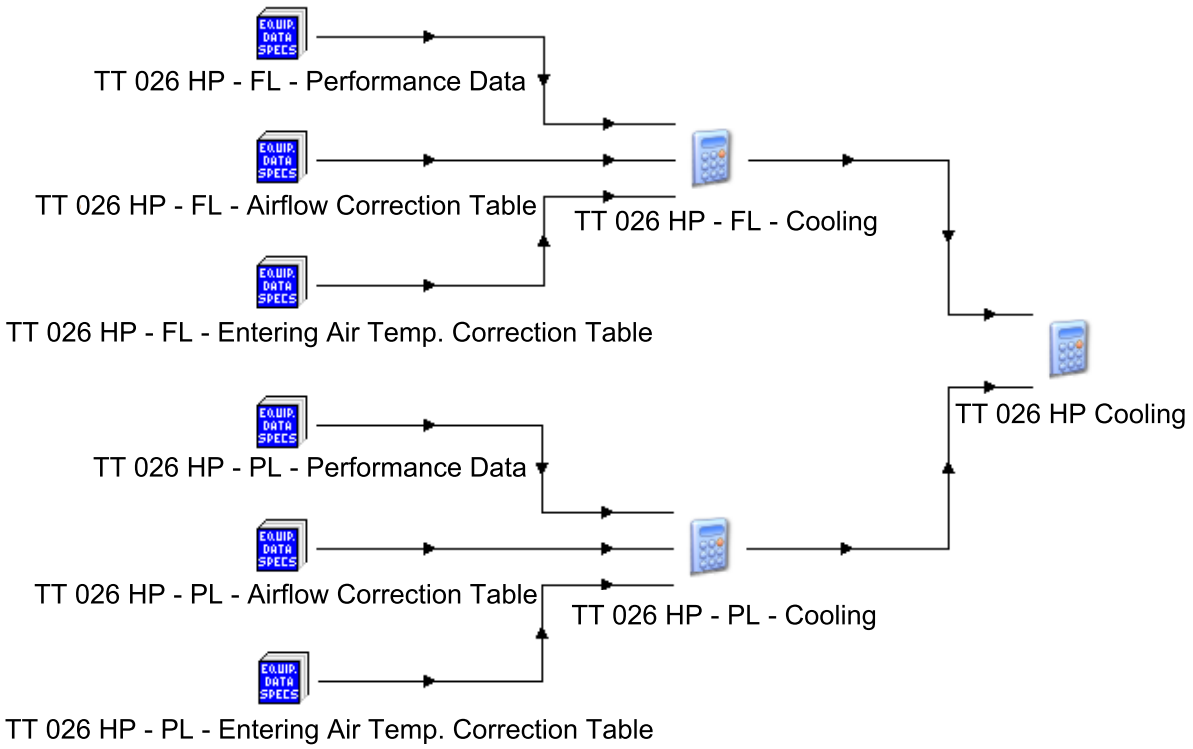

Figure 9.3 – Subcomponents in TRNSYS macro component for ClimateMaster TT 026 heat pump. HP, PL and FL refer to heat pump, part load and full load, respectively.

using the same manufacturer's datasheet, assuming the measured fluid inlet temperature as known input in the model. The data shown is collected during August 2013 when the heat pump was in cooling mode with fluid inlet temperatures of the same order as at the Varna Site. The ambient temperature measured at the site is included to show the positive correlation between the ambient temperature and measured fluid inlet and outlet temperatures.

9.1.5 Borehole Heat Exchangers Component

A novel reservoir heat transfer model to simulate the BHEs has been developed, and is presented and validated in Appendix B. TRNSYS does have built-in BHE models but their use is not meant for short-term transient behavior on the order of minutes to hours, which

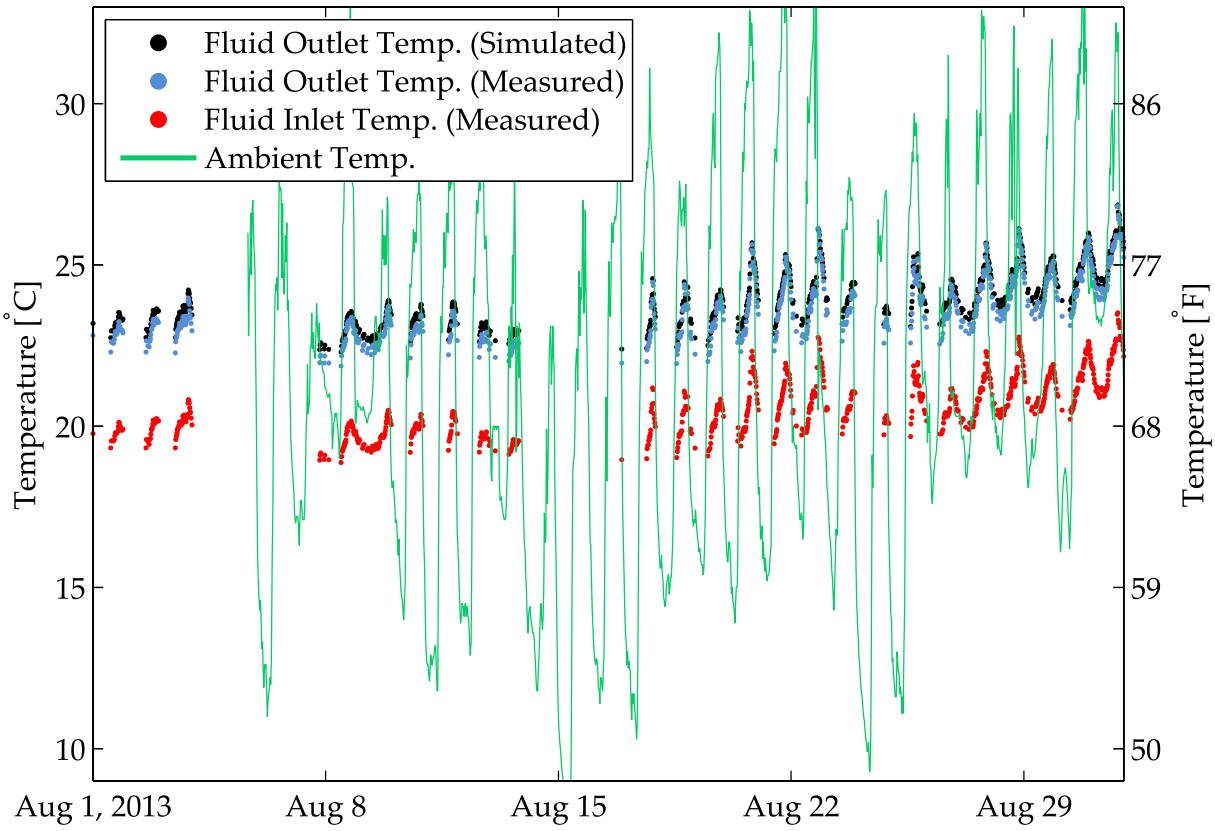

Figure 9.4 – Measured fluid inlet and outlet temperature, simulated fluid outlet temperature and measured local ambient temperature for ClimateMaster TT 049 residential heat pump system in Lansing, NY. Excellent agreement exists between measured and simulated fluid outlet temperature, justifying the use of the Manufacturer's datasheet for the TRNSYS heat pump component. No ambient temperature data was collected prior to August 5th, 2013.

are the time scales occurring in this study. As mentioned above, this model assumes the reservoir heat transfer is conduction only, which underestimates the heat dissipation in the presence of groundwater flow, such as at the Varna Site. Nevertheless, groundwater flow is not only difficult to model, but also challenging to measure and monitor. Therefore, a conduction-only situation was assumed for modeling to represent the most conservative scenario. In addition, conduction and advection can, to a first approximation, be lumped together into an "effective" thermal conductivity, as already mentioned in Section 8.3.2, and further discussed in Section 9.3.3. The BHE model has been implemented in MATLAB and is coupled to the TRNSYS model using Type 155, labeled as "BHE" in Figure 9.1.

The BHE model can handle various flow rates during the same simulation, e.g. when alternating between one and two active heat pumps. Also, it is possible to simulate turning off the system temporarily, e.g. when only providing cooling with the AE. The circulation pumps installed at the Varna Site can provide flow rates in the range 0 to about 40 GPM (0 to 2.5 l/s). With the DC turned off, a flow rate of 9 GPM requires about 0.2 kW of electricity consumption (for 4 x 234 m of pipe length). The underground initial (and far-field) temperature is assumed uniform at 9°C (48.2°F), the average annual temperature from the Elmira Corning Regional Airport TMY3 weather data.

9.1.6 Dry-Cooler Component

The dry-cooler (DC) cools down the circulating fluid by forced cross flow heat exchange with cold ambient air. Based on the manufacturer's datasheet, the following cooling correlation was derived for the model installed at the Varna site (Liebert 092 model):

$$Q_{DC} = 293.1 \cdot \frac{9}{5} \cdot (T_{f,DC,supply} - T_{amb}) \cdot (-0.310m^2 + 1.620m + 1.700) \cdot cf \tag{9.1}$$

with $T_{f,DC,supply}$, T_{amb}, m, and cf, the fluid supply temperature to the DC (in °C), the ambient temperature (in °C), the fluid mass flow rate (in kg/s), and a correction factor dependent on the fluid type and fluid supply temperature, respectively. For the water-ethylene glycol mixture in our case, cf has a value of 0.975 and about 0.94 for a $T_{f,DC,supply}$ of 26.67°C (80°F) and 10°C (50°F), respectively. The Liebert 092 model is designed for fluid flow rates between 18 to 36 GPM (1.1 to 2.3 l/s), much higher than the flow rates occurring at the Varna site as well as in our TRNSYS simulations, which are in the range 3.5 to 7 GPM (0.22 to 0.44 l/s). Therefore, the DC model selected for the TRNSYS model is the smallest Liebert model (033), designed for flow rates in the range 6-12 GPM (0.38-0.76 l/s), and with cooling correlation based on the manufacturer's datasheet as follows:

$$Q_{DC} = 293.1 \cdot \frac{9}{5} \cdot (T_{f,DC,supply} - T_{amb}) \cdot (-1.398m^2 + 2.654m + 0.465) \cdot cf\,. \tag{9.2}$$

The DC component is included in the model using the equation calculator, and is labeled "Dry-Cooler" in Figure 9.1.

9.1.7 Air-Economizer Component

The AE draws in cold outside air to efficiently cool the shelter without having to operate the heat pumps. Thus, electricity use operating costs will decrease when using the AE, however, maintenance increases and costs for replacing air filters are significant factors, as well as the risk of equipment malfunction due to entering dust particles. The fan has a rated air flow capacity of 802 l/s (1,700 CFM) and a power consumption of 560 W (0.75 HP) at 1 atm and 21.1°C (70°F). The nominal cooling capacity Q_{AE} (in W) is calculated as:

$$Q_{AE} = 0.802 \cdot \rho_{air} \cdot c_{p,air} \cdot (T_{shelter} - T_{amb}) \tag{9.3}$$

with ρ_{air} the air density ($\approx$ 353/(273.15 + T_{amb})), $c_{p,air}$ the air specific heat capacity (≈1 kJ/(kg·K)), and $T_{shelter}$ the shelter temperature (≈26°C), respectively. The controller can set different VFD setpoints for the AE fan. Following the affinity laws for axial and centrifugal fans and pumps (Peng, 2008), it is assumed the AE cooling Q_{AE} scales linearly and power W_{AE} scales cubicly with the flow rate, respectively. Although this assumption significantly simplifies the AE behavior (e.g. fan performance maps are neglected), the impact on the overall system performance is minor because the electric power consumption of the AE is much smaller than for the heat pumps. This component is modeled in TRNSYS using the equation calculator. It is assumed in this study that the same correlation for the AE (Equation (9.3)) holds for both hybrid GSHP and hybrid ASHP systems.

9.1.8 Controller Component

The controller regulates the cooling systems to keep the temperature in the shelter around a setpoint of 25.6°C (78°F). Figure 9.5 shows the shelter and ambient temperature during the month of April and part of May in 2015. The shelter temperature fluctuates within a hysteresis of about 1.7°C (3°F) between 25°C (77°F) and 26.7°C (80°F).

A controller component has been written and compiled in FORTRAN and incorporated in the TRNSYS model as an external DLL (Dynamic-Link Library), labeled "Controller" in Figure 9.1. The controller regulates the heat pump units, circulation pump, AE and DC to keep the shelter temperature between 25°C (77°F) and 26.7°C (80°F). Specific information such as setpoints in different cases is provided in Section 9.3.

9.1.9 Air-Source Heat Pump Component

The performance of the hybrid geothermal heat pump system will be compared with the current industry standard which is a wall-mounted HVAC system, with or without an air economizer. The cooling capacity and performance are modeled in TRNSYS using empirical correlations based on the performance datasheet of a single-stage traditional Marvair wall-mounted HVAC unit (Beckers et al., 2014). The correlation for the cooling capacity Q_{ASHP} (in kW) is:

$$Q_{ASHP} = 20.3 - 0.189 \cdot T_{amb} \tag{9.4}$$

with T_{amb} the ambient temperature in °C. The electrical power consumption W_{ASHP} (in kW) is estimated as:

$$W_{ASHP} = \frac{Q}{3.9234 - 0.0367 \cdot T_{amb}}\,. \tag{9.5}$$

No data is provided by the manufacturer on the effect of different shelter dry- and wet-bulb temperatures on the ASHP cooling capacity and power consumption. Therefore, the

impact is assumed the same as with the ClimateMaster TT 026 water-to-air heat pump (see Figure A.4 in Appendix A).

9.1.10 Performance Metrics and Financial Parameters

The financial performance metric investigated for a certain system (either GSHP or ASHP) is the total cost of ownership or TCO (also called life cycle cost), calculated as:

$$TCO = \sum_{t=0}^{lt} \frac{CF_i}{(1 + i_d - i_{inf})^i} \tag{9.6}$$

with CF_i the annual cash flow, and $(i_d - i_{inf})$ the net discount rate. It is assumed the capital costs are incurred in year zero ($t = 0$). Table 9.1 provides an overview of financial parameters considered in calculating the TCO (Beckers et al., 2014). An electricity rate of 14 ¢/kWh$_e$ is based on average commercial end-use rates for NY State. The drilling capital cost, 50 \$/m, is based on the market survey by Battocletti and Glassley (2013). Other metrics analyzed are the operational energy consumption and operational CO_2 emissions over the lifetime of the system. For the Varna Site, the average CO_2 emissions rate for grid-generated electricity is assumed 186 g/kWh$_e$, based on EPA (Environmental Protection Agency) eGRID 2012 data for New York State (EPA, 2015). The software MATLAB (MathWorks, 2012) is utilized to perform the performance metrics calculations based on the TRNSYS simulation results.

In the GSHP cases in Section 9.3, only two GSHP units are considered (\$5,000 each), unlike at the Varna Site where the number of units installed is three. It is assumed that the backup cooling system in case one of the GSHP units fails is a small, inefficient HVAC unit whose cost (~\$500) is included in CAP_{other} (\$5,000). Further, the ASHP units are replaced after 10 years. All other components have a lifetime of 20 years. In Section 9.3.3, the impact of several of the parameters of Table 9.1, including drilling cost and net discount rate, on the TCO is investigated using a sensitivity analysis.

Table 9.1 – TRNSYS model financial parameter values.

Inflation rate	i_{inf}	2 %
Discount rate	i_d	5 %
System lifetime	lt	20 years
Electricity rate	el	14 ¢/kWh$_e$
GSHP unit capital cost	CAP_{GSHP}	\$5,000
GSHP capital cost for pumps, piping & installation	CAP_{other}	\$5,000
Drilling capital cost	$CAP_{Drilling}$	50 \$/m
DC capital cost	CAP_{DC}	\$1,000
AE capital cost	CAP_{AE}	\$1,000
ASHP unit capital cost	CAP_{ASHP}	\$2,500
AE maintenance cost	MTN_{AE}	\$200
GSHP maintenance cost	MTN_{GSHP}	\$200/year
ASHP maintenance cost	MTN_{ASHP}	\$580/year

9.2 Overall TRNSYS Model Validation

In Section 9.1, various individual model components have been validated (e.g. heat pump, BHE) or are directly based on experimental measurements at the Varna Site (e.g. shelter). In this section, an overall validation of the TRNSYS model (excluding BHEs, DC and AE) is performed using data collected at the Varna Site during six weeks of high-frequency logging (1 min. interval) from April 1 to May 13, 2015. During this time period, the shelter setpoint temperature stayed constant, there were both cold and warm days, and no equipment maintenance or testing occurred. The shelter and ambient temperature measured at the Varna Site are shown in Figure 9.5.

The TRNSYS model simulation incorporates the actual ambient temperature, heat pump inlet temperature, and ACDC Plant heat generation measured at the site. The circulating fluid supply temperature is not simulated for but directly based on the Varna Site measurements because the BHE model does not include groundwater advection and due to the lack of data on the local groundwater flow. The TRNSYS model controller alternates between one heat pump operating in part load and two heat pumps in full load (as the Varna Site controller operates), to keep the shelter temperature between 25°C (77°F)

Table 9.2 – Overall TRNSYS model validation results. Validation is based on six weeks of high-frequency data (1 min. interval) collected at the Varna Site from April 1st to May 13th, 2015. A flow rate 4, 5, and 6 GPM corresponds to 0.26, 0.32, and 0.38 l/s. HP refers to heat pump. A heat pump power factor of 0.9 is assumed for calculating the electricity consumption.

Metric	Varna Site (Measured)	TRNSYS Model 4.0 GPM	TRNSYS Model 5.0 GPM	TRNSYS Model 6.0 GPM
HP Electricity Consumption	2010 kWh	2020 kWh	1913 kWh	1850 kWh
HP Part Load Running Time	325 h	380 h	399 h	409 h
HP Full Load Running Time	1321 h	1272 h	1235 h	1214 h

and 26.7°C (80°F). Due to flow meter technical issues, no accurate flow measurements have been obtained. However, approximate flow rates have been determined based on the temperature measurements as well as independent measurements with an acoustic clamp-on flow meter. The average flow rate per heat pump running is believed to be between 4.0 and 7.0 GPM (0.26 and 0.44 l/s) and therefore TRNSYS simulations for a range of flow rates have been performed.

The Varna Site measurements and TRNSYS model simulation results are provided in Table 9.2. The data collected on heat pump voltage, current, and running time are reliable and therefore the comparison with the simulations is based on electricity consumption and running time. In addition, the electricity consumption drives the TCO and is therefore arguably the most important parameter to validate. The results shows that the TRNSYS model assuming a flow rate between 4.0 and 6.0 GPM (0.26 and 0.38 l/s) per heat pump running, matches approximately the electricity consumption and heat pump running time data.

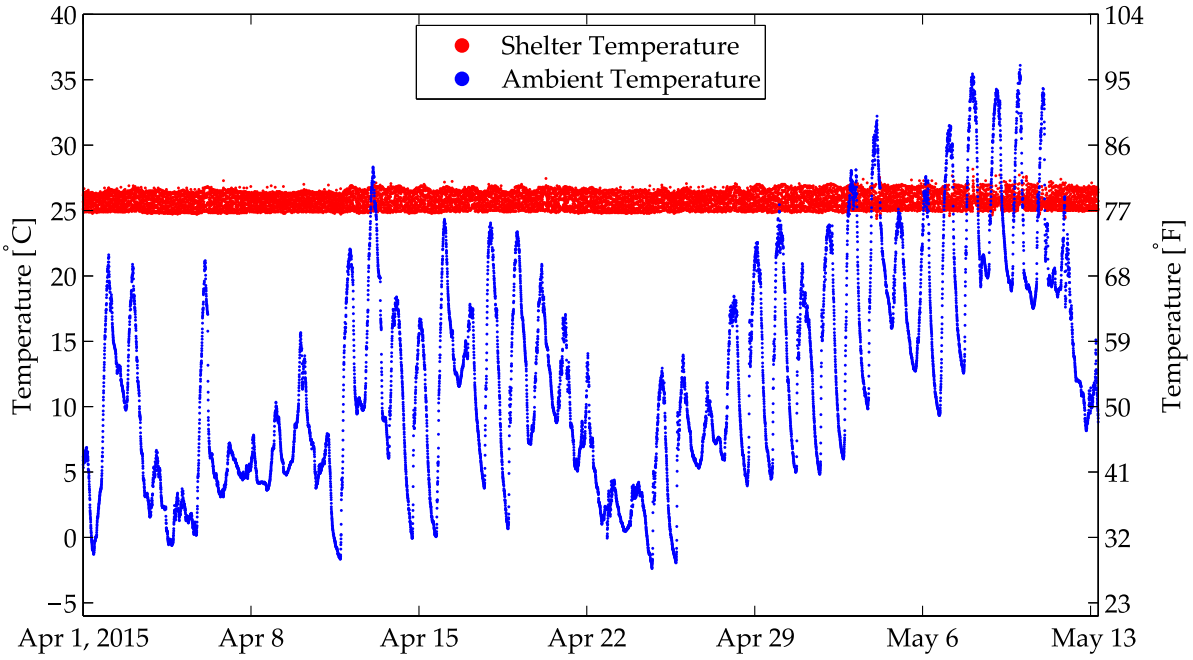

Figure 9.5 – Varna Site shelter and ambient temperature measured during April and May 2015. Plotting interval is 5 minutes.

9.3 System Analysis

9.3.1 Overview of Cases Studied

Various GSHP and ASHP configurations have been investigated. Five of them, believed to be the most relevant, are presented in detail below. Their base case parameters are summarized in Table 9.3. All cases consider the Varna shelter as described in Table 8.1, the weather based on the Elmira TMY3 climatic data, and 11.5 kW_{th} of heat generation in the base case scenario. The time step in the TRNSYS simulations is 10 minutes for the GSHP cases, and 1 minute for the ASHP cases. A shorter time step is required in the ASHP cases because the shelter cools down and heats up faster. The reason for this is that the ASHP cooling (Equation (9.4)) fluctuates between 0 and up to 20 to 30 kW_{th} while the GHSP units working together provide more moderate cooling around 11 kW_{th}.

Table 9.3 – TRNSYS base case parameters. BHE field data refers to properties of circulating fluid, pipe, grout and BHE inner geometry. Number and depth of BHEs is determined on a case by case to minimize the TCO.

Parameter	Case 1: GSHP	Case 2: GSHP + AE	Case 3: GSHP + DC	Case 4: ASHP	Case 5: ASHP + AE
Weather Data	Elmira Corning Regional Airport TMY3				
Shelter Data	as in Table 8.1				
Financial Data	as in Table 9.1				
Heat Generation	11.5 kW_{th}				
AE Setpoint	N/A	10°C	N/A	N/A	10°C
DC Setpoint	N/A	N/A	15°C	N/A	N/A
BHE Field Data	as in Table 8.2			N/A	N/A
BHE Spacing	10 m			N/A	N/A
Flow Rate per HP on	3.5 GPM			N/A	N/A
Reserv. Therm. Diff.	10^{-6} m^2/s			N/A	N/A
Reserv. Therm. Cond.	2.0 W/(m·K)			N/A	N/A

Case 1: GSHP only

The first case is the "GSHP only" case (case (a) in Figure 7.3) in which all the cooling is provided using two ClimateMaster TT 026 geothermal heat pump units (Table 8.1). Since the heat pumps operate most efficiently in first stage, the controller is set to run one heat pump in first stage and the second heat pump alternating between first and second stage, keeping the shelter temperature between 77°F (25°C) and 80°F (26.7°C). If the cooling requirements are not met on warm summer days, both heat pumps run in second stage. If too much cooling is provided during cold winter days, the second heat pump alternates between off and first stage, while the first heat pump runs permanently in first stage.

The dominant rock type in the geothermal reservoir at the Varna Site is shale with expected thermal conductivities around 1 W/(m·K) (see Table 8.4 and Section 8.3.3). Groundwater flow is present which likely explains the high effective ground thermal conductivity of 4 W/(m·K) obtained using a TRT at the site. The effective thermal conductivity occurring at any moment in the reservoir can be expected between these two values and therefore the BHE model assumes a conduction-only reservoir with thermal

conductivity of 2 W/(m·K) in the base case scenario. Different effective reservoir thermal conductivities are investigated using a sensitivity analysis. The BHE field consists of three 1-U BHE in parallel, each with depth of 150 m, which minimizes the TCO for this case. Pipe dimensions and material properties, as well as grout and circulating fluid properties are the same as at the Varna site (see Table 8.2). The flow rate is set at 3.5 GPM (0.22 l/s) per heat pump running, both for first or second stage operation, slightly lower than at the Varna site in order to lower the pump power. The eventual pump power requirements are case-specific and difficult to calculate exactly and therefore conservative values are assumed: 3.5 GPM (0.22 l/s) requires 0.05 kW and 7.0 GPM (0.44 l/s) requires 0.2 kW.

Case 2: GSHP + AE

The second case is similar to the first case but with an AE providing the cooling when the ambient temperature drops below 10°C (50°F) (case (b) in Figure 7.3). The VFD of the AE is controlled in order to provide cooling around 11 kW_{th}. The TCO is minimized using only two BHE's in parallel, each with depth of 150 m. When the AE is activated, the heat pumps and circulation pump are turned off.

Case 3: GSHP + DC

The third case is similar to the first case but a DC supplies supplemental heat rejection (case (d) in Figure 7.3). When the ambient temperature drops below 15°C (59°F), the circulating fluid leaving the heat pump units is cooled by the DC only and bypasses the BHE field. The TCO is minimized using a BHE field consisting of two boreholes with 130 m depth each. Other configurations have been investigated including the DC in series with the BHE field. However, those configurations resulted in higher TCOs than the configuration selected here.

Following the rules of thumb presented in Section 7.3 on design of supplemental heat rejection for hybrid geothermal heat pump systems, the DC in the base case does not provide annual net reservoir heat balance but covers roughly 65% of the cooling load. Other setpoints have been analyzed but 15°C is believed to be a good compromise: with a too low setpoint, the system does not taking full advantage of the efficient DC cooling capability with cold ambient air; a too high setpoint means lower cooling returns for the electricity invested.

Case 4: ASHP only

In the "ASHP only" case, all cooling is provided using an industry-standard wall-mounted Marvair HVAC unit. This option has the lowest initial investment cost but a high electricity consumption over the lifetime of the system.

Case 5: ASHP + AE

The fifth case is similar to the fourth case but with an AE providing cooling when the ambient temperature drops below 10°C (50°F). Again, the VFD of the AE is set to provide AE cooling fluctuating around 11 kW_{th}, as in Case 2.

9.3.2 Base Case Simulation Results and Discussion

The simulation results for the five cases are presented in Table 9.4. Provided are the TCO in $1,000, the electricity consumption in MWh_e, the CO_2 emissions in million metric tons, the average heat pump COP, and the BHE configuration that minimizes the TCO for the case considered. The electricity consumption and CO_2 emissions are calculated over the

Table 9.4 – TRNSYS base case simulation results. Lifetime electricity consumption and CO_2 emissions do not account for energy consumption and emissions during construction and installation of the system.

Case	TCO ($1,000)	Electricity Consumption (MWh_e)	CO_2 Emissions (million metric tons)	Average HP COP [-]	BHE Configuration
GSHP	87.6	460	85.6	4.21	3 x 150 m
GSHP + AE	59.9	222	41.3	4.27	2 x 150 m
GSHP + DC	75.7	421	78.2	5.47	2 x 130 m
ASHP	78.7	589	109.6	3.28	N/A
ASHP + AE	54.0	314	58.4	3.02	N/A

lifetime of the system but do not account for the installation. The average heat pump COP is calculated as the lifetime average heat pump cooling divided by the lifetime average heat pump power and circulation pump power (if applicable).

Case 5 (ASHP + AE) has the lowest TCO for the parameters assumed in the base case scenario, followed by Case 2 (GSHP + AE). The systems with AE perform well because the cold Upstate New York weather allows the use of an AE, which provides cooling very efficiently, for a significant amount of time throughout the year. If the use of an AE is undesirable for reasons highlighted in the Section 8.2 such as increased maintenance, the the GSHP + DC has the lowest TCO of the three remaining cases. Advantageous for ASHP-based systems is the low upfront capital costs, moderate ambient temperatures which result in reasonable COP's, no temperature built-up which negatively impacts the performance of GSHP systems over time, and no additional power requirements, e.g. for circulation pumps as with GSHP-based systems.

If the goal is to minimize energy consumption and CO_2 emissions, then GSHP-based systems perform best. While the cases presented in Table 9.4 have been optimized for minimum TCO, even lower amounts of electricity consumption and CO_2 emissions can be obtained by increasing the total BHE depth, which only slightly increases the TCO. This is further discussed in Section 9.3.3 where the impact of several parameters on the

performance metrics is studied with a sensitivity analysis.

The results presented in this and the next section should not be interpreted as optimal or final results but rather as representative numbers given the whole list of parameters in Table 9.3. Parameters not studied in detail but believed to only have a minor role are the inner BHE geometry and the heat pump manufacturer. Different AE and DC setpoints have been explored but not necessarily optimized for. Different control strategies of the DC, e.g. operating the DC at variable speeds depending on the ambient weather and fluid temperature, are available but are not analyzed here. The heat exchange between the shelter and ground, and the shelter and attached diesel generator room has been neglected. Nevertheless, based on first order calculations, this simplification is expected to only have a small impact. The weather is expected to have a major impact on the system performance, as already highlighted in Section 9.3. However, the study of its impact is part of the ongoing nationwide analysis in our group and is not further discussed in this work. Further, the economic results do not account for any subsidies, tax incentives or a potential carbon tax. Also leasing costs for land for the BHE field, which likely increase with number of BHE, are not included.

Where possible, correlations and models that describe the various system components have been validated or are directly based on measurements at the Varna Site, including for the heat pumps, shelter, circulation pump, BHEs, controller, and ACDC plant. However, inherent TRNSYS model uncertainty persists due to uncertainties with measurements and manufacturer's datasheet correlations, varying operating conditions, and model simplifications. In addition, the performance of some components, e.g. ASHP and DC, is solely based on the manufacturer's datasheet and has not been independently verified.

The circulation pump power, up to 0.7 kW_e at the Varna Site, has a significant impact on the overall TCO and performance of the system. Lowering the pump power can be achieved by lowering the flow rates (which has been done for the five TRNSYS cases) but

this also impacts the heat pump performance. For the same heat pump inlet temperature, a lower flow rate results in a slight decrease in heat pump COP. However, a lower flow rate typically leads to lower inlet temperatures which increases the performance and therefore the overall impact cannot directly be derived. However, much lower flow rates are discouraged because they would fall outside the recommended range based on the manufacturers datasheet (minimum 2.3 GPM (0.15 l/s) in part load and 3 GPM (0.19 l/s) in full load for one heat pump). Further, in the TRNSYS simulation, the circulation pump power correlation is kept the same for each BHE configuration, although a lower total BHE depth will decrease the pump power. Another way to decrease the pump power is to utilize a circulating fluid with lower viscosity. However, a low fluid freezing point is required for Case 3 (GSHP + DC) and desired for Case 2 (GSHP + AE), limiting the fluid options. Maybe in Case 1 pure water can be utilized since the heat pump mode is cooling only but then the system may not be shut down, even temporarily, during the winter to prevent any fluid freezing. All together, it is believed a small decrease in TCO, maybe up to 5 or 10%, for the GSHP cases may be obtained in case of circulation flow rate and pump optimization, but this is not further investigated here.

Different system configurations are possible besides the five cases presented in this chapter. One case is the GSHP + AE + DC as investigated in one configuration by Beckers et al. (2014). Due to the additional operational complexity and cost, this case is not further analyzed here. Another system is the GSHP + DC but with the DC in series with the BHE field. Based on a first analysis with the TRNSYS model, this configuration did not turn out to perform better than the configuration in Case 3. Moreover, other technologies are available, e.g. dual stage ASHP, GSHP with horizontal heat exchangers, or direct exchange GSHP, but they are not investigated here.

9.3.3 Sensitivity Analysis

A sensitivity analysis has been performed to address the uncertainty of several of the model parameters, as well as to assess the performance of each system configuration for different shelter operational and financial conditions. Specifically, the impact of total BHE depth, shelter heat generation, reservoir thermal conductivity, electricity rate, drilling costs, and net discount rate on TCO, electricity consumption and CO_2 emissions has been investigated and the results are presented in this section.

Total BHE Depth Sensitivity

For each case involving a GSHP system (Cases 1, 2 and 3), the TCO has been minimized with respect to the total BHE depth. Increasing the total BHE depth, either by increasing the number of BHEs or increasing the depth of each individual BHE, generally decreases the average circulating fluid supply temperature, which increases the average COP of the heat pumps and therefore lowers the lifetime electricity consumption. For example, Figure 9.6 shows the lifetime average heat pump COP and electricity consumption as a function of total BHE depth for Case 1 (GSHP only) in the base case scenario. The total number of boreholes is three, four and six if the total BHE depth is in the range 360 to 450 m, 480 to 600 m, and 630 to 720 m, respectively. The non-monotonic behavior can occur when the total BHE depth is adjusted by changing simultaneously the number of boreholes and the individual BHE depth, for example, 600 m = 4 x 150 m and 630 m = 6 x 105 m. Figure 9.6 illustrates that the system performance depends considerably on the total BHE depth, which was also highlighted in other works, for example (Casasso and Sethi, 2014) and (Esen and Turgut, 2015).

Although the operational electricity costs decrease with increasing total BHE depth, the capital investment costs increase due to higher drilling costs. The effect of the total

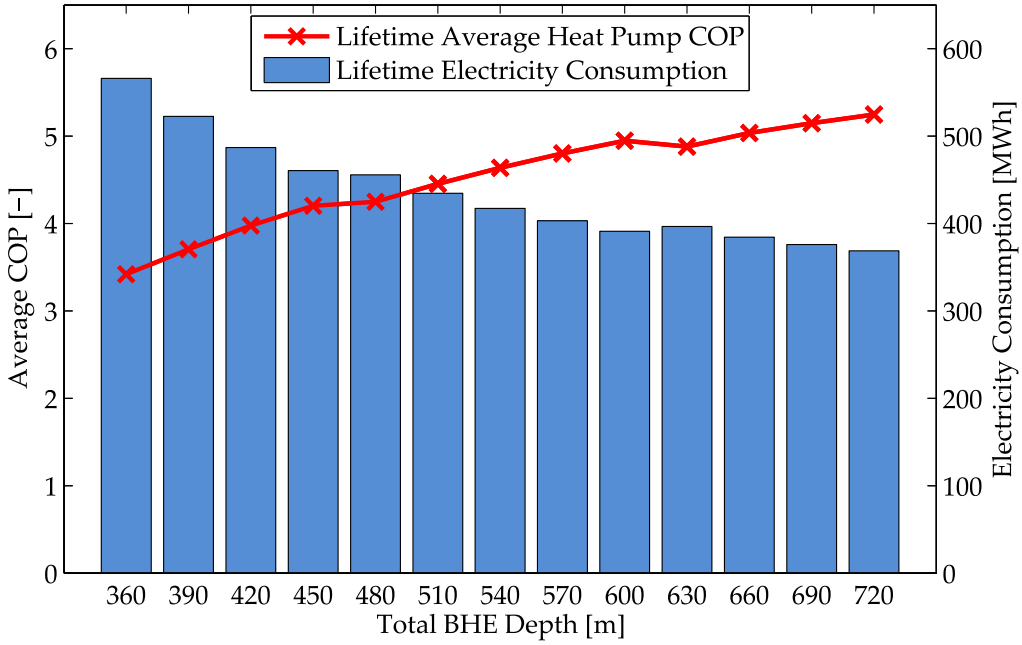

Figure 9.6 – Effect of total BHE depth on lifetime average heat pump COP (red crosses; left axis) and lifetime electricity consumption (blue bars; right axis) for Case 1 (GSHP only) in the base case scenario. The total number of boreholes is three, four and six for a total BHE depth of 360 to 450 m, 480 to 600 m, and 630 to 720 m.

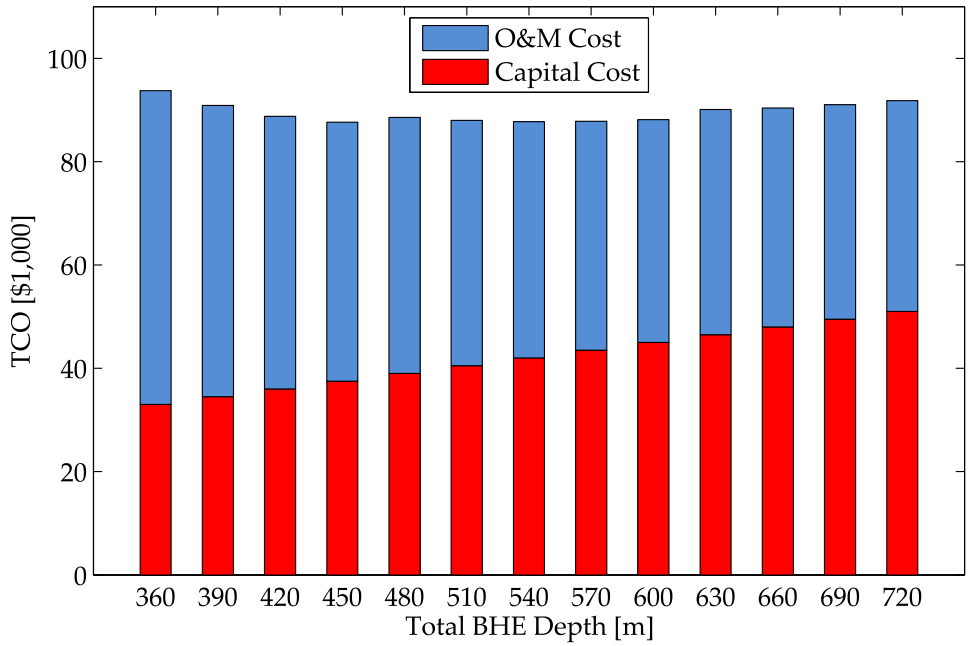

Figure 9.7 – Effect of total BHE depth on TCO for Case 1 (GSHP only) in base case scenario. TCO is broken down into capital cost (bottom red bars) and O&M cost (top blue bars). The O&M cost includes the costs for electricity consumption and maintenance (see also Table 9.1). The total number of boreholes is three, four and six for a total BHE depth of 360 to 450 m, 480 to 600 m, and 630 to 720 m.

BHE depth on the TCO, consisting of both the capital and discounted lifetime O&M costs, is shown in Figure 9.7 for Case 1 in the base case scenario. This figure shows that the TCO is weakly dependent on the total BHE depth. The minimum TCO was $87,600 for a total BHE depth of 450 m (3 x 150 m). For 540 m (4 x 135 m), the TCO is very close with $87,800, and the lifetime electricity consumption is only 417 MWh_e (9% decrease). Full simulation results are provided in Table C.1 in Appendix C.

The minor effect of the total BHE on the TCO, and considerable effect on the energy consumption around the minimum was found for each case studied involving a GSHP system. Therefore, if the goal is to decrease the energy consumption, one could slightly increase the total BHE depth from the numbers reported in Table 9.4 and in the tables in Appendix C, which all report BHE depths that minimize the TCO. Nevertheless, it is not recommended to increase the individual BHE depth beyond 150 m, because the effect of the geothermal gradient will start to influence performance, and there is a likely increase in risks in drilling and completing the wells. Equally important is that drilling permits are required in the U.S. for depths greater than 500 ft (152.4 m).

Shelter Heat Generation Sensitivity

Technology and size of telecommunication equipment can differ among shelters and even for the same shelter over time, and therefore different amounts of heat generated can be expected. Figure 9.8 shows the dependence of the TCO on the shelter heat generation for the different cases in Section 9.3.1, keeping all other parameters the same. The heat generation of 11.5 kW_{th} in the base case scenario is believed to be on the high end side and therefore smaller amounts of heat generation are considered. Lowering the heat generation lowers the TCO across the board for all five cases, and decreases the spread between the highest and lowest TCO (Case 1 and Case 5). Full simulation results are provided in Table C.2 in Appendix C.

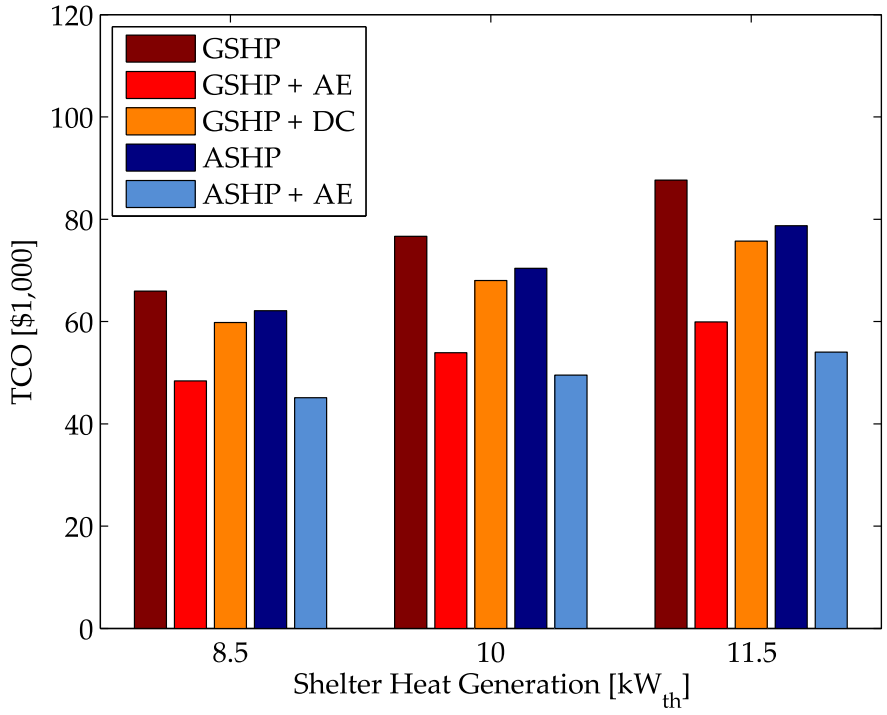

Figure 9.8 – Effect of shelter heat generation on TCO for Cases 1 to 5. All other parameters are the same as in the base case scenario.

Reservoir Thermal Conductivity Sensitivity

In the base case scenario, the effective reservoir thermal conductivity was set at 2 W/(m·K) as a compromise between the high value of 4 W/(m·K) obtained using a TRT and a low value of 1 W/(m·K), experimentally measured and often reported in literature as thermal conductivity for dry shale, the dominant rock type in the reservoir. The effect of a different thermal conductivity on the TCO for Cases 1 to 3 is shown in Figure 9.9, keeping all other parameters the same. The TCO for Cases 4 and 5 are independent of the reservoir thermal conductivity and are solely included in the plot for easy comparison. As expected, a higher thermal conductivity allows for a lower total BHE depth and decreases the TCO of the system. Full simulation results are provided in Table C.3 in Appendix C.

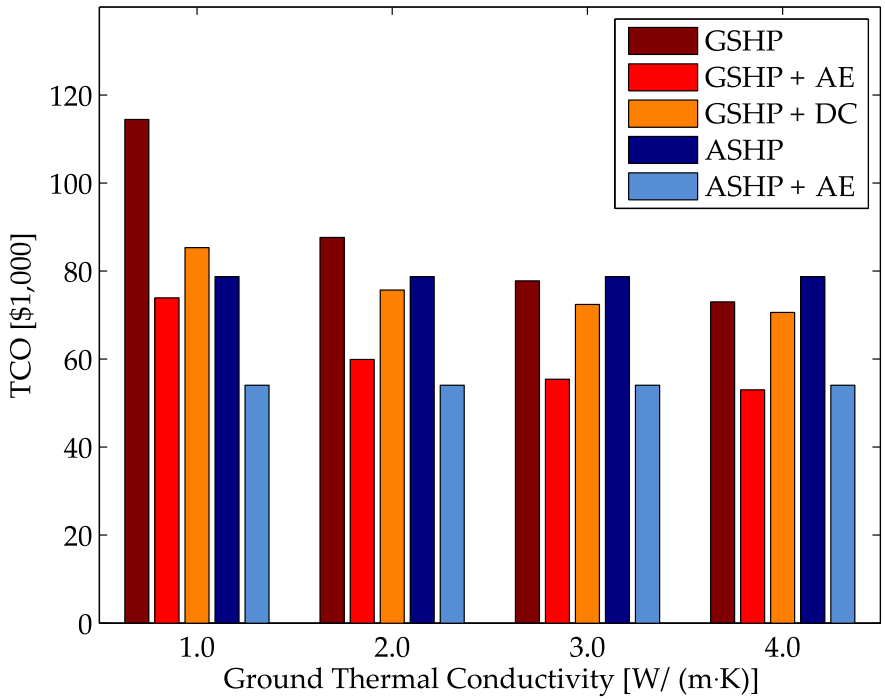

Figure 9.9 – Effect of reservoir thermal conductivity on TCO for Cases 1 to 3. TCO for Cases 4 and 5 are independent of reservoir thermal conductivity and are included for comparison. All other parameters are the same as in the base case scenario.

Electricity Rate Sensitivity

The electricity rate of 14 ¢/kWh$_e$ in the base case scenario is relatively high in comparison with electricity rates in other states, but might be low in comparison with future electricity rates. Figure 9.10 shows the impact of the electricity rate on the TCO for all five cases studied. As expected, higher electricity rates penalize systems with higher electricity consumption, e.g. Case 4 (ASHP). Full simulation results are provided in Table C.4 in Appendix C.

Net Discount Rate Sensitivity

A net discount rate of 3% in the base case scenario reflecting a long-term horizon might be a too low discount rate for the fast-changing telecommunication industry. Figure 9.11

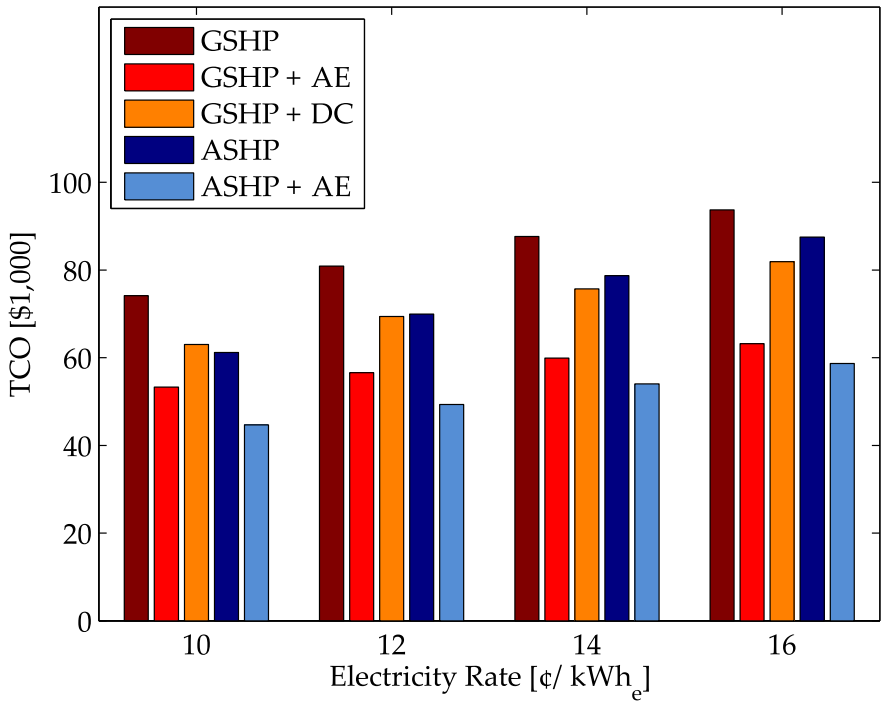

Figure 9.10 – Effect of electricity rate on TCO for Cases 1 to 5. All other parameters are the same as in the base case scenario.

shows the impact of the discount rate on the TCO for all five case studied. As expected, a higher discount rate lowers the TCO for all cases since future expenses are valued less today. For the other assumptions used, systems with lower upfront capital costs (ASHP-based systems) are favored with increasing discount rate. Full simulation results are provided in Table C.5 in Appendix C.

Drilling Cost Sensitivity

A drilling cost of 50 $/m used for the Varna Site might be high in comparison with drilling costs observed in other regions in the U.S. (Battocletti and Glassley, 2013), but too low in the case trouble arises during the drilling process. Figure 9.12 shows the effect of the drilling costs on the TCO for Cases 1 to 3. Cases 4 and 5 are included for easy comparison. As expected, higher drilling costs increase the TCO of the GSHP systems and also shifts

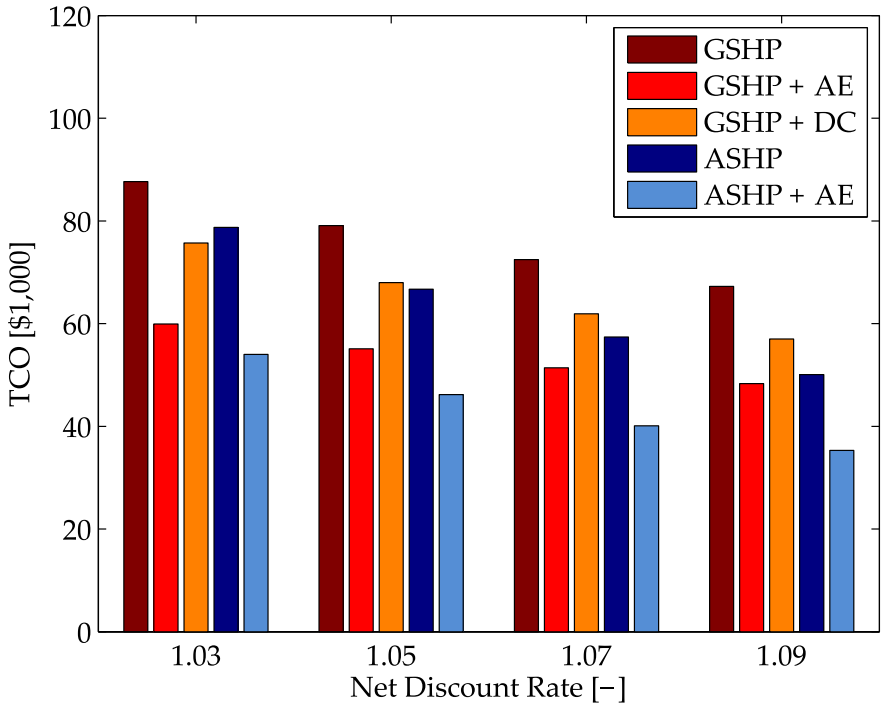

Figure 9.11 – Effect of net discount rate on TCO for Cases 1 to 5. All other parameters are the same as in the base case scenario.

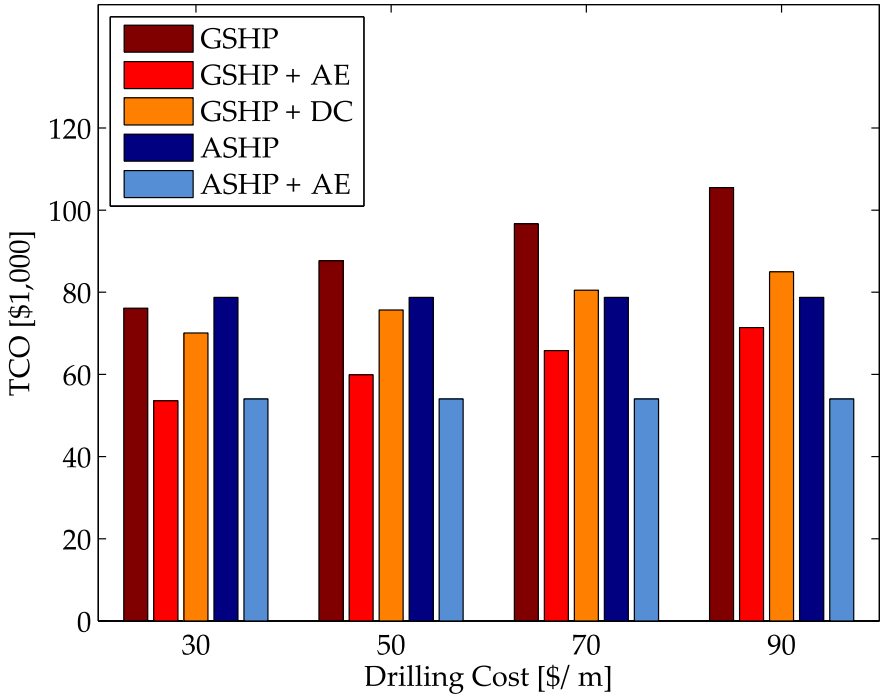

Figure 9.12 – Effect of drilling cost on TCO for Cases 1 to 3. TCO for Cases 4 and 5 are independent of drilling cost and are included for comparison. All other parameters are the same as in the base case scenario.

the optimum towards shallower total BHE depths. Full simulation results are provided in Table C.6 in Appendix C.

References

Battocletti, E. C. and Glassley, W. E. (2013). Measuring the Costs and Benefits of Nationwide Geothermal Heat Pump Deployment. Report prepared for U.S. Department of Energy, Geothermal Technologies Program under Award Number DE-EE0002747.

Beckers, K. F., Yavuzturk, C. C., and Tester, J. W. (2014). *Techno-Economic Modeling and Monitoring of Hybrid Ground-Source Heat Pump System with Borehole Heat Exchangers for Cooling-Dominated Cellular Tower Application*. 11th IEA Heat Pump Conference, Montreal, Canada.

Casasso, A. and Sethi, R. (2014). Sensitivity analysis on the performance of a ground source heat pump equipped with a double u-pipe borehole heat exchanger. *Energy Procedia*, 59 : 301–308.

EPA (2015). eGRID2012. U.S. Environmental Protection Agency, Washington, DC, United States.

Esen, H. and Turgut, E. (2015). Optimization of operating parameters of a ground coupled heat pump system by taguchi method. *Energy and Buildings*, 107 : 329–334.

MathWorks (2012). *MATLAB Release 2012a*, The Mathworks, Inc., Natick, Massachusetts, United States.

Peng, W. W. (2008). *Fundamentals of Turbomachinery*. John Wiley & Sons.

SEL (2014a). *TRNSYS 17 (TRaNsient SYstems Simulation program)*. Univer-

sity of Wisconsin - Madison, Solar Energy Laboratory (SEL). Available at http://sel.me.wisc.edu/trnsys/.

SEL (2014b). *TRNSYS 17 (TRaNsient SYstems Simulation program) Documentation - Volume 4 Mathematical Reference* . University of Wisconsin - Madison, Solar Energy Laboratory (SEL). Available at http://sel.me.wisc.edu/trnsys/.

Wilcox, S. and Marion, W. (2008). *Users Manual for TMY3 Data Sets*, Technical Report NREL/TP-581-43156. National Renewable Energy Laboratory (NREL), Golden, Colorado, United States.

CHAPTER 10

TECHNO-ECONOMIC ANALYSIS OF HYBRID GEOTHERMAL HEAT PUMP SYSTEMS FOR COOLING-DOMINATED APPLICATIONS: KEY CONCLUSIONS

As part of an ongoing study between Cornell and Verizon Wireless to investigate the performance of hybrid geothermal heat pump (GSHP) systems for cooling of cellular tower shelters, a TRNSYS model simulating GSHP and air-source heat pump (ASHP) systems has been developed. The model has been successfully tested with data from a full-scale hybrid GSHP system in Varna, NY, and has been applied to test various systems configurations under different parameters. For conditions at the Varna Site, in particular Upstate New York weather, shelter configuration and requirements, borehole heat exchanger (BHE) field and fluid properties, and for financial conditions assumed in Chapter 9 not considering any incentives, subsidies or taxes, the following conclusions can be drawn, specifically for conditions at the Varna Site:

- An ASHP combined with an air-economizer (AE) has the lowest TCO, followed by a GSHP with AE. If an AE is to be omitted, a GSHP + DC is the following option with lowest total cost of ownership (TCO). A GSHP only system has the highest TCO illustrating benefits of hybridizing a GSHP system.
- ASHP systems obtain low TCO because of: (1) low upfront capital costs for equipment and design, (2) no deteriorating performance due to reservoir temperature increase over time as with GSHP systems, and (3) good overall performance because of moderate ambient temperatures at the Varna Site and no auxiliary power requirements such as circulation pumps with GSHP systems.
- If the goal is to minimize energy consumption and CO_2 emissions, GSHP-based cases perform best. Increasing the total BHE depth can significantly increase the

energetic performance and lower the energy consumption, while only slightly increasing the TCO.

- Favoring GSHP-based systems are high ground thermal conductivities, low drilling costs, low discount rates, high electricity rates, and low set-point temperatures.

The TRNSYS model developed is being applied to other regions in the country as part of the ongoing nationwide analysis of utilizing hybrid GSHP systems for cooling of cellular tower shelters. It is expected that the local weather and average ground temperatures have a major impact on the performance of each configuration studied.

Not every possible configuration has been analyzed, not all cooling or heat pump technologies have been considered, and of the systems studied, not a full rigorous optimization has been performed since there are simply too many degrees of freedom. Nevertheless, it is believed the results are representative for the specific conditions used for the cases investigated, emphasizing that hybrid GSHP systems are a means of saving energy and CO_2 emissions, but not necessarily for saving money under these conditions. While the focus has been on cooling of cellular tower shelters, the results are expected to be transferable to other cooling-dominated applications, e.g. cooling of walk-in fridges and freezers in the food and beverages industry.

Part III

Slender-Body Theory for Transient Heat Conduction

CHAPTER 11

INTRODUCTION TO SLENDER-BODY THEORY

An earlier publication (Beckers et al., 2015) covers the material presented in Part III.

Simulating and predicting the heat exchange of slender bodies undergoing transient heat transfer in conductive media is of great interest and importance in the design and analysis of several applications. Examples are (1) wellbore heat transmission in oil, gas or geothermal wells, (2) reservoir heat transfer in ground-source heat pumps or underground thermal energy storage systems using slinky-coil, horizontal pipe or borehole heat exchangers, and (3) cooling or heating elements in concrete foundations and industrial processes.

Various heat transfer solution methods are available and in some cases sufficient, depending on the complexity and compactness of the slender body heat transfer problem. Simple geometries, e.g. a straight finite cylinder, can be handled with analytical methods such as the Laplace transform, separation of variables and Bessel functions, Green's functions and perturbation methods (Carslaw and Jaeger, 1959; Arpaci, 1966; Myers, 1971; Aziz and Na, 1984; Beck et al., 1992; Ozisik, 1993). More complex but compact geometries, meaning the slender body is e.g. irregularly curved but closely packed together, can be simulated with finite element (FEM) or finite volume methods (Patankar, 1980; Minkowycz et al., 2006). Nevertheless, using these numerical methods for non-compact geometries typically requires long computational times in order to achieve accurate results. In this paper, we present a hybrid method that efficiently handles these type of geometries. The method uses *slender-body theory*, an asymptotic analysis to allow for thin non-compact geometries, in combination with a numerical implementation to allow these geometries to have complex shapes. Hereby, one can reduce from discretizing a three-dimensional domain to discretizing over a one-dimensional axis of the slender body. Es-

pecially for longer time-scales, when the domain needed to be studied becomes $O(L_t^3)$ with L_t the total slender body length, much shorter computational times can be obtained and much less computer memory would be needed. However, without smart implementation strategies, the computational time is $O(N_t \cdot N_E^3 + N_t^2 \cdot N_E^2)$, while for FEM only $O(N_E^3 + N_t \cdot N_E^2)$, with N_E and N_t the number of elements and time steps, respectively. Also, the method requires a linear problem so no temperature dependence of the thermal conductivity is allowed. Further, simple medium geometries are desired so that the Green's function is either unbounded or can be readily found, e.g. with method of images.

Slender-body theory (SBT) in general refers to approximating the equations or underlying physics in a specific science field when dealing with bodies that are long in one dimension and short in the other two. These approximations are typically achieved by applying matched asymptotic expansions of inner and outer solutions, although sometimes only the inner or outer solution is considered. It originated and is most commonly used in the field of fluid dynamics. Munk (1924) was the first to apply slender-body approximations in order to calculate the aerodynamic forces on airship hulls. He treated the airship as an *elongated body of revolution* in a potential flow and argued that when calculating the velocity potential and air forces, different longitudinal cross-sections can be considered independent from each other. In 1927, von Kármán applied a different SBT approach in solving the same problem using a distribution of monopoles and dipoles on the axis of symmetry (von Kármán, 1927). Other examples of potential flow problems simplified with SBT are the study of wings (Jones, 1946), not-so-slender wings (Adams and Sears, 1953), ship hydrodynamics (Newman, 1964, 1970), and fish locomotion (Lighthill, 1960, 1971). Slender bodies in Stokes flow have been widely studied using SBT methods as well. Examples are the general works by Cox (1970; 1971), Keller and Rubinow (1976), Batchelor (1970), and Johnson (1980), and the studies on flagellar hydrodynamics (Johnson and Brokaw, 1979), fiber particle suspensions (Mackaplow and Shaqfeh, 1996, 1998), and motion of a slender torus Johnson and Wu (1979). Other applications of SBT can be found

in the fields of acoustic scattering (Junger and Feit, 1972; Ye et al., 1997), electromagnetic scattering (Geer, 1980), charged colloids (Chen and Koch, 1996), and steady-state heat transfer. A steady-state heat transfer problem often approximated using SBT is the heat transport in composites with slender inclusions (Rocha and Acrivos, 1973a,b; Chen and Acrivos, 1976; Acrivos and Shaqfeh, 1988; Shaqfeh, 1988; Fredrickson and Shaqfeh, 1989; Mackaplow et al., 1994), e.g. to derive the effective thermal conductivity. To the best of our knowledge, SBT has never been applied to transient heat conduction.

In Chapter 12, the slender body geometry, constraints and heat transfer problem are formally defined. A theoretical framework for solving the problem using Green's functions and matched asymptotic expansions is derived and the result is physically interpreted. Further, model extensions are discussed to treat various time-scales, medium properties and initial and boundary conditions. In Chapter 13, the theoretical basis is translated into a numerical method and strategies are provided for efficient implementation in order to obtain high speed, accuracy and versatility. Finally, these strengths are demonstrated in Chapter 14 using two case-studies in which the presented SBT numerical model is compared with a finite element model. The first case-study is the simulation of the heat exchange of two parallel finite cylinders at constant temperature; the second case-study is the simulation of one loop of a slinky-coil heat exchanger.

References

Acrivos, A. and Shaqfeh, E. (1988). The effective thermal conductivity and elongational viscosity of a nondilute suspension of aligned slender rods. *Physics of Fluids (1958-1988)*, 31 (7): 1841–1844.

Adams, M. C. and Sears, W. R. (1953). Slender-Body Theory-Review and Extension. *Journal of the Aeronautical Sciences (Institute of the Aeronautical Sciences)*, 20 (2): 85–98.

Arpaci, V. S. (1966). *Conduction heat transfer*. Addison-Wesley Pub. Co., Reading, Mass.

Aziz, A. and Na, T. Y. (1984). *Perturbation methods in heat transfer*. Hemisphere Publishing Corporation, Washington DC.

Batchelor, G. K. (1970). Slender-body theory for particles of arbitrary cross-section in stokes flow. *Journal of Fluid Mechanics*, 44 (03): 419–440.

Beck, J. V., Cole, K. D., Haji-Sheikh, A., and Litkouhi, B. (1992). *Heat conduction using Green's functions*. Hemisphere Publishing Corporation, Washington DC.

Beckers, K. F., Koch, D. L., and Tester, J. W. (2015). Slender-body theory for transient heat conduction: theoretical basis, numerical implementation and case studies. *Proceedings of the Royal Society of London A: Mathematical, Physical and Engineering Sciences*, 471 (20150494).

Carslaw, H. S. and Jaeger, J. C. (1959). *Conduction of heat in solids*. Clarendon Press, Oxford.

Chen, H. S. and Acrivos, A. (1976). On the effective thermal conductivity of dilute suspensions containing highly conducting slender inclusions. *Proceedings of the Royal Society of London A: Mathematical, Physical and Engineering Sciences*, 349 (1657): 261–276.

Chen, S. B. and Koch, D. L. (1996). Electrophoresis and sedimentation of charged fibers. *Journal of colloid and interface science*, 180 (2): 466–477.

Cox, R. G. (1970). The motion of long slender bodies in a viscous fluid. Part 1. General theory. *Journal of Fluid mechanics*, 44 (04): 791–810.

Cox, R. G. (1971). The motion of long slender bodies in a viscous fluid. Part 2. Shear flow. *Journal of Fluid Mechanics*, 45 (04): 625–657.

Fredrickson, G. H. and Shaqfeh, E. S. (1989). Heat and mass transport in composites of aligned slender fibers. *Physics of Fluids A: Fluid Dynamics (1989-1993)*, 1 (1): 3–20.

Geer, J. (1980). Electromagnetic scattering by a slender body of revolution: axially incident plane wave. *SIAM Journal on Applied Mathematics*, 38 (1): 93–102.

Johnson, R. E. and Brokaw, C. J. (1979). Flagellar hydrodynamics. A comparison between resistive-force theory and slender-body theory. *Biophysical journal*, 25 (1): 113–127.

Johnson, R. E. and Wu, T. Y. (1979). Hydromechanics of low-Reynolds-number flow. Part 5. Motion of a slender torus. *Journal of Fluid Mechanics*, 95 (02): 263–277.

Johnson, R. E. (1980). An improved slender-body theory for stokes flow. *Journal of Fluid Mechanics*, 99 (02): 411–431.

Jones, R. T. (1946). *Properties of low-aspect-ratio pointed wings at speeds below and above the speed of sound*. National Advisory Committee for Aeronautics, Washington DC.

Junger, M. C. and Feit, D. (1972). *Sound, structures, and their interaction*. MIT Press.

Keller, J. B. and Rubinow, S. I. (1976). Slender-body theory for slow viscous flow. *Journal of Fluid Mechanics*, 75 (04): 705–714.

Lighthill, M. J. (1960). Note on the swimming of slender fish. *Journal of fluid Mechanics*, 9 (02): 305–317.

Lighthill, M. J. (1971). Large-amplitude elongated-body theory of fish locomotion. *Proceedings of the Royal Society of London B: Biological Sciences*, 179 (1055): 125–138.

Mackaplow, M. B., Shaqfeh, E. S. G., and Schiek, R. L. (1994). A numerical study of heat and mass transport in fibre suspensions. *Proceedings of the Royal Society of London A: Mathematical, Physical and Engineering Sciences*, 447 (1929): 77–110.

Mackaplow, M. B. and Shaqfeh, E. S. G. (1996). A numerical study of the rheological properties of suspensions of rigid, non-Brownian fibres. *Journal of Fluid Mechanics*, 329: 155–186.

Mackaplow, M. B. and Shaqfeh, E. S. G. (1998). A numerical study of the sedimentation of fibre suspensions. *Journal of Fluid Mechanics*, 376: 149–182.

Minkowycz, W., Sparrow, E. M., and Murthy, J. (2006). *Handbook of numerical heat transfer*. John Wiley & Sons, London, UK, 2nd edition.

Munk, M. M. (1924). *The aerodynamic forces on airship hulls*. National Advisory Committee for Aeronautics, Washington DC.

Myers, G. E. (1971). *Analytical methods in conduction heat transfer*. McGraw-Hill Book Company, New York.

Newman, J. N. (1964). A slender-body theory for ship oscillations in waves. *Journal of Fluid Mechanics*, 18 (04): 602–618.

Newman, J. N. (1970). Applications of slender-body theory in ship hydrodynamics. *Annual Review of Fluid Mechanics*, 2 (1): 67–94.

Ozisik, M. N. (1993). *Heat conduction*. John Wiley & Sons, London, UK.

Patankar, S. (1980). *Numerical heat transfer and fluid flow*. CRC Press.

Rocha, A. and Acrivos, A. (1973a). On the effective thermal conductivity of dilute dispersions: General theory for inclusions of arbitrary shap. *The Quarterly Journal of Mechanics and Applied Mathematics*, 26 (2): 217–233.

Rocha, A. and Acrivos, A. (1973b). On the effective thermal conductivity of dilute dispersions: highly conducting inclusions of arbitrary shape. *The Quarterly Journal of Mechanics and Applied Mathematics*, 26 (4): 441–455.

Shaqfeh, E. S. (1988). A nonlocal theory for the heat transport in composites containing highly conducting fibrous inclusions. *Physics of Fluids (1958-1988)*, 31 (9): 2405–2425.

von Kármán, T. (1927). Berechnung der Druckverteilung an Luftschiffkörpern. *Abhandlungen aus dem Aerodynamischen Institut an der Technischen Hochschule Aachen*, (6): 3–17.

Ye, Z., Hoskinson, E., Dewey, R. K., Ding, L., and Farmer, D. M. (1997). A method for acoustic scattering by slender bodies. I. Theory and verification. *The Journal of the Acoustical Society of America*, 102 (4): 1964–1976.

CHAPTER 12

SLENDER-BODY THEORY FOR TRANSIENT HEAT CONDUCTION: THEORETICAL DERIVATION

12.1 Slender Body Geometry, Constraints and Heat Transfer Problem

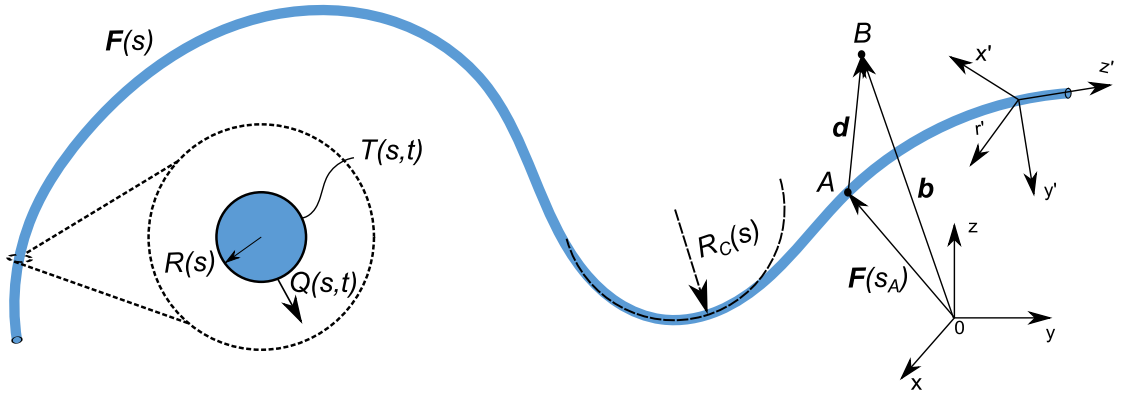

Figure 12.1 – Arbitrary slender body with center-line defined by $\boldsymbol{F}(s)$, local radius by $R(s)$ and local radius of curvature by $R_C(s)$ with s the arc-length along the center-line. The slender body has a surface temperature $T(s,t)$ with t the time, and exchanges heat $Q(s,t)$ with the surrounding conductive medium. A is a general point on the slender body center-line whose coordinates are provided by $\boldsymbol{F}(s_A)$. B is an arbitrary point in the medium with coordinates $\boldsymbol{b}$. The distance vector between the points A and B is represented by $\boldsymbol{d}$.

Figure 12.1 is a sketch of the type of slender-body transient heat conduction problem studied in this work. The geometry of the slender body is set by the functions $\boldsymbol{F}(s)$ and $R(s)$, which define, as a function of the arc-length s along the center-line, the location of the center-line and the radius in parametric form in the global (xyz)-coordinate system. A local $(x'y'z')$-coordinate system is also defined with z' parallel to s. The total length of the slender body is L_t and its radius of curvature is represented by the function $R_C(s)$. The slender body is situated in an infinite medium with constant and uniform thermal diffusivity α and thermal conductivity k. For slender-body theory (SBT) to be applicable, the pipe radius must be small compared with its length, radius of curvature, and the

thermal diffusion length:

$$\frac{R(s)}{L_t} \ll 1\,, \tag{12.1}$$

$$\frac{R(s)}{R_C(s)} \ll 1\,, \tag{12.2}$$

$$\frac{R(s)}{\sqrt{\alpha\tau}} \ll 1 \tag{12.3}$$

with τ a representative time-scale. Further, the pipe radius must be small compared to the distance to a nearby slender body. In Section 12.4, a finite medium will be considered with then the additional constraint that the pipe radius is small compared to the distance from boundaries. Also, in Section 12.3, the model will be expanded for handling thermal diffusion lengths on the order of the pipe radius or smaller and hereby lifting the constraint posed by Equation (12.3). The governing equation for transient heat conduction in the medium is:

$$\frac{1}{\alpha}\frac{\partial T_m}{\partial t} - \nabla^2 T_m = 0 \tag{12.4}$$

with $T_m(x, y, z, t)$ the temperature in the medium and t the time. It is assumed that the initial medium temperature is zero and the body is in perfect thermal contact with the medium.

We aim to find a relation between the temperature T at the surface of the slender body and the heat exchange Q between the slender body and the conductive medium. For the constraints given above, T and Q will show no angular dependence in the matching region to a first approximation, since higher order multipoles will decay away, and therefore will only be a function of s and t. The linear relationship sought between T and Q can now be written in its most general form as:

$$T(s,t) = \int_0^t \int_0^{L_t} f(s^*, t^*, s, t) Q(s^*, t^*) \mathrm{d}s^* \mathrm{d}t^* \tag{12.5}$$

implying that the temperature at a specific location and time depends on all past and current heat exchange along the entire body. In simple problems, either T or Q is set

and the other one is calculated for using Equation (12.5). In more complex problems with heat transfer processes occurring *inside* the slender body, e.g. internal advective heat flow, Equation (12.5) must be combined with other equations, as discussed in Section 12.4.

12.2 SBT Derivation for Transient Heat Conduction

The idea of SBT is to develop an inner and outer solution for the problem, which are valid nearby and faraway from the body, respectively, and then impose their compatibility in the matching region. For the inner solution in our case, the temperature disturbance locally is assumed independent from nearby sections, i.e. the body is replaced with an infinite cylinder with no axial or angular heat variation and the temperature calculation simplifies to a two-dimensional axisymmetric heat transfer problem. For the outer solution, the slender body is replaced with a distribution of point sources along its center-line, and the medium temperature calculation becomes a convolution over s and t of this heat distribution with the Green's function. This approach is equivalent to SBT for Stokes Flow, where in the inner region, the local velocity has no axial dependence, whereas in the outer region, the slender body can be replaced to a first approximation with a distribution of Stokeslets (Batchelor, 1970).

12.2.1 Inner Solution

To estimate the temperature of the conductive medium in close proximity to the slender body, i.e. $r' \to R$ in the local coordinate system in Figure 12.1, the slender body is locally simplified as an infinitely long cylinder undergoing steady-state heat transfer. The cylinder has no angular or axial variation in the heat exchange, which is justified provided the constraints in Equations (12.1) to (12.3). Hence, the problem in the inner region simpli-

fies to a two-dimensional axisymmetric steady-state heat conduction problem in radial coordinates with the temperature disturbed by a heat source located at the finite circular boundary. Higher-order multipoles due to curvature or asymmetric heat processes inside the body, e.g. with borehole heat exchangers, decay away quickly and are therefore neglected. At an arbitrary point A at the slender body (see Figure 12.1) at a certain time t, the slender body is at temperature $T(s_A, t)$ and exchanges heat $Q(s_A, t)$. The medium temperature in close proximity to A, defined as the inner solution T_{in}, is estimated in the local $(r'z')$-coordinate system as (Carslaw and Jaeger, 1959):

$$T_{in}(s_A, r', t) = T(s_A, t) - \frac{Q(s_A, t)}{2\pi k} \ln\left(\frac{r'}{R(s_A)}\right) \tag{12.6}$$

with k the medium thermal conductivity, $\ln(x)$ the natural logarithm, and $R(s_A)$ the local radius of the slender body. Equation (12.6) cannot be viewed as a solution of the inner region problem independent from the outer solution because we cannot specify both T and Q. Instead, we need to match this equation to an outer solution to obtain the relationship between T and Q.

12.2.2 Outer Solution

To estimate the medium temperature at time t at an arbitrary point B far away from the slender body, defined as the outer solution T_{out}, the slender body is replaced by a distribution of transient point sources with strength $Q(s, t)$ along its center-line. Using Green's functions, T_{out} is then calculated at B in the global (xyz)-coordinate system as (Carslaw and Jaeger, 1959):

$$T_{out}(\boldsymbol{b}, t) = \int_0^t \int_0^{L_t} G(\boldsymbol{b} - \boldsymbol{F}(s), t - t^*) Q(s, t^*) \mathrm{d}s \mathrm{d}t^* \tag{12.7}$$

with $\boldsymbol{b} - \boldsymbol{F}(s)$ the distance vector between B and every point along the center-line. Equation (12.7) represents the convolution of the heat distribution $Q(s, t)$ with the point source

solution $G(\boldsymbol{d}, \tau)$ (Green's function) calculated as:

$$G(\boldsymbol{d}, \tau) = \frac{1}{\rho c_p (4\pi\alpha\tau)^{(3/2)}} \exp\left(-\frac{|\boldsymbol{d}|^2}{4\alpha\tau}\right) \tag{12.8}$$

with ρ, c_p, and α the density, specific heat capacity and thermal diffusivity of the conductive medium, respectively, and $|\boldsymbol{d}|$ the length of the distance vector $\boldsymbol{d}$.

When matching, the outer solution will be evaluated for the general point B approaching asymptotically the center-line of the body at an arbitrary location, e.g. point A at $s = s_A$. However, with the double integral in its current form, a singularity arises due to dividing by zero at point A for $t^* = t$. The resolution of this singular lies in locally, around A, simplifying the slender-body as a straight pipe (for which an analytical solution exists) and adding and subtracting the resulting straight line source with constant heat exchange $Q(s_A, t)$ to the right-hand side (RHS) of Equation (12.7), an approach comparable with SBT for steady-state heat transfer (Shaqfeh, 1988). The starting time of the line source, t_0, can be any time between 0 and t but the end time must be t. The straight line has a length $2l$ much smaller than the local radius of curvature ($2l \ll R_C(s_A)$) due to geometry reasons, but much larger than the local radius ($2l \gg R(s_A)$), which will be beneficial for the short time-scale model extension (Section 12.3). Equation (12.7) becomes:

$$\begin{aligned} T_{out}(\boldsymbol{b}, t) = & \underbrace{\int_{t_0}^{t} \int_{s_A - l}^{s_A + l} G(\boldsymbol{b} - \boldsymbol{F}(s), t - t^*) \mathrm{d}t^* \mathrm{d}s \, Q(s_A, t)}_{K} \\ & + \underbrace{\int_{0}^{t} \int_{s_A - l}^{s_A + l} G(\boldsymbol{b} - \boldsymbol{F}(s), t - t^*) \left[Q(s, t^*) - H(t^* - t_0) Q(s_A, t)\right] \mathrm{d}t^* \mathrm{d}s}_{M} \\ & + \int_{0}^{t} \int_{\substack{0 \\ s \notin (s_A - l, s_A + l)}}^{L_t} G(\boldsymbol{b} - \boldsymbol{F}(s), t - t^*) Q(s, t^*) \mathrm{d}t^* \mathrm{d}s \end{aligned} \tag{12.9}$$

with H the Heaviside step function. In Equation (12.9), the singularity has been removed because, at point A for $t^* = t$, $Q(s, t^*) = Q(s_A, t)$ and therefore the argument in the double integral in term M is 0. Also, keeping in mind that the slender body is locally represented as a straight line section, term K can be calculated analytically which will produce an

$\ln(r')$ term that can be matched with the $\ln(r')$ term of the inner solution. In preparation for matching, the location of point B is expressed in the local $(r'z')$-coordinate system attached to point A. Term K is then calculated as:

$$K(r', z') = \int_{t_0}^{t} \int_{-l}^{l} \frac{\exp\left(\frac{-r'^2-(z'-s)^2}{4\alpha(t-t^*)}\right)}{\rho c_p (4\pi\alpha(t-t^*))^{(3/2)}} \mathrm{d}t^* \mathrm{d}s \,. \tag{12.10}$$

When matching, point B asymptotically approaches point A. Term K will be evaluated for $z' = 0$ and can therefore be rewritten as:

$$\begin{aligned} K(r', 0) &= \int_{t_0}^{t} \frac{\exp\left(\frac{-r'^2}{4\alpha(t-t^*)}\right)}{\rho c_p (4\pi\alpha(t-t^*))^{(3/2)}} \int_{-l}^{l} \exp\left(\frac{-s^2}{4\alpha(t-t^*)}\right) \mathrm{d}s \mathrm{d}t^* \\ &= \int_{t_0}^{t} \frac{\exp\left(\frac{-r'^2}{4\alpha(t-t^*)}\right)}{4\pi k(t-t^*)} \mathrm{erf}\left(\frac{l}{\sqrt{4\alpha(t-t^*)}}\right) \mathrm{d}t^* \\ &= \frac{1}{4\pi k}\left[\mathrm{E}_1\left(\frac{r'^2}{4\alpha(t-t_0)}\right) - \int_{\frac{l^2}{\alpha(t-t_0)}}^{\infty} \frac{1}{\phi} \exp\left(-\phi\frac{r'^2}{4l^2}\right) \mathrm{erfc}\left(\frac{1}{2}\sqrt{\phi}\right) \mathrm{d}\phi\right] \end{aligned} \tag{12.11}$$

with $\phi = \frac{l^2}{\alpha(t-t_0)}$, $\mathrm{E}_1(x)$ the exponential integral function $\left(\int_x^\infty \frac{\exp(-u)}{u}\mathrm{d}u\right)$, $\mathrm{erf}(x)$ the error function $\left(\frac{2}{\sqrt{\pi}}\int_0^x \exp(-u^2)\mathrm{d}u\right)$, and $\mathrm{erfc}(x)$ the complimentary error function $(1 - \mathrm{erf}(x))$ (Abramowitz and Stegun, 1964).

12.2.3 Matching

We now match the inner and outer solution, after adding and subtracting $Q(s_A, t^*)$ in term M of Equation (12.9) to split M into two parts, and with further taking into account that

$\mathrm{E}_1(x^2) \approx -\gamma - 2\ln(x)$ for small and positive x with γ Euler's constant (0.5772...):

$$\lim_{r'\to\infty} T_{in} = \lim_{r'\to 0} T_{out} \tag{12.12}$$

$$\Updownarrow$$

$$\begin{aligned} T(s_A,t) = & \left[-\frac{\gamma}{4\pi k} - \frac{1}{2\pi k}\ln\left(\frac{R(s_A)}{\sqrt{4\alpha(t-t_0)}}\right) - \frac{1}{4\pi k}\int_{\frac{l^2}{\alpha(t-t_0)}}^{\infty} \frac{1}{\phi}\mathrm{erfc}\left(\frac{1}{2}\sqrt{\phi}\right)\mathrm{d}\phi\right] Q(s_A,t) \\ & + \int_0^t \int_{s_A-l}^{s_A+l} \frac{\exp\left(\frac{-(s-s_A)^2}{4\alpha(t-t^*)}\right)}{\rho c_p(4\pi\alpha(t-t^*))^{(3/2)}} \left[Q(s_A,t^*) - H(t^*-t_0)Q(s_A,t)\right] \mathrm{d}t^*\mathrm{d}s \\ & + \int_0^t \int_{s_A-l}^{s_A+l} \frac{\exp\left(\frac{-(s-s_A)^2}{4\alpha(t-t^*)}\right)}{\rho c_p(4\pi\alpha(t-t^*))^{(3/2)}} \left[Q(s,t^*) - Q(s_A,t^*)\right] \mathrm{d}t^*\mathrm{d}s \\ & + \int_0^t \int_{0,\, s\notin(s_A-l,s_A+l)}^{L_t} G(\boldsymbol{F}(s_A) - \boldsymbol{F}(s), t-t^*) Q(s,t^*)\mathrm{d}t^*\mathrm{d}s\,. \end{aligned} \tag{12.13}$$

Equation (12.13) provides the relationship, posed by Equation (12.5), between the slender body temperature and heat exchange. It consists of four terms: the first term is the temperature as if the slender body locally is a finite line source (FLS) with constant strength $Q(s_A,t)$ during the time period t_0 to t and over the total length $2l$. Careful analysis reveals this term consists of two parts. The first part, in the form $-\gamma - 2\ln(x)$, is a simplification of $\mathrm{E}_1(x^2)$ for small x and represents the temperature change due to an infinite line source (Carslaw and Jaeger, 1959). The second part, the integral term, accounts for the finite length ($2l$) by subtracting the temperature change due to two semi-infinite line sources, one on either end. The second and third terms in Equation (12.13) can be viewed as corrections to the first term by now accounting for the local heat source variation in space and time. The second term is the temperature contribution from the same finite line source but now with a heat pulse strength that is still constant along the line source but varies over time, $Q(s_A,t^*)$, subtracted by $Q(s_A,t)$ for the time period t_0 to t. In the third term, the line source has the actual heat source $Q(s,t^*)$ varying over space and time, subtracted by $Q(s_A,t^*)$. Finally, the fourth term in Equation (12.13) is the temperature contribution from all other previous and current point sources along the center-line of the slender body.

12.3 Extension of Model to Short Time-Scales

Equation (12.13) is only valid for heat transfer processes occurring over long time-scales, i.e. ($R(s) \ll \sqrt{\alpha\tau}$) (see Equation (12.3)). For short time-scale phenomena, with the heat transfer diffusion length on the order of the pipe radius or smaller, Equation (12.13) should be adjusted to represent a cylindrical source rather than a line source. The temperature in the finite cylindrical source (FCS) model, T_{FCS}, with radius R and constant heat pulse Q from t_0 to t is given by (Carslaw and Jaeger, 1959):

$$T_{FCS}(t) = \left[\frac{2}{\pi^3 k} \int_0^\infty \frac{1 - \exp\left(-\phi^2 \frac{\alpha(t-t_0)}{R^2}\right)}{\phi^3 (J_1^2(\phi) + Y_1^2(\phi))} d\phi - \frac{1}{4\pi k} \int_{\frac{l^2}{\alpha(t-t_0)}}^\infty \frac{1}{\phi} \text{erfc}\left(\frac{1}{2}\sqrt{\phi}\right) \text{d}\phi \right] Q \tag{12.14}$$

with $J_1(x)$ and $Y_1(x)$ the first order Bessel function of the first kind and second kind, respectively. Equation (12.14) readily replaces the FLS model in the first term of Equation (12.13). The effect of $Q(s_A, t)$ changing over time, represented by the second term in Equation (12.13), should be calculated with the FCS model as well. In continuous form, this can only be written analytically in the Laplace domain. However, a solution can be found in the time domain when discretizing Q as a series of n constant heat pulses (as will be applied when numerically implementing),

$$Q(s_A, t) = \sum_n \Big[Q_n(s_A)(H(t - t_{n-1}) - H(t - t_n)) \Big] \tag{12.15}$$

with $Q_n(s_A)$ the constant heat pulse at time step n. No FCS model is available when $Q(s, t)$ varies spatially along the cylindrical source, represented by the third term in Equation (12.13). However, when considering $2l$ to be the length of a computational element on which Q is constant (as will be applied in Chapter 13), allowed in the case of spatially-smooth variations in Q along the center-line of the body, this term can be neglected. Finally, the fourth term remains unaltered, since it accounts for temperature contributions caused by heat sources at a distance larger than $R(s_A)$ away for the point of interest (A).

All together, the solution for $T(s_A, t)$ applicable at short time-scales becomes:

$$\begin{aligned} T(s_A,t) = & \left[\frac{2}{\pi^3 k}\int_0^\infty \frac{1-\exp\left(-\phi^2\frac{\alpha(t-t_0)}{R(s_A)^2}\right)}{\phi^3(J_1^2(\phi)+Y_1^2(\phi))}d\phi - \frac{1}{4\pi k}\int_{\frac{l^2}{\alpha(t-t_0)}}^\infty \frac{1}{\phi}\mathrm{erfc}\left(\frac{1}{2}\sqrt{\phi}\right)\mathrm{d}\phi\right] Q(s_A,t) \\ & + \sum_n \left[\frac{2}{\pi^3 k}\int_0^\infty \frac{\exp\left(-\phi^2\frac{\alpha(t-t_n)}{R(s_A)^2}\right)-\exp\left(-\phi^2\frac{\alpha(t-t_{n-1})}{R(s_A)^2}\right)}{\phi^3(J_1^2(\phi)+Y_1^2(\phi))}d\phi\right. \\ & \qquad \left. - \frac{1}{4\pi k}\int_{\frac{l^2}{\alpha(t-t_{n-1})}}^{\frac{l^2}{\alpha(t-t_n)}} \frac{1}{\phi}\mathrm{erfc}\left(\frac{1}{2}\sqrt{\phi}\right)d\phi\right](Q_n(s_A) - H(t_n-t_0)Q(s_A,t)) \\ & + \int_0^t \int_{\substack{0 \\ s\notin(s_A-l,s_A+l)}}^{L_t} G(\boldsymbol{F}(s_A)-\boldsymbol{F}(s), t-t^*)Q(s,t^*)\mathrm{d}t^*\mathrm{d}s \end{aligned} \tag{12.16}$$

with the assumption that t_0 now corresponds to one of the time steps. Equation (12.16) is also valid for long time-scales, however, from a computational point of view, using Equation (12.13) in calculations is preferred, as will be further discussed in Chapter 13.

12.4 Other Model Extensions

The equations developed so far assume an infinite, conductive medium with uniform zero initial temperature, and constant, isotropic and uniform thermal properties. This section discusses how to remove several of these constraints, as well as how to incorporate heat transfer processes inside the slender body.

The effect of a far-field or initial temperature distribution can be accounted for by modeling it as an imposed field $T_i(x, y, z, t)$ without the slender body and then superimposing this field to the disturbance field caused by the slender body, i.e. adding $T_i(x, y, z, t)$ to the RHS of Equation (12.9) and therefore to the RHS of Equation (12.13) or (12.16). In the most simple cases, the imposed field is found directly such as for a uniform non-zero initial temperature, $T_i(x, y, z, t) = T_0$, or for a linear far-field temperature profile, $T_i(x, y, z, t) = T_0(z) = T_{surface} + \omega z$ (with ω the geothermal gradient).

For a non-infinite medium, the infinite medium model can still be an accurate representation in cases when the distance from the slender body to the medium boundary is much larger than the thermal diffusion length. An example is the simulation of the heat transmission with deep geothermal, oil or gas wells. Otherwise, a different (and more onerous) Green's function must be used with a complete list of Green's functions for all types of boundary conditions provided by Beck et al. (1992). Some can be readily found by using method of images, such as constant temperature or zero heat flux condition at a planar boundary (Beck et al., 1992; Duffy, 2015). Several of the solution methods provided by Beck et al. can be derived using the imposed field technique, introduced above for dealing with the initial condition. For example, a distribution of heat sources at a boundary must be convoluted over space and time with the Green's function for an infinite medium, and then superimposed to the disturbance field caused by the slender body, calculated with SBT using a zero heat flux Green's function.

Simple cases of a medium involving fluid flow, or anisotropic or non-uniform thermal properties can be simulated by using a different (and again more complicated) Green's function. One-dimensional constant velocity fluid flow causing heat advection, instead of pure heat conduction, can be accounted for by using the moving point source Green's function (Carslaw and Jaeger, 1959; Molina-Giraldo et al., 2011). However, this is only directly applicable for the long time-scale solution, and should be combined with a different model, e.g. the solid cylindrical source model (Zhang et al., 2013), for the short time-scale solution. Also a Green's function exists in the case of anisotropic thermal properties, for which the thermal conductivity can now be represented by a tensor (Yan-Po, 1977). Further, for a two-layered medium with isotropic properties, an exact Green's function is provided by Carslaw and Jaeger (1959). For any number of layers, Abdelaziz et al. (2014) provide an approximate method using interlayer heat exchange adjustments, and laws of composite materials for estimating representative thermal properties. Again, the extensions for anisotropic and non-uniform thermal properties are only directly applicable

at long time-scales when the cylindrical source models can be represented by line source models. Incorporating temperature-dependent thermal properties with the SBT model is not possible since this would lead to non-linear equations.

In simple cases, either T or Q at the surface of the slender body is specified with the other being solved for. In more complex problems with heat processes occurring inside the body, additional relations are required and calculated for simultaneously with Equation (12.13) or (12.16). For example, for advective heat transfer due to pipe fluid flow, a first additional relation is (Bergman et al., 2011):

$$Q(s,t) = \frac{T_f(s,t) - T(s,t)}{R_t(s)} \tag{12.17}$$

with $T_f(s,t)$ the temperature of the fluid and $R_t(s)$ the effective thermal resistance of the pipe calculated as the sum of the thermal resistances of the conductive heat transfer through the pipe and the convective heat transfer between the fluid and the pipe wall (Bergman et al., 2011):

$$R_t(s) = \frac{\ln(R(s)/R_{inner}(s))}{2\pi k_p(s)} + \frac{1}{2\pi h(s) R_{inner}(s)} \tag{12.18}$$

with $R(s)$ and $R_{inner}(s)$ the outer and inner radius of the pipe, respectively. Further, $k_p(s)$ is the thermal conductivity of the pipe material and $h(s)$ is the convective heat transfer coefficient which can be calculated with appropriate Nusselt-correlations for forced internal convection (Bergman et al., 2011). A third equation is required, which represents the energy balance of the fluid inside the pipe (with neglecting the heat conduction within the fluid):

$$\rho_f c_{p,f} \frac{\partial T_f(s,t)}{\partial t} + \rho_f c_{p,f} U(s) \frac{\partial T_f(s,t)}{\partial s} = \frac{Q(s,t)}{\pi R_{inner}^2(s)} \tag{12.19}$$

with ρ_f, $c_{p,f}$ and $U(s)$ the density, specific heat capacity and velocity of the fluid, respectively, and the fluid inlet temperature being a boundary condition. Various finite difference methods are available to handle the time and spatial derivative, with different levels of accuracy and complexity (Minkowycz et al., 2006). For the second case-study for

example (Section 14.2), Equation (12.19) is numerically implemented using an upwind differencing scheme. For other types of heat exchangers such as single-U (1-U), double-U (2-U) and coaxial borehole heat exchangers, similar equations can be developed.

Finally, one can derive from Equation (12.13) the SBT solution for steady-state heat conduction by replacing $Q(s_A, t)$ with $Q(s_A)$, and letting time approach infinity. The time convolution integral of the transient Green's function (Equation (12.8)) for any starting time t_0 translates into the steady-state Green's function (Beck et al., 1992):

$$\lim_{t\to\infty} \int_{t_0}^{t} \frac{\exp\left(-\frac{|\boldsymbol{d}|^2}{4\alpha(t-t^*)}\right)}{\rho c_p (4\pi\alpha(t-t^*))^{(3/2)}} \mathrm{d}t^* = \frac{1}{4\pi k\,|\mathbf{d}|}\,. \tag{12.20}$$

The SBT solution for steady-state heat transfer with curved slender bodies in a conductive medium is now found as:

$$T(s_A) = \frac{1}{2\pi k}\ln\left(\frac{2l}{R(s_A)}\right) Q(s_A) + \int_{s_A-l}^{s_A+l} \frac{Q(s)-Q(s_A)}{4\pi k\,|s-s_A|}\mathrm{d}s + \int_{\substack{0 \\ s\notin(s_A-l,s_A+l)}}^{L_t} \frac{Q(s)}{4\pi k\,|\boldsymbol{F}(s_A)-\boldsymbol{F}(s)|}\mathrm{d}s \tag{12.21}$$

with $T(s_A)$ the surface temperature of the slender body at any point s_A along its center-line. The first two terms in Equation (12.21) represent the temperature due to a local straight line source with length $2l$. The third term in Equation (12.21) accounts for the line distribution along each of the other cylindrical elements making up the curved body. The second term in Equation (12.13) is not present in Equation (12.21) because the local heat source no longer varies with time. Equation (12.21) provides a description of the interaction through steady-state heat conduction among a collection of cylindrical elements that approximate a curved slender body that is equivalent to the treatment in Equation (2.18) of Mackaplow et al. (1994) of steady-state heat conduction in a composite with many discrete straight highly-conductive fiber inclusions.

References

Abdelaziz, S. L., Ozudogru, T. Y., Olgun, C. G., and Martin, J. R. (2014). Multilayer finite line source model for vertical heat exchangers. *Geothermics*, 51: 406–416.

Abramowitz, M. and Stegun, I. A. (1964). *Handbook of mathematical functions: with formulas, graphs, and mathematical tables*. Number 55. Courier Corporation, Mineola, New York.

Batchelor, G. K. (1970). Slender-body theory for particles of arbitrary cross-section in stokes flow. *Journal of Fluid Mechanics*, 44 (03): 419–440.

Beck, J. V., Cole, K. D., Haji-Sheikh, A., and Litkouhi, B. (1992). *Heat conduction using Green's functions*. Hemisphere Publishing Corporation, Washington DC.

Bergman, T. L., Lavine, A. S., Incropera, F. P., and Dewitt, D. P. (2011). *Introduction to heat transfer*. John Wiley & Sons, 6th edition.

Carslaw, H. S. and Jaeger, J. C. (1959). *Conduction of heat in solids*. Clarendon Press, Oxford.

Duffy, D. G. (2015). *Greens functions with applications*. CRC Press, Boca Raton, Florida.

Mackaplow, M. B., Shaqfeh, E. S. G., and Schiek, R. L. (1994). A numerical study of heat and mass transport in fibre suspensions. *Proceedings of the Royal Society of London A: Mathematical, Physical and Engineering Sciences*, 447 (1929): 77–110.

Minkowycz, W., Sparrow, E. M., and Murthy, J. (2006). *Handbook of numerical heat transfer*. John Wiley & Sons, London, UK, 2nd edition.

Molina-Giraldo, N., Blum, P., Zhu, K., Bayer, P., and Fang, Z. (2011). A moving finite line source model to simulate borehole heat exchangers with groundwater advection. *International Journal of Thermal Sciences*, 50 (12): 2506–2513.

Shaqfeh, E. S. (1988). A nonlocal theory for the heat transport in composites containing highly conducting fibrous inclusions. *Physics of Fluids (1958-1988)*, 31 (9): 2405–2425.

Yan-Po, C. (1977). Analytical solution for heat conduction in anisotropic media in infinite, semi-infinite, and two-plane-bounded regions. *International Journal of Heat and Mass Transfer*, 20 (10): 1019–1028.

Zhang, W., Yang, H., Lu, L., and Fang, Z. (2013). The analysis on solid cylindrical heat source model of foundation pile ground heat exchangers with groundwater flow. *Energy*, 55: 417–425.

CHAPTER 13

SLENDER-BODY THEORY FOR TRANSIENT HEAT CONDUCTION: NUMERICAL FRAMEWORK

In Chapter 13, we develop one possible numerical framework for the slender-body theory (SBT) model for transient heat conduction derived in the previous chapter. Figure 13.1 shows with a simplified diagram the 6 steps taken in developing this framework. The slender body heat transfer problem is discretized in the space (step 1) and time domain (step 2), which converts the integrals in the SBT solution (Equation (12.13) or (12.16)) into summations. The most cumbersome calculation is the double summation over all previous heat pulses emitted by all neighboring slender body elements. Therefore, simplifications are applied in the space (step 3) and time domain (step 4) when calculating these heat pulse contributions. The computational time can further be decreased by combining point sources in the space (step 5) as well as in the time domain (step 6), a method also known as the Fast Multipole Method or FMM. The following sections explain each step in more detail and develop the SBT numerical equations, which are implemented in a computer algorithm.

13.1 Space and Time Discretization of SBT Model

A computer implementation of the SBT model requires to numerically solve Equation (12.13) or (12.16) for each location s and time t. The integrals in these equations can be converted into summations by discretizing the slender body into a set of straight pipe elements i and discretizing the time into time steps m (steps 1 and 2 in Figure 13.1). This converts the continuous functions $Q(s,t)$ and $T(s,t)$ into the discrete functions $Q_{i,m}$ and $T_{i,m}$, respectively. $Q_{i,m}$ represents the constant heat exchange (in units of W/m) for the

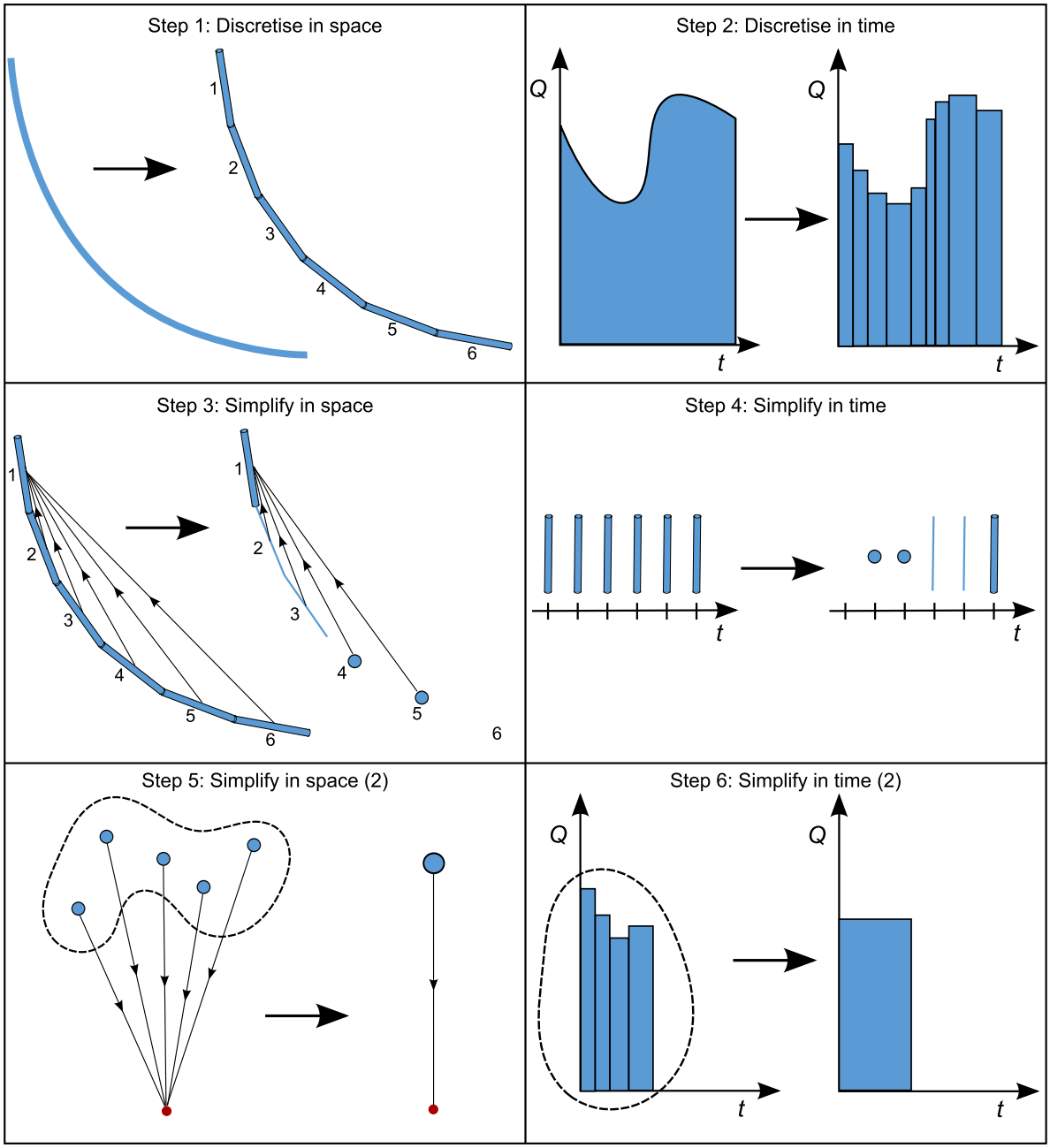

Figure 13.1 – Diagram illustrating the 6 steps in developing the SBT numerical framework. A slender body is discretized into straight pipe elements (step 1). The heat exchange at each element is discretized in time as a series of heat pulses (step 2). In many cases, without much loss in accuracy but with less computational complexity, pipe elements can be simplified as infinite or finite line sources, point sources or even neglected both in space (step 3) and time domain (step 4). To further decrease the computational time, point sources can be combined in space (step 5) as well as in time domain (step 6).

entire pipe element i during time step m; $T_{i,m}$ represents the temperature at the mid-point of pipe element i at the end of time step m.

The local geometry of the slender body sets a maximum length for the pipe elements by requiring that the set of elements still accurately represents the shape of the body. In numerical tests with the SBT algorithm, we used sample calculations with a heated toroidal ring to show that a maximum element length to radius of curvature ratio of about 0.7 results in at least 98% accuracy. On the other hand, there is no minimum length and the user can discretize the body as fine as deemed necessary to achieve the desired accuracy with element lengths on the order of the pipe radius or smaller possible. However, to simplify the numerical implementation, we choose here to set the element lengths, labeled as L_i for element i, equal to the length of the local constant line source ($2l$) of the outer solution (see Section 12.2). Each element length L_i is now larger than the local pipe radius but not necessarily identical to the other element lengths, since l can vary along the slender body axis. For spatially-smoothly varying Q along the center-line of the slender body, this simplification is not believed to jeopardize the accuracy. Further, it automatically sets the third term in Equation (12.13) to zero, a simplification already applied when deriving Equation (12.16).

There are no model constraints on the time step length. The user can choose non-uniform time steps as fine or coarse as required in obtaining the desired trade-off between accuracy and computational time. To simplify the numerical implementation, we choose to have the starting time t_0 of the constant line source $Q(s_A, t)$ so that $t - t_0$ corresponds to each time step length.

For the space and time discretization schemes selected above, Equation (12.16) (or (12.13)) is now converted into a linear equation in Q with $T_{i,m}$ the temperature at the selected element i after current time step m and $Q_{j,n}$ the heat source emitted by element j

during time step n:

$$
\begin{aligned}
T_{i,m} &= \sum_j \sum_n (f_{i,j,m,n} \cdot Q_{j,n}) \\
&= (f_{i,i,m,m} \cdot Q_{i,m}) && \text{(current heat pulse by selected element)} \\
&\quad + \sum_{n \neq m} (f_{i,i,m,n} \cdot Q_{i,n}) && \text{(previous heat pulses by selected element)} \\
&\quad + \sum_{j \neq i} (f_{i,j,m,m} \cdot Q_{j,m}) && \text{(current heat pulse by neighboring elements)} \\
&\quad + \sum_{j \neq i} \sum_{n \neq m} (f_{i,j,m,n} \cdot Q_{j,n}) && \text{(previous heat pulses by neighboring elements)} .
\end{aligned} \tag{13.1}
$$

Terms 1 and 2 in Equation (12.13) and (12.16) correspond to the first and second term in Equation (13.1) (current and previous heat pulses emitted by selected element ($j = i$)). Further, term 4 in Equation (12.13) or term 3 in Equation (12.16) is split into two parts in Equation (13.1) (third and fourth term) by distinguishing between current ($n = m$) and previous ($n < m$) heat pulses emitted by neighboring elements ($j \neq i$). The terms $f_{i,j,m,n}$ now represent standard, easy to calculate models, which are the topic of Section 13.2.

Other approaches exist to discretize or numerically solve Equation (12.13) or (12.16). One could decouple $2l$ from the pipe element lengths to allow for very fine grids in order to capture abrupt spatial changes in Q, occurring over length-scales on the order of the pipe radius or smaller. Another approach is to represent $Q(s,t)$ as a summation of polynomials and numerically solve for the polynomial coefficients, as highlighted by Batchelor (1970). However, these methods are not further investigated in this discussion.

13.2 Equations for $f_{i,j,m,n}$

The term $f_{i,j,m,n}$, introduced in Equation (13.1), can be interpreted as the temperature response at the mid-point of pipe element i at time step m caused by a unit heat pulse of 1

W/m emitted by pipe element j during time step n. From Equations (12.13) and (12.16), it is derived that $f_{i,j,m,n}$ represents simple models such as cylindrical, line or point source models, which can often be calculated analytically. To save on computational time, a method is presented in Appendix D that uses decision trees and non-dimensional numbers, based on length- and time-scales of the heat transfer problem, to select the most simple model that still accurately calculates each term $f_{i,j,m,n}$. For example, heat sources occurring far away in space and/or time (see steps 3 and 4 in Figure 13.1), could be represented by point sources or even neglected rather than calculated with the full cylindrical or line source models. Appendix D provides all equations to calculate f for each term in Equation (13.1) and explains in more detail the accuracy obtained by applying these simplifications.

13.3 Fast Multipole Method, other Implementation Strategies, and Computational Time

The computational time of the SBT algorithm can further be decreased by combining point sources in the space and time domain (steps 5 and 6 in Figure 13.1). This method is called the Fast Multipole Method (FMM) and was pioneered by Greengard and Rokhlin (1987). Although advanced decision criteria could be developed to determine which point sources to combine at which times, here a more rudimentary method is adopted. Previous pulses once represented by the most simple point source model (i.e. the PS_3 model, introduced in Appendix D) can be combined if $\mathrm{TDR}\cdot\sqrt{\mathrm{Fo}_{\mathrm{L,PP,E}}}$, with TDR and $\mathrm{Fo}_{\mathrm{L,PP,E}}$ non-dimensional numbers defined in Table D.1 and appearing in the PS_3 equation, is larger than a certain value, e.g. 100, and correspondingly the f become relatively small (but not negligible). A certain number of point sources, e.g. five, could then be grouped together and represented by a new point source with a $Q\cdot(t_n - t_{n-1})$ equal to the sum of the

$Q{\cdot}(t_n - t_{n-1})$ of the original point sources (conservation of energy) and with the new t_n and t_{n-1} (end and start time of a heat pulse) set in this way that the new f exactly matches the sum of the old f, e.g. at the time of combining the pulses. This simplification can be done at multiple levels, i.e. five new point sources each replacing five old point sources can later be combined themselves. Also, in the space domain, different pipe elements located at different positions can have a similar spacing, e.g. within 5%, with respect to a selected element. Once represented by a point source, the heat pulses from these different elements can simply be added together and only one f needs to be calculated.

Other implementation strategies to decrease the computational time are to calculate certain terms that often reoccur throughout the simulation once in advance. Examples are $(L_i/4\pi k)$, several non-dimensional numbers, special functions such as $\mathrm{erf}(x)$ and $\mathrm{E}_1(x)$ and the integrals in the cylindrical source model. Also, because each Equation (13.1) for every pipe element is coupled with each other, the solution algorithm requires solving a linear set of equations at each time step, for which either direct or iterative methods can be used. Since the matrix system in some cases is sparse and/or symmetrical, fast solution methods could be utilized, which are built-in into software packages such as MATLAB (MathWorks, 2012).

An SBT computer program based on the numerical framework presented requires implementing Equation (13.1), the non-dimensional numbers, heat source model equations and decision trees from Appendix D to calculate $f_{i,j,m,n}$, and depending on the problem possibly equations from Section 12.4 (model extensions), e.g. to include heat transfer phenomena inside the slender body or for specific boundary conditions. A simulation requires solving Equation (13.1) at each time step simultaneously for each pipe element. For SBT, the total number of elements N_E is $O(N_L)$ with N_L the discretization of the slender body. Without any simplifications (steps 3 to 6 of Figure 13.1 neglected), and with utilizing a direct solver based on LU decomposition for solving the matrix system, the

computational time is $O(N_t \cdot N_E^3 + N_t^2 \cdot N_E^2)$, with N_t the number of time steps. In contrast, for FEM (finite element methods), with L a characteristic length for the medium domain, the number of elements N_E is $O(N_L \cdot (L/R)^2)$ or $O(N_L \cdot (\sqrt{\alpha t}/R)^2)$, whichever is smaller, but the computational time is only $O(N_E^3 + N_t \cdot N_E^2)$. The number of elements N_E for SBT is typically several orders of magnitude smaller than N_E for FEM which results in lower computational times in many cases. However, the SBT model is no longer advantageous for more spatially-complex but compact problems, especially in combination with a large number of time steps. With the simplifications and strategies provided, the computational time will decrease but it is difficult to determine by how much because it depends on several factors such as decision tree limits, matrix solver algorithm, and spatial and time lengths and discretizations. In terms of computer memory, the SBT model can also be superior since an FEM simulation typically requires large amounts of data storage for meshing, matrix assembly and solving.

References

Batchelor, G. K. (1970). Slender-body theory for particles of arbitrary cross-section in stokes flow. *Journal of Fluid Mechanics*, 44 (03): 419–440.

Greengard, L. and Rokhlin, V. (1987). A fast algorithm for particle simulations. *Journal of computational physics*, 73 (2): 325–348.

MathWorks (2012). *MATLAB Release 2012a*, The Mathworks, Inc., Natick, Massachusetts, United States.

CHAPTER 14

SLENDER-BODY THEORY FOR TRANSIENT HEAT CONDUCTION: CASE-STUDIES

In this chapter, two case-studies are presented to validate and illustrate the applicability, speed and versatility of the slender-body theory (SBT) numerical model developed in Chapter 13. The first case-study is a theoretical example of two parallel cylinders in close proximity and at constant temperature, representing probably the most fundamental heat transfer problem with interacting slender bodies, for which no analytical solution exists. The second case-study is an applied example of one loop of a slinky-coil heat exchanger, typically used in geothermal heat pump systems that employ horizontal trenches for heat exchange with the ground. In each case, the SBT numerical model, implemented in MATLAB R2012a using all of the simplifications and strategies discussed, is compared with the FEM (finite element methods) software package COMSOL Multiphysics 4.3 (COMSOL, 2012) in terms of computational time. In order to make a fair comparison, the discretization schemes are chosen such that comparable accuracy is obtained. All simulations are carried out on a standard Intel Core i3-2120 (3.3 GHz) desktop computer with 6 GB RAM and Windows 7 as operating system. Both in MATLAB and COMSOL, a direct solver is used to solve the linear system of equations.

14.1 Two Parallel Cylinders at Constant Temperature

Two parallel cylinders with length $L_t = 10$ m, radius $R = 0.05$ m and spacing $S = 1$ m are placed in an infinite conductive medium with thermal conductivity $k = 1$ W/(m·K) and thermal diffusivity $\alpha = 10^{-6}$ m^2/s (Figure 14.1). The medium has an initial temperature of 0°C and both cylinders are kept at a constant temperature of 10°C. We aim to solve for the transient heat exchange Q (W/m) at both short and long time-scales, occurring at the

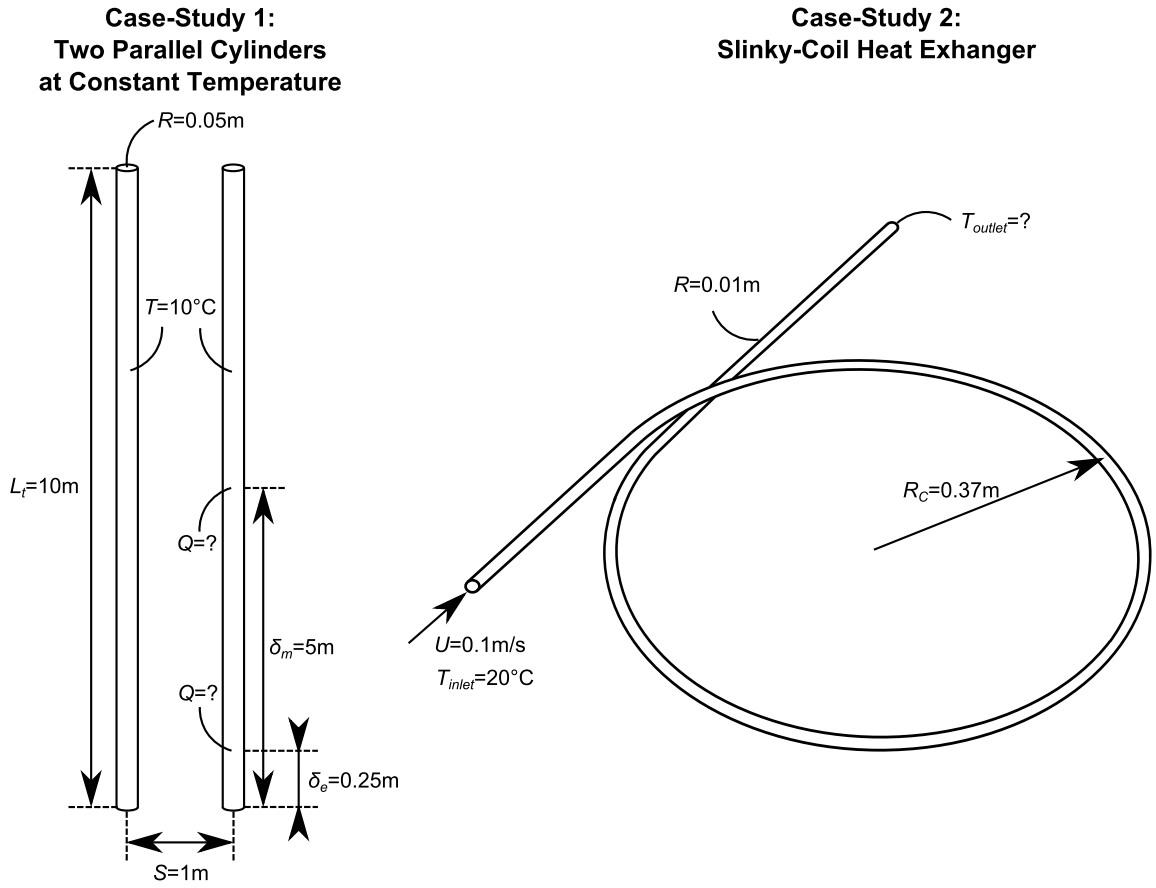

Figure 14.1 – Two case-studies to demonstrate the SBT numerical model developed in Chapter 13. The first case-study (left) is the simulation of the heat flux Q at the mid-point and end-point of two parallel identical cylinders at constant temperature and in close proximity. The second case-study (right) is the simulation of the outlet temperature of one loop of a slinky-coil heat exchanger. Drawings are not to scale.

mid-point ($\delta_m = 5$ m) and close to the end-point ($\delta_e = 0.25$ m) of the cylinders, averaged over the circumference. Due to the symmetry of the problem, both cylinders will have the same heat flux.

In the SBT model, each cylinder is discretized into 20 identical pipe elements for a total number of 40 grid points, which is identical to modeling one cylinder and applying the method of images to force a zero flux boundary condition at the mid-plane between both cylinders. The time is discretized into 150 time steps from 0 to 10^9 s. The COMSOL model is a 3-dimensional model of a quarter of one cylinder (axial cross section of the half length), with zero heat flux condition at the appropriate boundaries, in order to make full

use of the symmetry embedded in this problem, and constant temperature of 0°C at the other (far-field) boundaries. This quarter of a cylinder is placed in a cuboid with height of 35 m and width and depth of 30 m, at its correct location close to one of the corners. The number of grid points along the cylindrical body is 500, the total number of mesh elements is about 130,000 and the relative tolerance is set to 0.1. With these spatial and time discretization schemes, the SBT and COMSOL model show a comparable accuracy of about 99% on average over the entire time span, with reference to a highly accurate COMSOL model with very fine mesh (1,000,000 cells) and very low relative tolerance (10^{-6}). This reference COMSOL model has been validated at short time-scales with the analytical solution of a single, infinitely long cylinder at constant temperature (Carslaw and Jaeger, 1959).

The result for Q at the mid-point and end-point as a function of time is shown in Figure 14.2 with the heat flux and time non-dimensionalized as $Q/(k\Delta T)$ and $\sqrt{\alpha t}/S$, respectively, with ΔT the temperature difference between the cylindrical surface and the far-field ($\Delta T = 10$°C). The non-dimensional time can be interpreted as the ratio of the diffusion distance $\sqrt{\alpha t}$ to the spacing between the cylinders S. The result for one cylinder only is included to illustrate the tube-tube interactions which start to occur at a non-dimensional time of about 0.5 corresponding to a thermal diffusion length of 0.5 m. The difference in Q between the mid-point and end-point becomes evident at a non-dimensional time of about 0.2, corresponding to a thermal diffusion length of 0.2 m. The computational time for the SBT model is 7 s and for the COMSOL model about 10 min. This case-study illustrates the high computational speed of the SBT model, and its versatility in easily handling short and long time-scales and multiple, disconnected, interacting slender bodies of finite length. Even higher speeds in this as well as in the next case-study can likely be obtained when implementing the SBT model using a compiled language such as C instead of an interpreted language as with MATLAB. However, this is not further investigated.

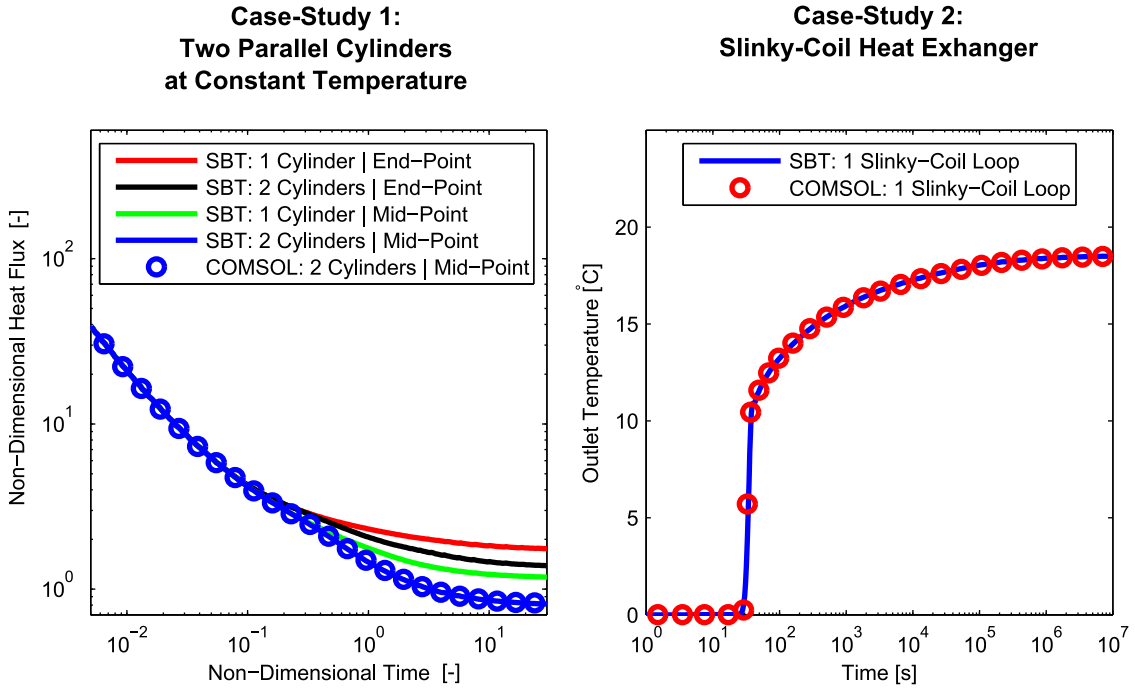

Figure 14.2 – Results for the two case-studies presented in Figure 14.1. The result for the first case-study (left) is the non-dimensional heat exchange ($Q/(k\Delta T)$) as a function of the non-dimensional time ($\sqrt{\alpha t}/S$) at the mid-point and end-point of one and two parallel cylinders at constant temperature. The result for the second case-study (right) is the fluid outlet temperature of one loop of a slinky-coil heat exchanger.

14.2 Slinky-Coil Heat Exchanger

In the second case-study, the outlet temperature of water flowing inside one loop of a slinky-coil heat exchanger as a function of time is simulated for (see Figure 14.1). The heat exchanger has a total length L_t of 3.325 m, a loop radius R_C of 0.37 m, a pipe radius R of 1 cm, a pipe wall thickness Th_p of 0.1 cm, and a pipe material thermal conductivity k_p of 1 W/(m·K). At the cross-over point, the pipes are within 0.5 cm of each other. The density ρ_f, specific heat capacity $c_{p,f}$, inlet temperature T_{inlet}, and mean velocity U of the water are 1000 kg/m^3, 4200 J/(kg·K), 20°C, and 0.1 m/s, respectively. The convective heat transfer coefficient between the water and the pipe is set at h = 1000 W/(m^2·K). Further, the infinite conductive medium has a thermal diffusivity α of 10^{-6} m^2/s, thermal conductivity k of 3 W/(m·K), and initial temperature of 0°C.

For the SBT equations, the heat exchanger is discretized into 30 identical pipe elements and the time is discretized into 50 linear time steps from 1 to 50 s, followed by 100 logarithmically-spaced time steps from 50 s up to 10^7 s. In the COMSOL model, the heat exchanger is placed at the center of a cube, representing the infinite medium, with edge length of 10 m. The total number of elements is about 80,000 and the relative tolerance is set to 0.02. Further, in both the SBT and COMSOL simulations, the conductive medium model is coupled to a one-dimensional advective heat flow model representing the fluid flow inside the slinky-coil heat exchanger (see Section 13.3) with a spatial discretization of 180 and 200 elements in the SBT and COMSOL model, respectively. The spatial and time discretization schemes chosen for both models provide a comparable accuracy of about 99% on average over the entire time span, in comparison with a highly accurate COMSOL model with very low relative tolerance of 10^{-6} and a fine mesh of about 350,000 cells.

The water outlet temperature simulated with the SBT and COMSOL model is shown in Figure 14.2. The calculation time for the SBT model is 6 s while for the COMSOL model about 19 min. This case-study illustrates the SBT model running at high computational speeds and easily handling short and long time-scales, curved bodies, and heat transfer inside a slender body. Moreover, the slender body approaching itself at the cross-over point, which is a violation of one of the constraints provided in Section 12.1, does not appear to have a noticeable impact on the outlet temperature. The reason is that the two parts only lie within the inner region of one another for a short distance $O(R)$, and since $L_t/R \gg 1$, the heat transfer from this region is small $O(R/L_t)$.

Slinky-coil heat exchangers are typically modeled using finite element modeling (FEM) numerical software (Wu et al., 2010; Congedo et al., 2012; Fujii et al., 2012; Chong et al., 2013) or g-functions (Xiong et al., 2015). This case-study shows SBT provides an alternative, computationally-fast approach. Other types of heat exchangers for geothermal or ground-source heat pump applications, e.g. parallel horizontal pipes, and single-U

(1-U) and double-U (2-U) borehole heat exchangers, can be simulated using SBT as well. Potential oversimplifications often applied in other models for simulating these heat exchangers, such as constant longitudinal heat exchange Q along a single-U borehole heat exchanger, can then be avoided.

References

Carslaw, H. S. and Jaeger, J. C. (1959). *Conduction of heat in solids*. Clarendon Press, Oxford.

Chong, C. S. A., Gan, G., Verhoef, A., Garcia, R. G., and Vidale, P. L. (2013). Simulation of thermal performance of horizontal slinky-loop heat exchangers for ground source heat pumps. *Applied Energy*, 104: 603–610.

COMSOL (2012). *COMSOL Multiphysics 4.3*, COMSOL Inc., Burlington, Massachusetts, United States.

Congedo, P., Colangelo, G., and Starace, G. (2012). CFD simulations of horizontal ground heat exchangers: a comparison among different configurations. *Applied Thermal Engineering*, 33: 24–32.

Fujii, H., Nishi, K., Komaniwa, Y., and Chou, N. (2012). Numerical modeling of slinky-coil horizontal ground heat exchangers. *Geothermics*, 41: 55–62.

Wu, Y., Gan, G., Verhoef, A., Vidale, P. L., and Gonzalez, R. G. (2010). Experimental measurement and numerical simulation of horizontal-coupled slinky ground source heat exchangers. *Applied Thermal Engineering*, 30 (16): 2574–2583.

Xiong, Z., Fisher, D. E., and Spitler, J. D. (2015). Development and validation of a Slinky™ ground heat exchanger model. *Applied Energy*, 141: 57–69.

CHAPTER 15

SLENDER-BODY THEORY FOR TRANSIENT HEAT CONDUCTION: CONCLUSIONS

The slender-body theory (SBT) was initially developed and is most often used in the field of fluid dynamics to simplify the flow and pressure field solution of a slender body problem using matched asymptotic expansions of an inner and outer solution. In this work, the SBT was developed for slender, curved bodies with circular cross section undergoing transient heat transfer in a conductive medium. The theoretical derivation is based on matching the temperature field of an infinitely long cylindrical source as inner solution with the temperature field of a finite line source as outer solution. By replacing the line source model with the cylindrical source model in the final result, a solution was obtained applicable at all time-scales. One possible numerical model was developed by discretizing the SBT theoretical result in the space and time domain. High computational speeds were obtained by applying simplifications such as modeling cylindrical and line sources as point sources, combining point sources with the Fast Multipole Method, or even neglecting point sources when allowed. Two case-studies were included to demonstrate the SBT model operating at high computational speeds, capturing tube-tube interactions and finite lengths, and handling curved bodies, short and long time-scales, and heat transfer processes inside a slender body.

The slender-body theory for transient heat conduction can be an attractive solution technique, especially in the case of complex and non-compact geometries, when no analytical solutions are available and finite element methods require long computational times and large amount of computer memory. Examples of applications are simulating the heat transmission in deviated oil, gas or geothermal wells, designing geothermal reservoirs for underground energy storage or heat pump applications, and modeling heating or cooling elements in industrial processes.

CHAPTER 16

OVERALL CONCLUSIONS AND RECOMMENDATIONS FOR FUTURE WORK

16.1 Overall Conclusions

Techno-economic simulations with the newly-developed computer model GEOPHIRES show that low-grade (~30°C/km) deep geothermal resources are attractive for direct-use heat and cogeneration but not necessarily for solely electricity production. Hybridizing the system, e.g. with biomass, can increase the performance. Utilizing medium-grade (~50°C/km) and high-grade (~70°C/km) resources for solely electricity production is currently already fairly attractive but expected to be even more so in the near future with anticipated improvements in reservoir productivity and thermal drawdown rate.

A techno-economic analysis of hybrid geothermal heat pump systems for cooling-dominated applications, with particular focus on cooling of cellular tower shelters, was conducted. A full-scale and fully equipped hybrid geothermal heat pump system providing cooling to a Verizon Wireless cellular tower shelter in Varna, NY was successfully designed, constructed, and tested, and has been reliably and efficiently operated for two years. A TRNSYS model was developed, validated, and applied to various system configurations to evaluate performance under transient conditions. The conditions analyzed are those of Upstate New York weather, and shelter, cooling, and financial parameters similar to those at the Varna Site. Without considering any subsidies or tax incentives, an air-source heat pump combined with air-economizer is the most cost-effective option followed by a ground-source heat pump hybridized with air-economizer. In terms of energy consumption and CO_2 emissions, hybrid geothermal heat pump systems perform best, illustrating the advantages of hybridizing to counteract the reservoir thermal imbalance due to the cooling-dominated nature of this application. Air-source heat pump systems

are cost-effective for the conditions studied because of low upfront equipment and design costs, no issues with reservoir temperature increase over time, and efficient system performance due to moderate ambient temperatures and lack of auxiliary equipment such as fluid circulation pumps.

In the third part of the dissertation, a novel heat transfer model using the slender-body theory to simulate transient heat transfer of slender, curved bodies in a conductive medium has been presented. The model is most attractive to simulate heat transfer with complex and non-compact geometries for which finite element numerical simulations might be too cumbersome, and no analytical solutions exist. Two case-studies, the first one of two parallel cylinders in close proximity at constant temperature, and the second of one loop of a slinky-coil heat exchanger, show excellent agreement but much faster computational times for the slender-body theory model in comparison with a finite element model. Possible applications are transient heat transfer simulations for deep, deviated oil, gas and geothermal wells, shallow geothermal borehole and slinky-coil heat exchangers, and heating and cooling elements in industrial processes.

16.2 Recommendations for Future Work

It is recommended to upgrade future versions of GEOPHIRES with updated capital and operation & maintenance cost correlations, especially drilling costs since they typically are the largest upfront cost and can change significantly over time. Also the heat-to-electricity conversion efficiency correlations could be upgraded to account for the latest advancements in power plant technology. Since the four reservoir models currently implemented in GEOPHIRES are rather simple, it might be beneficial to incorporate more advanced models, e.g. in TOUGH2, or perform simulations with actual geothermal production data.

GEOPHIRES is continuously being used in our research group, e.g. in a geothermal play fairway analysis project for the Appalachian Basin, as well as in a few U.S. national laboratories and universities. Modifying the code for different platforms beyond Windows, perhaps even with an online version, might expand its user database and increase its reach to other research groups and organizations. Beneficial for future upgrades would be to convert the programming language from FORTRAN to e.g. Python and upgrade the legacy code currently part of the GEOPHIRES source code.

While the GEOPHIRES simulations predict attractive performance of deep geothermal energy for direct-use heat applications, actual systems are still required to confirm cost-competitiveness, scalability, and power output under real-life conditions. Across the world, several successful examples already exist, e.g. geothermal district heating systems in Iceland, Paris, and Boise. Nonetheless, for widespread deployment, non-hydrothermal resources should be exploited, i.e. hot dry rock with EGS technology or hot sedimentary aquifers. Proper research, development & demonstration support is recommended for developing pilot plants serving various direct-use applications, including district heating as well as industrial processes, e.g. biomass drying, food pasteurization, and fish farming, potentially combined in a cascaded way.

The study on hybrid geothermal heat pump systems for cooling-dominated applications continues in our group with the analysis of the system performance in different regions in the country, with different weather, geological and economic conditions. In addition, a detailed study of the impact of groundwater flow, the circulating fluid, advanced dry-cooler control schemes, and different cooling technologies such as direct-exchange heat pumps, on the overall system financial and technical performance would be interesting.

While geothermal heat pumps are a well-known technology in the residential sector allowing to save the homeowner energy and usually also money, great potential lies as

well in the commercial and industrial sector. Specifically for cooling-dominated operation, analysis and development of hybrid geothermal heat pump systems for various applications beyond cellular tower shelters is recommended, e.g. cooling of small data centers, or cooled storage of food and beverages. In addition, a stable multi-year tax incentive program is recommended to shorten payback periods and level the playing field with other energy saving technologies.

APPENDIX A

PERFORMANCE DATASHEETS FOR CLIMATEMASTER HEAT PUMP TRANQUILITY 27 TWO-STAGE (TT) 026

This appendix provides performance datasheets for the ClimateMaster Tranquility 27 Two-Stage (TT) 026 water-to-air heat pump (ClimateMaster, 2012), which are incorporated in the TRNSYS hybrid geothermal heat pump system model discussed in Chapter 9. Performance tables for the heat pump in part load and full load are given in Figures A.1 and A.2, respectively. TC, SC and HR refer to total cooling, sensible cooling, and total heat rejection in thousands of BTU/hour; kW refers to the power consumption in kW and EER is the energy efficiency ratio (see also Chapter 7). These cooling performance parameters are a function of the entering water temperature (EWT), the fluid flow rate (GPM), and the dry-bulb (DB) and wet-bulb (WB) entering air temperature (EAT).

The performance data provided in Figures A.1 and A.2 is only valid for standard entering air temperatures and air flow rates. For deviations in dry-bulb and wet-bulb air temperature, and air flow rate, correction tables are provided in Figure A.3 and Figure A.4, respectively.

References

ClimateMaster (2012). Tranquility 27 Two-Stage (TT) Series Submittal Data, Models TTD/H/V 026-072, 60Hz - HFC-410A. Technical Report, ClimateMaster, Oklahoma City, Oklahoma, United States.

850 CFM Nominal Airflow Heating, 750 CFM Nominal Airflow Cooling

Performance capacities shown in thousands of Btuh

EWT °F	GPM	WPD		Cooling - EAT 80/67 °F						Heating - EAT 70°F				
		PSI	FT	TC	SC	Sens/Tot Ratio	kW	HR	EER	HC	kW	HE	LAT	COP
20	4.5	2.5	5.8	Operation not recommended						11.5	1.10	7.7	80.5	3.1
30	2.3	0.7	1.7	23.3	17.9	0.77	0.59	25.3	39.2	12.7	1.10	8.9	81.8	3.4
	3.4	1.3	3.0	23.1	18.0	0.78	0.55	25.0	41.7	13.2	1.10	9.5	82.4	3.5
	4.5	2.0	4.6	22.9	18.1	0.79	0.54	24.8	42.3	13.5	1.10	9.8	82.7	3.6
40	2.3	0.5	1.2	22.9	17.7	0.77	0.67	25.2	34.4	14.7	1.11	10.9	84.0	3.9
	3.4	1.0	2.4	23.2	17.9	0.77	0.61	25.3	38.2	15.4	1.11	11.7	84.8	4.1
	4.5	1.6	3.8	23.3	17.9	0.77	0.59	25.3	39.7	15.8	1.11	12.1	85.2	4.2
50	2.3	0.4	1.0	22.2	17.4	0.78	0.76	24.8	29.0	16.8	1.11	13.0	86.3	4.4
	3.4	0.9	2.0	22.8	17.6	0.77	0.69	25.1	33.0	17.8	1.11	14.0	87.3	4.7
	4.5	1.4	3.2	23.0	17.7	0.77	0.66	25.2	35.0	18.2	1.11	14.4	87.8	4.8
60	2.3	0.4	1.0	21.1	17.0	0.81	0.88	24.1	24.1	19.0	1.12	15.2	88.7	5.0
	3.4	0.8	1.8	21.9	17.3	0.79	0.79	24.6	27.7	20.1	1.12	16.3	89.8	5.3
	4.5	1.3	2.9	22.3	17.4	0.78	0.75	24.8	29.6	20.7	1.12	16.8	90.5	5.4
70	2.3	0.4	1.0	19.9	16.6	0.83	1.01	23.3	19.7	21.2	1.12	17.4	91.0	5.5
	3.4	0.8	1.8	20.8	16.9	0.81	0.91	23.9	22.8	22.4	1.13	18.5	92.3	5.8
	4.5	1.2	2.7	21.2	17.1	0.80	0.87	24.2	24.4	23.0	1.13	19.1	93.0	6.0
80	2.3	0.5	1.1	18.6	16.0	0.86	1.16	22.5	16.0	23.3	1.13	19.4	93.3	6.0
	3.4	0.8	1.8	19.5	16.4	0.84	1.05	23.1	18.5	24.5	1.13	20.6	94.6	6.3
	4.5	1.2	2.7	20.0	16.6	0.83	1.00	23.4	19.9	25.1	1.14	21.2	95.3	6.5
90	2.3	0.5	1.2	17.2	15.4	0.89	1.32	21.7	13.1	25.2	1.14	21.3	95.4	6.5
	3.4	0.8	1.9	18.1	15.8	0.87	1.21	22.3	15.0	26.4	1.15	22.5	96.7	6.7
	4.5	1.2	2.7	18.6	16.0	0.86	1.16	22.5	16.0	26.9	1.15	23.0	97.3	6.9
100	2.3	0.5	1.2	16.0	14.8	0.92	1.50	21.1	10.7	Operation not recommended				
	3.4	0.8	1.9	16.8	15.2	0.90	1.38	21.5	12.1					
	4.5	1.2	2.7	17.2	15.4	0.89	1.33	21.7	13.0					
110	2.3	0.5	1.1	14.9	14.1	0.95	1.69	20.7	8.8					
	3.4	0.8	1.8	15.6	14.5	0.93	1.57	20.9	9.9					
	4.5	1.1	2.6	15.9	14.7	0.92	1.51	21.1	10.5					
120	2.3	0.3	0.8	14.2	13.7	0.97	1.90	20.6	7.4					
	3.4	0.6	1.5	14.6	13.9	0.96	1.77	20.6	8.2					
	4.5	1.0	2.4	14.9	14.1	0.95	1.71	20.7	8.7					

Interpolation is permissible; extrapolation is not.
All entering air conditions are 80°F DB and 67°F WB in cooling, and 70°F DB in heating.

Figure A.1 – Performance datasheet for ClimateMaster heat pump Tranquility 27 TT 026 in part load.

950 CFM Nominal Airflow Heating, 850 CFM Nominal Airflow Cooling

Performance capacities shown in thousands of Btuh

EWT °F	GPM	WPD		Cooling - EAT 80/67 °F						Heating - EAT 70°F				
		PSI	FT	TC	SC	Sens/Tot Ratio	kW	HR	EER	HC	kW	HE	LAT	COP
20	6.0	3.7	8.6	Operation not recommended						16.6	1.44	11.7	84.2	3.4
30	3.0	1.1	2.5	30.7	21.8	0.71	0.98	34.0	31.3	18.1	1.47	13.1	85.6	3.6
	4.5	2.0	4.6	30.7	21.7	0.71	0.92	33.9	33.6	18.9	1.48	13.8	86.3	3.7
	6.0	3.1	7.1	30.7	21.6	0.70	0.89	33.7	34.6	19.3	1.49	14.2	86.8	3.8
40	3.0	0.9	2.0	30.1	21.6	0.72	1.08	33.8	27.9	20.7	1.51	15.5	88.1	4.0
	4.5	1.6	3.8	30.6	21.8	0.71	1.00	34.0	30.5	21.7	1.53	16.5	89.1	4.2
	6.0	2.6	6.0	30.7	21.8	0.71	0.97	34.0	31.7	22.2	1.53	17.0	89.6	4.2
50	3.0	0.7	1.6	29.2	21.2	0.73	1.20	33.3	24.4	23.4	1.55	18.1	90.8	4.4
	4.5	1.4	3.2	29.9	21.5	0.72	1.11	33.7	27.0	24.6	1.57	19.3	92.0	4.6
	6.0	2.3	5.2	30.2	21.6	0.72	1.07	33.9	28.3	25.3	1.59	19.9	92.6	4.7
60	3.0	0.7	1.5	28.0	20.7	0.74	1.33	32.5	21.1	26.3	1.60	20.8	93.6	4.8
	4.5	1.3	2.9	28.9	21.1	0.73	1.23	33.1	23.5	27.7	1.63	22.2	94.9	5.0
	6.0	2.0	4.7	29.3	21.3	0.73	1.18	33.4	24.8	28.5	1.64	22.9	95.7	5.1
70	3.0	0.6	1.5	26.6	20.1	0.75	1.47	31.6	18.0	29.2	1.65	23.6	96.4	5.2
	4.5	1.2	2.7	27.6	20.5	0.74	1.37	32.3	20.2	30.8	1.68	25.1	98.0	5.4
	6.0	1.9	4.4	28.1	20.7	0.74	1.31	32.6	21.4	31.7	1.70	25.9	98.8	5.5
80	3.0	0.7	1.5	25.0	19.4	0.77	1.64	30.6	15.3	32.1	1.70	26.3	99.2	5.5
	4.5	1.2	2.7	26.1	19.9	0.76	1.52	31.3	17.2	33.9	1.74	28.0	101.0	5.7
	6.0	1.8	4.2	26.7	20.1	0.75	1.46	31.7	18.2	34.9	1.76	28.9	101.9	5.8
90	3.0	0.7	1.6	23.4	18.7	0.80	1.82	29.6	12.9	35.0	1.76	29.0	102.0	5.8
	4.5	1.2	2.7	24.5	19.2	0.78	1.70	30.3	14.5	36.9	1.80	30.7	103.8	6.0
	6.0	1.8	4.1	25.1	19.4	0.77	1.63	30.6	15.3	37.9	1.82	31.6	104.8	6.1
100	3.0	0.7	1.6	21.8	18.1	0.83	2.02	28.7	10.8	Operation not recommended				
	4.5	1.2	2.7	22.9	18.5	0.81	1.89	29.3	12.1					
	6.0	1.8	4.1	23.4	18.7	0.80	1.82	29.6	12.8					
110	3.0	0.7	1.5	20.3	17.7	0.87	2.25	28.0	9.0					
	4.5	1.1	2.6	21.3	17.9	0.84	2.10	28.5	10.1					
	6.0	1.7	4.0	21.8	18.1	0.83	2.03	28.7	10.7					
120	3.0	0.5	1.2	19.0	17.4	0.91	2.50	27.5	7.6					
	4.5	1.0	2.4	19.8	17.5	0.89	2.34	27.8	8.5					
	6.0	1.7	3.9	20.2	17.6	0.87	2.26	28.0	8.9					

Interpolation is permissible; extrapolation is not.
All entering air conditions are 80°F DB and 67°F WB in cooling, and 70°F DB in heating.

Figure A.2 – Performance datasheet for ClimateMaster heat pump Tranquility 27 TT 026 in full load.

a) Part Load

Airflow	Cooling				Heating		
% of Rated	Total Capacity	Sensible Capacity	Power	Heat of Rejection	Heating Capacity	Power	Heat of Extraction
60%	0.925	0.788	0.913	0.922	0.946	1.153	0.896
69%	0.946	0.829	0.926	0.942	0.959	1.107	0.924
75%	0.960	0.861	0.937	0.955	0.969	1.078	0.942
81%	0.972	0.895	0.950	0.968	0.977	1.053	0.959
88%	0.983	0.930	0.965	0.979	0.985	1.032	0.974
94%	0.992	0.965	0.982	0.990	0.993	1.014	0.988
100%	1.000	1.000	1.000	1.000	1.000	1.000	1.000
106%	1.007	1.033	1.020	1.009	1.006	0.989	1.011
113%	1.012	1.064	1.042	1.018	1.012	0.982	1.019
119%	1.016	1.092	1.066	1.025	1.018	0.979	1.027
125%	1.018	1.116	1.091	1.032	1.022	0.977	1.033
130%	1.019	1.132	1.112	1.037	1.026	0.975	1.038

b) Full Load

Airflow	Cooling				Heating		
% of Rated	Total Capacity	Sensible Capacity	Power	Heat of Rejection	Heating Capacity	Power	Heat of Extraction
60%	0.920	0.781	0.959	0.927	0.946	1.241	0.881
69%	0.942	0.832	0.964	0.946	0.960	1.163	0.915
75%	0.956	0.867	0.696	0.959	0.969	1.115	0.937
81%	0.969	0.901	0.975	0.970	0.978	1.076	0.956
88%	0.981	0.934	0.982	0.981	0.986	1.043	0.973
94%	0.991	0.967	0.990	0.991	0.993	1.018	0.988
100%	1.000	1.000	1.000	1.000	1.000	1.000	1.000
106%	1.007	1.033	1.011	1.008	1.006	0.990	1.010
113%	1.013	1.065	1.023	1.015	1.012	0.986	1.017
119%	1.018	1.098	1.036	1.021	1.017	0.983	1.024
125%	1.021	1.131	1.051	1.026	1.021	0.981	1.030
130%	1.023	1.159	1.063	1.030	1.024	0.979	1.034

Figure A.3 – Airflow correction tables for ClimateMaster heat pump Tranquility 27 TT 026 for part load (a) and full load (b) operation.

a) Part Load

Cooling													
Entering Air WB°F	Total Capacity	Sensible Cooling Capacity Multiplier - Entering DB °F										Power	Heat of Rejection
		60	65	70	75	80	80.6	85	90	95	100		
45	0.832	1.346	1.461	1.603	*	*	*	*	*	*	*	0.946	0.853
50	0.850	1.004	1.174	1.357	*	*	*	*	*	*	*	0.953	0.870
55	0.880	0.694	0.902	1.115	1.331	*	*	*	*	*	*	0.964	0.896
60	0.922		0.646	0.875	1.103	1.329	1.356	*	*	*	*	0.977	0.932
65	0.975			0.639	0.869	1.096	1.123	1.320	*	*	*	0.993	0.979
66.2	0.990			0.582	0.812	1.039	1.066	1.262	1.482	*	*	0.997	0.991
67	1.000			0.545	0.774	1.000	1.027	1.223	1.444	*	*	1.000	1.000
70	1.040				0.630	0.853	0.880	1.075	1.297	1.517	*	1.011	1.035
75	1.117					0.601	0.627	0.821	1.046	1.275	1.510	1.033	1.101

b) Full Load

Cooling													
Entering Air WB°F	Total Capacity	Sensible Cooling Capacity Multiplier - Entering DB °F										Power	Heat of Rejection
		60	65	70	75	80	80.6	85	90	95	100		
45	0.876	1.286	1.302	1.389	*	*	*	*	*	*	*	0.981	0.895
50	0.883	1.002	1.099	1.241	*	*	*	*	*	*	*	0.985	0.901
55	0.903	0.706	0.871	1.060	1.271	*	*	*	*	*	*	0.989	0.918
60	0.935		0.617	0.844	1.079	1.319	1.349	*	*	*	*	0.993	0.945
65	0.979			0.595	0.849	1.096	1.128	1.342	*	*	*	0.998	0.982
66.2	0.991			0.531	0.789	1.040	1.070	1.284	1.522	*	*	0.999	0.993
67	1.000			0.486	0.747	1.000	1.030	1.245	1.481	*	*	1.000	1.000
70	1.035				0.583	0.842	0.873	1.090	1.327	1.552	*	1.003	1.030
75	1.105					0.552	0.584	0.811	1.057	1.290	1.510	1.008	1.088

Figure A.4 – Air temperature correction tables for ClimateMaster heat pump Tranquility 27 TT 026 for part load (a) and full load (b) operation.

APPENDIX B

BOREHOLE HEAT EXCHANGER TRANSIENT HEAT TRANSFER MODEL

This appendix presents a computationally-efficient, hybrid heat transfer model for simulating short- and long-term transient heat exchange with borehole heat exchangers (BHEs) in a conduction-dominated medium. This model is incorporated in the TRNSYS model discussed in Chapter 9.

B.1 Borehole Heat Exchanger Heat Transfer Problem

A simplified single-U (1-U) BHE is shown in Figure B.1. A heat exchanger fluid, typically water plus antifreeze, flows downwards and then upwards through the pipe while exchanging heat with the surrounding grout and soil or rock (ground). The ground undergoes heat transfer through conduction only with corresponding governing equation:

$$\frac{1}{\alpha_s}\frac{\partial T_s}{\partial t} - \nabla^2 T_s = 0 \tag{B.1}$$

with T_s and α_s the ground temperature and thermal diffusivity, respectively. It is assumed the ground has uniform and constant thermophysical properties, and has a far-field, initial, and surface temperature of T_0. The grout and the pipes undergo transient heat conduction as well with the same governing equation (Equation (B.1)) applicable with the thermal diffusivity for the grout and pipe material, respectively. At each boundary, the temperature T and heat flux Q are preserved.

The fluid at temperature T_f exchanges heat with the pipe wall at temperature T_p though convection. The governing equation when neglecting thermal diffusion within the water because of high Peclet numbers is:

$$\rho c_p \frac{\partial T_f}{\partial t} + \rho c_p U \frac{\partial T_f}{\partial z} = \frac{2h}{r_{p,i}}(T_p - T_f) \tag{B.2}$$

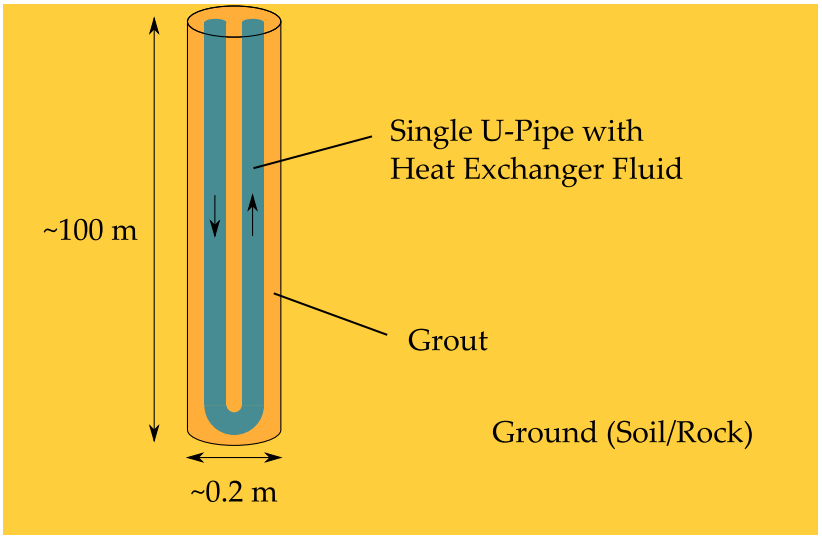

Figure B.1 – Simplified diagram of single-U BHE. Drawing not to scale.

with ρ, c_p, and U the density, specific heat capacity, and velocity of the fluid, respectively. The heat transfer coefficient h can be calculated with appropriate Nusselt correlations for forced fluid flow inside a pipe. The internal radius of the pipe is represented by $r_{p,i}$. The independent variables t and z are the time and vertical coordinate along the fluid direction, respectively. The temperature at the inlet T_{inlet} is a specified boundary condition and the outlet temperature T_{outlet} is being solved for.

B.2 Existing BHE Heat Transfer Models

The heat transfer problem presented in the previous section is rather difficult to solve because of the presence of various medium properties, and both short and long time-scales, and short and long length-scales. Several solution methods are available from simple but less accurate analytical tools to full three-dimensional but computationally-intense finite element models. Some excellent overviews of simulation tools have been provided by Yavuzturk (1999), Xu (2007), Yang et al. (2010), Al-Khoury (2012), and He (2012).

In simple models, the heat transfer in the ground is often simplified using the infinite line source model (Ingersoll et al., 1954), infinite cylindrical source model (Carslaw and Jaeger, 1959), or finite line source model (Zeng et al., 2002). The (average) temperature at the borehole wall T_b is calculated by typically assuming constant heat exchange along the BHE with the surrounding ground. This heat exchange can be discretized in the time domain, leading to response factor functions, also called g-functions (Eskilson, 1987). A g-function can be defined as the (average) temperature rise at the borehole wall caused by a unit heat pulse active for a certain time period. Superposition is used to account for various heat pulses and for multiple BHE in a field. One is not restricted to the aforementioned analytical tools to derive g-functions; any method including numerical tools can be applied. In the BHE hybrid heat transfer model presented in the next section, g-functions are calculated using the slender body-theory approach, discussed in Part III of the dissertation. Originally developed for long time-scales, g-functions have been extended to short time-scales by Yavuzturk (1999) by adjusting them to account for transient effects inside the BHE. Another popular model for the heat transfer in the ground is the Duct Storage Model (DST), developed by (Hellström, 1991). In this model, the temperature in the field is calculated as the superposition of the solution to three heat transfer problems: (1) a global heat conduction problem of the heat exchange between the entire field and the surrounding undisturbed ground (numerically solved), (2) a local heat conduction problem in the ground directly surrounding one BHE (numerically solved), and (3) a steady-state heat conduction problem for heat transfer between the local and global domain (analytically solved).

A ground heat transfer model is coupled at the borehole wall to a heat transfer model inside the BHE. Often the thermal mass of the grout, pipes and fluid are neglected, which is only accurate for long-term simulations. In this case, the BHE is solely represented by a set of thermal resistances, e.g. the borehole thermal resistance R_b, and internal resistance R_a, discussed in more detail in other works such as (He, 2012). Several models have been

developed to calculate these resistances with an overview provided by Lamarche et al. (2010). The thermal mass inside the BHE can be accounted for by incorporating a thermal capacity for the grout, fluid and maybe even pipes. Examples are the models by Bauer et al. (2011a) and Maestre et al. (2015), which are valid at short time-scales.

Other interesting methods for solving the BHE heat transfer problem, applicable at short and long time-scales, are utilizing the Fourier transform (Al-Khoury, 2010), or Laplace transform (Bandyopadhyay et al., 2008; Beier, 2014). Finally, the most accurate approach but requiring the longest computational times, are simulating the heat transfer problem with full three-dimensional numerical models based on finite volume methods, e.g. (Rees and He, 2013), or finite element methods, e.g. (Diersch et al., 2011a,b).

B.3 Novel Hybrid BHE Heat Transfer Model

In the study on hybrid geothermal heat pump systems (Part II of this dissertation), a large number of cases are investigated, with system lifetimes up to 20 years and heat pump operational time scales of less than one hour. Therefore, it is essential to have a computationally-fast BHE heat transfer model that can handle both long and short time-scales. Inspired by the work of Bauer et al. (2011a) and Maestre et al. (2015), a novel model is presented in this section which includes elements of both these works while incorporating some modifications as well.

For the heat transfer in the ground outside the BHE, we will rely on g-functions since this methodology has been shown many times to perform well. In this approach, an average borehole wall temperature T_b, after discretizing the heat exchange Q in the time domain, is calculated for time step n as:

$$T_{b,n} = T_0 + \frac{1}{2\pi k} \sum_i Q_i \left[g\left(\frac{t_n - t_{i-1}}{t_s}\right) - g\left(\frac{t_n - t_i}{t_s}\right) \right] \tag{B.3}$$

with t_s a time scale, typically set at $L^2/(9\alpha)$ with L the length of the BHE, and with k the thermal conductivity of the medium. As defined earlier, T_0 is the initial, far-field, and surface temperature. The summation in Equation (B.3) ads up the temperature contributions from each heat pulse Q_i with i from 1 to n with t_0 being the start time (0 s). The g-function itself depends, besides the time, on the length and radius of the BHE as well as the BHE field configuration. Figure B.2 illustrates the g-functions for several configurations for a BHE length of 100 m and radius of 0.1 m. The spacing in between the BHEs is 5 m. They are calculated using the slender-body theory model (Part III) and represent the average borehole wall temperature assuming a unit heat pulse uniform in space along the BHE and constant in time from 0 to t, with the BHE(s) placed in a semi-infinite medium with constant temperature T_0 at the surface.

To decrease the computational time in simulations with many time steps, a load-aggregation algorithm is applied, based on the work by Yavuzturk (1999). With this algorithm, past heat pulses are combined within time blocks of e.g. 500 hours and represented by their average value for each time period.

In contrast to some previous work on g-functions such as by Yavuzturk (1999), the g-functions at short time-scales here are not adjusted to account for transient heat effects occurring inside the BHE. Rather, they represent the temperature at the borehole wall caused by a unit heat pulse occurring at the borehole wall, similar to their definition for long time-scales. In this work, the short time-scale effects are captured by the internal BHE heat transfer model discussed below. As a result, the heat exchange Q in Equation (B.3) represents the heat exchange between the BHE and the ground, which is not necessarily equal to the heat exchange between the fluid and the BHE, unless the heat exchange inside the BHE has reached steady-state.

The BHE itself is discretized internally along the vertical direction as well as in the horizontal cross-sectional plane, shown in Figure B.3. Unlike the models of Bauer et al.

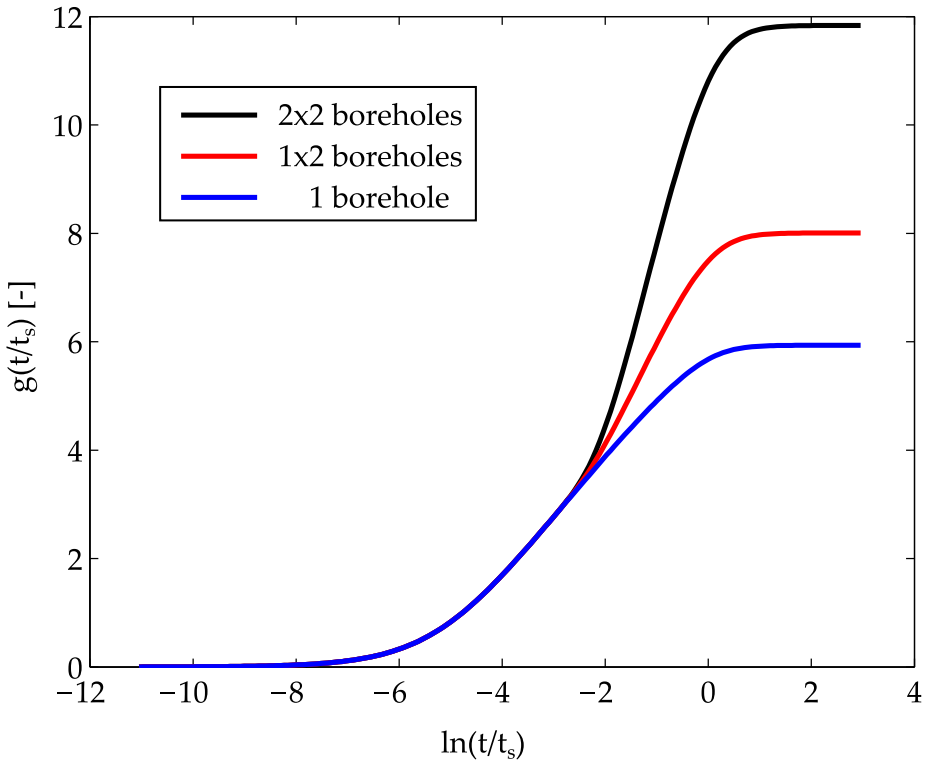

Figure B.2 – Plot of g-functions as a function of dimensionless time for several BHE field configurations, calculated with slender-body theory model (Part III). The time scale t_s is defined as $L^2/(9\alpha)$. The BHE length L and radius r_b are 100 m and 0.1 m, respectively. Spacing between boreholes is 5 m.

(2011a) and Maestre et al. (2015), the grout around each pipe is represented by several nodes instead of only one, in order to allow for better capturing the short time-scale phenomena (see Section B.4). The number of cylindrical shells around each pipe in Figure B.3 is two but it could be any number as long as the largest shells still fit together in the BHE. Each pipe and grout zone has a heat capacity C and is represented by a temperature T. The heat transfer in between contacting zones has a corresponding thermal resistance R. The subscripts d and u refer to the side of the BHE at which the fluid flows downwards and upwards, respectively. It is assumed the BHE is symmetrical, i.e. the upward and downward pipe are identical and located on the horizontal axis at the same distance from the center. The network of thermal resistances and capacities within one layer is shown in Figure B.4.

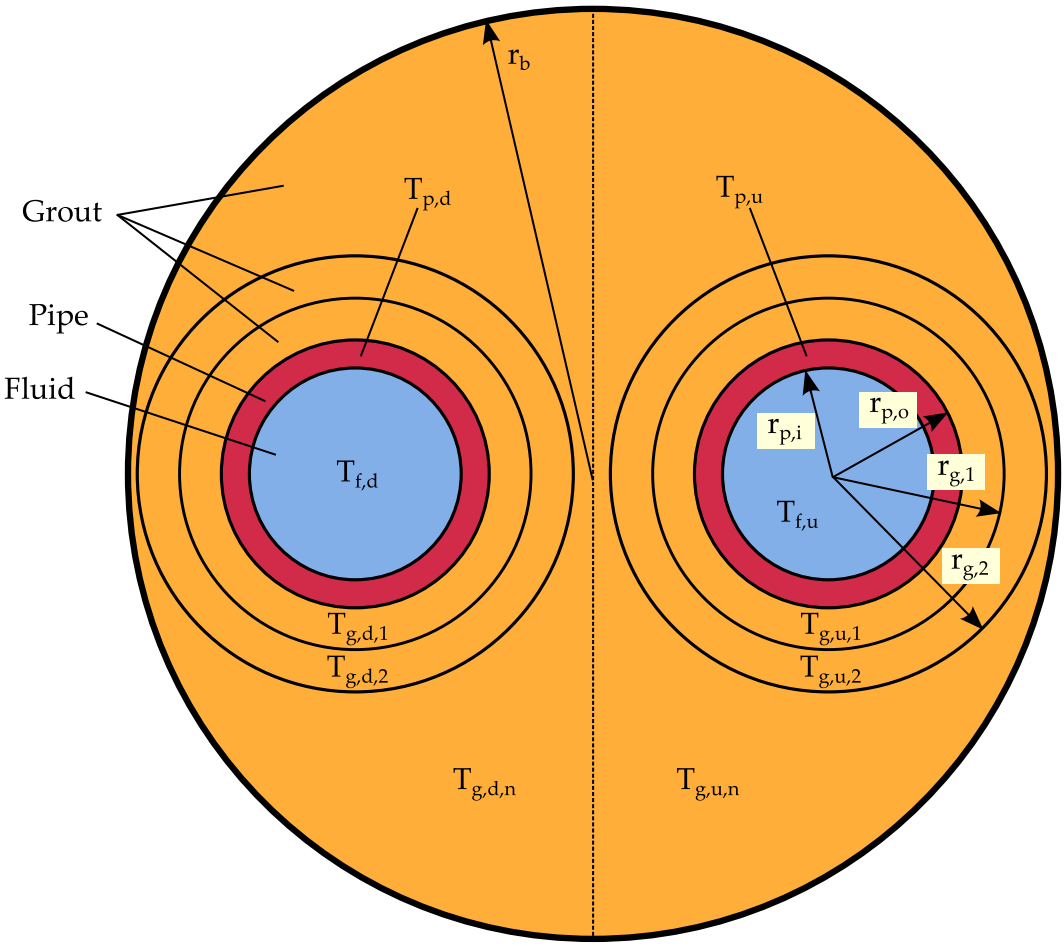

Figure B.3 – Cross section of BHE illustrating spatial discretization in horizontal plane. Left section (subscript d) refers to side with fluid flowing downwards. Right section (subscript u) refers to side with fluid flowing upwards. Grout directly surrounding the pipes is discretized into cylindrical shells to allow for accurate capturing of short-term transient heat exchange.

The units of C and R are J/K and m·K/W. The heat capacity of the pipe and grout zones are simply calculated as the specific heat capacity and density of the material times the area of the zone times the thickness of the layer times. For example, the heat capacity of the pipe C_p is calculated as:

$$C_p = \rho_p c_{p,p} \pi (r_{p,o}^2 - r_{p,i}^2) \Delta z \tag{B.4}$$

with ρ_p and $c_{p,p}$ the density and specific heat capacity of the pipe material, respectively, and Δz the layer thickness. The thermal resistances for the cylindrical shells can easily be calculated using simple expressions. For example, the thermal resistance for heat

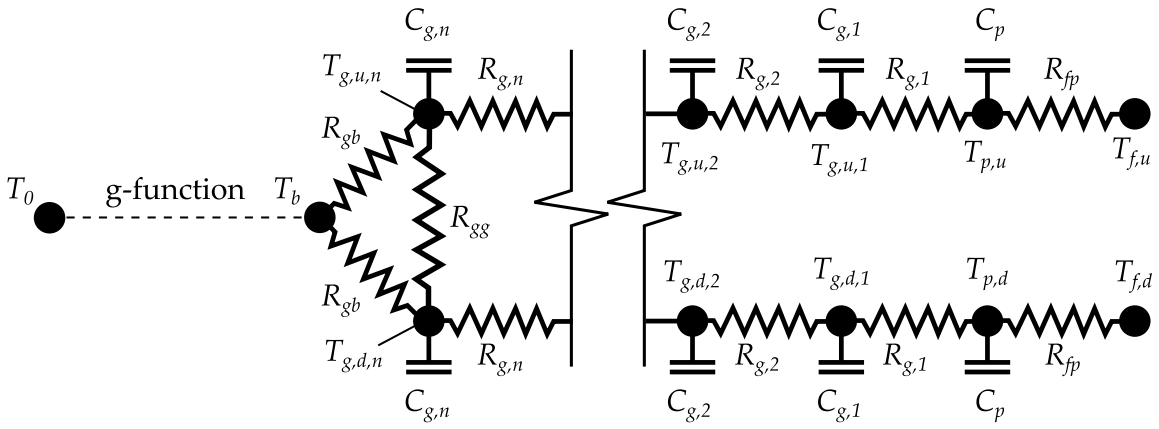

Figure B.4 – Network of thermal resistances (R) and capacities (C) within 1 horizontal layer of a discretized BHE. Each black solid circle corresponds to a temperature T in the network. The subscripts f, p, g, b, u, d, and n refer to fluid, pipe, grout, borehole wall, upwards, downwards, and n$^{\text{th}}$ grout zone.

exchange between the fluid and the pipe R_{fp} involves a convective and conductive component:

$$R_{fp} = \frac{1}{\pi k_f Nu} + \frac{1}{2\pi k_p} \ln\left(\frac{r_{p,o} + r_{p,i}}{2r_{p,i}}\right) \tag{B.5}$$

with k_f and k_p the thermal conductivity of the fluid and pipe, respectively, and Nu the Nusselt number for forced flow inside the pipe (Bergman et al., 2011). The thermal resistance between the first grout zone and the pipe is calculated as:

$$R_{g,1} = \frac{1}{2\pi k_p} \ln\left(\frac{2r_{p,o}}{r_{p,o} + r_{p,i}}\right) + \frac{1}{2\pi k_g} \ln\left(\frac{r_{g,1} + r_{p,o}}{2r_{p,o}}\right) \tag{B.6}$$

with k_g the thermal conductivity of the grout. The more exotic thermal resistances $R_{g,n}$, R_{gg}, and $R_{g,b}$ are calculated with equations provided by Bauer et al. (2011b).

The BHE is discretized in the vertical direction along the BHE into several layers, as shown in Figure B.5. The layers are coupled through fluid advection within the upward and downward pipe, and conduction in the grout and pipes as represented by thermal resistances $R_{gg,n}$ to R_{pp}. These resistances are easily calculated using expressions for one-dimensional conduction in rectangular coordinates. R_{pp} for example, the thermal resistance between two pipe segments, is calculated as:

$$R_{pp} = \frac{\Delta z}{k_p \pi (r_{p,o}^2 - r_{p,i}^2)} \tag{B.7}$$

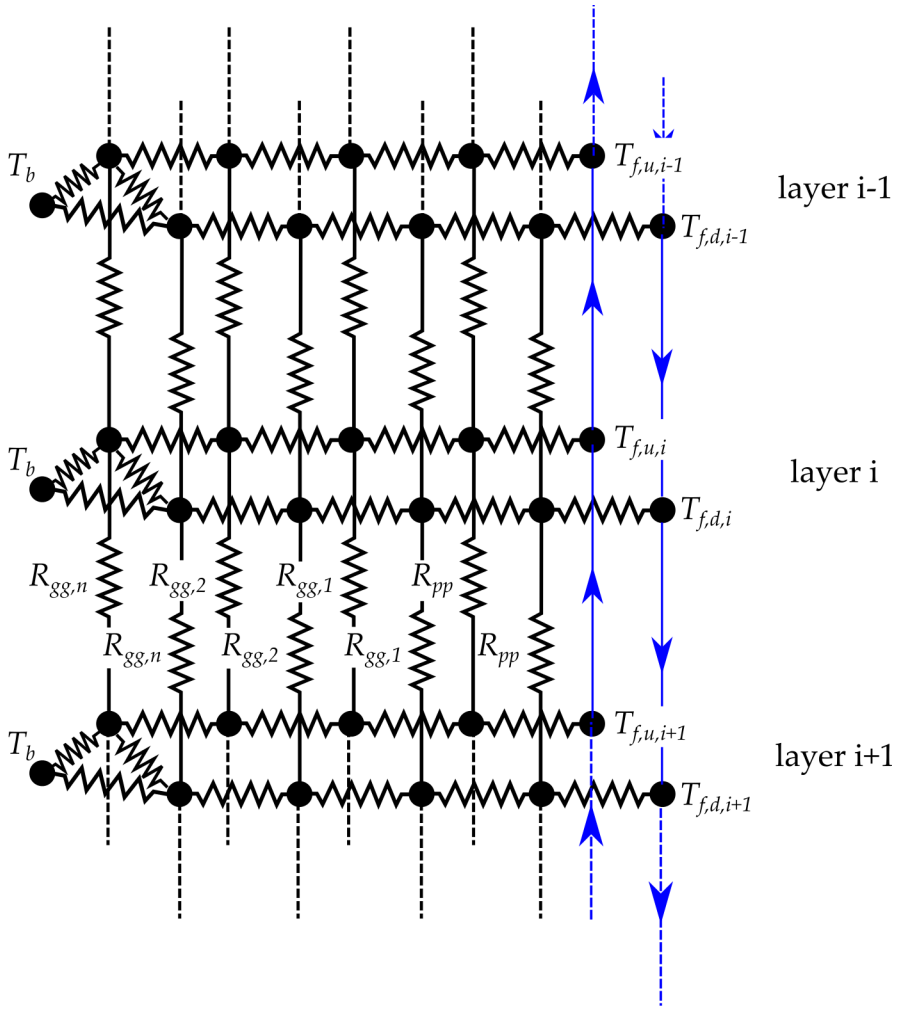

Figure B.5 – Diagram showing layered thermal network within BHE. Different layers are coupled through conductive heat exchange in the grout and pipes with corresponding thermal resistances $R_{gg,n}$ to R_{pp}, and fluid advection within the pipes labeled by blue arrows. Each layer has an identical borehole wall temperature T_b.

which assumes uniform vertical discretization for which Δz, the layer thickness, is equal to the distance between two pipe temperature nodes. The borehole wall temperature T_b is identical for each layer, a characteristic of the g-functions approach.

A simple energy balance can be constructed for each temperature node in the thermal network. For example, for the first grout cylindrical shell on the downward side:

$$C_{g,1}\frac{\partial T_{g,d,1,i}}{\partial t} = \frac{T_{g,d,2,i} - T_{g,d,1,i}}{R_{g,1}} + \frac{T_{p,d,i} - T_{g,d,1,i}}{R_{fp}} + \frac{T_{g,d,1,i+1} - T_{g,d,1,i}}{R_{gg,1}} + \frac{T_{g,d,1,i-1} - T_{g,d,1,i}}{R_{gg,1}} \tag{B.8}$$

with the additional subscripts i, $i+1$, and $i-1$ referring to the layer number. A simple

implicit scheme is utilized for the time integration to ensure high stability. More advanced schemes such as Runge-Kutta methods are available, but are not investigated here.

For the fluid energy balance, we directly incorporate the analytical solution for fluid flow in a pipe with constant wall temperature. For a certain pipe segment and during a certain time step, the wall temperature, here the pipe temperature T_p, can be assumed constant. When neglecting the thermal diffusion within the fluid, the outlet temperature is calculated as (Van Genuchten and Alves, 1982):

$$T_{outlet} = T_p + (T_{inlet} - T_p) \cdot \exp\left(-\frac{\Delta z}{R_{fp} v}\right) \tag{B.9}$$

with T_{inlet} the segment inlet temperature, and assuming that the fluid reached the end of the segment. In Equation (B.9), the parameter v is calculated as:

$$v = \rho c_p U \pi r_{p,i}^2 = m c_p \tag{B.10}$$

with m the fluid mass flow rate. For the heat transfer within the BHE, the time step size chosen internally in the algorithm corresponds to the time period for the fluid flowing through one pipe segment. As a result, the inlet temperature in Equation (B.9) is the outlet temperature of the previous segment at the previous internal time step. By relying on the analytical solution and with judicious choice of the internal time step, numerical diffusion is limited, and high stability and accuracy are obtained. During a simulation, the flow rate m is allowed to vary.

The above equations have been implemented as a simulation tool in MATLAB (MathWorks, 2012) and coupled to TRNSYS (see Chapter 9). It can be considered a hybrid BHE heat transfer model, since it relies on both analytical as well as numerical equations, and involves both g-functions as well as a thermal resistance - capacity ("*RC*") network. Other types of heat exchangers (e.g. double-U (2-U) and coaxial) are not discussed here but can be implemented with the presented model as well.

Table B.1 – Case-study parameter values for validating BHE heat transfer model.

BHE length	L	100 m
BHE radius	r_b	0.065 m
Pipe inner radius	$r_{p,i}$	0.0131 m
Pipe outer radius	$r_{p,o}$	0.0160 m
Spacing between center of pipes	w	0.06 m
Ground thermal conductivity	k_s	2.2 W/(m·K)
Ground thermal diffusivity	α_s	$9.9548 \cdot 10^{-7}$ m^2/s
Grout thermal conductivity	k_g	2.3 W/(m·K)
Grout thermal diffusivity	α_g	$1.0502 \cdot 10^{-6}$ m^2/s
Pipe thermal conductivity	k_p	0.38 W/(m·K)
Pipe thermal diffusivity	α_p	$1.6579 \cdot 10^{-7}$ m^2/s
Fluid density	ρ	1000 kg/m^3
Fluid specific heat capacity	c_p	4130 J/(kg·K)
Fluid thermal conductivity	k	0.6405 W/(m·K)
Fluid dynamic viscosity	μ	$0.54741 \cdot 10^{-3}$ kg/(m·s)
Fluid mass flow rate	m	0.25 kg/s
Fluid inlet temperature	T_{inlet}	80°C
Initial temperature	T_0	10°C
Vertical discretization	N	20

B.4 Validation Case-Study

The presented hybrid BHE heat transfer model is validated in this section with a short time-scale case-study, identical to one of the case-studies discussed by Bauer et al. (2011a). The outlet temperature for a single-U BHE with fully described geometry and material and fluid properties is simulated for known inlet temperature for a time period of 180 minutes. All parameters are listed in Table B.1.

The simulation results for the outlet temperature as a function of time are shown in Figure B.6. The result of the model with one node for the pipe and four nodes for the grout (at each side) compares well with the result of an ANSYS reference simulation (taken from (Bauer et al., 2011a)). A model with only one node for the grout at each side overpredicts the temperature initially but eventually produces the same result.

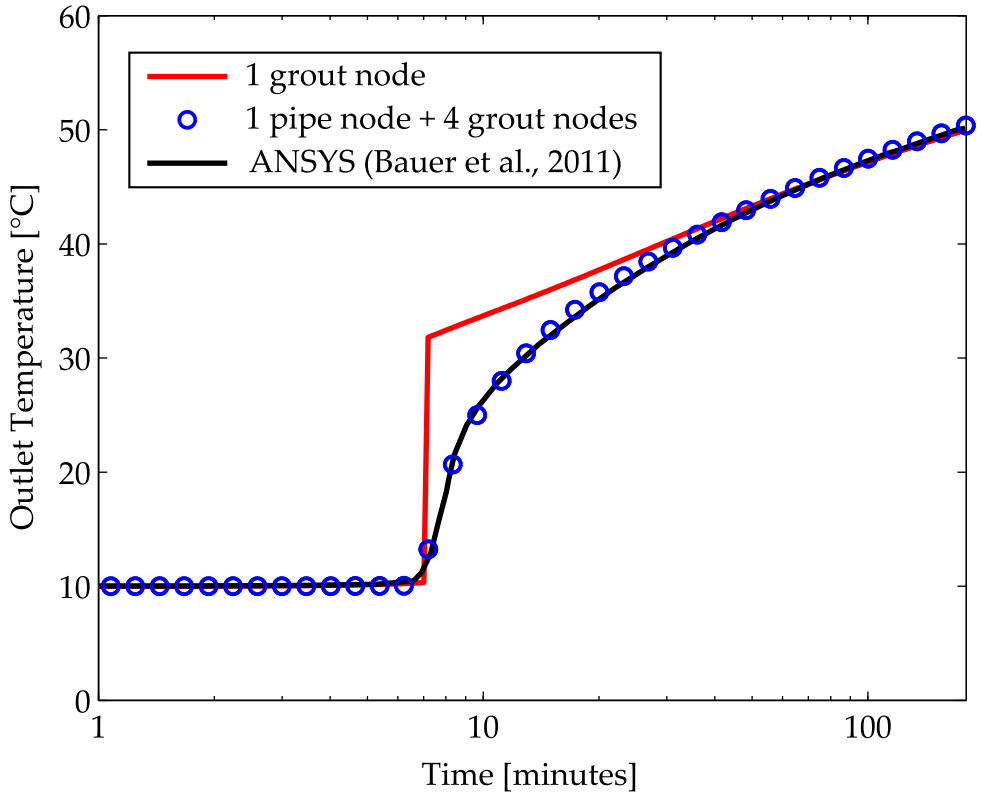

Figure B.6 – Case-study simulation results for validating hybrid BHE heat transfer model show good agreement between model with one node for pipe and four nodes for grout (at each side) and ANSYS reference case. Model with one node for the grout initially overpredicts the outlet temperature but eventually predicts the same result.

References

Al-Khoury, R. (2010). Spectral framework for geothermal borehole heat exchangers. *International Journal of Numerical Methods for Heat & Fluid Flow*, 20 (7): 773–793.

Al-Khoury, R. (2012). *Computational Modeling of Shallow Geothermal Systems*. CRC Press.

Bandyopadhyay, G., Gosnold, W., and Mann, M. (2008). Analytical and semi-analytical solutions for short-time transient response of ground heat exchangers. *Energy and Buildings*, 40 (10): 1816–1824.

Bauer, D., Heidemann, W., and Diersch, H.-J. (2011a). Transient 3d analysis of borehole heat exchanger modeling. *Geothermics*, 40 (4): 250–260.

Bauer, D., Heidemann, W., Müller-Steinhagen, H., and Diersch, H.-J. (2011b). Thermal resistance and capacity models for borehole heat exchangers. *International Journal of Energy Research*, 35 (4): 312–320.

Beier, R. A. (2014). Transient heat transfer in a u-tube borehole heat exchanger. *Applied Thermal Engineering*, 62 (1): 256–266.

Bergman, T. L., Lavine, A. S., Incropera, F. P., and Dewitt, D. P. (2011). *Introduction to heat transfer*. John Wiley & Sons, 6th edition.

Carslaw, H. S. and Jaeger, J. C. (1959). *Conduction of heat in solids*. Clarendon Press, Oxford.

Diersch, H.-J., Bauer, D., Heidemann, W., Rühaak, W., and Schätzl, P. (2011a). Finite element modeling of borehole heat exchanger systems: Part 1. fundamentals. *Computers & Geosciences*, 37 (8): 1122–1135.

Diersch, H.-J., Bauer, D., Heidemann, W., Rühaak, W., and Schätzl, P. (2011b). Finite element modeling of borehole heat exchanger systems: Part 2. numerical simulation. *Computers & Geosciences*, 37 (8): 1136–1147.

Eskilson, P. (1987). *Thermal Analysis of Heat Extraction Boreholes*. PhD Dissertation, Lund University, Lund, Sweden.

He, M. (2012). *Numerical modelling of geothermal borehole heat exchanger systems*. PhD Dissertation, De Montfort University, Leicester, United Kingdom.

Hellström, G. (1991). *Ground Heat Storage: Thermal Analyses of Duct Storage Systems*. PhD Dissertation, Lund University, Lund, Sweden.

Ingersoll, L., Zobel, O. J., and Ingersoll, A. C. (1954). *Heat Conduction: With Engineering Geological And Other Applications*. Oxford And Ibh Publishing Co.; Calcutta; Bombay; New Delhi.

Lamarche, L., Kajl, S., and Beauchamp, B. (2010). A review of methods to evaluate borehole thermal resistances in geothermal heat-pump systems. *Geothermics*, 39 (2): 187–200.

Maestre, I. R., Gallero, F. J. G., Gómez, P. Á., and Pérez-Lombard, L. (2015). A new rc and g-function hybrid model to simulate vertical ground heat exchangers. *Renewable Energy*, 78: 631–642.

MathWorks (2012). *MATLAB Release 2012a*, The Mathworks, Inc., Natick, Massachusetts, United States.

Rees, S. J. and He, M. (2013). A three-dimensional numerical model of borehole heat exchanger heat transfer and fluid flow. *Geothermics*, 46: 1–13.

Van Genuchten, M. T. and Alves, W. J. (1982). Analytical solutions of the one-dimensional convective-dispersive solute transport equation. Technical Report, United States Department of Agriculture, Technical Bulletin No. 1661, 151p.

Xu, X. (2007). *Simulation and optimal control of hybrid ground source heat pump systems*. PhD Dissertation, Oklahoma State University, Stillwater, Oklahoma, United States.

Yang, H., Cui, P., and Fang, Z. (2010). Vertical-borehole ground-coupled heat pumps: a review of models and systems. *Applied Energy*, 87 (1): 16–27.

Yavuzturk, C. (1999). *Modeling of vertical ground loop heat exchangers for ground source heat pump systems*. PhD Dissertation, Oklahoma State University, Stillwater, Oklahoma, United States.

Zeng, H., Diao, N., and Fang, Z. (2002). A finite line-source model for boreholes in geothermal heat exchangers. *Heat TransferAsian Research*, 31 (7): 558–567.

APPENDIX C

TRNSYS SIMULATION RESULTS

This chapter provides detailed simulation results for the various TRNSYS cases studied in Chapter 9. Reported are the total cost of ownership (TCO) in $1,000, the lifetime electricity consumption in MWh_e, lifetime CO_2 emissions in million metric tons, the average heat pump (HP) coefficient of performance (COP) (dimensionless) and the borehole heat exchanger (BHE) configuration. The lifetime electricity consumption and CO_2 emissions do not account for the installation of the system. For cases involving a ground-source heat pump (GSHP), the average heat pump COP does account for the electricity consumption of the fluid circulation pump. Table C.1 provides the results for the total BHE depth sensitivity analysis for Case 1 (GSHP only). Tables C.2, C.3, C.4, C.5, and C.6 provide the results of the sensitivity analysis of the shelter heat generation, reservoir thermal conductivity, electricity rate, net discount rate, and drilling costs, respectively. ASHP, AE, and DC refer to air-source heat pump, air-economizer, and dry-cooler, respectively.

Table C.1 – Effect of total BHE depth on system performance in Case 1 (GSHP only) in base case scenario.

Total BHE Depth	BHE Configuration	TCO ($1,000)	Electricity Consumption (MWh_e)	CO_2 Emissions (million metric tons)	Average HP COP [-]
360 m	3 x 120 m	93.8	566	105.3	3.42
390 m	3 x 130 m	90.9	522	97.2	3.70
420 m	3 x 140 m	88.8	487	90.5	3.97
450 m	3 x 150 m	87.6	460	85.6	4.20
480 m	4 x 120 m	88.6	455	84.7	4.25
510 m	4 x 127.5 m	88.0	435	80.8	4.45
540 m	4 x 135 m	87.8	417	77.6	4.64
570 m	4 x 142.5 m	87.8	403	75	4.8
600 m	4 x 150 m	88.1	391	72.7	4.95
630 m	6 x 105 m	90.1	396	73.7	4.88
660 m	6 x 110 m	90.4	384	71.5	5.03
690 m	6 x 115 m	91.0	376	69.9	5.15
720 m	6 x 120 m	91.8	369	68.6	5.25

Table C.2 – Sensitivity of TRNSYS simulation results to shelter heat generation. All other parameters are kept the same as in the base case scenario. Results for 11.5 kW_{th} are provided in Table 9.4.

Case	TCO ($1,000)	Electricity Consumption (MWh_e)	CO_2 Emissions (million metric tons)	Average HP COP [-]	BHE Configuration
8.5 kW_{th} Shelter Heat Generation					
GSHP	66.0	277	51.5	5.09	3 x 130 m
GSHP + AE	48.4	145	26.9	4.76	2 x 115 m
GSHP + DC	59.8	302	56.1	6.00	2 x 95 m
ASHP	62.1	430	79.9	3.28	N/A
ASHP + AE	45.1	228	42.4	3.02	N/A
10 kW_{th} Shelter Heat Generation					
GSHP	76.7	352	65.4	4.76	3 x 150 m
GSHP + AE	53.9	178	33.2	4.59	2 x 135 m
GSHP + DC	68.0	366	68.1	5.58	2 x 110 m
ASHP	70.4	510	94.8	3.28	N/A
ASHP + AE	49.5	271	50.4	3.02	N/A

Table C.3 – Sensitivity of TRNSYS simulation results to reservoir thermal conductivity. All other parameters are kept the same as in the base case scenario. Results for 2.0 W/(m·K) are provided in Table 9.4.

Case	TCO ($1,000)	Electricity Consumption (MWh_e)	CO_2 Emissions (million metric tons)	Average HP COP [-]	BHE Configuration
1.0 W/(m·K) Reservoir Thermal Conductivity					
GSHP	114.4	507	94.4	3.81	6 x 150 m
GSHP + AE	73.9	258	47.9	3.67	4 x 127.5 m
GSHP + DC	85.3	447	83.1	5.09	3 x 133.33 m
3.0 W/(m·K) Reservoir Thermal Conductivity					
GSHP	77.8	371	69.1	5.21	3 x 143.33 m
GSHP + AE	55.4	197	36.7	4.83	2 x 130 m
GSHP + DC	72.4	408	75.9	5.67	2 x 110 m
4.0 W/(m·K) Reservoir Thermal Conductivity					
GSHP	73.0	359	66.7	5.39	3 x 120 m
GSHP + AE	53.0	189	35.1	5.06	2 x 115 m
GSHP + DC	70.6	405	75.3	5.72	2 x 95 m

Table C.4 – Sensitivity of TRNSYS simulation results to electricity rate. All other parameters are kept the same as in the base case scenario. Results for 14 ¢/kWh$_e$ are provided in Table 9.4.

Case	TCO ($1,000)	Electricity Consumption (MWh$_e$)	CO_2 Emissions (million metric tons)	Average HP COP [-]	BHE Configuration
10 ¢/ kWh$_e$ Electricity Rate					
GSHP	74.2	460	85.6	4.20	3 x 150 m
GSHP + AE	53.3	228	42.5	4.15	2 x 145 m
GSHP + DC	63.0	438	81.4	5.22	2 x 115 m
ASHP	61.2	589	109.6	3.28	N/A
ASHP + AE	44.7	314	58.4	3.02	N/A
12 ¢/ kWh$_e$ Electricity Rate					
GSHP	80.9	460	85.6	4.20	3 x 150 m
GSHP + AE	56.6	222	41.3	4.27	2 x 150 m
GSHP + DC	69.4	425	79.1	5.40	2 x 125 m
ASHP	70.0	589	109.6	3.28	N/A
ASHP + AE	49.4	314	58.4	3.02	N/A
16 ¢/ kWh$_e$ Electricity Rate					
GSHP	93.7	403	75.0	4.80	4 x 142.5 m
GSHP + AE	63.2	222	41.3	4.27	2 x 150 m
GSHP + DC	81.9	416	77.4	5.54	2 x 135 m
ASHP	87.5	589	109.6	3.28	N/A
ASHP + AE	58.7	314	58.4	3.02	N/A

Table C.5 – Sensitivity of TRNSYS simulation results to net discount rate. All other parameters are kept the same as in the base case scenario. Results for 3% net discount rate are provided in Table 9.4.

Case	TCO ($1,000)	Electricity Consumption (MWh_e)	CO_2 Emissions (million metric tons)	Average HP COP [-]	BHE Configuration
5% Net Discount Rate					
GSHP	79.1	460	85.6	4.20	3 x 150 m
GSHP + AE	55.1	222	41.3	4.27	2 x 150 m
GSHP + DC	68.0	425	79.1	5.40	2 x 125 m
ASHP	66.7	589	109.6	3.28	N/A
ASHP + AE	46.2	314	58.4	3.02	N/A
7% Net Discount Rate					
GSHP	72.5	467.5	86.9	4.14	3 x 146.67 m
GSHP + AE	51.4	228	42.5	4.15	2 x 145 m
GSHP + DC	61.9	438	81.4	5.22	2 x 115 m
ASHP	57.4	589	109.6	3.28	N/A
ASHP + AE	40.1	314	58.4	3.02	N/A
9% Net Discount Rate					
GSHP	67.3	467.5	86.9	4.14	3 x 146.67 m
GSHP + AE	48.3	243	45.3	3.89	2 x 135 m
GSHP + DC	57.0	445	82.8	5.12	2 x 110 m
ASHP	50.1	589	109.6	3.28	N/A
ASHP + AE	35.3	314	58.4	3.02	N/A

Table C.6 – Sensitivity of TRNSYS simulation results to drilling cost. All other parameters are kept the same as in the base case scenario. Results for 50 $/m are provided in Table 9.4.

Case	TCO ($1,000)	Electricity Consumption (MWh_e)	CO_2 Emissions (million metric tons)	Average HP COP [-]	BHE Configuration
30 $/m Drilling Cost					
GSHP	76.1	391	72.7	4.95	4 x 150 m
GSHP + AE	53.6	189	35.3	5.02	3 x 133.33 m
GSHP + DC	70.1	405	75.4	5.72	2 x 150 m
70 $/m Drilling Cost					
GSHP	96.6	460	85.6	4.20	3 x 150 m
GSHP + AE	65.8	228	42.5	4.15	2 x 145 m
GSHP + DC	80.5	438	81.4	5.22	2 x 115 m
90 $/m Drilling Cost					
GSHP	105.5	467	86.9	4.14	3 x 146.67 m
GSHP + AE	71.4	243	45.3	3.89	2 x 135 m
GSHP + DC	85.0	445	82.8	5.12	2 x 110 m

APPENDIX D

NON-DIMENSIONAL NUMBERS, HEAT SOURCE MODEL EQUATIONS, AND DECISION TREES FOR CALCULATING $f_{i,j,m,n}$

This appendix provides the procedure and equations for calculating $f_{i,j,m,n}$, the terms that emerged in Equation (13.1) after discretizing the (slender-body theory) SBT theoretical result for developing the numerical framework (Chapter 13), which was used in the case-studies (Chapter 14). As mentioned in Section 13.2, $f_{i,j,m,n}$ can be interpreted as the temperature rise at the mid-point of element i at the end of time step m due to a unit heat pulse by element j during time step n. Without simplifications, the numerical framework would require for each pipe element at each time step to evaluate the full Equation (12.13) or (12.16), i.e. calculating the full finite cylindrical or line source model and the contributions from all previous and neighboring heat pulses. However, simplifications are possible to save on computational time with no significant loss in accuracy. These simplifications are neglecting the finite radius or length of a pipe element, or neglecting the element as a whole, which translates into different models for calculating $f_{i,j,m,n}$.

Six well-known models are identified to calculate $f_{i,j,m,n}$, ordered from more to less representing the actual geometry and from more to less computationally-intense to evaluate: the Finite Cylindrical Source (FCS) model, Infinite Cylindrical Source (ICS) model, Finite Line Source (FLS) model, Infinite Line Source (ILS) model, Point Source (PS) model, and

Table D.1 – Non-dimensional numbers utilized in equations and decision trees for calculating $f_{i,j,m,n}$. In these numbers, Fo, TDR, SLR, R, L, S, CP, PP, S and E refer to Fourier number, time durations ratio, spacing to length ratio, pipe radius, pipe length, spacing between two pipes, current pulse, previous pulse, start of pulse, and end of pulse, respectively.

$\mathrm{Fo}_{\mathrm{R,CP}} = \frac{\alpha(t_m - t_{m-1})}{R_j^2}$	$\mathrm{Fo}_{\mathrm{L,CP}} = \frac{\alpha(t_m - t_{m-1})}{L_j^2}$	$\mathrm{Fo}_{\mathrm{S,CP}} = \frac{\alpha(t_m - t_{m-1})}{S_{i,j}^2}$
$\mathrm{Fo}_{\mathrm{R,PP,S}} = \frac{\alpha(t_m - t_{n-1})}{R_j^2}$	$\mathrm{Fo}_{\mathrm{L,PP,S}} = \frac{\alpha(t_m - t_{n-1})}{L_j^2}$	$\mathrm{Fo}_{\mathrm{S,PP,S}} = \frac{\alpha(t_m - t_{n-1})}{S_{i,j}^2}$
$\mathrm{Fo}_{\mathrm{R,PP,E}} = \frac{\alpha(t_m - t_n)}{R_j^2}$	$\mathrm{Fo}_{\mathrm{L,PP,E}} = \frac{\alpha(t_m - t_n)}{L_j^2}$	$\mathrm{Fo}_{\mathrm{S,PP,E}} = \frac{\alpha(t_m - t_n)}{S_{i,j}^2}$
$\mathrm{TDR} = \frac{t_m - t_n}{t_n - t_{n-1}}$	$\mathrm{SLR} = \frac{S_{i,j}}{L_j}$	

Table D.2 – Heat source model equations to calculate $f_{i,j,m,n}$ for selected pipe (Carslaw and Jaeger, 1959). The different models are: Finite Cylindrical Source (FCS), Infinite Cylindrical Source (ICS), Finite Line Source (FLS), Infinite Line Source (ILS), Point Source (PS), and Point Neglected (PN) Model.

$f_{i,i,m,m}$ (Selected Pipe & Current Pulse)

FCS: $f_{i,i,m,m} = \frac{2}{\pi^3 k}\int_0^\infty \frac{1-\exp\left(-\phi^2 \mathrm{Fo}_{\mathrm{R,CP}}\right)}{\phi^3\left(J_1^2(\phi)+Y_1^2(\phi)\right)}\mathrm{d}\phi - \frac{1}{4\pi k}\int_{\frac{1}{4\mathrm{Fo}_{\mathrm{L,CP}}}}^\infty \frac{1}{\phi}\mathrm{erfc}\left(\frac{1}{2}\sqrt{\phi}\right)\mathrm{d}\phi$

ICS: $f_{i,i,m,m} = \frac{2}{\pi^3 k}\int_0^\infty \frac{1-\exp\left(-\phi^2 \mathrm{Fo}_{\mathrm{R,CP}}\right)}{\phi^3\left(J_1^2(\phi)+Y_1^2(\phi)\right)}\mathrm{d}\phi$

FLS: $f_{i,i,m,m} = \frac{1}{4\pi k}\mathrm{E}_1\left(\frac{1}{4\mathrm{Fo}_{\mathrm{R,CP}}}\right) - \frac{1}{4\pi k}\int_{\frac{1}{4\mathrm{Fo}_{\mathrm{L,CP}}}}^\infty \frac{1}{\phi}\mathrm{erfc}\left(\frac{1}{2}\sqrt{\phi}\right)\mathrm{d}\phi$

ILS: $f_{i,i,m,m} = \frac{1}{4\pi k}\mathrm{E}_1\left(\frac{1}{4\mathrm{Fo}_{\mathrm{R,CP}}}\right)$

$f_{i,i,m,n}$ (Selected Pipe & Previous Pulses)

FCS: $f_{i,i,m,n} = \frac{2}{\pi^3 k}\int_0^\infty \frac{\exp\left(-\phi^2 \mathrm{Fo}_{\mathrm{R,PP,E}}\right)-\exp\left(-\phi^2 \mathrm{Fo}_{\mathrm{R,PP,S}}\right)}{\phi^3\left(J_1^2(\phi)+Y_1^2(\phi)\right)}\mathrm{d}\phi - \frac{1}{4\pi k}\int_{\frac{1}{4\mathrm{Fo}_{\mathrm{L,PP,S}}}}^{\frac{1}{4\mathrm{Fo}_{\mathrm{L,PP,E}}}} \frac{1}{\phi}\mathrm{erfc}\left(\frac{1}{2}\sqrt{\phi}\right)\mathrm{d}\phi$

ICS: $f_{i,i,m,n} = \frac{2}{\pi^3 k}\int_0^\infty \frac{\exp\left(-\phi^2 \mathrm{Fo}_{\mathrm{R,PP,E}}\right)-\exp\left(-\phi^2 \mathrm{Fo}_{\mathrm{R,PP,S}}\right)}{\phi^3\left(J_1^2(\phi)+Y_1^2(\phi)\right)}\mathrm{d}\phi$

FLS: $f_{i,i,m,n} = \frac{1}{4\pi k}\left[\mathrm{E}_1\left(\frac{1}{4\mathrm{Fo}_{\mathrm{R,PP,S}}}\right) - \mathrm{E}_1\left(\frac{1}{4\mathrm{Fo}_{\mathrm{R,PP,E}}}\right) - \int_{\frac{1}{4\mathrm{Fo}_{\mathrm{L,PP,S}}}}^{\frac{1}{4\mathrm{Fo}_{\mathrm{L,PP,E}}}} \frac{1}{\phi}\mathrm{erfc}\left(\frac{1}{2}\sqrt{\phi}\right)\mathrm{d}\phi\right]$

ILS: $f_{i,i,m,n} = \frac{1}{4\pi k}\left[\mathrm{E}_1\left(\frac{1}{4\mathrm{Fo}_{\mathrm{R,PP,S}}}\right) - \mathrm{E}_1\left(\frac{1}{4\mathrm{Fo}_{\mathrm{R,PP,E}}}\right)\right]$

PS_1: $f_{i,i,m,n} = \frac{L_i}{4\pi k R_i}\left[\mathrm{erfc}\left(\frac{1}{2\sqrt{\mathrm{Fo}_{\mathrm{R,PP,S}}}}\right) - \mathrm{erfc}\left(\frac{1}{2\sqrt{\mathrm{Fo}_{\mathrm{R,PP,E}}}}\right)\right]$

PS_2: $f_{i,i,m,n} = \frac{L_i}{4\pi\sqrt{\alpha\pi k}}\left(\frac{1}{\sqrt{t_m - t_n}} - \frac{1}{\sqrt{t_m - t_{n-1}}}\right)$

PS_3: $f_{i,i,m,n} = \frac{L_i}{8\pi k \mathrm{TDR}\sqrt{\alpha\pi(t_m - t_n)}}$

Point Neglected (PN) model. The PN model simply means setting the temperature contribution to zero by neglecting the element. The equations for these heat source models, as well as the methodology to select the most appropriate model rely on dimensionless numbers, listed in Table D.1. In these numbers, R_j and L_j are the radius and length of pipe element j emitting the heat pulse, $S_{i,j}$ is the spacing between the centers of pipe element i, where the temperature is calculated at, and pipe element j, the source of the heat pulse, TDR refers to the ratio of time durations, SLR refers to spacing-to-length ratio, CP and PP refer to current pulse and previous pulse, and S and E refer to start and end of a previous heat pulse, respectively. Furthermore, the time steps are in general labeled as t_k with t_0 the time starting point set at 0 s. t_m is the current time and t_n is the end time of heat pulse

Table D.3 – Heat source model equations to calculate $f_{i,j,m,n}$ for neighboring pipes (Carslaw and Jaeger, 1959). The different models are: Finite Cylindrical Source (FCS), Infinite Cylindrical Source (ICS), Finite Line Source (FLS), Infinite Line Source (ILS), Point Source (PS), and Point Neglected (PN) Model.

$f_{i,j,m,m}$ (Neighboring Pipes & Current Pulse)

FLS: $f_{i,j,m,m} = \frac{1}{4\pi k} \int_0^{L_j} \frac{1}{S_{i,j}(z')} \operatorname{erfc}\left(\frac{S_{i,j}(z')}{\sqrt{4\alpha(t_m - t_{m-1})}}\right) dz'$

PS_1: $f_{i,j,m,m} = \frac{1}{4\pi k \mathrm{SLR}} \operatorname{erfc}\left(\frac{1}{2\sqrt{\mathrm{Fo}_{\mathrm{S,CP}}}}\right)$

PS_2: $f_{i,j,m,m} = \frac{1}{4\pi k \mathrm{SLR}} \left(1 - \frac{1}{\sqrt{\pi \mathrm{Fo}_{\mathrm{S,CP}}}}\right)$

PN: $f_{i,j,m,m} = 0$

$f_{i,j,m,n}$ (Neighboring Pipes & Previous Pulses)

FLS: $f_{i,j,m,n} = \frac{1}{4\pi k} \int_0^{L_j} \frac{1}{S_{i,j}(z')} \left[\operatorname{erfc}\left(\frac{S_{i,j}(z')}{\sqrt{4\alpha(t_m - t_{n-1})}}\right) - \operatorname{erfc}\left(\frac{S_{i,j}(z')}{\sqrt{4\alpha(t_m - t_n)}}\right)\right] \mathrm{d}z'$

PS_1: $f_{i,j,m,n} = \frac{1}{4\pi k \mathrm{SLR}} \left[\operatorname{erfc}\left(\frac{1}{2\sqrt{\mathrm{Fo}_{\mathrm{S,PP,S}}}}\right) - \operatorname{erfc}\left(\frac{1}{2\sqrt{\mathrm{Fo}_{\mathrm{S,PP,E}}}}\right)\right]$

PS_2: $f_{i,j,m,n} = \frac{L_j}{4\pi\sqrt{\alpha\pi k}} \left(\frac{1}{\sqrt{t_m - t_n}} - \frac{1}{\sqrt{t_m - t_{n-1}}}\right)$

PS_3: $f_{i,j,m,n} = \frac{L_j}{8\pi k \mathrm{TDR}\sqrt{\alpha\pi(t_m - t_n)}}$

PN: $f_{i,j,m,n} = 0$

n. Also, $(t_m - t_{m-1})$ is the time duration of the current heat pulse, and $(t_m - t_{n-1})$ and $(t_m - t_n)$ are the time that has past since the beginning and end of heat pulse n, respectively.

The equations to calculate $f_{i,j,m,n}$ are provided in Tables D.2 and D.3. They are grouped into four categories, corresponding to the four terms in Equation (13.1), by distinguishing between selected ($j = i$) and neighboring ($j \neq i$) pipe elements, and current ($n = m$) and previous ($n < m$) heat pulses. In the equations, $J_1(x)$, $Y_1(x)$, erfc(x), and $\mathrm{E}_1(x)$ refer to first order Bessel function of the first kind, first order Bessel function of the second kind, complimentary error function, and exponential integral, respectively (Abramowitz and Stegun, 1964). The temperature contribution from a previous heat pulse $Q_{i,n}$, emitted during the time period t_{n-1} to t_n, is calculated as the sum of the contributions by a heat pulse with the same strength active from t_{n-1} to t_m (current time) and a heat pulse with

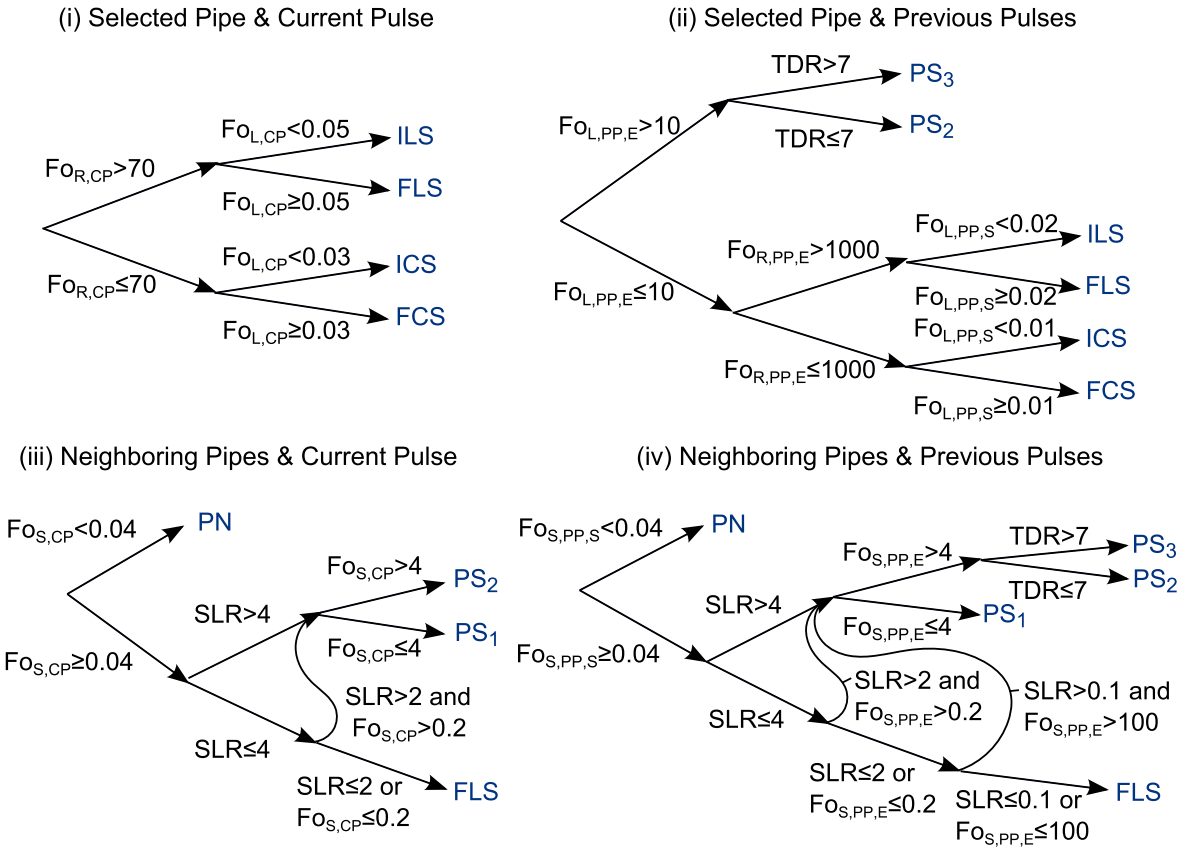

Figure D.1 – Four decision trees are provided to select the least computationally-intense model to still accurately calculate f. FCS, ICS, FLS, ILS, PS and PN refer to Finite Cylindrical Source, Infinite Cylindrical Source, Finite Line Source, Infinite Line Source, Point Source and Point Neglected, respectively. The non-dimensional numbers are defined in Table D.1. The accuracy obtained in calculating f is at least 99% for dominant terms, and 95% for non-dominant terms. These decision trees are valid if $10 \leq \frac{L_j}{R_j} \leq 1000$ for each element j.

opposite strength active from t_n to t_m.

Figure D.1 provides decision trees that have been developed to recommend the least computationally-intense model that still accurately calculates f. The limits in the decision trees are calculated to obtain an accuracy of at least 99% in calculating dominant f and at least 95% for non-dominant f in Equation (13.1). The dominant terms are the f for the current and *recent* pulses for the selected pipe and the *nearby* pipes and are characterized by having a value of up to several orders of magnitude larger than the non-dominant f. Different decision tree limits could be developed for low-, medium- and high-accuracy simulations with corresponding high, medium, and low computational speed. The decision

tree limits have been derived in MATLAB by finding the values of the non-dimensional numbers for which the solution of a certain simplified model deviates no more than e.g. 99% with respect to the solution of the most accurate model available, e.g. the FCS model in the case of the first two decision trees.

References

Abramowitz, M. and Stegun, I. A. (1964). *Handbook of mathematical functions: with formulas, graphs, and mathematical tables*. Number 55. Courier Corporation, Mineola, New York.

Carslaw, H. S. and Jaeger, J. C. (1959). *Conduction of heat in solids*. Clarendon Press, Oxford.